UNIVERSITEIT VAN PRETORIA
UNIVERSITY OF PRETORIA
YUNIBESITHI YA PRETORIA
Denkleiers • Leading Minds • Dikgopolo tša Dihlalefi

Tailoring optical tweezers for quantum dot based fluorescence sensing

by

Ané Kritzinger

Submitted in fulfilment of the requirements for the degree
Master of Chemistry
In the Faculty of Natural & Agricultural Sciences
University of Pretoria
Pretoria
June 2022

Supervisor: Prof PBC Forbes (UP)
Co-supervisor: Prof A Forbes (WITS)

Declaration

I, Ané Kritzinger, declare that the dissertation, which I hereby submit for the degree Master of Chemistry at the University of Pretoria, is my own work and has not previously been submitted by me for a degree at this or any other tertiary institution.

5 June 2022

Abstract

Optical trapping is a venerable topic and has been an invaluable and pioneering tool in biological research, but it has been mostly unexplored by the analytical science community. This study lays the groundwork for a novel analytical technique by combining holographic optical tweezers and fluorescence spectroscopy of quantum dots (QDs).

QDs are artificial semiconducting nanoparticles with fascinating optical properties, making them ideal for fluorescence sensing applications. In this study, QD fluorescent probes fit for optical trapping were created, which included the synthesis of L-cysteine capped CdSe/ZnS core/shell QDs and the coupling thereof to micro-sized polymer beads through EDC/NHS chemistry. The synthesis process was optimized in order to gain control over the QD size, fluorescence emission, adhesion, agglomeration formation and purity of the sample. Several techniques including fluorescence spectroscopy, transmission electron microscopy (TEM), Fourier transform infrared (FTIR) and absorbance spectroscopy were used to characterize the structural and optical properties of the QDs and QD fluorescent probes. To showcase the sensing ability of these QD probes, they were used to detect atrazine, a harmful herbicide, at environmentally relevant surface water concentrations.

Optical trapping or tweezing describes the manipulation of nano- to micro-sized particles through momentum transfer from tightly focused light. In this study, the advantages of employing vectorial light in optical traps were explored, especially for the control of fluorescent particles. A holographic optical tweezer (HOT) that leverages on vectorially structured light with integrated fluorescence detection was

ABSTRACT

built. The setup included a diode laser with wavelength $\lambda = 532$ nm, a spatial light modulator (SLM), an interferometer to combine the beams, an inverted microscope for trapping and imaging, and a photon counting fluorescence detection stage. This advanced setup allowed for the delivery of tuneable forms of light from purely scalar to purely vector beams resulting in tailored intensity gradient landscapes of the trapping beam. Trap stiffness calibration was performed with 2 μm polymer beads and *in-situ* fluorescence measurements of an optically trapped QD probe was achieved. This study focused specifically on propagation invariant vector flat-top beams which showed potential to reduce photobleaching of QDs in a single wavelength optical trap. The aim of the research presented in this dissertation is to advance the nascent field of chemistry applications in optics.

Acknowledgments

This research project would not have been possible without the support and guidance of a rather remarkable group of people.

My supervisor, Professor Patricia Forbes, thank you for believing in me and trusting me with this exciting research. Thank you for always being optimistic, available and ready with advice. My co-supervisor, Professor Andrew Forbes, thank you for welcoming me into your group. I am grateful for your wise guidance, encouragement and creativity that have helped me become a better researcher. It has truly been a privilege to be supervised by two exceptional scientists and I am thankful for the invaluable opportunities you have granted me.

I want to express my gratitude to Dr Valeria Rodríguez-Fajardo for being a terrific mentor, teacher and friend; thank you for helping me find my way in the optics world. I would also like to thank Dr Sifiso Nsibande for all his advice and assistance in the chemistry lab. To all my colleagues at WITS and UP, thank you for your friendship, friendly faces and encouragement.

The three people I am most thankful for are my dad, mom and sister. Thank you for your unwavering support, wisdom, love and the countless cups of tea.

Lastly, all the glory to my Lord and Saviour, Jesus Christ.

Research outputs

Conference presentations

Ané Kritzinger, Valeria Rodríguez-Fajardo, Sifiso A Nsibande, Andrew Forbes and Patricia BC Forbes, "Fluorescence spectroscopy of CdSe/ZnS core/shell quantum dots in an optical tweezer", **Poster presentation** at the Royal Society of Chemistry Chemical Nanosciences and Nanotechnology Early Career Virtual Poster Symposium, 24 March 2021.

Ané Kritzinger, Valeria Rodríguez-Fajardo, Sifiso A Nsibande, Andrew Forbes and Patricia BC Forbes, "Trapping quantum dot-tagged beads with an optical tweezer", **Oral flash talk** at The Royal Society of Chemistry and The South African Chemical Institute's Young Chemists' Symposium 2021, 8-9 July 2021. (*Won second prize for the best MSc flash talk.*)

Ané Kritzinger, Valeria Rodríguez-Fajardo, Sifiso A Nsibande, Andrew Forbes and Patricia BC Forbes, "Fluorescence spectroscopy of quantum dots in an optical tweezer", **Oral presentation** at the 2021 annual conference of the South African Institute of Physics, 26-30 July 2021.
(*Won the prize for the best MSc presentation in the Photonics division.*)

Ané Kritzinger, Valeria Rodríguez-Fajardo, Patricia BC Forbes and Andrew Forbes, "Vectorial flat-top beams for optical trapping", **Oral presentation** at the 2021 OSA-SA Photonics conference, 19-21 September 2021, Stellenbosch, South Africa.

Ané Kritzinger, Valeria Rodríguez-Fajardo, Sifiso A Nsibande, Andrew Forbes and Patricia BC Forbes, "A vectorial structured light holographic optical trap for control of fluorescent particles", **Oral presentation** at SPIE Photonics Europe 2022, 3-7 April 2022, Strasbourg, France.

Conference proceeding

Ané Kritzinger, Valeria Rodríguez-Fajardo, Sifiso A Nsibande, Andrew Forbes and Patricia BC Forbes, A vectorial structured light holographic optical trap for control of fluorescent particles, Proc. SPIE 12152, Mesophotonics: Physics and Systems at Mesoscale, 121520A (24 May 2022). DOI: 10.1117/12.2626569 [Full text in Appendix C.1]

Journal paper

Ané Kritzinger, Andrew Forbes and Patricia BC Forbes. Optical trapping and fluorescence control with vectorial structured light. *Nanoscale* (Submitted) [Full text in Appendix C.2]

Co-author journal paper

Isaac Nape, Keshaan Singh, Asher Klug, Wagner Buono, Carmelo Rosales-Guzmán, Amy McWilliam, Sonja Franke-Arnold, **Ané Kritzinger**, Patricia BC Forbes, Angela Dudley and Andrew Forbes. Revealing the invariance of vectorial structured light in perturbing media. *Nature Photonics*. (Accepted) [Full text in Appendix C.3]

Contribution: performed the optical trapping experiments.

Contents

List of Figures

List of Tables

Abbreviations

APD	Avalanche photodiode
CAM	Complex amplitude modulation
CCD	Charge coupled device
CD	Conduction band
CPS	Counts per second
D-M	D-shaped mirror
DMDCS	Dimethyldichlorosilane
DMD	Digital micromirror device
DM	Dichroic mirror
EDC	1-Ethyl-3-(3-dimethylaminopropyl) carbodiimide hydrochloride
EDX	Energy-dispersive X-ray spectroscopy
FRET	Förster resonance energy transfer
FTIR	Fourier-transform infrared spectroscopy
FWHM	Full width at half maximum
GLMT	Generalized Lorenz-Mie theory
HOT	Holographic optical tweezers
HWP	Half wave plate
LCoS	Liquid crystal on silicon

LC	Liquid crystal
LED	Light emitting diode
LG	Laguerre-Gaussian
NA	Numerical aperture
NHS	N-hydroxysuccinimide
OA	Oleic acid
ODE	Octadecene
PBS	Polarizing beam splitter
PXRD	Powder X-ray diffraction
QD	Quantum dot
QWP	Quater wave plate
QY	Quantum yield
Rh	Rhodamine 6G
SLM	Spatial light modulator
TEM	Transmission electron microscope
TIRF	Total internal reflection fluorescence
TOPO	Trioctylphosphine oxide
TOP	Trioctylphosphine
TPE	Two-photon excitation
VB	Valence band

Chapter 1

Introduction and overview

The release of pesticides, heavy metal ions, pharmaceutical products and other chemical pollutants into water bodies is a major threat to environmental sustainability. The ever pressing need to monitor the levels of these pollutants in water is the driving force behind the research presented in this dissertation.

The movement towards using nanoparticles for environmental sensing and monitoring has gained a lot of momentum in recent years [1–4]. Compared to conventional sensing techniques, nanoparticles have proven to enhance sensitivity, increase selectivity, add simplicity and speed up the detection process. One example of such a nanomaterial are quantum dots (QDs) which are artificial semiconducting nanocrystals with interesting optical and structural properties, making them an ideal tool for fluorescence sensing applications [5,6].

With the development of single molecule technologies came new insight into the structure and dynamics of single molecules that are masked in ensemble or bulk analysis [7–9]. These technologies have also allowed ultra-sensitive detection, with limits of detection as low as pico and even femtomolar [10]. Arguably the most famous single-molecule technique is optical tweezers, which make use of tightly focused laser light to trap and manipulate nano- to micro-sized particles. While optical tweezing has revolutionized biological research [11], it has been mostly unexplored by the analytical science community. This research project paves a way towards an ultra-sensitive analytical technique by combining optical tweezers

with fluorescence spectroscopy of QDs.

To make this technique more versatile and help overcome issues that arise when integrating fluorescence spectroscopy into optical tweezers, like photobleaching, a third component may be introduced into the system – structured light [12,13]. The employment of structured light (varying the intensity, phase and polarization of light) in optical tweezers has made it possible to not only trap but to direct, move and orient particles. These structured light traps are a well-established technique today and since most structured beams are created by means of a hologram, they are called holographic optical tweezers (HOTs) [14,15]. Structured light beams can broadly be classified as scalar or vector beams. Scalar beams are structured in amplitude and phase whereas vector beams are tailored in polarization as well. Conventionally, HOT setups employ scalar light, however, the added benefits of vectorial light traps have only been explored in recent years [16–18]. In this dissertation, the advantages of a vectorial HOT are further explored, especially for the control of fluorescent particles.

The three-fold combination of fluorescence spectroscopy of quantum dots, optical tweezers and structured light is therefore investigated in this study for an ultimate application in pollutant sensing. The proposed novel analytical instrument is illustrated conceptually in Figure 1.1. Here a QD probe (synthesized using bead assisted chemistry) is optically trapped in a microfluidic channel that allows water samples to flow through. The fluorescence emission from the QD probe, measured *in-situ* and excited with the trapping laser, is used to determine the presence of the pollutants (qualitatively or quantitatively). In this instrument, the trapping beam can be tailored to not only be the conventional Gaussian mode but any structured light beam to increase the potential applications thereof.

The aim of this research project was to complete three 'building blocks' needed to
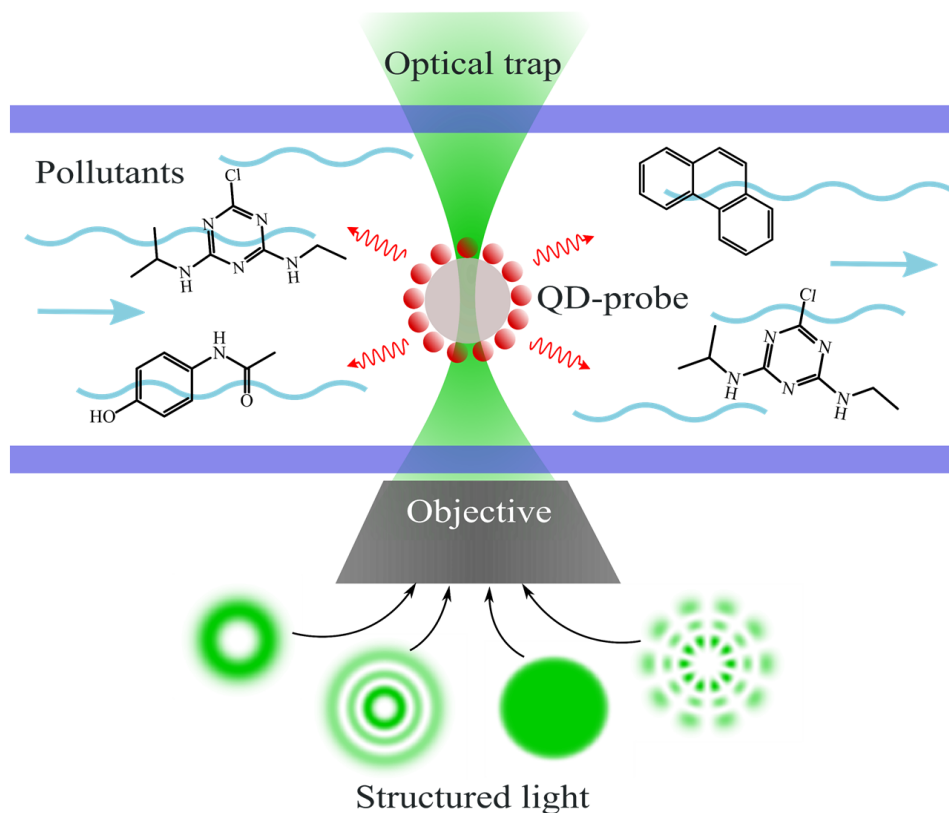
Figure 1.1: A conceptual illustration of the novel analytical technique. A QD fluorescent probe is optically trapped in a holographic optical tweezer setup. The sample is in a microfluidic channel that allows a water sample to flow through, using the fluorescence emission of the QD probe to detect the presence of organic pollutants. The optical tweezer is tailored so that any structured light beam can be used as the tightly focused trapping beam.

ultimately develop this novel analytical technique. Firstly, QD fluorescent probes that can be trapped in an optical tweezer setup were synthesised (Chapter 2). Secondly, an optical tweezer setup with an integrated fluorescence microscope was built (Chapter 3). Lastly, structured light was added to create a vectorial HOT (Chapter 4).

Chapter 2 starts with a discussion on QDs, explaining their optical properties, synthesis methods and applications. The synthesis process of L-cysteine capped CdSe/ZnS QDs and the coupling thereof to micro-sized polymer beads are reported

in this chapter. TEM analysis, fluorescence spectroscopy, FTIR analysis and absorbance spectroscopy were some of the methods used to characterize the optical and structural properties of the QDs and QD probes. Lastly, to prove the QD probes can be used to detect pollutants, atrazine (a harmful herbicide) was detected at environmentally relevant concentrations.

The fundamental concepts of optical tweezers are discussed in **Chapter 3**, including the trapping beam requirements, the optical forces inside the trap and the main components needed to build an optical tweezer. The experimental setup of an optical trap is presented along with successful trapping of 2 μm diameter particles and trap strength calibration. The final part of this chapter discusses how to experimentally integrate a fluorescence microscope into the setup and shows the fluorescence detection of an optically trapped QD probe.

In **Chapter 4**, structured light and spatial light modulators, the device used to generate these structured beams, are introduced and explained. Here the setup of a vectorial holographic optical tweezer is demonstrated. The specific structured light beam under investigation in this study is a vector flat-top beam. The added benefits of trapping with a vector flat-top beam over the conventional Gaussian beam are discussed theoretically and confirmed experimentally. The effect of these structured light beams on QD photobleaching inside optical tweezers is explored in the last part of Chapter 4. Finally, the conclusion and outlook of this study are presented in **Chapter 5**.

Chapter 2

Quantum dot fluorescent sensors

The synthesis of a quantum dot (QD) fluorescent probe is discussed in this chapter. It starts with an introduction to QDs in Section 2.1. The synthesis and characterization of water-soluble CdSe/ZnS QDs and the coupling thereof to micro-sized polymer beads are presented in Sections 2.2 and 2.3, respectively. Finally, Section 2.4 reports on the detection of atrazine, a water pollutant, using the QD fluorescent probe.

2.1   Introduction to quantum dots

The first work on QDs was published in the early 1980s by the Russian physicist Alexey Ekimov, demonstrating the synthesis of CuCl crystals in a glass matrix [19]. The behavior of these nanocrystals was explained theoretically by Efros in 1982 [20]. Inspired by their work, the American scientist Brus synthesized the first colloidal quantum dots in 1983, these QDs were dispersed in water and were much easier to handle [21]. The term 'quantum dots' however only came later and has since been used to describe these semiconducting nanoparticles [22].

This section will give an introduction to QDs which includes the fundamental concepts of QDs (Section 2.1.1), synthesis and characterization methods (Sections 2.1.2 and 2.1.3), general applications of QDs (Section 2.1.4) and more specifically how they are used as fluorescence sensors (Section 2.1.5).

2.1.1 Quantum dot fundamentals

In bulk semiconductors, electronic energy levels are in the form of a valence band (VB) and a conduction band (CB). Most of the electrons are in the VB and can be excited to the CB if given sufficient energy. The energy difference between the VB and CB is called the bandgap (E_g) of the material. When the dimensions of a semiconductor material are in the nanometer scale, as in the case of QDs, the movement of the electrons is confined and the material exhibits quantum mechanical effects [23]. The energy levels of such nanoparticles become discrete, similar to that of molecules, giving QDs intermediate electronic properties between their bulk semiconductor material and molecules; Figure 2.1 shows the difference in the electronic states of a bulk semiconductor, a nanocrystal semiconductor (QD) and a molecule [24].
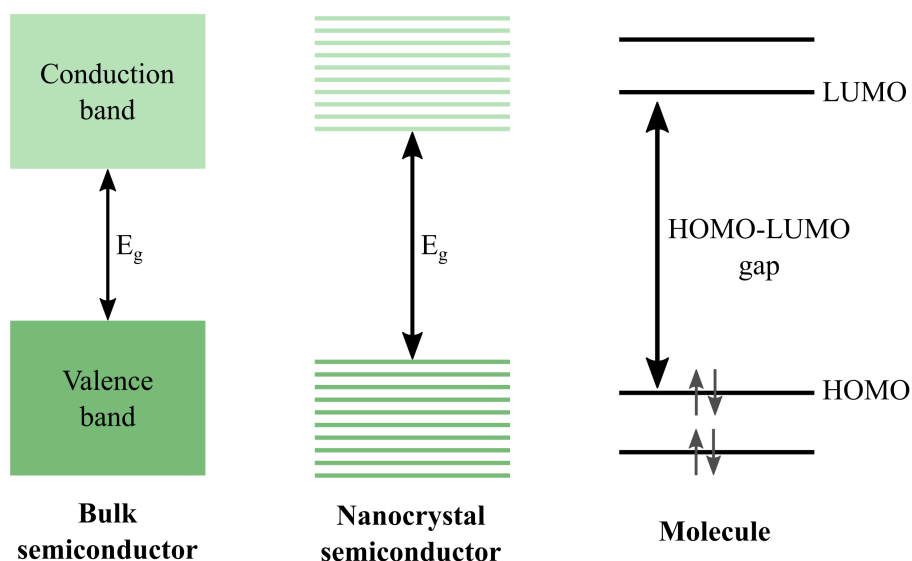
Figure 2.1: Comparison of the energy level diagrams of a bulk semiconductor, nanocrystal semiconductor (QD) and a molecule. The energy levels of a QD are discrete giving QDs electronic properties between that of the bulk material and its molecular analogue. LUMO – lowest unoccupied molecular orbital; HOMO – highest occupied molecular orbital.

If an electron in the VB absorbs a photon with energy equal to or greater than E_g, it can overcome the energy gap, move to the CB and create a hole in the VB (the process is illustrated in Figure 2.2). This electron-hole pair is called an exciton and the distance between the excited electron and the hole is called the exciton Bohr radius. The dimensions of QDs are smaller than the material's exciton Bohr radius, confining the movement of excitons in three dimensions - this is known as quantum confinement [25]. The result of quantum confinement is that the bandgap is dependent on the physical size of the QD. When an excited electron in the CB recombines with a hole in the VB a photon is emitted with an energy dependent on the bandgap of the QD; the final step in Figure 2.2 shows the relaxation of the electron.
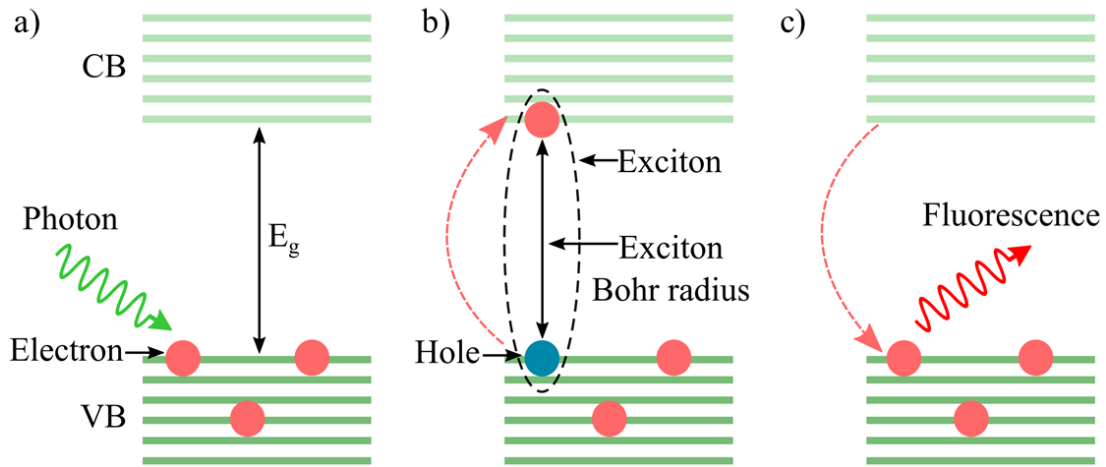
Figure 2.2: Fluorescence principle in QDs. a) An electron in the valence band (VB) absorbs a photon with energy greater or equal to the bandgap (E_g), b) the electron gets excited into the conduction band (CB) and a hole is created in the VB. The electron-hole pair is called an exciton and the distance between them is the exciton Bohr radius. c) When the electron recombines with the hole a photon is released with energy equal to E_g.

When the excited electron relaxes from the CB minimum to the VB maximum as depicted in Figure 2.2c it is called band edge emission. Other pathways of fluorescence emission also occur in QDs. There can exist trap states in the bandgap

due to defects or impurities in which the electron or hole can be trapped, changing the fluorescence emission wavelength of the QD [25]. Excited electrons higher in the CB sometimes lose energy in a non-radiative manner to lower energy levels or to trap states and later relax to the ground state by emitting a photon.

QDs are therefore fluorescent and their bandgap or fluorescence emission wavelength is size-tunable – a larger particle will emit photons with a longer wavelength [26]. Figure 2.3 illustrates the relationship between the size, bandgap and emission spectrum of QDs. As the size of a QD increases, the bandgap decreases and a red-shift of the emission spectrum is seen. The emission spectra presented here were obtained experimentally by growing QDs of different sizes (see Section 2.2.1 for detail).

A model developed by Brus relates the particle size to the bandgap energy (E_g) of a QD [27, 28],

$$E_{g(\text{QD})} = E_{g(\text{bulk material})} + \frac{\hbar^2 \pi^2}{2R^2} \left[\frac{1}{m_e} + \frac{1}{m_h} \right] - \frac{1.8\text{e}^2}{\epsilon R}, \tag{2.1}$$

where R is the radius of the QD, e is the charge of the electron and ϵ the dielectric constant of the solid. m_e and m_h are the effective masses of an electron and a hole in the material (m_e and m_h are unique for each type of QD). The second term in Equation 2.1 is essentially the quantum energy of the well-known particle-in-a-box problem and the third term relates to the Coulombic interaction between the exciton. The bandgap energy is increased by the $1/R^2$ term and decreased by the $1/R$ term. So for small R values, the effective bandgap will increase with decreasing particle size (refer to Figure 2.3).

Although the size-tunable fluorescence emission of QDs is their most famous property, QDs have multiple other advantageous properties making them an irreplaceable tool in the chemistry toolbox. QDs have broad absorption spectra
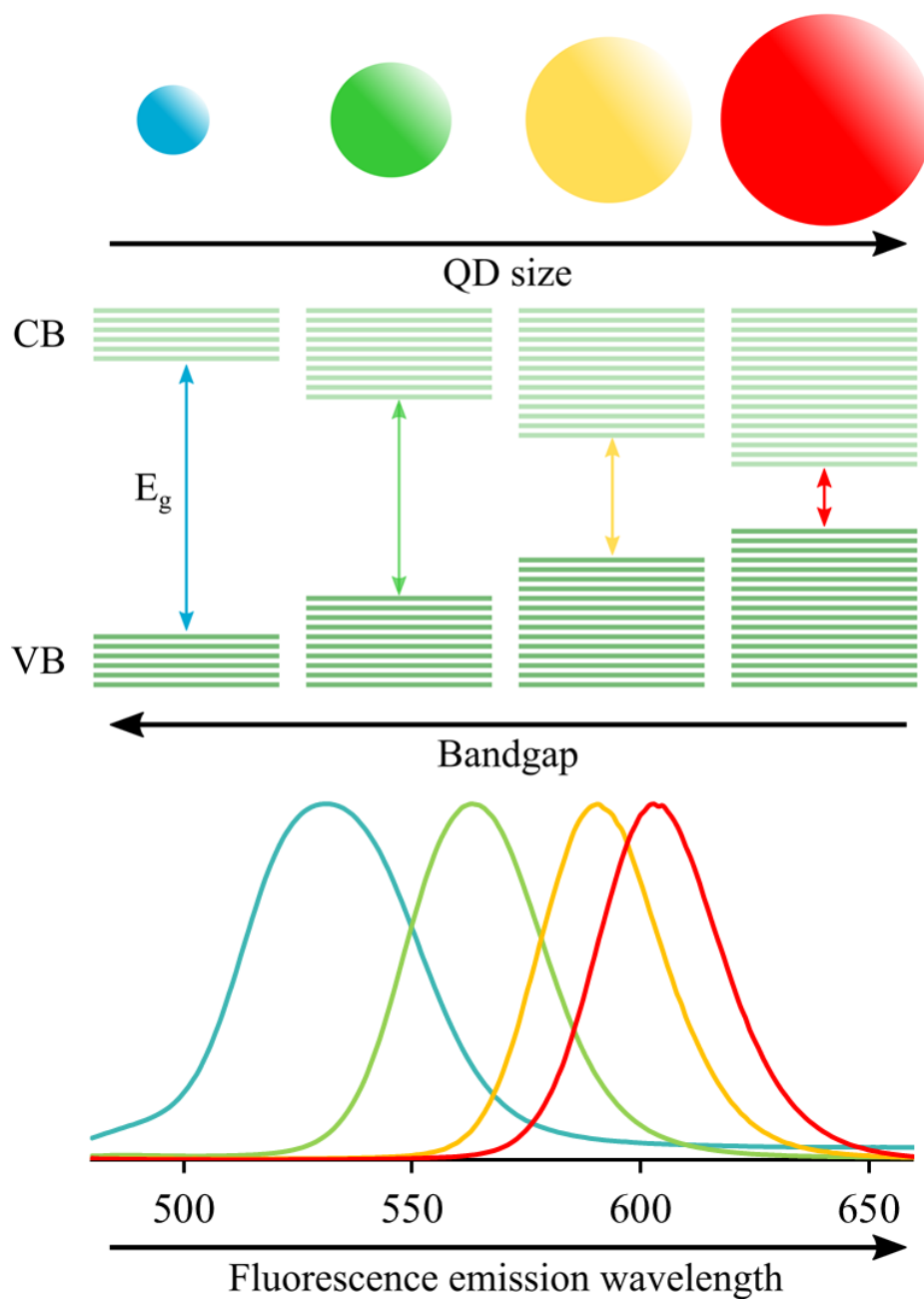
Figure 2.3: Bandgap energy and emission wavelength variation as the size of a QD changes. Larger particles have a smaller bandgap, a red-shift is therefore seen in the emission spectra as the particle size increases.

and narrow symmetrical emission spectra [29]. Their long fluorescent lifetimes, high quantum yields and good photostability are some of the superior properties of QDs compared to organic dyes [30]. These properties make QDs highly favorable for fluorescent sensing, labeling and imaging. QDs can also exhibit the process of multiple exciton generation, in which a single absorbed photon can excite more than one electron giving QDs exciting applications in solar cells [25].

The major drawback of QDs is their potential toxicity, especially for *in vivo* studies [31]. The health and environmental risks of nanoparticles due to their small size are still uncertain. Multiple factors including QD size, composition, structure (core vs. core/shell), concentration and coating can play a role in the toxicity of QDs [32]; the toxicity therefore differs greatly from one type of QD to another. The main concern is the heavy metals that QDs are usually made of, especially cadmium. Cd is a popular metal to use in the core of QDs but it is a toxic material. To prevent leakage of heavy metals like Cd, the inner core of the QD can be capped with a less toxic material such as ZnS to form a shell; adding other capping agents like bovine serum albumin or silica also helps to reduce their toxicity [33]. More environmentally friendly materials, such as carbon and silicon, are also being used to make QDs with great success and promising applications [34, 35].

2.1.2 Synthesis methods

QDs mainly consist of semiconductors or metals like cadmium, tellurium, selenium, indium and zinc. The synthesis methods of QDs can broadly be divided into two groups: (1) the bottom-up and (2) the top-down approaches [36]. In the latter approach, QDs are obtained by etching a bulk semiconductor to obtain nanosized particles. Techniques such as electron beam lithography, electrochemistry, chemical etching and reactive ion etching have been successfully used to obtain QDs [25, 37].

The top-down approach is however slow and requires expensive equipment and is therefore not a routinely used technique [36].

The bottom-up approaches refer to methods where small units (atoms, molecules or ions) self-assemble to form nanoparticles. Some of the bottom-up techniques include the sol-gel method, chemical vapour deposition, microemulsion, spray pyrolysis and hot-injection colloidal synthesis; more detail on these methods can be found in references [25] and [37]. The colloidal synthesis approach is the most popular and well-studied method; it is also the method of choice for the synthesis of QDs in this study. The colloidal method gives precise control over the QD size and results in monodispersed solutions of QDs with a small size distribution [38].

Before giving more detail about the colloidal synthesis method, we must first consider the structure of QDs. QDs usually consist of a core/shell type structure, where the core refers to the inner materials and the shell to a thin layer of material surrounding the core. Examples of core compositions are CdSe, CdS, GaAs, ZnSe, HgTe and InAs, just to name a few. QDs can consist of only a core, but the addition of a shell prevents leakage of heavy metals from the core, increases the quantum efficiency, stabilizes the QDs and assists with surface modifications [39]. The most common is a ZnS shell, but other shells like InP, CdSe and silica have also been reported [37]. The notation core/shell is used to describe QDs, therefore CdSe/ZnS QDs refer to QDs that have a CdSe core and a ZnS shell. The third component of QDs is the organic molecules (ligands) on their surface. These molecules can be hydrophobic or hydrophilic depending on the type of QD, the synthesis method followed and the end application of the QD [37]. Popular hydrophobic and hydrophilic ligands are trioctylphosphine oxide (TOPO) and L-cysteine, respectively [40]. Figure 2.4 illustrates the structure of a QD including the core, shell and organic ligand.
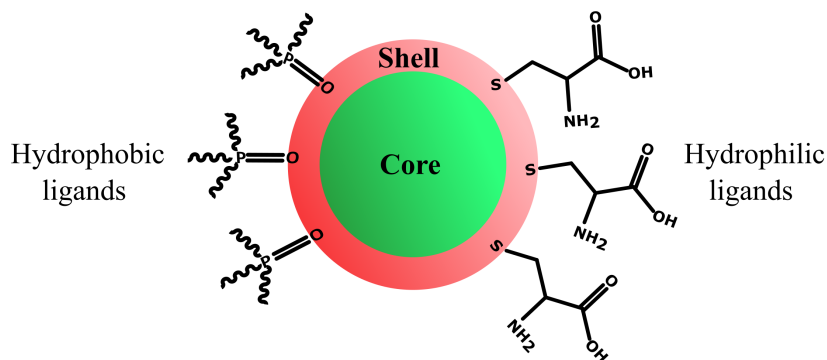
Figure 2.4: The core/shell structure of a QD capped with either hydrophobic or hydrophilic ligands. A common hydrophobic capping agent is trioctylphosphine oxide (TOPO) whereas a common hydrophilic capping agent is L-cysteine.

In the hot-injection colloidal synthesis method, semiconductor precursors are injected into a hot solution of an organic solvent to produce the quantum dots [38]. This reaction requires organometallic precursors, organic solvents and a surfactant (the solvent usually acts as the surfactant as well). The precursor must be carefully chosen since it needs to dissociate to create active species that can nucleate and form nanocrystals. The choice of precursor depends on the specific metal; for example elemental selenium is used as a precursors when Se is added in the core or shell but Cd-salts or Cd-phosphonates are preferred Cd-precursors [38]. The reaction is done under temperatures of around 300 °C, thus organic solvents that can be used at such high temperatures include octadecene, TOPO or hexadecylamine. The size of the QDs is controlled by the injection speed, temperature and growth time [37]. Detail of the colloidal synthesis method followed in this study is given is Section 2.2

Most QDs synthesized by the hot-injection method are hydrophobic due to the octadecene and TOPO ligands on their surface, they are therefore soluble in non-polar solvents like toluene and hexane. Most environmental and biological

applications require water-soluble particles [29]. The QDs can be made water-soluble by 1) exchanging the hydrophobic ligands with hydrophilic ones or by 2) encapsulating the QDs and their hydrophobic ligands with an amphiphilic molecule like a phospholipid or 3) by adding a functionalized silica coating [38].

2.1.3 Characterization techniques

A range of techniques can be used to characterize the optical and structural properties of QDs. Here, the working principle of the techniques and the QD properties they elucidate are briefly summarized; see the given references for a more detailed and technical discussion on each technique.

UV-Vis spectroscopy is used to determine the absorption (or transmission) spectrum of compounds [41]. The absorption of QDs is particularly important since this will decide which wavelengths are suitable for fluorescence excitation. As already mentioned, QDs absorb over a broad range of wavelengths, usually having maximum absorption at the shorter wavelengths thereafter decreasing until little absorbance is seen for the near infra-red wavelengths. Because of the broad absorption spectrum, several excitation sources (from UV to visible light) can be used for QDs - a superior property of QDs compared to other dyes.

Fluorescence spectroscopy on the other hand measures the emission spectrum of compounds. Here, a monochromatic light source is used to excite electrons in the molecule from the ground state to some excited state (as discussed in Section 2.1.1), then the emitted radiation spectrum as the electrons relax back to the ground state is measured [42]. The intensity of the emitted light is proportional to the excitation intensity in fluorescence spectroscopy, whereas in absorbance spectroscopy the ratio of the incident and transmitted intensity is measured [43]. The emission spectrum can also be used to infer secondary information like the

QD bandgap, the presence of trap states and the size distribution [42].

UV-Vis and fluorescence spectroscopy are used to determine an important optical property of QDs (or any fluorophore) namely the quantum yield (QY). QY is the ratio of the emitted photons to the absorbed photons; it is therefore a measure of the fluorescence efficiency or quality of the QD [42]. Another way to think about QY is that it measures the fraction of electrons that decay through radiation (emitting a photon), not through other non-radiative processes like heat or vibration dispersion. The QY can either be determined through a comparative method using a reference standard with a known QY like rhodamine 6G or the absolute QY can be measured with an integrating sphere [44, 45].

Transmission electron microscopy (TEM) is used to visualize QDs since this technique has a spatial resolution of only a few nanometers. TEM works on the same principle as a conventional light microscope, but instead of using light to image the sample, it uses an electron beam; since the electron beam has a smaller wavelength than light, it can reach a much higher resolution. In TEM, a high-energy electron beam is focused onto a thin sample. After the electrons interact with the sample, the transmitted electrons are detected with a fluorescent screen or digital device allowing us to form an image [46]. TEM is therefore used to determine the structural integrity, morphology and size distribution of the QDs.

Energy-dispersive X-ray spectroscopy (EDX) is a method used for determining the elemental composition of samples with a high spatial resolution [47]. This method is usually combined with TEM in order to visualize as well as map the elemental composition of a sample. In TEM/EDX, the incident high energy electron beam used to visualize the sample also excites atoms in the sample which then emits X-rays distinctive of a specific element.

In powder X-ray diffraction (PXRD) a characteristic diffraction pattern of the

bulk powder is obtained by irradiating the sample with X-rays [47]. This technique is used to determine the crystal structure and lattice parameters of QDs, the purity of a sample can also be confirmed by comparing the diffraction pattern with standard references. The most common crystal structures of quantum dots are hexagonal wurtzite or cubic zinc blende [37, 48].

In order to characterize the chemical composition of the QD surface, Fourier-transform infrared spectroscopy (FTIR) is used. In FTIR, the interaction (transmittance or absorbance) of infrared light with molecules is measured. The chemical composition of compounds can be inferred from the IR spectra since different vibrational modes of molecules absorb different frequencies [49]. Therefore, from the peak positions of the FTIR spectrum (usually measured from 400 cm^{-1} to 4000 cm^{-1}) the molecules or functional groups present on the surface of QD can be identified.

Lastly, Raman spectroscopy (just like FTIR) is used to determine the vibrational modes of a sample which are used to identify molecules and functional groups in the sample. Where FTIR relies on the absorption of light, Raman spectroscopy uses light scattering (more specifically, the scattered light with a different wavelength than that of the incident light). Raman spectroscopy is not only used to obtain the chemical composition of samples but information regarding the crystallinity of sample can also be inferred [50].

2.1.4 Applications

The development of QD-technologies has evolved into a field of its own, QDs have come a long way from sitting in a glass matrix in 1981 with little application, to being in our commercial television displays today. LEDs made from QDs have a high color quality (better than that of the high-definition TV) due to their

accurate spectral tunability and narrow emission peaks ($\sim$ 30 nm FWHM), making QD-LED displays more vibrant and closer to 'real life' colors [51]. QD-LEDs are also more energy efficient and therefore have a promising future in display technology.

QDs have been extensively used for biological labelling and imaging [52, 53]. In biological imaging, different dyes are use to 'stain' tissues or cells that have different molecular properties with different colors, QDs assist with this since their colour and surface chemistry can easily be modified to target specific molecules [54]. Their high quantum yields and resistance to photobleaching make QDs superior to organic dyes [30] in this regard. Due to their narrow emission peaks, QDs have also helped simplify simultaneous detection of multiple colour signals [29].

QD-based solar cells have gained a lot of attention in recent years; the review by Lin and Peng discusses the current status of these solar cells [55]. There are three main QD solar cells namely, QD-sensitised solar cells, heterojunction solar cells and QD Schottky solar cells [37, 56], however recently QDs have also been incorporated in perovskite solar cells [57].

Another result of the unique properties of QDs is their sensing ability. QDs have been used to detect analytes, including pollutants [58], pesticides [6], metal ions [59], enzymes [59], antibiotics [60], food ingredients and contaminants [61] and a myriad more. The principle of sensing with QDs is explained in Section 2.1.5.

QDs have also found applications in catalysis [62], electrochemistry [63], QD-lasers [64] and quantum computing [65].

2.1.5 Principle of fluorescence sensing with QDs

QDs can be used as sensors since their fluorescence emission is extremely sensitive to the surface environment. The presence of a target analyte can result in either

fluorescence quenching or enhancement of the QDs due to a physical or chemical interaction [6]. The change in fluorescence intensity therefore allows for quantitative detection of the analyte.

One of the most successful approaches to sensing with QDs is based on Förster or fluorescence resonance energy transfer (FRET) systems. In FRET, energy is transferred from a donor molecule to a nearby acceptor molecule causing fluorescence enhancement or quenching [5]. A non-radiative energy transfer happens upon relaxation of an excited electron in the donor molecule and is due to dipole-dipole couplings between the donor and acceptor molecules [66]. For FRET to occur, the distance between the donor and acceptor molecules usually must be within 10 nm; the specific distance required for an acceptor-donor pair is called the Förster distance [67]. Another requirement of FRET is that the emission spectrum of the donor molecule must overlap with the absorption spectrum of the acceptor molecule; a larger overlap means an increase in the Förster distance [67, 68]. QDs are usually the donors in FRET systems but successful systems where the QDs are acceptors have also been shown [26]. More detail on FRET in QD-systems can be found in the exceptionally in-depth 2017 review of Hildebrandt *et al.* [67], whereas the history and theoretical models of FRET are well-documented by Jones and Bradshaw [66].

The fluorescence intensity or emission wavelength of QDs can also change by physical interaction where analyte molecules (usually metal ions) passivate the QD surface or create defects on the surface that creates new pathways for non-radiative energy loss [24, 26]. Sensing with QDs has also been achieved through charge transfer or electron transfer mechanisms [67, 69].

The quality of the QD sensors, like their sensitivity and selectivity, mainly depends on the coating, capping molecules, and surface chemistry of the QDs [58]. Many

surface modification strategies have been developed to increase the selectivity of QD sensors [6, 59, 68].

2.2 Synthesis of L-cysteine capped CdSe/ZnS quantum dots

This section will report on the synthesis of L-cysteine capped CdSe/ZnS QDs used in this study. The choice of QDs is based on research previously done by our group where CdSe/ZnS QDs were used for pollutant detection [70–72]. The hot-injection colloidal synthesis method was used since it yields QDs with high QY, narrow size distribution and lets the researcher finely control the size and consequently the emission wavelength of the QDs [37]. The synthesis of QDs falls in both the material and molecular chemistry fields; this makes the reproducibility of QD synthesis difficult since it is exceptionally sensitive to conditions like temperature, injection speed and reaction time [38]. The reason for functionalizing the QD surface with L-cysteine is two-fold. Firstly, these QDs will be used for water pollutant detection thus they need to be water-soluble. Secondly, the amine group in L-cysteine enables coupling to micro-sized beads containing carboxyl groups through EDC/NHS chemistry (explained in Section 2.3).

This section starts with a detailed description of the synthesis method followed (Section 2.2.1) and the characterization of the QDs is presented in Section 2.2.2. The synthesis method was optimized by four repetitions with slight changes each time to ensure high-quality QDs with properties fit for our application. Section 2.2.3 reports on the optimization process and gives insight into the nuances of the synthesis method.

In this study, the QDs will be used as sensor probes in an optical tweezer which

is discussed in Chapter 3. The setup of the optical tweezer includes a longpass dichroic mirror (Thorlabs, Germany); the transmittance of this mirror is 97 % for wavelengths of 582-825 nm. In order to detect the fluorescence emission of the QDs in the optical tweezer setup, it needs to be transmitted by the dichroic mirror and therefore have an emission wavelength greater than 582 nm. To ensure most of the emission peak is longer than 582 nm, a maximum fluorescence emission wavelength of 595 nm or longer was needed.

2.2.1 Method

Chemicals

Cadmium oxide (CdO), octadec-1-ene (ODE), oleic acid (OA), trioctylphosphine oxide (TOPO), selenium (Se), zinc oxide (ZnO), sulfur (S), L-cysteine, methanol and acetone were purchased from Sigma Aldrich (USA). Chloroform, ethanol and potassium hydroxide (KOH) were purchased from Associated Chemical Enterprises (South Africa). Argon gas baseline 5.0 from Afrox (South Africa) was used. Deionized water used during the syntheses was from an in-house Drawell Eco-Q deionized water system (China).

Method overview

Figure 2.5 is a schematic of the synthesis of L-cysteine capped CdSe/ZnS core/shell QDs. The synthesis can be divided into five steps: 1) metal precursor preparation, 2) core nucleation and growth, 3) shell growth, 4) ligand exchange and 5) purification.
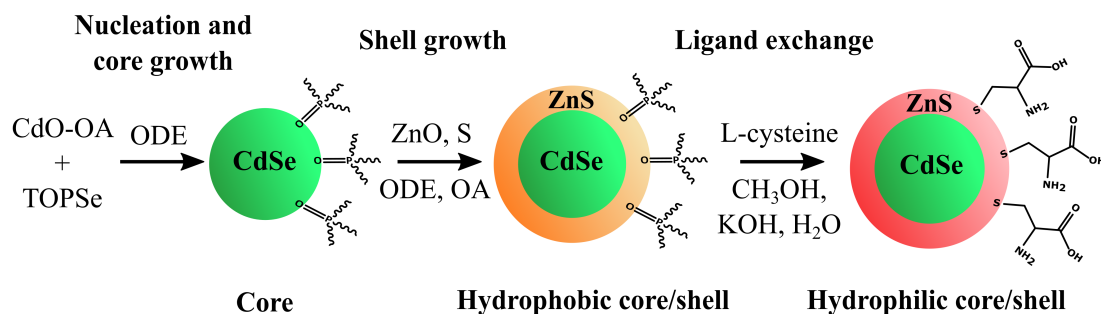
Figure 2.5: L-cysteine capped CdSe/ZnS QD synthesis steps.

Metal precursors

Three precursor solutions were prepared:

- Selenium precursor: 0.30 g Se, 1.94 g TOPO and 25 ml ODE.

- Zinc precursor: 0.21 g ZnO, 10 ml OA and 15 ml ODE.

- Sulphur precursor: 0.087 g S, 10 ml OA, 15 ml ODE.

These solutions were stirred at 40 °C for 5 hr to ensure thorough mixing.

Nucleation, core and shell growth

The one-pot experimental setup used for the synthesis is shown in Figure 2.6; a three-necked round bottom flask was fitted with a condenser, thermometer and an argon gas inlet and positioned on a heating mantle. The whole reaction was done under argon conditions. 1.3 g CdO, 50 ml ODE and 30 ml OA were added to the flask and stirred vigorously at 260 °C until a colourless solution formed indicating the formation of the Cd-OA complex. The Se-precursor was added to the flask (25 ml) and nucleation and core growth were allowed to proceed for 15 min at a temperature of around 240 °C.

After 15 min of core growth, 30 ml of the solution was quickly extracted for later analysis and the epitaxial ZnS shell growth around the core was initiated. 10 ml
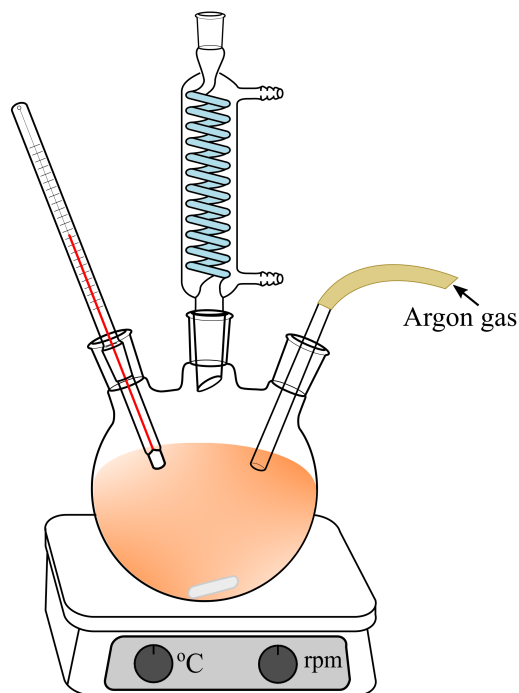
Figure 2.6: Experimental setup for QD synthesis. A three-necked round bottom flask was placed on a heating mantle and fitted with a condenser, thermometer and an argon gas inlet.

of the Zn-precursor, and swiftly thereafter 10 ml of the S-precursor, were added to the core solution. Shell growth was left to proceed for 40 min at a temperature of 240 °C. The fluorescence emission of the QDs was continuously monitored throughout the synthesis (470 nm excitation wavelength). Figure 2.7 shows the fluorescence emission and appearance of the CdSe core QDs under UV-light after 1, 5, 10 and 15 min of core growth and of the CdSe/ZnS core/shell QDs after 10, 20 and 40 min of shell growth. Longer growth time lead to larger particles (smaller bandgap) and therefore a red-shift in the fluorescence emission wavelength occurred. After 40 min the reaction was cooled to room temperature by pouring the solution into a large beaker in an ice bath to stop particle growth and ensure a narrow size-distribution. The QDs were purified with methanol by centrifugation which then yielded the hydrophobic CdSe/ZnS QDs capped with OA and TOPO.
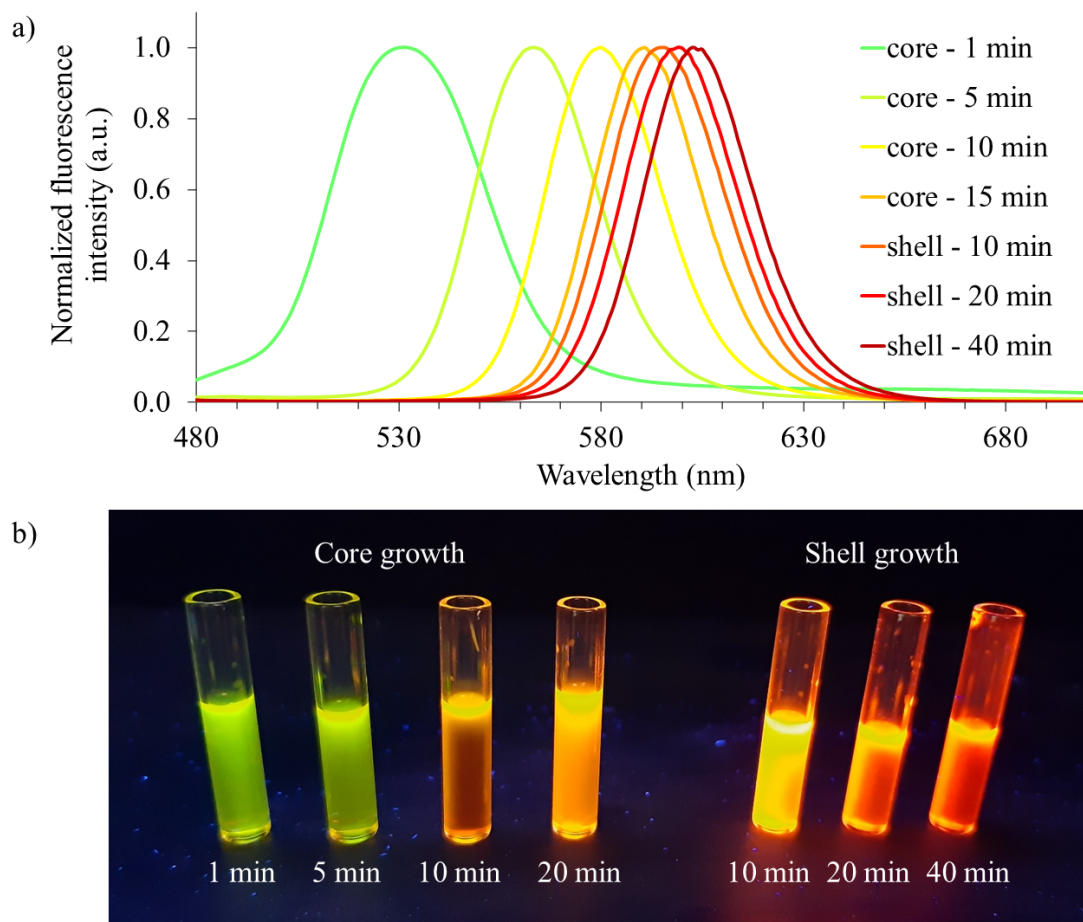
Figure 2.7: a) The normalized fluorescence intensity of the CdSe core and CdSe/ZnS core/shell QDs at different times during the synthesis and b) the corresponding appearance of the QDs under UV-light.

Ligand exchange

A ligand-exchange reaction was carried out to functionalize the surface of the CdSe/ZnS QDs with L-cysteine. A solution of 4.4 g KOH, 60 ml methanol and 3 g L-cysteine was prepared and placed in an ultrasonic bath for 10 min to ensure all the L-cysteine dissolved. The hydrophobic CdSe/ZnS QD solution was suspended in chloroform and added to the L-cysteine solution. Deionized water was slowly added to the mixture (at room temperature) while stirring which changed the

transparent orange solution to milky. After an hour of stirring, the solution was left to stand overnight to ensure complete separation of the organic and aqueous phases.

Purification

The L-cysteine capped QDs, now in the aqueous phase, were purified by centrifugation with ethanol ($\times 4$) and acetone ($\times 2$). Rigorous purification was necessary to remove the excess organic compounds from the surface of the QDs to achieve a monodispersed QD solution with no agglomerates. Figure 2.8 outlines the purification by centrifugation process that was followed. Firstly, around 3 ml of the QDs in the aqueous layer were poured into a 15 ml centrifuge tube and filled with the washing solvent (ethanol and later acetone). The tube was shaken vigorously to remove all the unwanted surfactants (sometimes ultra-sonication was used). The solution was then centrifuged for 10 min at 6000 rpm to precipitate the QDs. The supernatant (containing the unwanted organic compounds) was discarded and the QDs redispersed in deionized water. The process was repeated four times with ethanol and then twice with acetone. After all the QDs were purified they were left to dry in the fume hood.
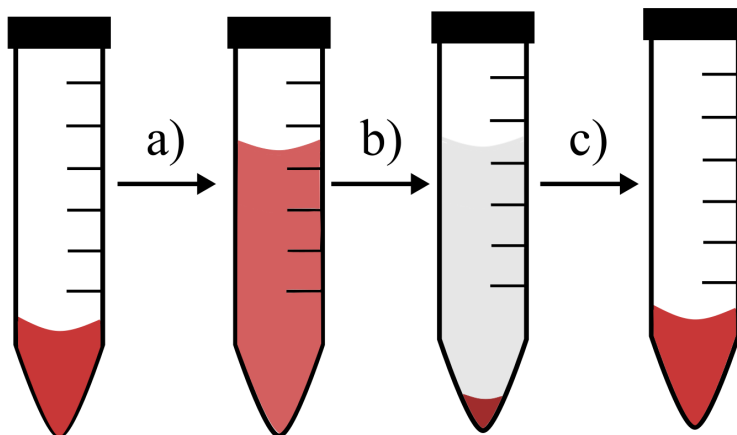
Figure 2.8: Purification by centrifugation steps. The purification process started with the L-cysteine capped QDs dispersed in a small volume of water, a) the washing solvent (ethanol or acetone) was added, shaking or sonication was used to properly disperse the QDs in the solvent. b) The solution was centrifuged for 10 min (6000 rpm) to precipitate the QDs. c) The supernatant was discarded and the QDs redispersed in water. The process was then repeated several times with different solvents.

2.2.2 Characterization

The characterization of L-cysteine capped CdSe/ZnS QDs are given in this section. Small amounts of the hydrophobic CdSe core QDs and CdSe/ZnS core/shell QDs were extracted during the synthesis and characterized to compare with the final product where relevant.

Apparatus

Fluorescence emission spectra were recorded on a Horiba Jobin Yvon Fluoromax-4 spectrofluorometer (Horiba Instruments Inc., USA). UV-visible absorption measurements were recorded on a Cary Eclipse spectrophotometer (Varian Pty Ltd, Australia). Transmission electron microscopy (TEM) images were taken using a JEOL JEM 2100F (JOEL Ltd, Japan) operated at 200 kV. ImageJ was used for image analysis of the TEM images to obtain the size distribution of the QDs.

Carbon film 200 Mesh Cu grids were used for TEM analysis, purchased from Agar Scientific (UK). FTIR measurements were recorded on a Bruker Alpha-T spectrometer (Bruker Optik GmbH, Germany). Fluorescence microscopy was done with a Zeiss LSM 880 confocal laser scanning microscope (Germany). Rhodamine 6G, purchased from Sigma Aldrich (USA), was used as the reference for determining the QY of the QDs.

UV-vis absorbance

The absorbance spectrum of the L-cysteine capped QDs is shown in Figure 2.9. The broad absorbance spectrum is characteristic of QDs. The two absorption wavelengths indicated on the spectrum were of importance during this study. Firstly, 470 nm was the excitation wavelength used for fluorescence emission monitoring during synthesis and for characterization purposes. While synthesising QDs the absorbance spectrum is not known but tracking the fluorescence emission as the particles grow is necessary; 470 nm is therefore a 'safe' choice for excitation since most QDs absorb well at this wavelength. The second important wavelength was 532 nm since this was the wavelength of the laser in the optical tweezer setup used for excitation (see Section 3.2.1 for detail).
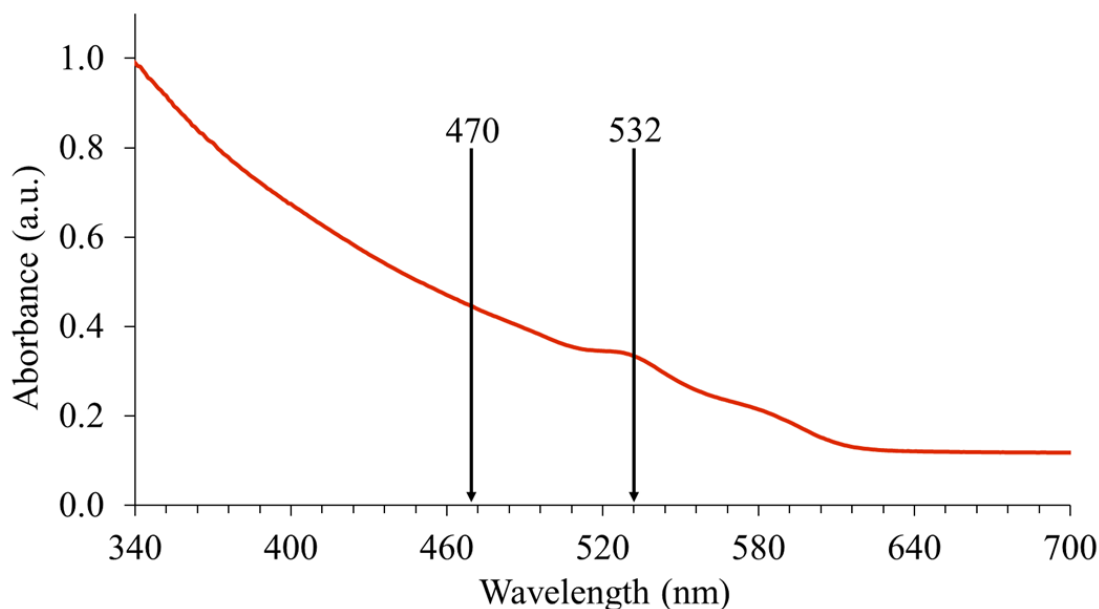
Figure 2.9: UV-vis absorbance of L-cysteine capped CdSe/ZnS QDs in water.

Fluorescence emission

The normalised fluorescence spectra of the CdSe, CdSe/ZnS and L-cysteine capped CdSe/ZnS QDs are shown in Figure 2.10. The inset in Figure 2.10 shows the appearance of these QDs under UV-light. The fluorescence emission peak of the core was at 574 nm, the shell was then added and allowed to grow until the emission was 584 nm. The shell growth therefore caused a red-shift of 10 nm in the fluorescence emission. A further red-shift of 18 nm was seen upon functionalization of the QD surface with L-cysteine which resulted in a final QD product with a fluorescence emission peak at 602 nm. As expected, the emission spectra were symmetrical and narrow; the full width at half maximum (FWHM) of the L-cysteine capped QDs was 37 nm.
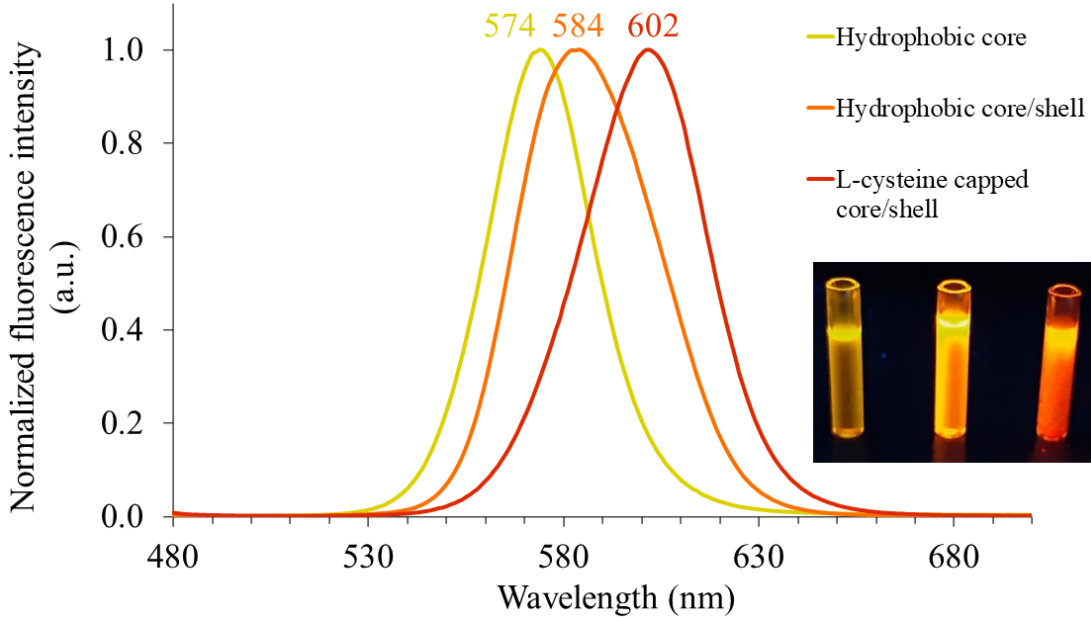
Figure 2.10: The normalized fluorescence intensity (excitation wavelength 470 nm) of the hydrophobic CdSe QDs, the hydrophobic CdSe/ZnS QDs (in chloroform) and the L-cysteine capped CdSe/ZnS QDs in water. The inset shows the appearance of these QDs under UV-light in order of increasing emission wavelength.

Quantum yield

As mentioned in Section 2.1.3, the QY of a fluorophore is the ratio of emitted photons to absorbed photons. The comparative method was used to determine the QY (Φ_{QD}) of the QDs using rhodamine 6G (Rh) as the reference [44, 73].

$$\Phi_{\mathrm{QD}} = \Phi_{\mathrm{std}} \cdot \left(\frac{F_{\mathrm{QD}}}{F_{std}} \right) \cdot \left(\frac{A_{std}}{A_{\mathrm{QD}}} \right) \cdot \left(\frac{n_{QD}^2}{n_{std}^2} \right), \tag{2.2}$$

where F is the integrated fluorescence intensity, A the absorbance at the excitation wavelength and n the refractive index of the solvent used for the standard Rh sample (std) and the QD sample.

To more accurately determine the QY of the QDs (relative to Rh), the absorbance

27

and fluorescence emission spectra of the L-cysteine capped CdSe/ZnS QDs and the standard Rh were determined at five different concentrations (see Figures 2.11a and b). In order to minimize re-absorption effects in the samples, the absorbance at the excitation wavelength (505 nm) was kept below 0.1 for all samples. By plotting the integrated fluorescence intensity against the absorbance for the QD and Rh samples and determining the gradient (see Figure 2.11c), Equation 2.2 can be rewritten as

$$\Phi_{\text{QD}} = \Phi_{std} \cdot \left(\frac{\text{gradient}_{\text{QD}}}{\text{gradient}_{std}} \right) \cdot \left(\frac{n_{\text{QD}}^2}{n_{std}^2} \right). \tag{2.3}$$

Using Equation 2.3 to calculate the QY of the QDs with the gradients reported in Figure 2.11c, the absolute QY of Rh in water given by $\Phi_{std} = 0.90$ [74] and $n_{\text{QD}} = n_{std} = 1.333$, the QY of the L-cysteine capped CdSe/ZnS QDs was determined to be **48%**. Even though the comparative method is well-established for determining QYs, the QY reported by this method must only be used as an estimation since many factors can influence the results [73].
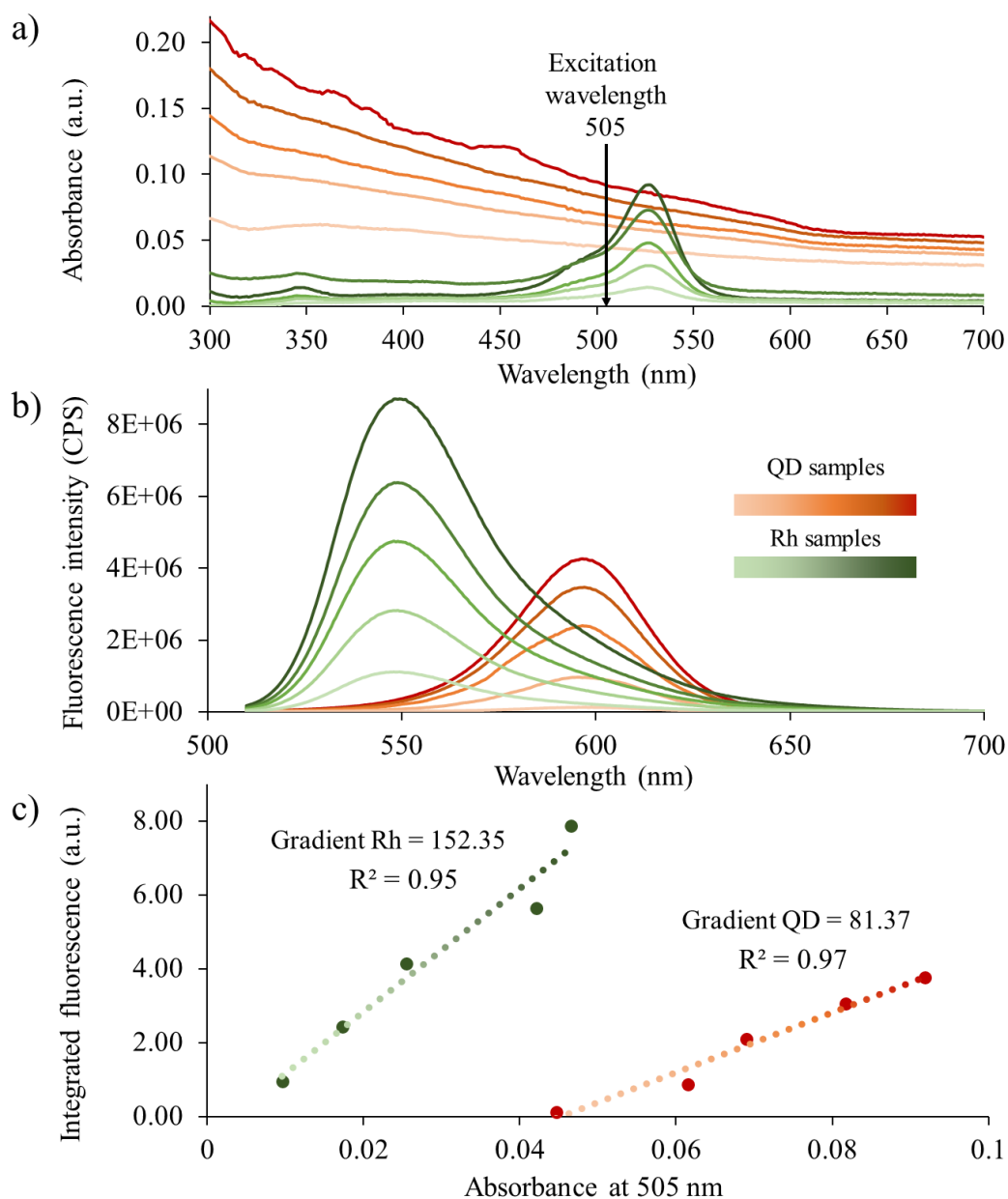
Figure 2.11: Quantum yield determination. a) Absorbance and b) fluorescence emission spectra of L-cysteine capped CdSe/ZnS QDs (orange graphs) and rhodamine 6G (green graphs) samples of different concentrations (in water). c) Linear plots of the integrated fluorescence intensity against absorbance of the QDs and rhodamine 6G (Rh) used for the quantum yield calculation.

TEM analysis and size-distribution

TEM analysis was carried out to determine the morphology and size distribution of the core and core/shell QDs. From the TEM images of the hydrophobic CdSe and CdSe/ZnS QDs, shown in Figure 2.12a and b, it is clear that the QDs were spherical and monodispersed (in chloroform). Between 700-800 particles on a TEM image were used to determined the size distribution of the core and core/shell QDs using the image processing software ImageJ. These size-distributions are shown as insets in Figure 2.12. The core QDs had an average diameter of 3.8 ± 0.4 nm (average $\pm$ standard deviation). The core/shell QDs were 5.2 ± 0.6 nm in diameter, confirming successful coating with a thin ZnS shell approximately 1.4 nm thick. The size distribution of the core was narrower than that of the core/shell QDs, as can be seen from the fitted Gaussian curves.

The TEM image of the L-cysteine capped CdSe/ZnS QDs is shown in Figure 2.13. The water-soluble QDs are less dispersed than the hydrophobic QDs due to hydrogen bonding that exists between the L-cysteine molecules on the surface of these QDs. The change in agglomeration behaviour confirmed a change in the capping agent of the QDs.
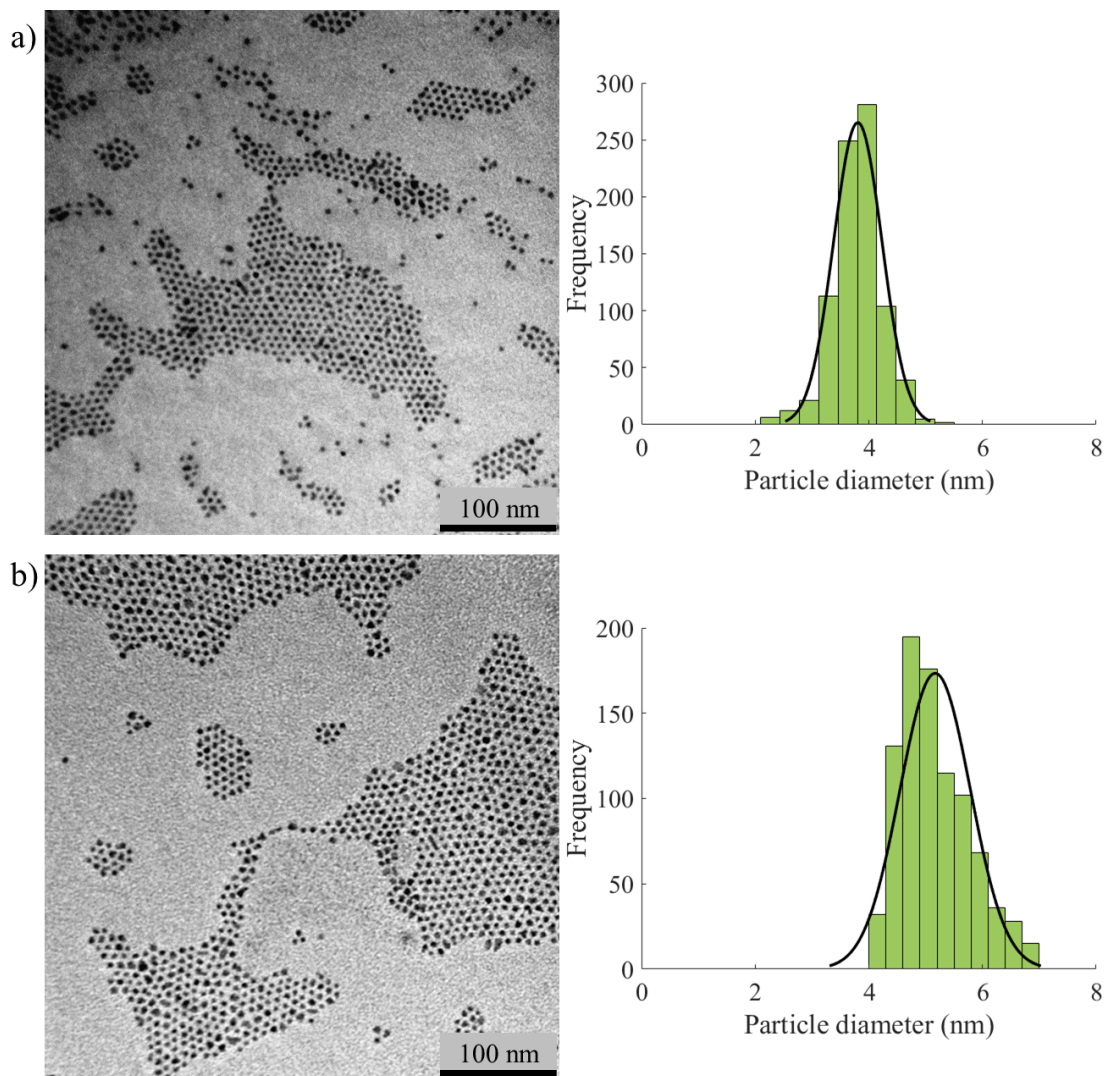
Figure 2.12: TEM images of a) CdSe QDs and b) CdSe/ZnS QDs with their corresponding size distributions. The average diameter of the core and core/shell QDs were 3.8 ± 0.4 nm and 5.2 ± 0.6 nm, respectively.
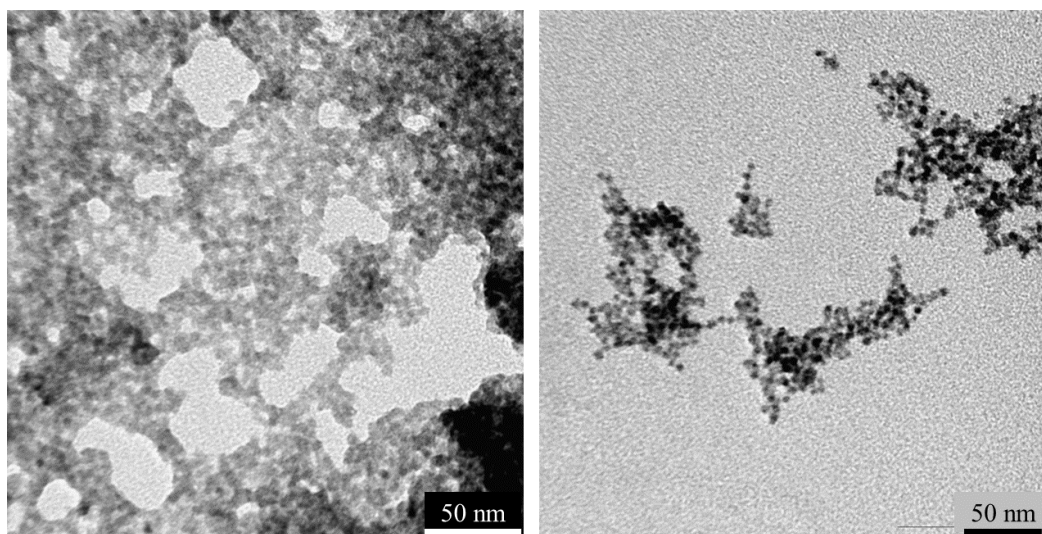
Figure 2.13: TEM images of L-cysteine capped CdSe/ZnS QDs. These water-soluble QDs are less dispersed than the hydrophobic QDs due to the hydrogen bonding that exists between the L-cysteine molecules on the surface of the QDs.

FTIR analysis

In order to determine the surface chemistry of the QDs and to confirm the success of the ligand exchange reaction, FTIR spectra of the hydrophobic QDs, L-cysteine capped QDs, pure TOPO and L-cysteine were measured – see Figure 2.14. Before assigning the peak positions to the vibrational modes of the molecules, three main observations of these spectra are considered. Firstly, all the spectra and peak positions correspond well to reported literature [70, 72, 75–78]. Secondly, the spectra of the core and core/shell QDs for both the hydrophobic and water-soluble QDs are almost identical, confirming that FTIR analysis of nanoparticles mainly gives information on the surface chemistry (not the core or shell) of these particles. Lastly, the spectra of the hydrophobic QDs match well to the spectrum of pure TOPO, whereas the spectra of the water-soluble QDs are completely different (confirming a change in capping agent) and corresponds to the spectrum of pure

L-cysteine. Therefore, by comparing these spectra to literature and to each other, the success of the syntheses was confirmed.

The spectrum of TOPO shows peaks at 2918 and 2849 cm^{-1} corresponding to the symmetric and asymmetric stretching of the CH$_2$ groups in the alkyl chains. These peaks are also seen in the spectra of the TOPO capped hydrophobic QDs. The characteristic P$=$O and P$-$C stretching of pure TOPO were observed at 1145 and 1464 cm^{-1}, respectively. The absence of the P$=$O peak in the hydrophobic QDs confirms the coordination of TOPO to the QD surface. The peaks at 1530 and 1434 cm^{-1} in the hydrophobic QD spectra can be ascribed to the P$-$C stretching of coordinated TOPO [76].

The C$=$O and C$-$O stretches of the carboxylic group in L-cysteine are seen around 1550 and 1390 cm^{-1} in the L-cysteine capped QDs and the broad peak $\sim$3200 cm^{-1} is from the O$-$H stretch. The S$-$H vibration (2550 - 2750 cm^{-1}) of L-cysteine disappeared in the spectra of the L-cysteine capped QDs confirming covalent bond formation between L-cysteine and ZnS for the CdSe/ZnS QDs and the formation of Cd$-$S in the water-soluble CdSe core QDs [75]. The FTIR analysis verified (along with the other characterization techniques) the successful synthesis of L-cysteine capped CdSe/ZnS QDs.
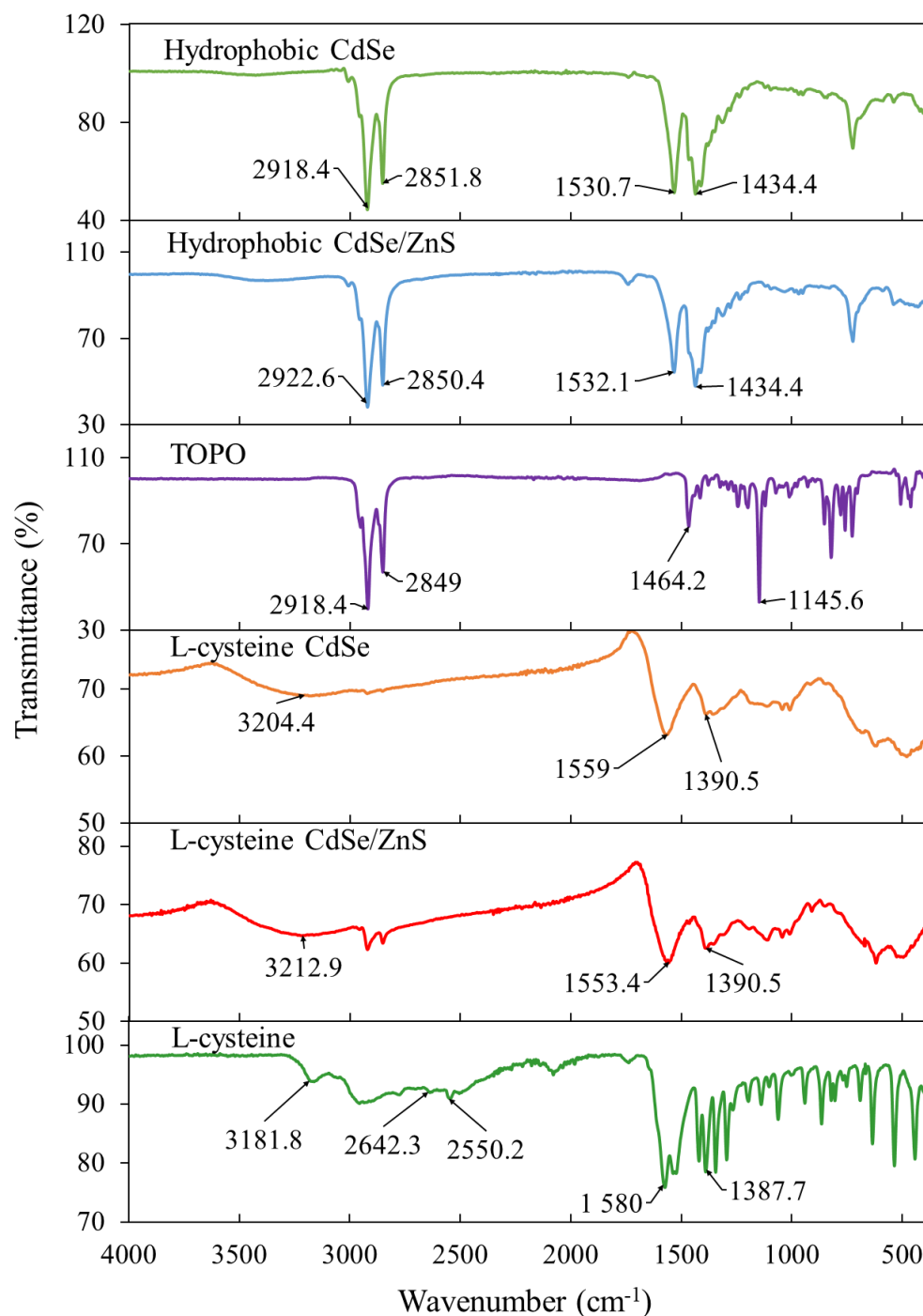
Figure 2.14: FTIR spectra of the hydrophobic and L-cysteine capped core and core/shell QDs as well as the spectra of TOPO and L-cysteine.

2.2.3 Method optimization

The QD synthesis was repeated four times with only slight changes in the method followed. The four repetitions are referred to as batches 1, 2, 3 and 4. This section focuses on observations made during the syntheses and addresses some important steps that needed to be followed to make good quality QDs. The detail of the reaction conditions and properties of each batch of QDs can be found in Table A.1. The optimization process mainly focused on 1) ensuring the QDs have an appropriate fluorescence emission wavelength ($\geq$590 nm) for our application and 2) that the QD sample is monodispersed with no agglomerates present (in order to uniformly coat the micro-sized beads as discussed in Section 2.3).

Precursor mixing

Thorough mixing of the precursor solutions is important. In order to properly dissolve the TOPO in the selenium precursor, the ODE and TOPO were heated to 80°C and mixed until a colourless solution formed before the Se powder was added.

Previous methods followed by our research group suggested making the precursor solutions a day before the QD synthesis and mixing them overnight [72]. This was done for both batches 1 and 2 and worked well for batch 1; however batch 2 was made on a much colder day than batch 1 and the Se-precursor solidified overnight, which might have had an influence on the nucleation process. Since our laboratory is not temperature controlled, the precursor solutions for the next two batches were mixed at 40 °C for 5 hr to increase the reproducibility of the method and make it less dependent on the fluctuating ambient temperature.

Nucleation temperature

As mentioned in the method (Section 2.2.1), the CdO solution was first stirred at 260 °C to form a colourless solution, the exact temperature of this step was not as important since the only goal was to obtain the colourless Cd-OA solution. However, nucleation of CdSe QDs was activated when the Se-precursor was added, for this step the exact temperature was crucial. Nucleation was done at a temperature between 255-265 °C and reported as $\sim$ 260 °C since the exact temperature was difficult to control with the mechanical heating mantle. A difference in nucleation can, however, be seen when comparing the fluorescence emission of the CdSe core QDs of batches 3 and 4 summarized in Table 2.1. For both these batches, 25 mL of the Se-precursor was added to the colourless Cd-OA solution at a temperature of around 260 °C, but the temperatures probably were not exactly the same. After 1 min of core growth, batch 3 had a fluorescence emission peak at 531 nm compared to 562 nm for batch 4. Interesting enough, after 15 min of core growth, the QDs of batch 3 were larger with emission at 591 nm compared to the emission of 574 nm for batch 4. Temperature was not the only factor that could have influenced the nucleation and growth of the QDs but it played a big role; another factor that might have influenced the nucleation was the injection speed of the Se-precursor.

Table 2.1: Comparison of CdSe QD nucleation and core growth of batches 3 and 4.

Growth time (min)	Fluorescence emission peak (nm)	
	Batch 3	Batch 4
1	531	562
2	553	567
5	563	571
10	580	573
15	591	574

The extreme sensitivity of QD formation to conditions like temperature is what makes reproducibility difficult. More investigation and experiments are necessary to make a definitive conclusion on the influence of temperature (and other factors) on nucleation and growth of the core QDs.

Addition of extra shell precursor

For the first batch of QDs, the CdSe core grew to have a fluorescence emission peak of 570 nm before 10 ml of each shell precursor was added. After 75 min of shell growth, the emission peak stabilized at 588 nm. Since we aimed for an emission peak maximum of 595 nm, as mentioned in the introduction of Section 2.2, another 7 ml of each shell precursor (Zn and S) was added and the shell was left to grow for another 20 min (this was repeated once more). The results are summarized in Table 2.2. The addition of more shell precursors, however, did not increase the QD size by epitaxial growth since the fluorescence emission peak stayed at 588 nm. The TEM images of batch 1, see Figure 2.15, showed that although single QDs were observed, a lot of large agglomerations were present in the sample. These agglomerations were most likely due to the extra Zn and S added that formed particles themselves. To prevent these agglomerations, all the shell precursors were added at once in the subsequent synthesis attempts (batches 2-4) and the large agglomerations were absent in these samples.

Table 2.2: Fluorescence emission peak monitoring throughout the QD synthesis of batch 1.

Growth time (min)	Fluorescence emission peak (nm)
CdSe core	
15	570
Added 10 ml of Zn and S precursors	
5	587
15	590
30	586
50	588
75	588
Added 7 ml of Zn and S precursors	
20	588
Added another 7 ml of Zn and S precursors	
20	588
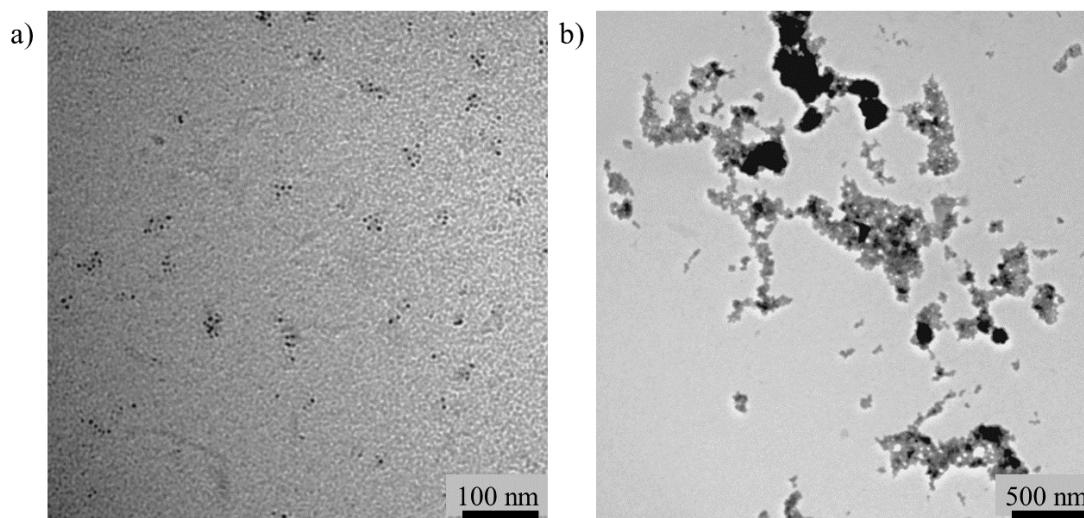
Figure 2.15: TEM images of a) individual QDs and b) large agglomerations present in the sample of batch 1 due to the addition of extra Zn and S precursor.

Purification of QDs

The purification of the L-cysteine capped QDs can be rigorous and time consuming, but is a crucial step in order to have a monodispersed QD sample. Figure 2.16a shows the appearance of crude L-cysteine capped CdSe/ZnS QDs before purification. The crude sample is clumped together with many impurities between the QDs that no individual QD can be seen. The large surface area of QDs gives organic impurities a lot of space to attach to the QDs and therefore the need for thorough purification. Figure 2.16b shows the TEM image of purified L-cysteine capped QDs where individual QDs are visible.

Batches 1 and 2 required a lot of purification. Different washing solvents were used: acetone, chloroform, methanol, ethanol and a acetone:chloroform:water 2:1:1 mixture. For batch 2 it was necessary to repeat the purification by centrifugation steps up to 17 times with different solvents to remove all the impurities. To make the final purification step easier, the hydrophobic CdSe/ZnS QDs were purified by
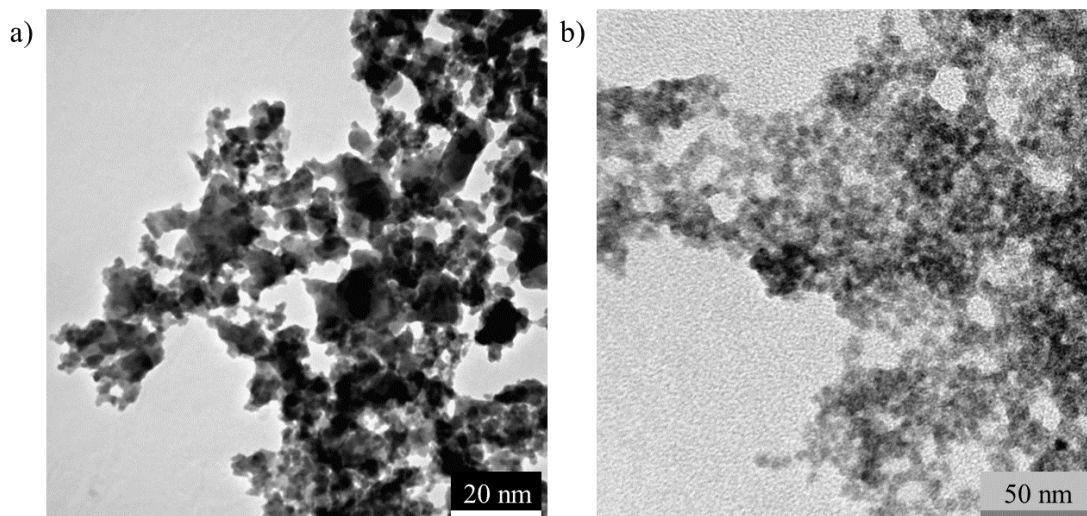
Figure 2.16: TEM images of a) crude and b) purified L-cysteine capped CdSe/ZnS QDs.

centrifugation with methanol before the ligand exchange reaction; this was done for batches 3 and 4. Including this step significantly reduced the purification time for the final L-cysteine capped QDs and only ethanol ($\times$4) and acetone ($\times$2) were used as washing solvents as reported in Section 2.2.1.

Fluorescence quenching

After purification of the L-cysteine-capped CdSe/ZnS QDs, their fluorescence intensity was quenched. Figure 2.17 shows the appearance of the L-cysteine before and after purification under ambient and UV light. From the appearance of these QDs under the UV-light it is clear that the QDs have diminished fluorescence intensity. However, after the QDs were dried and redispersed in water, it was observed that the fluorescence intensity recovered after some time. Figure 2.18 shows the fluorescence intensity of the L-cysteine capped CdSe/ZnS QDs as it
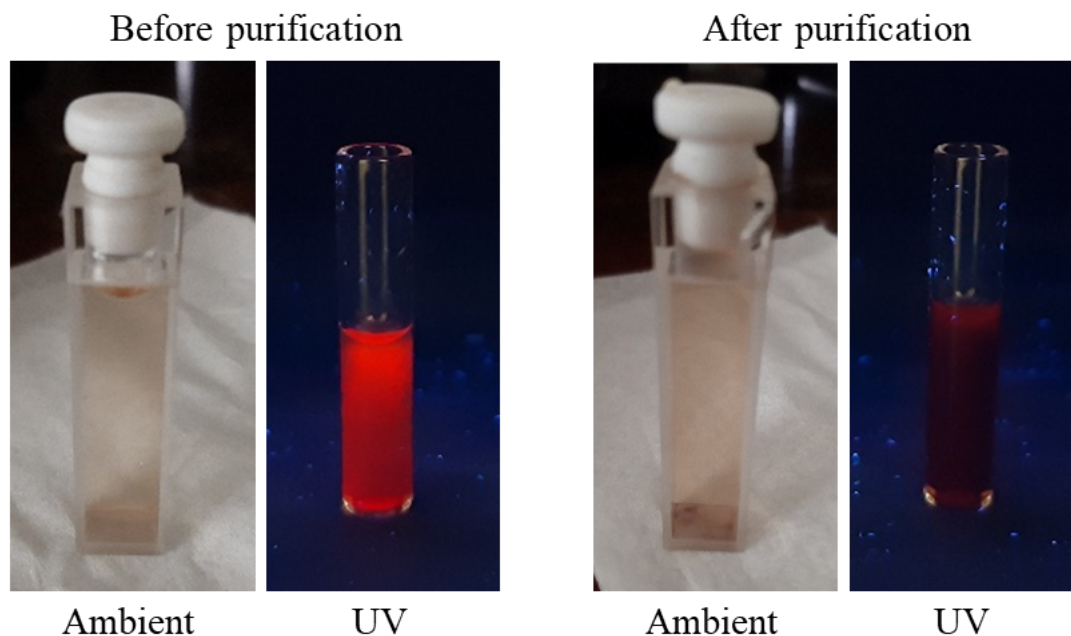
Figure 2.17: Appearance of L-cysteine capped CdSe/ZnS QDs under ambient and UV-light showing fluorescence quenching after purification

recovered over a period of six days. The first measurement was taken directly after the purified QDs were redisperesd in water.

This quenching phenomenon can be explained by the research published by Noh *et al.* [79]. In this work they showed that the fluorescence of water-soluble CdSe QDs quenched when the QDs formed aggregates. The quenching of our QDs happened towards the end of the purification process. While purifying, the QD concentration increases since the QDs are precipitated out of the deionized water used during the ligand exchange reaction. The crude QDs were dispersed in about 200 ml of deionized water after the ligand exchange reaction; whilst at the end of purification the QDs were dispersed in only 10 ml of acetone before they were left to dry in the fume hood. We know that the L-cysteine capped QDs exhibit hydrogen bonding and tend to clump together. It can be hypothesized that the L-cysteine QDs formed aggregates when highly concentrated and dispersed in acetone which caused the fluorescence quenching. When the QDs were redispersed in water the aggregates dispersed and the fluorescence emission recovered. Although this explanation of the quenching phenomenon of our QDs is supported by literature, more investigation is required to confirm the hypothesis. It is critical however to ensure that the the fluorescence intensity of the QDs is stable before using them as sensors.
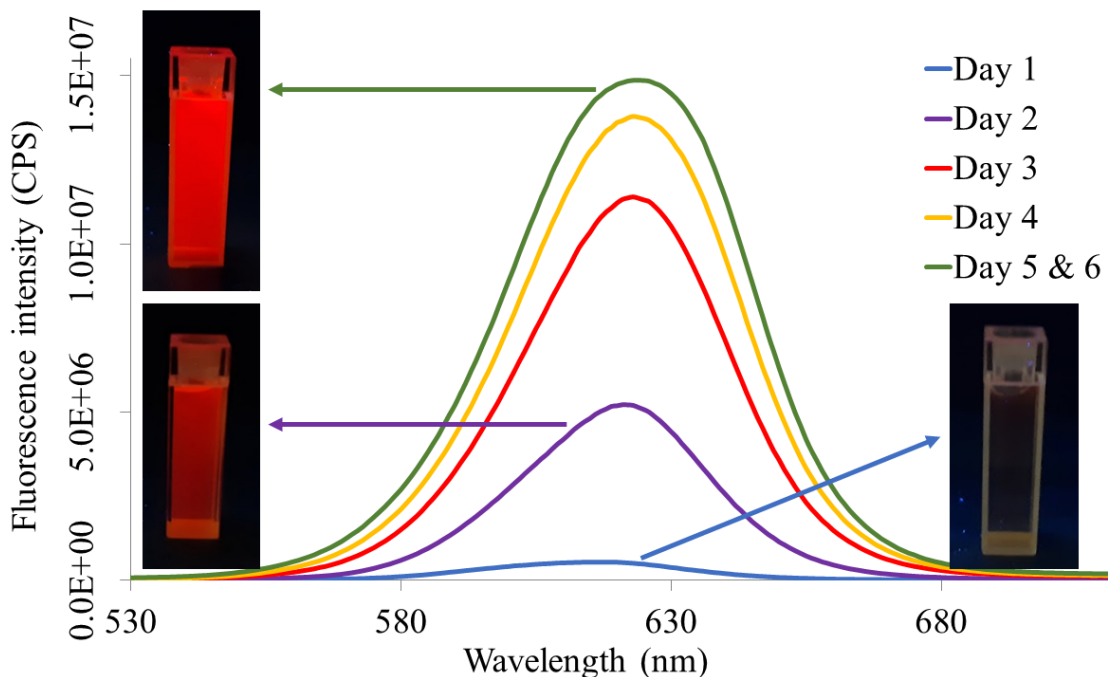
Figure 2.18: Fluorescence intensity recovery of L-cysteine capped CdSe/ZnS QDs over six days. The photo insets show the appearance of the sample under UV-light on certain days.

2.3 Synthesis of QD-tagged beads

This section reports on the coupling of the L-cysteine capped QDs to micro-sized polymer beads. Single QDs with a diameter of 5.2 ± 0.6 nm are too small to be trapped in our optical tweezer setup (discussed in Chapter 3), therefore, bead-assisted chemistry was used. Polymer beads with a diameter of 2 μm were coated with the QDs to create a fluorescent probe suitable for optical trapping.

Section 2.3.1 gives a description of the synthesis method followed in order to couple the QDs to the bead surface and Section 2.3.2 reports on the characterization of the QD-tagged beads. The coupling method was optimized by five repetitions with modifications each time, to ensure high-quality fluorescent probes which are discussed in Section 2.3.3.

2.3.1 Method

Chemicals

N-(3-dimethylaminopropyl)-N'-ethylcarbodiimide hydrochloride (EDC) and N-hydroxysuccinimide (NHS) were purchased from Sigma Aldrich (USA). L-cysteine capped CdSe/ZnS QDs were prepared as discussed in Section 2.2. Invitrogen^{TM} 2 μm carboxyl functionalized latex beads were purchased from Thermo Fisher Scientific (South Africa). Deionized water used during the syntheses was from an in-house Drawell Eco-Q deionized water system (China).

EDC/NHS chemistry

Figure 2.19 illustrates the coupling reaction of the QDs and micro-sized beads. Well-known and widely used EDC/NHS chemistry was used to bond the QDs to the surface of the polymer beads. The commercial polymer beads were made from polystyrene and were functionalized with carboxyl groups on the surface; the carboxyl group on the bead and the primary amine group of the L-cysteine on the
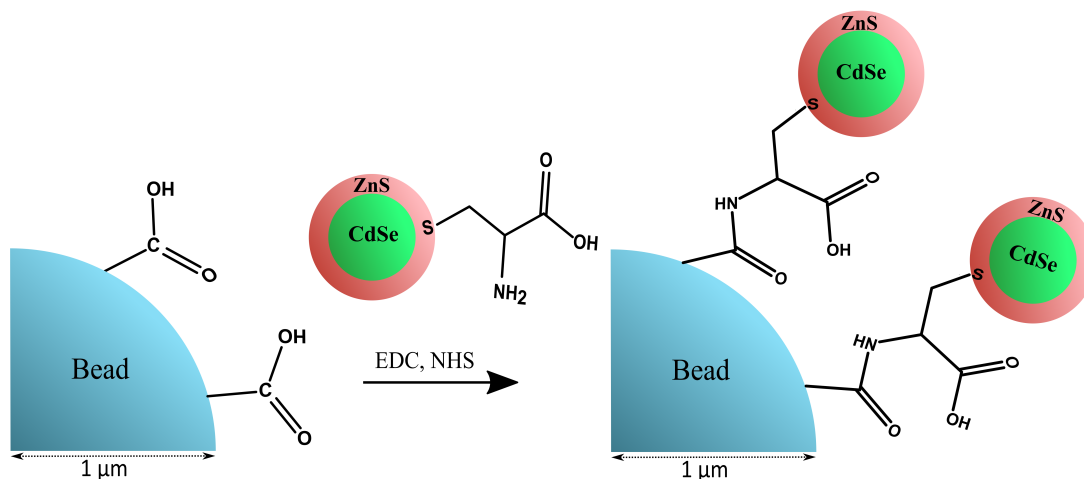
Figure 2.19: The coupling reaction of L-cysteine capped QDs to the surface of micro-sized beads through EDC/NHS chemistry.

QDs were used to form a covalent bond between the bead and the QDs.

The reaction scheme of the EDC/NHS conjugation reaction is given in Figure 2.20. EDC reacts with the carboxyl groups on the micro-sized polystyrene bead to form an active O-acylisourea intermediate. In an aqueous solution, this intermediate can undergo hydrolysis to regenerate the carboxylic acid and form an isourea byproduct; this unwanted reaction can be minimized by adding excess EDC [80]. NHS is added to stabilize the intermediate; the NHS-ester intermediate reacts readily with amine nucleophiles, like the primary amine from the L-cysteine group on the QDs, to form the stable amide conjugate [81].
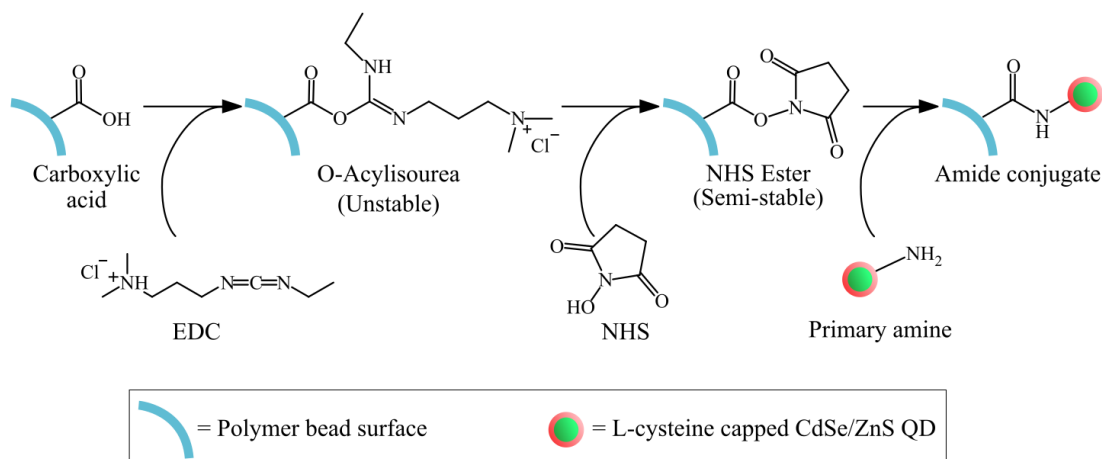
Figure 2.20: EDC/NHS crosslinking reaction scheme. A three-step reaction where EDC first reacts with carboxylic acid to form an unstable O-acylisourea intermediate. The addition of NHS creates a more stable NHS-ester intermediate which then reacts readily with an amine-containing molecule to form the amide conjugate.

For the coupled product to be a successful fluorescence probe it must meet some requirements. Firstly, the synthesis of the QD-coupled beads must be reproducible, this is important since each batch of fluorescent probes must give the same response when detecting an analyte. Another requirement is that the beads must be evenly and consistently coated with the QDs throughout the sample. The beads must

also be coated with enough QDs so that the fluorescence emission coming from a single bead can be detected by a photo-detector in the optical tweezer setup. A final requirement is that the coupled sample cannot have any impurities in it that could potentially influence the fluorescence emission coming from the coupled beads, like excess unreacted QDs or large agglomerations of QDs.

The coupling reaction method was optimized to meet all the above mentioned requirements (see Section 2.3.3 for the optimization process). The final optimized procedure was as follows:

The optimized coupling method

2.5 ml of EDC (0.1 M) and 2.5 ml NHS (0.1 M) were added to 50 μl of the polymer beads (diluted in 1 ml water) and stirred for 30 min in an ice bath to activate the carboxylic acid groups on the beads. Excess EDC was removed by centrifugation with deionized water. After centrifuging, the activated beads were redispensed in 4 ml water and 3 mg of QDs was added. The QDs were dispersed in 4 ml water before the coupling reaction in order for the fluorescence intensity to fully recover (see Section 2.2.3). The coupling reaction was left to proceed in an ultrasonic bath for 3 h to ensure even coating of the QDs on the beads. The QD-tagged bead product was purified by centrifugation with water ($\times$3) and stored in deionized water in the fridge.

2.3.2   Characterization

The characterization of the QD-tagged beads is presented in this section. The most important characterization method was TEM analysis since the success of the reaction and the amount of QDs on the surface of the beads were determined through this method. Other characterization techniques included absorbance, fluorescence emission, FTIR analysis and fluorescence microscopy.

TEM analysis

TEM images of uncoated commercial polymer beads and the QD-tagged beads are compared in Figures 2.21a and b. The appearance of a whole bead and the surface of the uncoated and tagged bead are shown in this figure. The commercial beads were spherical and had an average diameter of 1.88 ± 0.02 μm, determined by analysing the TEM images with ImageJ; this corresponds well with the size of 1.9 μm stated by the manufacturer. The uncoated polymer beads had a smooth surface whereas the surface of the QD-tagged beads were rough or 'fuzzy' confirming the success of the coupling reaction. The distribution of the QDs on the surface was fairly uniform with no large aggregates present.
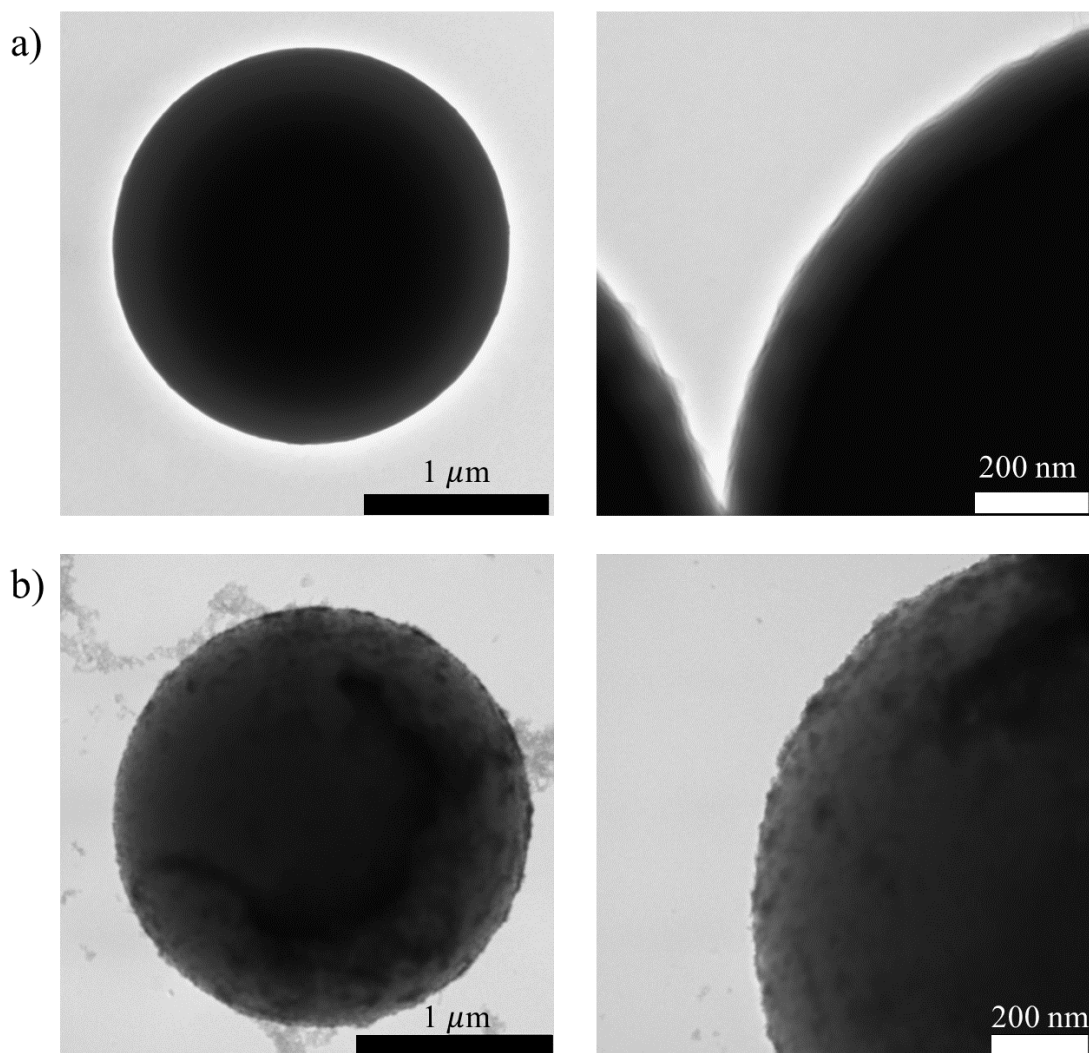
Figure 2.21: TEM images of a) an uncoated polymer bead and b) a QD-tagged bead. The TEM image of a whole bead and the surface of a bead are shown. The surface of the uncoated bead is smooth whereas the presence of the QDs can be observed on the surface of the QD-tagged bead.

Figure 2.22 shows the reproducibility of the QD-tagged bead synthesis. Firstly, to test that the QD coating is uniform for the beads in a synthesis batch, the surface of different beads in that sample was imaged (reproducibility within a sample). Secondly, to test whether the QD coating is consistent when repeating the synthesis, the surface of beads in three different batches was imaged (reproducibility

between samples). These TEM images are shown in Figure 2.22, the rows represent different beads within the same sample and the columns represent the beads between different samples. These TEM images confirmed that the QD coating on the beads was sufficiently uniform and consistent for different samples.

Reproducibility within a sample
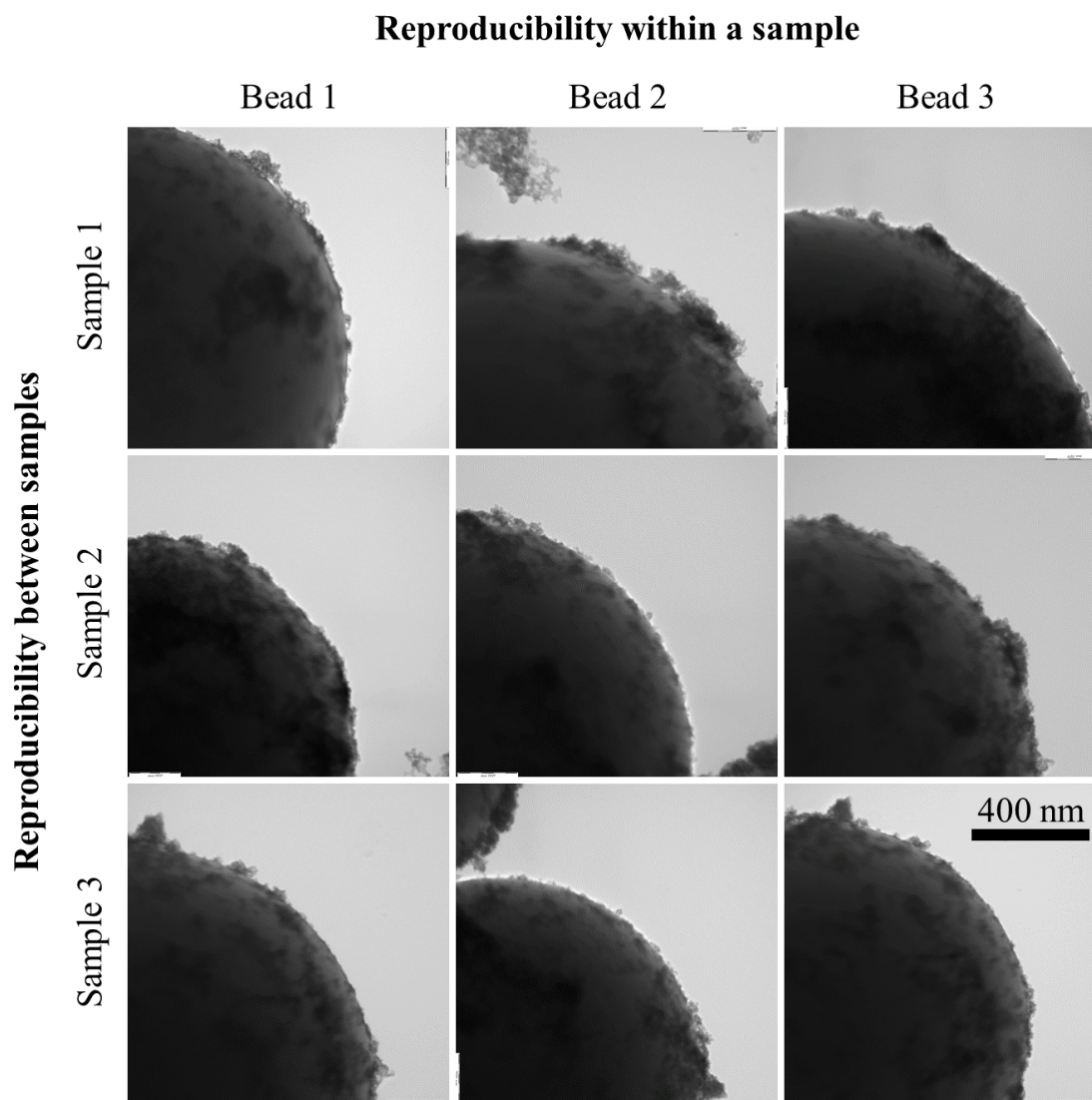
Figure 2.22: Reproducibility test within a sample (rows) and between samples (columns) of the QD-tagged bead synthesis. The reproducibility of the coupling reaction is demonstrated by the TEM images of the surface of three QD-tagged beads in three different samples.

Absorbance and fluorescence emission

The absorbance and normalized fluorescence spectra of the QD-tagged beads are shown in Figure 2.23. The coupling reaction caused a slight blue shift in the fluorescence emission peak of the QDs from 602 nm to 597 nm.
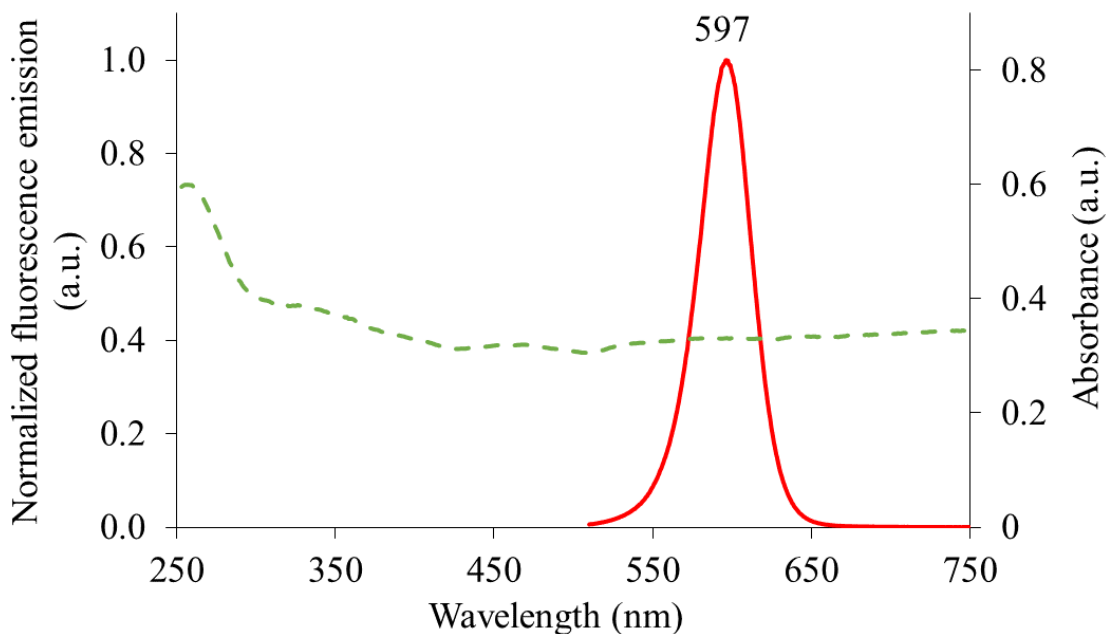
Figure 2.23: Normalized fluorescence emission at $\lambda_{\text{excite}} = 470$ nm (red line) and absorbance (green dashed line) of the QD-tagged beads in water.

FTIR analysis

Figure 2.24 compares the FTIR spectra of the two starting materials (L-cysteine capped QDs and the polystyrene beads) with the QD-tagged bead product. The spectrum of the product is dominated by the beads with the addition of two new peaks at 1733 and 1220 cm^{-1}. These peaks can be ascribed to the amide linkage formed between the carboxylic acid on the beads and the L-cysteine on the QDs with the C=O stretch corresponding to 1733 cm^{-1} and C$-$N to 1220 cm^{-1} [82–84].
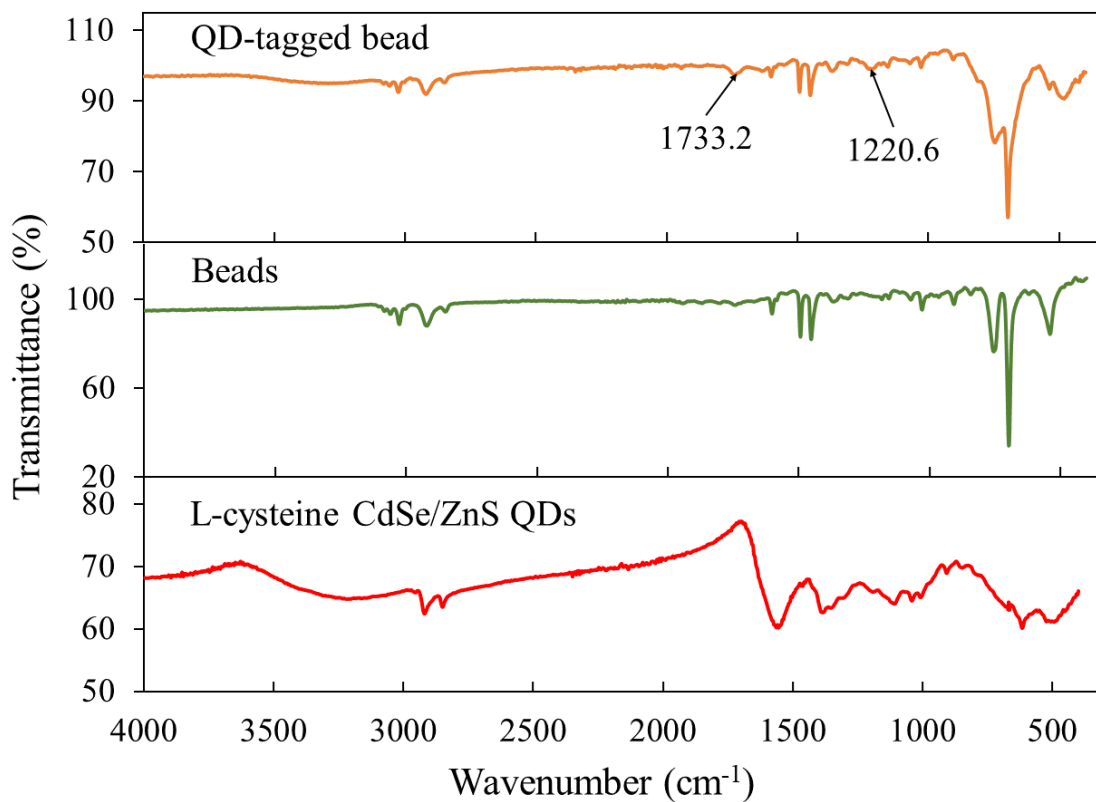
Figure 2.24: FTIR spectra of the QD-tagged beads, uncoated commercial beads and L-cysteine capped QDs.

Fluorescence microscopy

The appearance of the QD-tagged beads under the confocal microscope is shown in Figure 2.25. This technique allows the visualization of the presence and spread of the QDs on the surface of the beads (excitation wavelength of 532 nm). It is clear that the QDs are concentrated on the surface of the spherical beads (with a 2 μm diameter).
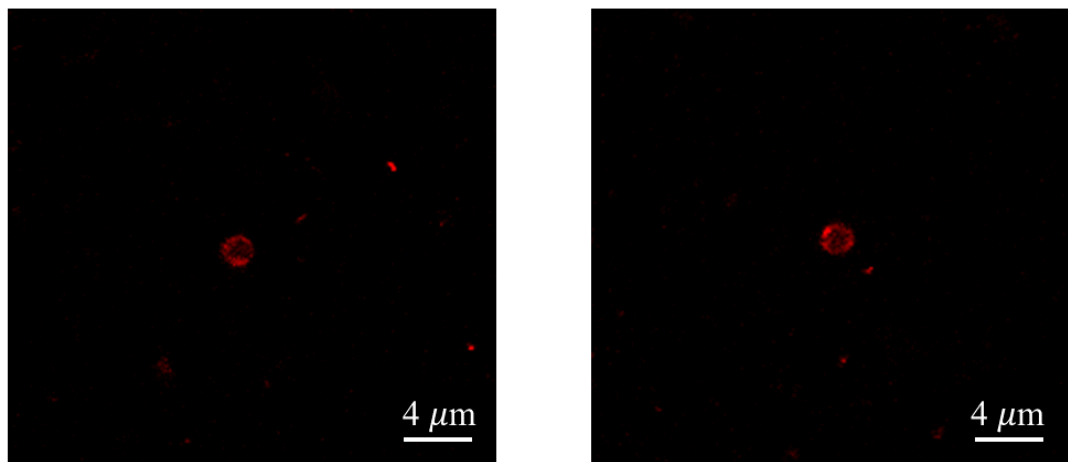
Figure 2.25: QD-tagged beads under the fluorescence microscope.

2.3.3 Method optimization

The QD-tagged bead synthesis was repeated five times with slight changes in the method followed. The five repetitions are referred to as attempts 1 to 5 (not to be confused with the QD syntheses which were referred to as batches 1–4). This section focuses on observations made during the syntheses and addresses some important steps that needed to be followed to make high quality QD-tagged probes. The detail of the reaction conditions for each attempt of QD-tagged bead synthesis can be found in Table A.2.

Order of steps

In one of the initial attempts of the coupling reaction, the whole reaction was carried out in one beaker without washing the activated beads before adding the QDs. After TEM analysis of this attempt, it was soon realized that the unreacted EDC in the beaker activated not only the carboxyl groups on the beads but also the carboxyl groups of the L-cysteine on the QDs. These activated QDs then reacted with themselves and formed large aggregates. Figure 2.26a shows a TEM

image of this attempt. As can be seen, the QDs did couple to the beads but the coating was very uneven with some of the large aggregates attached to the beads and others not. For the next attempt, the activated beads were washed with water before adding the QDs to remove any access EDC; the TEM image of the product from this attempt is shown in Figure 2.26b. The large aggregates were absent in this attempt and the QD coating on the beads was much more uniform.
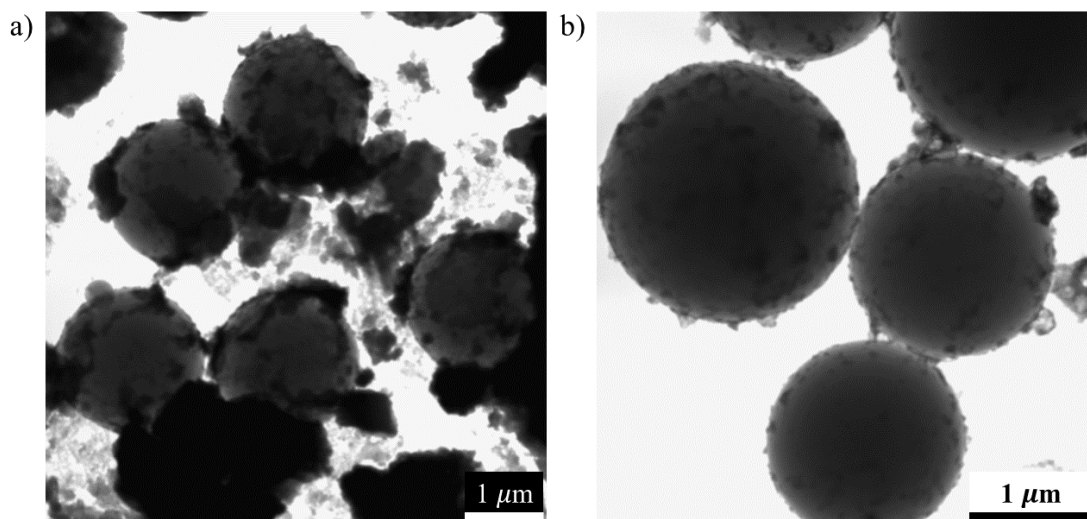
Figure 2.26: QD-tagged bead sample a) when EDC was present throughout the reaction and b) when excess EDC was removed before adding the QDs. In a) the carboxyl groups on the QDs were activated causing the QDs to react with themselves to form large agglomerations. In b) the excess EDC was removed before adding the QDs preventing formation of large agglomerates.

The activated beads were washed with deionized water, therefore, it is important to add the NHS before washing since the unstable O-acylisourea intermediate can undergo hydrolysis to reform the carboxylic acid. As explained previously, the NHS-ester is more stable towards hydrolysis. The order in which the reactants are added is therefore critically important in EDC/NHS chemistry.

QD coating

As mentioned in Section 2.3.1, for the QD-tagged beads to be successful fluorescent probes it is necessary that the coating of the QDs is uniform and consistent. Initially it was difficult to obtain a uniform QD-coating throughout the sample and even over a single bead. Consider the bead in Figure 2.27a, the amount of QDs on the surface of this bead ranged from almost nothing on the one side to large clumps on the other. The inconsistency in the QD coating throughout a QD-tagged bead sample is further demonstrated in Figure A.1 where beads in the same sample were imaged having no QDs to large agglomerates of QDs on their surface. In attempt to solve this problem, the amount of QDs added during synthesis was increased, this however had very little effect on the QD coating and did not improve the distribution consistency (see Figure A.2). The uniformity however greatly improved when the reaction was done in an ultra-sonic bath compared to the previous attempts that used only a magnetic stirrer bar, as shown in Figure 2.27b. The reason for the improvement is again the tendency of the L-cysteine capped QDs to clump together because of hydrogen bonding. By sonicating the reaction, the QDs were more dispersed during the coupling reaction and coated the beads more uniformly. The sonication greatly improved the reproducibility as can be seen by comparing Figure A.1 with the reproducibility of the optimized synthesis shown in Figure 2.22.
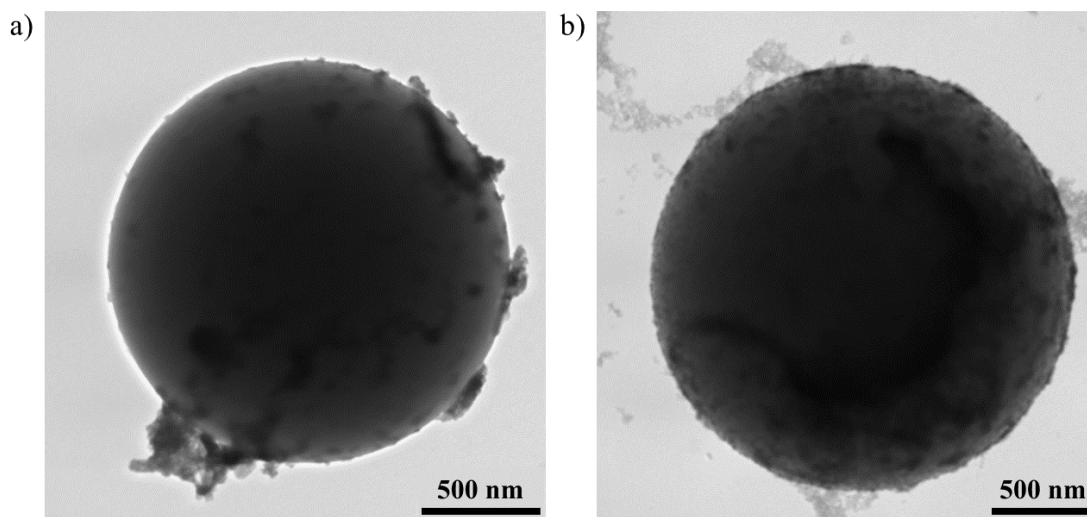
Figure 2.27: QD-tagged bead showing a) non-uniform coating and b) uniform coating. The inconsistency of the QD-coating was avoided by performing the reaction in an ultra-sonic bath rather than only stirring.

Purification solvent and storage

Lastly, I would like to point out the importance of carefully studying the system under investigation before attempting a synthesis. For example, in attempt 1 of the coupling reaction, the QD-tagged beads were purified with acetone in order to speed up drying of the product in the fume hood (same as in the QD synthesis). A solid product is usually preferred because of the ease of weighing and preparing solutions with known concentrations. The TEM analysis of attempt 1, however, showed no intact beads only a mass of product and the success of the coupling could not be determined (refer to Figure A.3). The polymer beads were deformed/ dissolved by the acetone used for purification as confirmed by the TEM images of commercial beads dispersed in acetone; compare Figures 2.28a and b where the beads were dispersed in water and acetone, respectively. The beads left in acetone deformed and merged into each other, whereas the beads in water were spherical with clearly defined edges. For the rest of the attempts, only water was

used for purification and the product was stored in deionized water in the fridge. The choice of acetone as washing solvent was based on the QD synthesis but was incompatible with the new reactant (polymer beads) of this system.
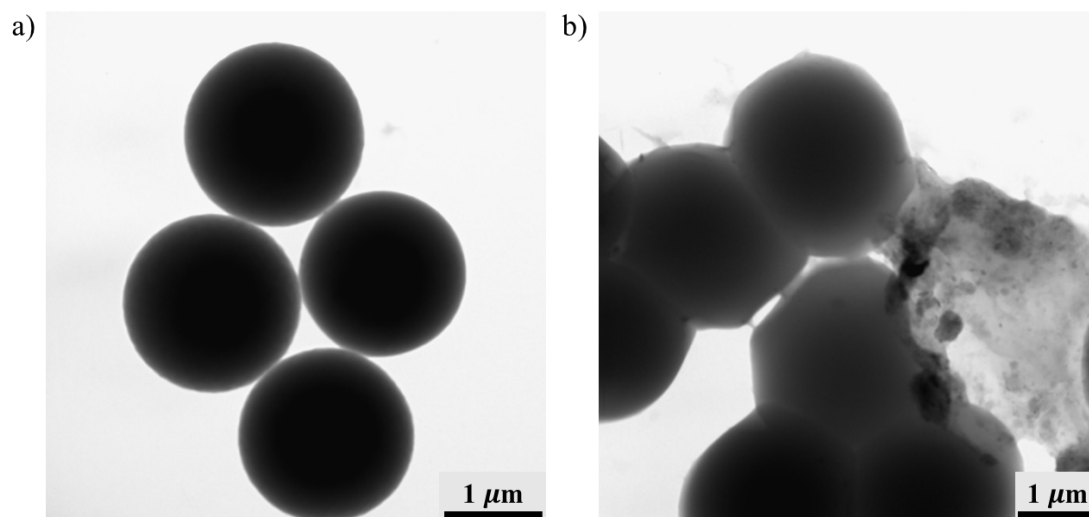
Figure 2.28: Commercial polymer beads dispersed a) in water and b) in acetone. In b) the acetone dissolved the polymer beads causing them to deform and merge together.

2.4 Atrazine sensing

To prove the QD-tagged beads can be successful fluorescence sensors, they were used to detect atrazine, a herbicide with risks to human health. This method is however not limited to atrazine sensing; as mentioned previously a wide range of analytes can be detected with QD sensors. This section starts with a discussion on the importance of atrazine monitoring in the environment and concludes with the detection of atrazine using the QD-tagged beads.

2.4.1 Background

Atrazine is a synthetic pre- and post-emergent herbicide, developed in the early 1950s and was first commercially sold in the United States in 1959 [85]. This herbicide is used to control broadleaf weeds in maize, sugarcane, sorghum and wheat crops with maize being predominant [86,87]. It disturbs the natural photosynthesis process of weeds thereby inhibiting their growth [88]. Atrazine is still one of the most widely utilized pesticides worldwide because of its effectiveness and low cost [88,89].

The usage of atrazine is however controversial because of its ability to contaminate the environment and the risks it imposes to non-target organisms. Atrazine's potential to contaminate surface and ground water is mainly due to its high mobility and long half-life [90]. Atrazine is moderately soluble in water (33 μg/ml at 22 °C) and poorly adsorbed in soil, thus contaminating the ground water by leaching and runoff [85,89]. The half-life of atrazine in water and soil is highly dependent on the sample conditions and can range from a few weeks to several years depending on the pH, temperature, concentration, light exposure and soil type [85,86,91]. The metabolites of atrazine have varying persistence and can be more toxic than atrazine itself [89]. Two atrazine degradation products that have been detected in surface water are desisopropyl atrazine and desethyl atrazine [91].

Atrazine is classified as an endocrine disruptor, causing hormonal imbalance in animals [86,92]. This herbicide can also cause hermaphroditism in frogs and can induce transgenerational health risks in fish and rats [92–94]. Other studies reported chromosomal abnormalities and estrogenic dysfunction in mammals due to atrazine [89,95]. The carcinogenicity of atrazine is an ongoing debate, some studies have established a correlation between cancer and atrazine exposure while others concluded that there is "inadequate information to assess carcinogenic

potential" [95, 96]. Other impacts of atrazine on aquatic fauna and flora and non-target plants have been extensively investigated and reviewed [86, 88, 89, 97]. The use of atrazine is banned in several countries and was banned by the European Union in 2004 because of its health and environmental concerns [98].

The main users of atrazine currently are the United States, China, Brazil and India [88]. A recent study investigating the presence of pesticides in surface water from 2012 to 2019 found that atrazine was the most detected herbicide in surface water globally [91]. Although banned in the EU, atrazine was recently found in the surface waters of Spain, Greece and Portugal showing the importance of monitoring this herbicide even in countries where it is banned [91].

South Africa is one of the largest users of pesticides in sub-Sahara Africa where 1014 tons of atrazine was sold in 2009 [90]. A study by Dabrowski, Shadung and Wepener in 2014 identified atrazine as the most hazardous pesticide in South Africa. This result was obtained after considering the potential toxicity, mobility and use of more than 152 pesticides [90]. Another recent article reported the presence of atrazine in the tap water of a school in Mpumalanga, South Africa [99].

Monitoring the concentrations of atrazine in ground and surface water is therefore necessary in order to prevent the risk of human exposure.

2.4.2 Atrazine detection with QD-tagged beads

Firstly, an outline is given of the procedure followed for fluorescence sensing of atrazine. To prepare the QD sensor solution, the QD-tagged beads were dissolved in deionized water and were sonicated for 10 min to ensure thorough dispersion of the QD-tagged beads. To prevent self-quenching during sensing, a dilute QD-tagged bead concentration of 25 g·L^{-1} was used. 0.5 mL of the respective standard atrazine solution (concentrations ranged from 5 to 25 $\times 10^{-7}$ M) was added to 1.5

mL of the sensor solution, and was left to interact for 5 min before measuring the fluorescence emission (PESTANAL®, analytical grade atrazine standard was purchased from Sigma Aldrich, USA). An excitation wavelength of $\lambda_{\text{excite}} = 470$ nm was used for all fluorescence measurements. The fluorescence emission spectra are shown in Figure 2.29a where a quenching effect of the QD fluorescence intensity was seen due to the interaction of atrazine (a higher atrazine concentration caused a larger decrease in the fluorescence intensity).

To setup a linear calibration curve, F_0/F was plotted against atrazine concentration in Figure 2.29b. F and F_0 refer to the fluorescence intensity peak of the solution with and without atrazine, respectively. A good linearity was obtained with a $R^2 = 0.96$. The guideline limit from the World Health Organization of atrazine in water is 4.6×10^{-7} M [72], thus the concentrations of atrazine used here are in the required range for regulatory tests. For the purpose of this study, the test presented here was sufficient to confirm that sensing with the synthesised QD-tagged beads is possible. The sensing process may be further optimized in the future with regards to sensor concentration, pH and interaction time, and then continuing with real water analysis [72].

Note that here the detection of atrazine was done through bulk analysis, meaning the fluorescence emission of a solution of QD-tagged beads was measured. This suffices as proof that sensing is possible with these probes. However, for single particle analysis (the fluorescence emission of an individual QD-tagged bead) this sensing process will need to be repeated and optimized in the single particle analyser (optical tweezer).
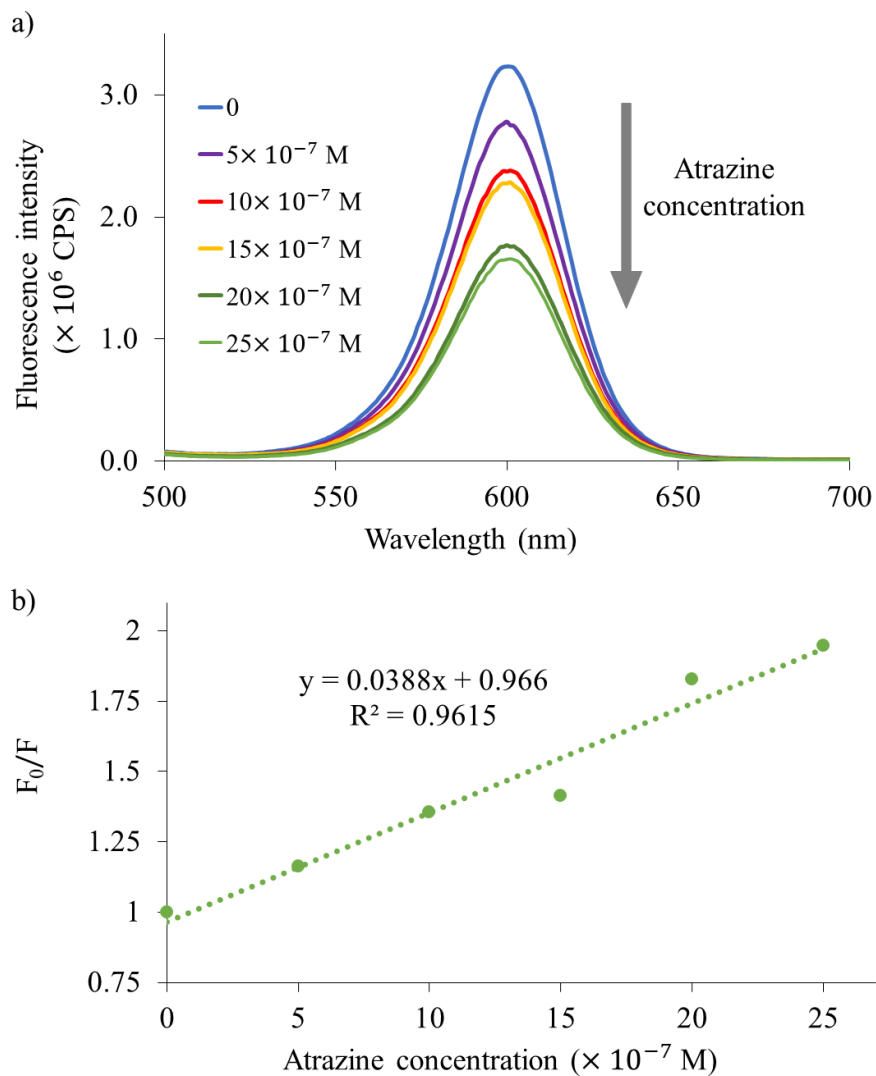
Figure 2.29: a) Fluorescence emission spectra of the QD-tagged beads in the presence of different atrazine concentrations. The fluorescence intensity of the QDs was quenched in the presence of atrazine. b) A linear calibration graph showing F_0/F against the atrazine concentration where F_0 and F are the fluorescence peak intensity of the QD-tagged sample without and with atrazine, respectively.

2.5   Chapter summary

This chapter started with a review of quantum dots and their properties. The synthesis of L-cysteine capped CdSe/ZnS QDs and the coupling thereof to micro-sized beads were presented. The optimization process of these methods were discussed and the importance of some synthesis steps was highlighted. Various characterization techniques were presented to confirm the structural an optical properties of the QDs and QD-tagged beads. Finally, these synthesized QD fluorescent probes were used to detect atrazine (a harmful herbicide).

Chapter 3

Optical tweezers

Optical tweezers make use of tightly focused light to trap and manipulate nano- to micro-sized particles in a non-contact manner. This technique has found countless applications in the fields of physics and biology ever since its advent in 1970 by Arthur Ashkin [100]. The invaluable contribution of this invention to science won its creator the 2018 Nobel Prize in Physics [101].

This chapter starts by explaining the basic concepts of optical tweezers (Section 3.1). The experimental setup and trapping results are shown in Section 3.2 and the technical details of combining optical tweezers with fluorescence spectroscopy are discussed in Section 3.3.

3.1 Fundamentals of optical tweezers

A few fundamental aspects of optical tweezers are discussed in this section to better understand their working. The discussion includes a description of the beam shape and propagation of the most common trapping beam, i.e. the Gaussian beam (Section 3.1.1). Theoretical models of the trapping forces based on the particle size are given in Section 3.1.2. The essential optical components needed to build an optical tweezer are described in Section 3.1.3. Finally, in Section 3.1.4 some applications of optical tweezers are discussed.

3.1.1 The Gaussian beam

Gaussian beams get their name from their intensity profiles being a Gaussian distribution in all the planes normal to the propagation direction. Gaussian beams are the output beam of most lasers, including laser pointers, and are routinely used as the trapping beam in optical tweezers. The intensity of a Gaussian beam is given by

$$I(r, z) = I_0 \exp\left(-2\left(\frac{r}{\omega(z)}\right)^2\right), \tag{3.1}$$

where $I_0 = \frac{2P}{\pi\omega^2(z)}$ is the maximum intensity, P is the power of the beam, r the radial coordinate and ω the beam width which depends on the propagation distance z. Figure 3.1 shows the intensity profile of a Gaussian beam; as illustrated the intensity of the beam changes and the most intense part of the beam is at the centre. This intensity gradient of the Gaussian beam is an important property necessary for optical trapping.
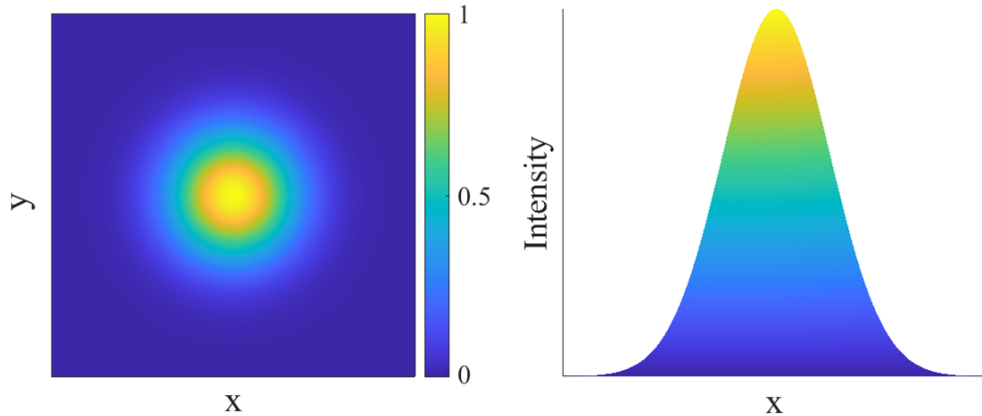
Figure 3.1: The radial intensity of a Gaussian beam.

The width of the beam is defined as the radius at which the field amplitude falls to $1/e$ of the axial value (i.e. the intensity falls to $1/e^2$). As mentioned above, the width of the Gaussian beam depends on the propagation direction (z), this

relation is described by the following equation

$$\omega(z) = \omega_0 \sqrt{1 + \frac{(z - z_0)^2}{z_R^2}}, \qquad (3.2)$$

where $z_R = \frac{\pi \omega_0^2}{\lambda}$ is called the Rayleigh length and ω_0 the waist radius, i.e. the beam width at $z = z_0$. Figure 3.2 illustrates how the beam width changes with propagation, the white lines illustrate the $1/e^2$ intensity boundary of the beam. Gaussian beams are therefore subject to diffraction as they propagate, but their intensity profile stays Gaussian.
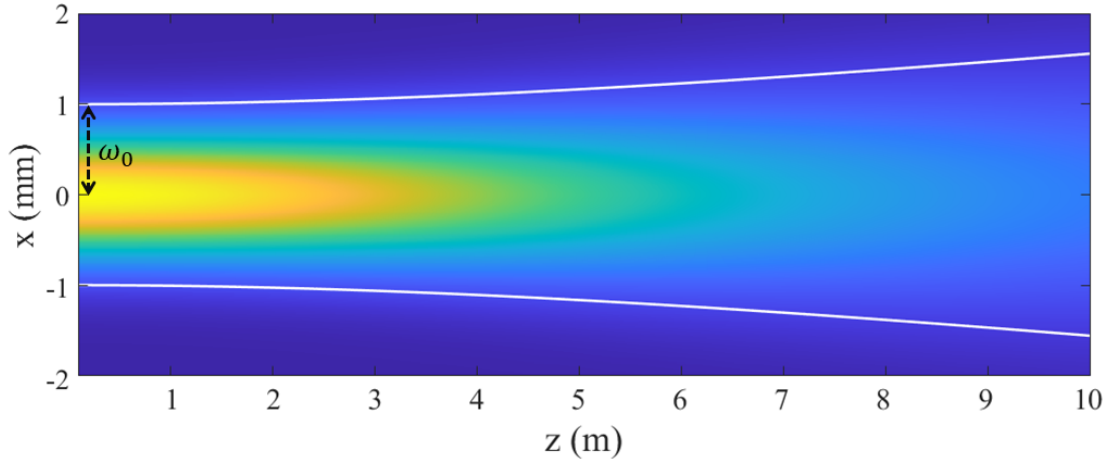
Figure 3.2: Profile a Gaussian beam as it propagates in the z-direction, with the $1/e^2$ boundary in white.

3.1.2 Forces in optical traps

Particles can be trapped by tightly focused light. The dynamics of a trapped particle can traditionally be described by two forces, the scattering force and the gradient force [102]. The former force is also known as the radiation pressure and is due to the reflection of light incident on a particle. This scattering force acts on the particle in the direction of light propagation, therefore, pushing the particle

away from the beam. The gradient force is due to refraction of incident rays on a particle; this force acts in the direction of the most intense region of the beam (the spatial intensity gradient) and is also known as the trapping force. To obtain a stable trap, the gradient force must dominate over the scattering force (in the axial direction) which is only realized when a steep intensity gradient exists. The fact that light carries linear momentum is the key to why it can exert a force on a particle. In our macroscopic world, it is difficult to observe this property of light but on microscopic scale, the force resulting from the change in momentum, as light refracts through a particle, is large enough to overcome the Brownian (random) motion of a particle and trap it.

The situation described above only holds when the refractive index of the particle (n_p) is greater than that of the surrounding medium (n_m). If the former is less than the latter, the resulting gradient force will be in the opposite direction to the intensity gradient, pushing the particle away from the beam. We will assume $n_p > n_m$ unless otherwise stated.

The scattering and gradient forces, which are in the piconewton range, can be described by different theories depending on the size of the particle being trapped [103]. A brief overview of these theories is given below.

The ray optics regime

This regime, also known as the Mie-regime, models the trapping forces when the radius (a) of the trapped particle is much larger than the wavelength of the trapping laser ($a \gg \lambda$). Figure 3.3 illustrates what happens when two rays of light refract through a transparent particle. When light refracts it changes direction and therefore experiences a change in momentum. From Newton's second law we know that a change in momentum results in a force (or impulse) since $F = \Delta p / \Delta t$. And according to Newton's third law the particle must then experience a force of

the same magnitude, but in the opposite direction. A ray of light with a higher intensity will produce a stronger force acting on the particle. Therefore, when a Gaussian beam is used for trapping, as depicted in Figure 3.3, the particle experiences a net force towards the centre (the most intense region) of the beam. The scattering force causes the trapping position to be slightly offset from the centre. Without an intensity gradient, the particle cannot be trapped since the gradient forces from refraction of the rays will cancel.
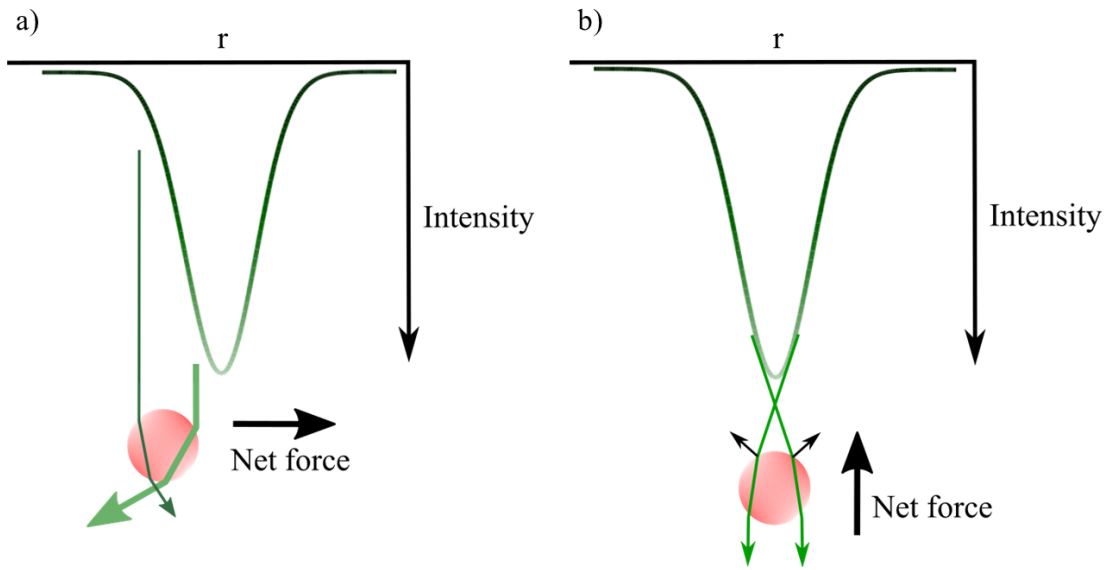
Figure 3.3: A net gradient force acts on the particles due to the refraction of rays in the a) lateral and b) axial directions. The gradient force must dominate to form a stable trap in the axial direction.

The forces can be calculated using simple ray optics [104]; the expressions for the gradient and scattering forces of a ray with power P striking a spherical particle are as follows

$$F_{grad}(\theta) = \frac{n_m P}{c} \left\{ R \sin\left(2\theta\right) - \frac{T^2 \left(\sin\left(2\theta - 2\phi\right) + R \sin\left(2\theta\right)\right)}{1 + R^2 + 2R \cos\left(2\phi\right)} \right\}, \qquad (3.3)$$

$$F_{scat}(\theta) = \frac{n_m P}{c} \left\{ 1 + R \cos(2\theta) - \frac{T^2 \left(\cos(2\theta - 2\phi) + R \cos(2\theta)\right)}{1 + R^2 + 2R \cos(2\phi)} \right\}, \qquad (3.4)$$

where θ is the angle of incidence, ϕ the refraction angle and c the speed of light. R and T are the Fresnel reflection and transmission coefficients of the particle surface at θ, respectively. Here, it is assumed that the beam is incident at the centre of the sphere and the relationship between θ and ϕ is given by Snell's law ($n_m \sin\theta = n_p \sin\phi$). The contribution of each force can be analysed by considering the dimensionless parameter Q called the trapping efficiency, where $Q = \frac{cF}{n_m P}$ (i.e. the Q-value for each force is the expression in the curly brackets of Equations 3.3 and 3.4). Figure 3.4 compares the scattering and gradient forces for a range of incident angles by plotting their trapping efficiencies or Q-values. The incident angle of the rays is dependent on the numerical aperture of the objective lens [104].
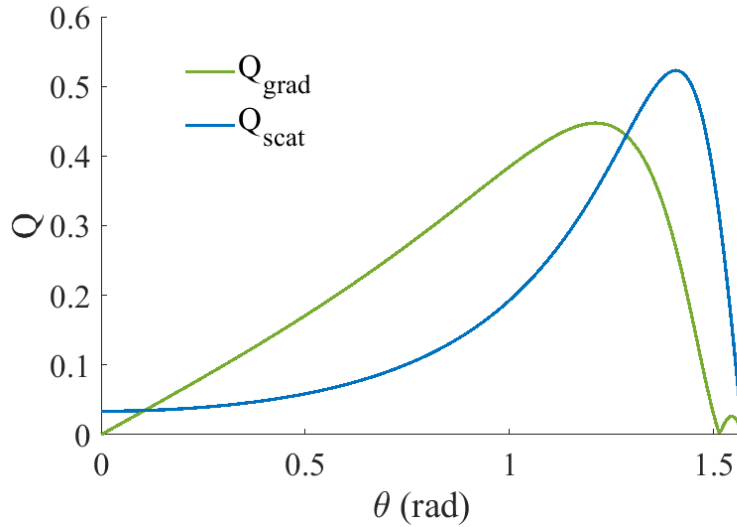
Figure 3.4: Comparison of the gradient and scattering force at different angles of incidence for a single ray striking a spherical particle (the ray optics regime). For a stable trap the range where Q_{grad} is greater than Q_{scat} is of interest.

The Rayleigh regime

The second case to consider is when the size of the trapped particle is much smaller than the wavelength of the trapping light ($a \ll \lambda$). In this case, the particle can be treated as a point dipole in an optical field [103]. As the light with a varying electric field passes through the particle, dipoles are generated. The electric dipole will experience a force in the inhomogeneous electric field. The forces can again be separated into a gradient and scattering force. The gradient force is proportional to the intensity gradient of the beam, whereas the scattering force is proportional to the intensity of the beam [102]. The two forces for the case of a sphere are given by the following expressions [102, 105, 106]:

$$F_{grad}(r) = \frac{2\pi n_m a^3}{c} \left(\frac{m^2 - 1}{m^2 + 2} \right) \nabla I(r) \tag{3.5}$$

$$F_{scat}(r) = \frac{8\pi n_m k a^6}{3c} \left(\frac{m^2 - 1}{m^2 + 2} \right)^2 I(r) \tag{3.6}$$

where $k = \frac{2\pi}{\lambda}$ is the wavenumber, $m = \frac{n_p}{n_m}$ is the ratio of the refractive indices of the particle and the medium, $I(r)$ the intensity of the beam and $\nabla I(r)$ the intensity gradient. Figure 3.5 is a plot of the gradient force (normalized) of a Gaussian beam. Since the gradient force is proportional to the intensity gradient, we see the force is a maximum where the intensity of the beam is the steepest.
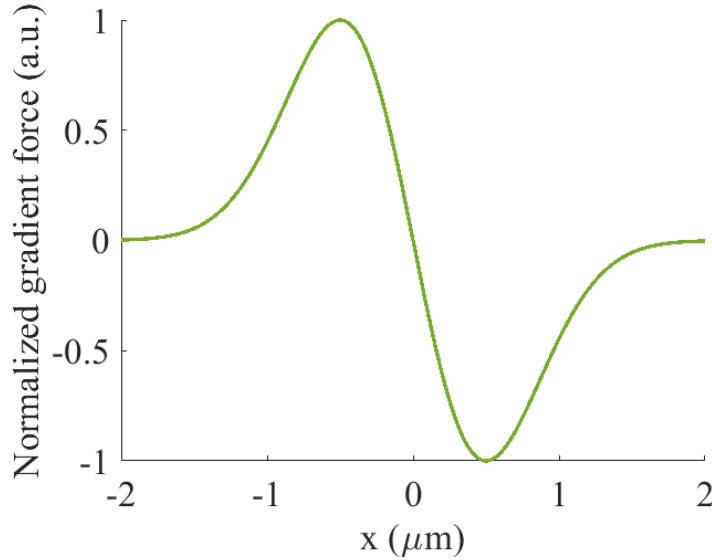
Figure 3.5: Normalized gradient force of a Gaussian beam in the Rayleigh regime.

The Lorentz-Mie regime

The last regime closes the gap between the Rayleigh and ray optics theories. The Lorenz-Mie regime is used to describe the forces on a particle with sizes comparable to that of the laser wavelength ($a \approx \lambda$), which is the case for most applications. A more rigorous electromagnetic theory is required to describe this regime. One such theory is the generalized Lorentz-Mie theory (GLMT) that can be used to model the optical forces on homogeneous isotropic spherical particles [103]. The GLMT is a well-known theory but requires a significant amount of computation; the mathematical description of this theory can be found in [107] and [108]. A second method, called the T-matrix formulation, is used to model optical forces on spherical and non-spherical particles [109, 110]. A complete comparison between the GLMT and the T-matrix method is given by Gouesbet [111]. A mathematical toolbox developed by Nieminen et al. that uses the T-matrix formulation was used for all calculation in this regime [112]. This toolbox can be used to model the

forces in an optical trap for Gaussian, Laguerre-Gaussian and Hermite-Gaussian beams.

Figure 3.6 shows the graphs of the trapping efficiency of a spherical particle in the lateral and axial positions in a Gaussian trap as a function of the displacements in the respective directions. The trapping efficiency is defined the same as in the ray optics regime, i.e. $Q = \frac{cF}{n_m P}$, where F is the force in newton, n_m is the refractive index of the medium and P the power of the laser. A polystyrene particle ($n_p = 1.59$) is modelled in water ($n_m = 1.33$), trapped by a laser of wavelength $\lambda = 532$ nm and with a radius of λ (≈ 0.5 μm). We see in Figure 3.6 that the maximum and minimum of each graph is observed at 0.5 μm. It is at these extreme points that the greatest intensity gradient and therefore the largest restoring force exists. From the graphs, it is clear that the trap strength is greater in the lateral direction. The difference in magnitude of the maximum and minimum in the z-direction (Figure 3.6b) can be explained by the presence of the scattering force in this direction. This last regime completes the description of the forces in an optical trap.
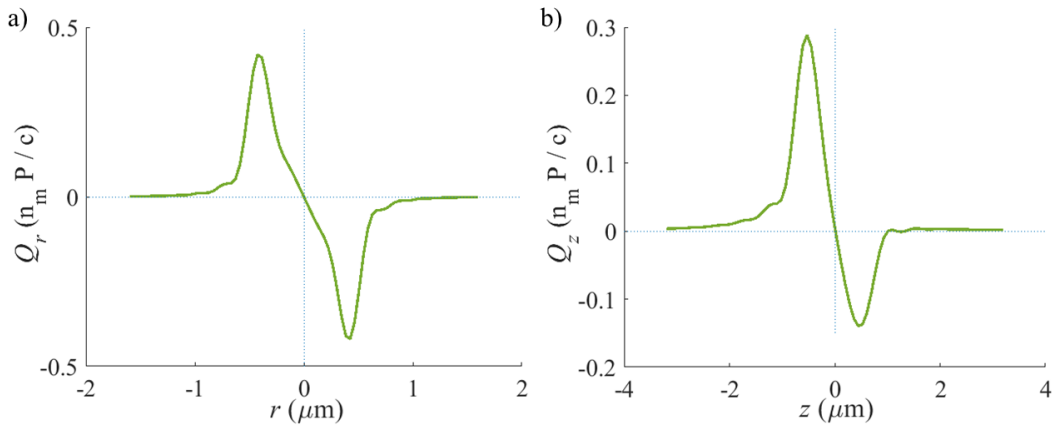
Figure 3.6: The force on a spherical particle (radius 0.5 μm) in a Gaussian beam trap modelled by the T-matrix formulation. The trapping efficiency in the a) lateral and b) axial position as a function of the displacement in the respective directions.

3.1.3 Optical components

An optical trap is usually created by tightly focusing a laser beam through an objective lens with a high numerical aperture (NA). This can be achieved by a relatively simple optical setup, Figure 3.7 illustrates the setup of a generic optical tweezer. The important components thereof include a laser, a beam expansion telescope, an objective lens, a sample holder and an imaging system.
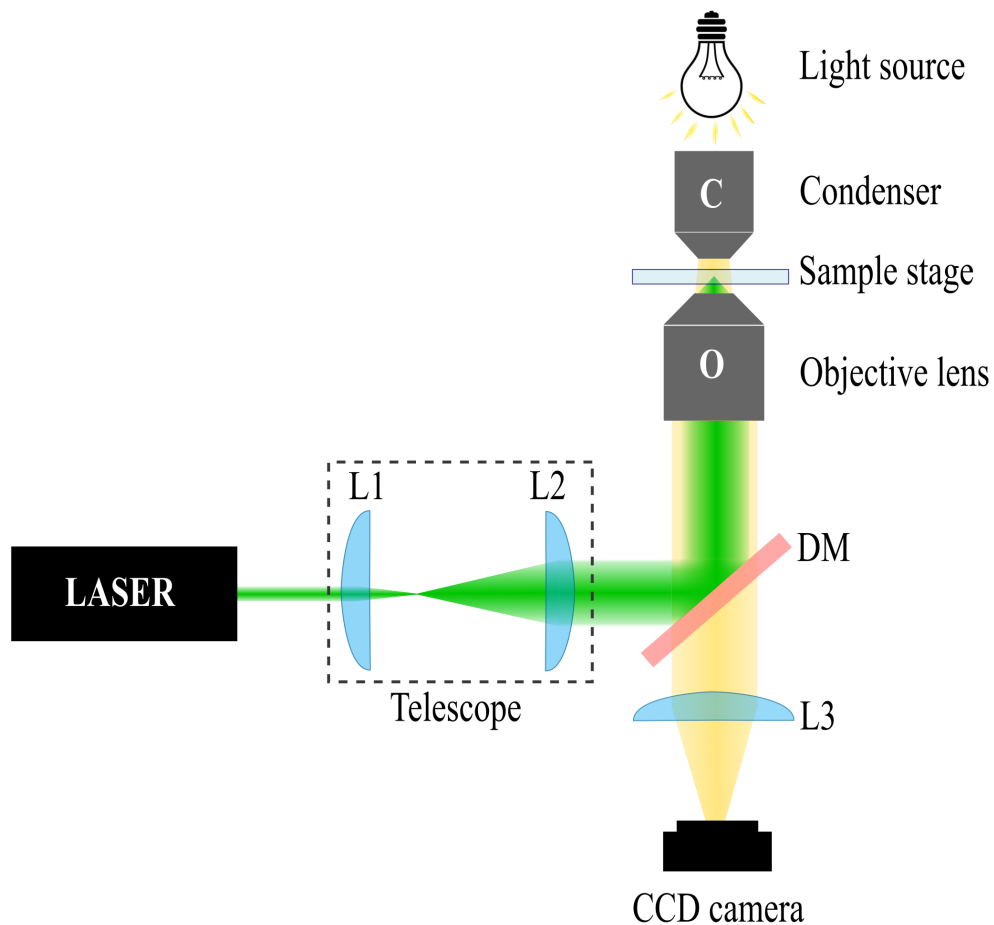
Figure 3.7: A basic optical tweezer setup, which includes a trapping laser, beam expansion telescope (lenses L1 and L2), a high NA objective, a sample stage, an illumination source and a camera to image the sample. DM – dichroic mirror.

The trapping beam is first expanded by a telescope in order to overfill the objective's back aperture. Overfilling the objective improves trapping by creating a high intensity gradient at the focal point necessary for trapping [102]. The beam is reflected off a dichroic mirror and directed through the objective lens from below (i.e. an inverted microscope) where it focuses and traps a particle within the sample. A light source illuminates the sample from above, the illumination light is transmitted by the dichroic mirror and imaged to a CCD camera. Some important aspects of each of these components are now considered.

Requirements of the **trapping laser** include single transverse output mode, minimal power fluctuations and good pointing stability [102]. A single transverse output mode, like the Gaussian mode, ensures that the laser beam can be tightly focused. Pointing instability can cause the position of the trap to vary within the sample, since the beam is focused to such a small spot. Whereas constant power output is needed to prevent variations in the trap stiffness. Depending on the optical setup and sample under investigation, a power output from 2 mW to 1 W is sufficient for optical trapping, however tapping at lower powers is also possible [113]. Lastly, the wavelength of the trapping laser can be in the visible to near infrared range depending on the application, near infrared lasers are usually chosen for biological samples since it incurs the least amount of damage to the sample.

The success of the optical trap mainly depends on the **objective lens**, particularly on its numerical aperture (NA). The NA of an objective is defined as

$$NA = n \sin \alpha \,, \tag{3.7}$$
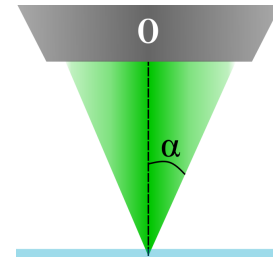
where α is half the maximum cone angle of light acceptance (see inset) and n the

refractive index of the immersion medium (i.e. the medium between the objective and the cover slip). A larger NA results in a larger angle of acceptance (α) meaning a tightly focused beam. A NA between 1.2 and 1.4 is sufficient to create a stable trap with a steep intensity gradient. High NA objectives are usually oil immersion objectives since the oil has a refractive index close to that of the cover slip. For the high NA objective to be used to its full potential it is important that the beam slightly overfills the back aperture of the objective to create the tight focus. The immersion medium (oil, water or glycerol) of the objective and its working distance will limit the physical depth at which particles can be trapped within the sample. A range of objective lenses are available with varying prices, where the more expensive lenses show less spherical aberrations and each having a different transmission at a specific wavelength [102]. All of these specifications need to be taken into account when choosing an objective lens. The objective is most commonly inserted in the optical setup as an inverted microscope, that is when the laser beam is directed upwards through the objective (as in Figure 3.7). This type of setup is the most stable since gravity works against the scattering force, minimizing its effect [109].

To observe the trapping of the sample, the same objective lens is used to image the sample plane to the **CCD camera**. The white light used for illumination is focused by a condenser lens. The dichroic mirror reflects the trapping laser light and transmits the imaging light; more color filters are usually necessary to prevent overexposure of the camera. The CCD camera is used for digital video microscopy to determine the position of the particle. Position detection can also be done through photonic force microscopy that uses a quadrant photo detector.

The **sample** is commonly suspended in an aqueous medium, however experiments have been conducted where the particles are suspended in gases or even in vacuum [114]. The liquid sample containing a very low concentration of the particles is

placed on a microscope slide and protected by a coverslip. The sample can be placed on a piezoelectric stage that enables extremely sensitive movement of the sample.

Optical tweezer setups usually include beam **steering optics** before the objective lens which are used to control the position of the optical trap [102]. The beam steering can be done mechanically by a simple mirror or digitally with more sophisticated devices like a spatial light modulator (SLM) [113]. With SLMs other properties of light like amplitude and phase can also be controlled, therefore including these devices in the optical tweezer setup makes it more versatile and gives it exciting applications, but is not essential for trapping [18]. More on SLMs in Chapter 4. After implementing beam steering, a second telescope (4f-system) is added to ensure the beam reaches the back aperture of the objective lens as shown in Figure 3.8.
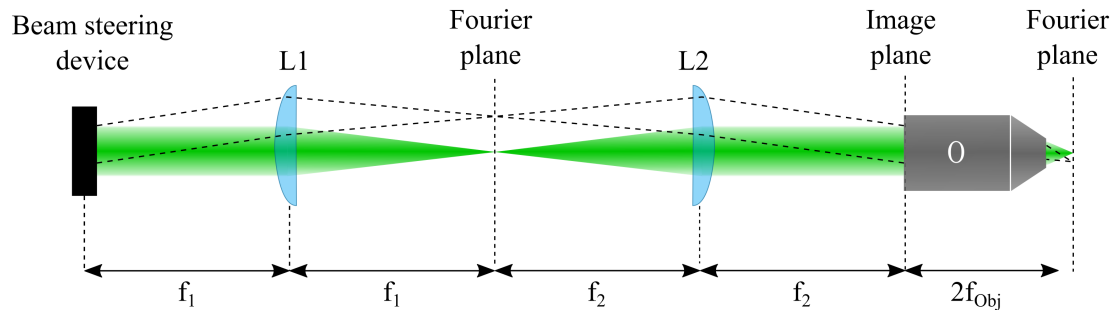
Figure 3.8: A 4f telescope is added after a beam steering device, like a mirror of spatial light modulator, to ensure that the beam reaches the back aperture of the objective lens. f_1 and f_2 are the focal lengths of L1 and L2, respectively.

3.1.4   Applications

Optical tweezers have found broad-reaching applications in the fields of physics [109], biology [11], spectroscopy [115] and nanotechnology [116]. This section touches on

some of these innovative and invaluable applications, while additional uses and detail on specific applications can be found in the given references.

Optical tweezers are ideal for studying biological molecules since they can manipulate nanometer dimension matter and measure piconewton forces, which is the range of inter- and intracellular forces of biomolecules [116]. Optical traps have been used to model single- and double stranded DNA and RNA [117], describe the folding process of nucleic acids [118], characterize the mechanochemistry of myosin (a motor protein) [119] and observe the response of different biomolecules upon exerting spatially resolved forces with the optical trap [116]. Single cells, bacteria and viruses have also been studied in optical traps [120]. These are only a few of the numerous applications of optical tweezers in life science which have been extensively reviewed [15, 116, 120, 121].

The combination of optical traps with other technologies such as SLMs [122], microfluidics [123], plasmonics [120] and fluorescence spectroscopy [124] has made optical tweezing a more powerful and versatile technique. In particular, the combination of optical tweezers with single molecule fluorescence has made the observation of chemical and structural changes possible within the optical tweezer setup; Section 3.3 will elaborate on this technique. Optical traps created with structured light beams have become a powerful technique called holographic optical tweezers (HOT), a discussion on the advances of this technique is given in Section 4.1.5.

Interesting and more advanced applications of optical tweezers include optical force printing, where nanoparticles are positioned on a substrate in a controlled manner by means of the scattering force [125], the trapping of gas microbubbles [109] and liquid microdroplets [126] to better understand their properties and interaction with other molecules. Optical tweezers are also being used to study the interaction

of circular polarised light (which has chiral properties) with chiral matter, in particular to use this polarised light to optically separate enantiomers [127, 128]. Optical tweezing can be used to assemble micro- and nanostructures and actuate micromachines which has made it an indispensable tool in nanotechnology and optomechanics [15, 116]. Plasmonic, acoustic and electron beam trapping have also gained a lot of attention in recent years [18, 109]. New applications and advances of optical tweezers are emerging every day across different disciplines. We are therefore still a long time away from realising the full potential and impact of optical tweezers.

3.2 Trapping experimentally

Detail of the optical tweezer setup used in this study is discussed in this section as well as how sample preparation was done (Sections 3.2.1 to 3.2.3). Proof of trapping micro-sized particles and calibration of the optical trap are given in Sections 3.2.4 and 3.2.5, respectively.

3.2.1 Setup of an optical tweezer

A diagram of the experimental setup of the optical tweezer is shown in Figure 3.9. A diode laser with wavelength $\lambda =$532 nm ($\omega_0 = 0.65$ mm, Oxxius LaserBoxx LCX - 532, France) was used for trapping. The beam was expanded by a simple telescope (L1: 50 mm; L2: 500 mm) before it was directed to the SLM. As already mentioned, an SLM is a digital device used to control the amplitude and phase of a beam. However, for this section the SLM can be considered as an extra mirror since only a Gaussian beam was generated with the device, which is the output beam of the laser. The significance and operation of the SLM will become apparent in Chapter 4. The SLM is aligned to only modulate horizontal polarized light;
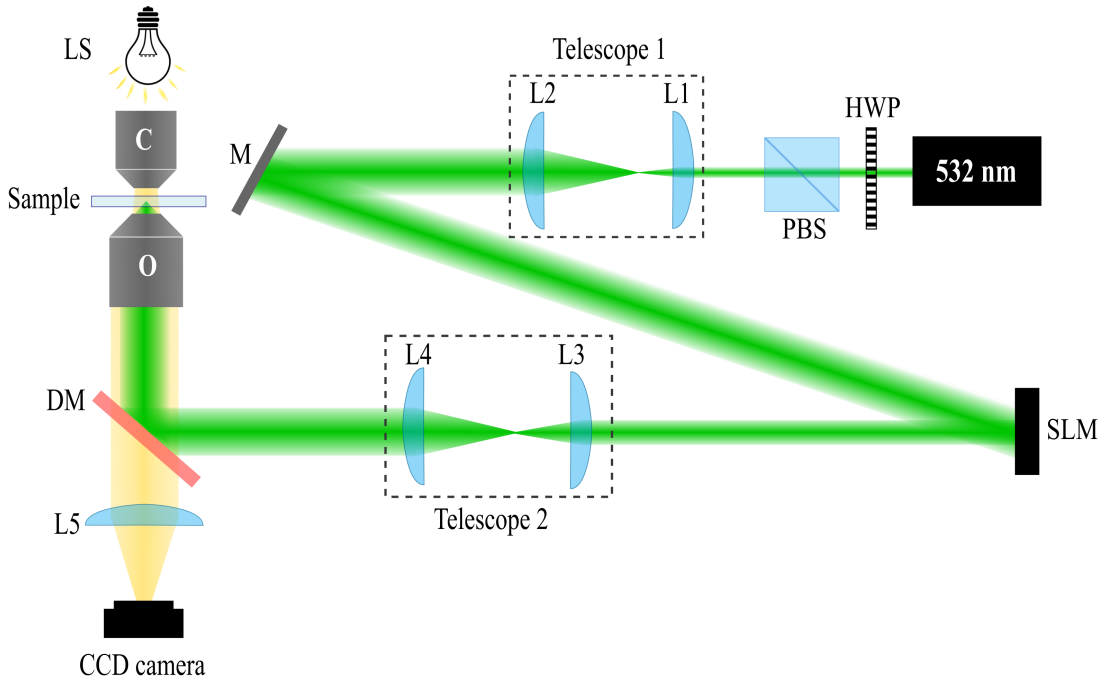
Figure 3.9: Schematic of the optical tweezer experimental setup. The laser beam with a wavelength of $\lambda = 532$ nm is expanded with telescope 1. The beam is then directed onto a SLM. A half-wave plate (HWP) and polarizing beam splitter (PBS) are added in the setup to control the power of the laser beam and ensure horizontally polarized light is incident on the SLM. A second telescope is implemented to ensure overfilling of the objective lens. The beam is reflected by a dichroic mirror (DM) and focused by the objective lens (100X, NA=1.3) to create the optical trap inside the sample chamber. An LED white light source (LS) and a condenser lens (10X) are used to illuminate the sample. The imaging light is transmitted through the DM and imaged (with the eyepiece lens L5) to a CCD camera.

and since the light from the laser is vertically polarized, a half-wave plate (HWP) was added in the setup before the SLM. The HWP along with the polarizing beam splitter (PBS) were used to control the power of the laser beam. A second telescope (L3: 100 mm; L4: 150 mm) was added after the SLM to ensure the beam generated by the SLM reached and overfilled the back aperture of the objective lens. The laser beam was reflected by a dichroic mirror (567 nm longpass) and directed through the objective lens (NA = 1.3, 100X, oil, ∞-corrected, Nikon Plan Fluor, Japan) from below. The high numerical aperture objective lens focused the laser beam and created the optical trap in the sample chamber. The sample was placed on a movable stage that can be finely controlled in the vertical and horizontal directions. See Section 3.2.2 for the details on preparing the sample and how it was placed in the setup. An inverted microscope was implemented with a white LED light and condenser objective (10X, Nikon E Plan) illuminating the sample from above. The illumination light (yellow beam in Figure 3.9) traveled back through the 100X objective lens, was transmitted by the dichroic mirror and imaged to a CCD (charge coupled device) camera with an eyepiece lens (L5: 200 mm).

Figure 3.10 shows an image of the Gaussian beam obtained experimentally by the optical setup described above. The cross-section of the beam is shown on the right which clearly shows the Gaussian profile. The image of the beam was taken in the image plane (near field) after L4.
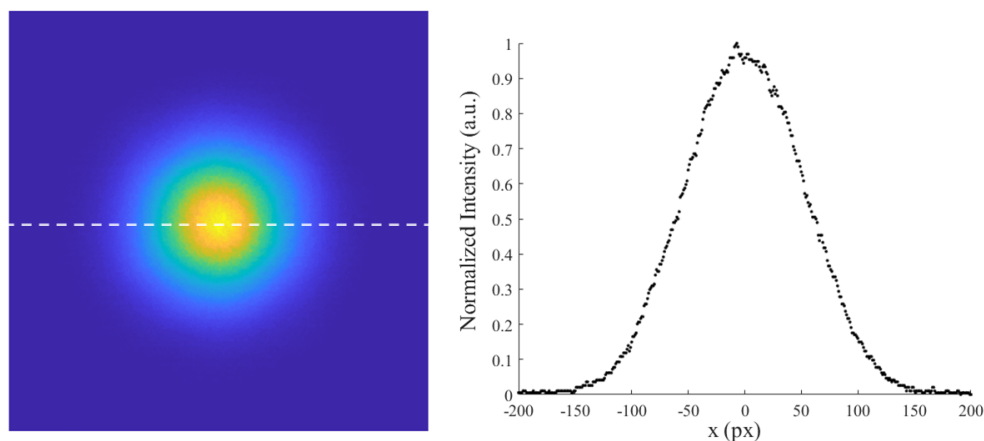
Figure 3.10: An image (left) and cross-section (right) of an experimentally generated Gaussian beam imaged to a CCD in the near field.

3.2.2 Sample preparation

Figure 3.11 shows how the samples were prepared and introduced into the optical setup. Firstly, a spacer (ring reinforcement sticker) was placed in the centre of a glass microscope slide (26 mm x 75 mm) to create a small well for the solution. A droplet of a dilute solution of the particles to be trapped was then placed in the well; a coverslip (22 mm x 18 mm) was placed on top and sealed around the edges with clear nail polish. Since the sample is placed in an inverted microscope setup, it is necessary that the seal is completely dry and the cover slip fixed to the microscope slide before placing it in the setup. A drop of immersion oil was then positioned on the cover slip before placing it facing the objective lens; the placement of the sample inside the trap is shown schematically and with a photo in Figures 3.11b and c. As seen in Figure 3.11b, the beam passes through the coverslip to create the trap inside the sample, it is therefore important to place and fix the coverslip as flat as possible, otherwise the trapping beam becomes aberrated.

The polystyrene beads mentioned in Section 2.3.1, that were used to synthesize the
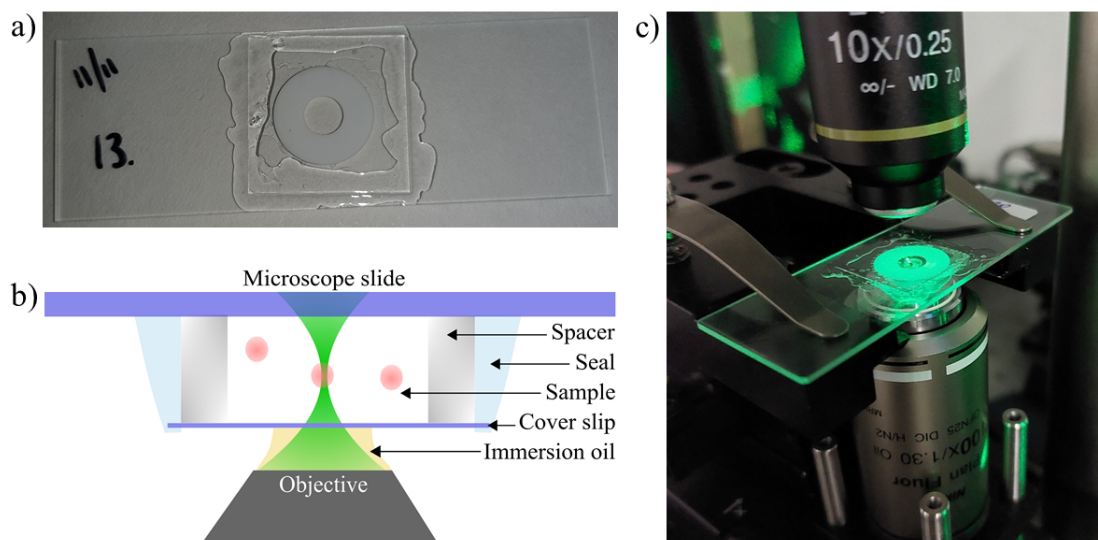
Figure 3.11: Sample preparation: a) A droplet of the sample is placed on a microscope slide in the the centre of a spacer, a coverslip is placed on top and sealed with clear nail polish. b) A schematic (not on scale) and c) a photo of how the sample fits into the optical tweezer setup.

QD-tagged beads, were used (uncoated) for trapping experiments and calibration. A dilute solution was prepared by dissolving 5 μl of the beads in 2 ml deionised water and placing the solution in an ultrasonic bath for 5 min before putting a drop on the microscope slide. Figure 3.12 shows the appearance of these particles under a transmission electron microscope (TEM) and in the optical setup. The TEM image confirmed the 2 μm diameter of the beads. The sample appears to be illuminated with red light, however, this is only due to the dichroic mirror only letting through light with a wavelength > 580 nm.
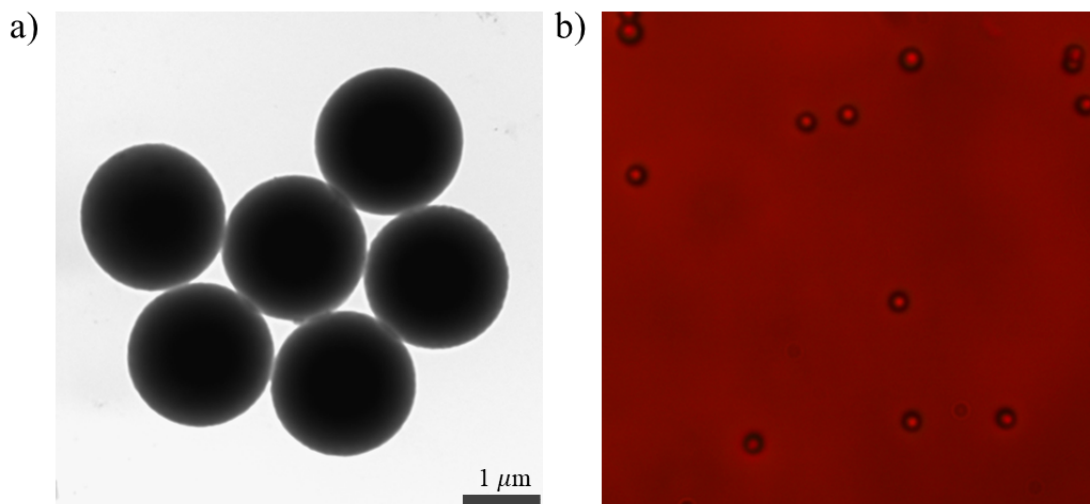
Figure 3.12: The sample consisting of polystyrene particles with 2 μm diameter. The appearance of these particles under a) a transmission electron microscope (TEM) and b) in the optical tweezer setup.

3.2.3 Tricks to trapping

This section is included to discuss two practical aspects (or tricks) that were important to obtain optimal and efficient optical trapping with the system. The first trick has to do with alignment of the trap and the second with sample preparation.

Trap alignment

Alignment of the laser beam through all the components in the system is crucial to obtain proper results in any optical experiment. Here the alignment of the trap portion of the optical tweezer setup is discussed.

The high magnification, high NA objective that creates the tightly focused beam, is very sensitive to misalignment. In the inverted microscope setup the laser beam's direction changes from being parallel to the optical table to being perpendicular to the table as shown in Figure 3.13a. The perpendicular beam must be well
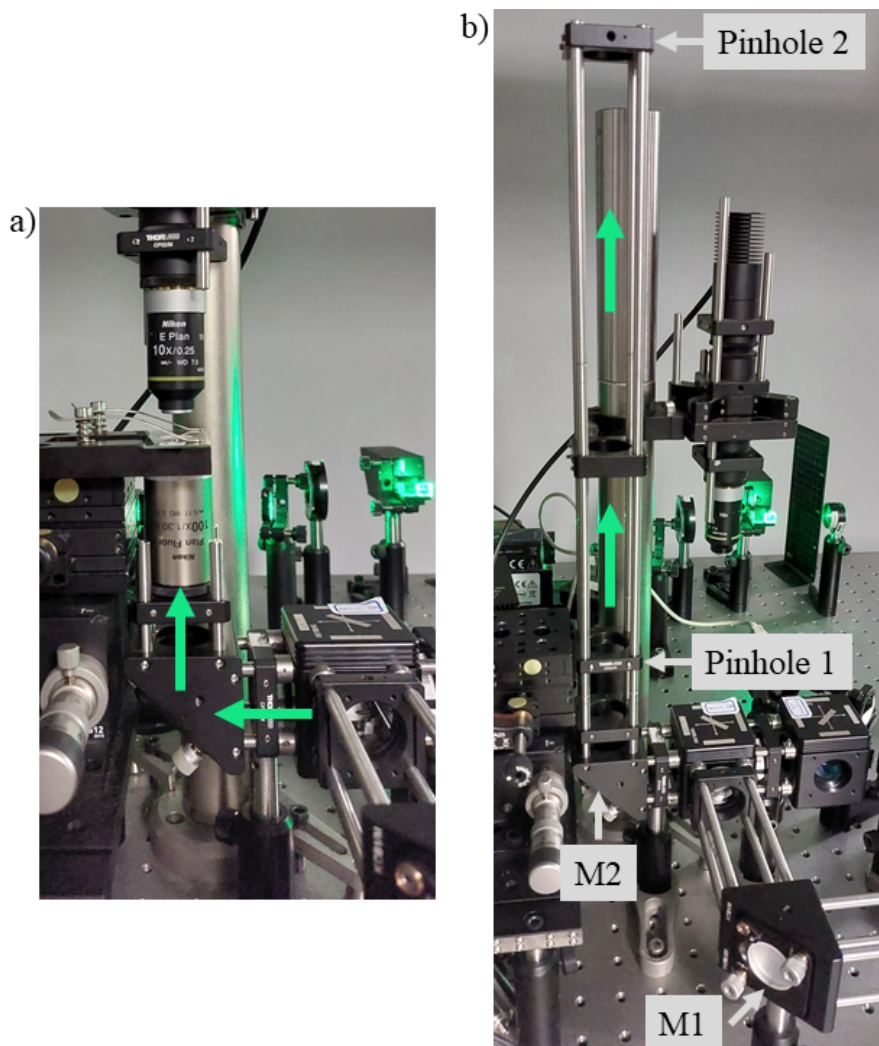
Figure 3.13: a) Image of the optical tweezer setup showing where the beam changes direction from parallel ($\leftarrow$) to perpendicular ($\uparrow$) to the optical table. b) The setup used to align the trap; the objective, sample stage and condenser lens were removed and a long cage system was built upwards. Mirrors 1 and 2 were used to ensure the laser beam goes through pinholes 1 and 2, respectively. Lastly, a mirror was placed at the position of pinhole 2, to ensure the back reflection of the beam is also aligned.

aligned, since it is this beam that enters the objective. To direct a laser beam to a new position with a specific angle, two mirrors (and two pinholes) are needed – this process is called 'beam walking'. Figure 3.13b shows how the beam was experimentally aligned in this part of the setup. Firstly, the objective, sample holder and condenser lens were removed and a cage system was built going upwards (in the direction of the objective lens). Two pinholes were placed in the cage system as far away from each other as possible; if the laser beam goes through both pinholes, the beam will be well aligned with respect to the objective lens. Mirror M1 (the position mirror) was used to control the position of the beam at pinhole 1, and mirror M2 (the angle mirror) the position at pinhole 2. Therefore, by iteratively adjusting mirrors 1 and 2 to direct the beam through the respective pinholes, alignment of the trapping beam was achieved. Several alignment methods were tested, however the method reported here (even though a bit tedious) worked the best for this setup.

Glass deactivation

Untreated glassware contains silanol groups (Si-OH), these groups make the surface of the glass hydrophilic, causing polar compounds to adsorb to the surface through hydrogen bonding. In this study, the polystyrene beads used in trapping experiments, contained carboxylic acid groups (which are polar) on their surface (the reason for this is discussed in Section 2.3.1). Thus, due to these polar groups, the beads immobilized on the surface of untreated glass. This caused a problem when attempting to trap the particles. To solve this problem, the glassware (microscope slides and cover slips) was deactivated before assembling the samples. Deactivation of glassware increased its hydrophobicity and prevented the unwanted adsorption of polar compounds. Deactivation can be achieved by reacting glassware with dimethyldichlorosilane (DMDCS). Figure 3.14 illustrates

the reaction of untreated glassware with DMDCS.
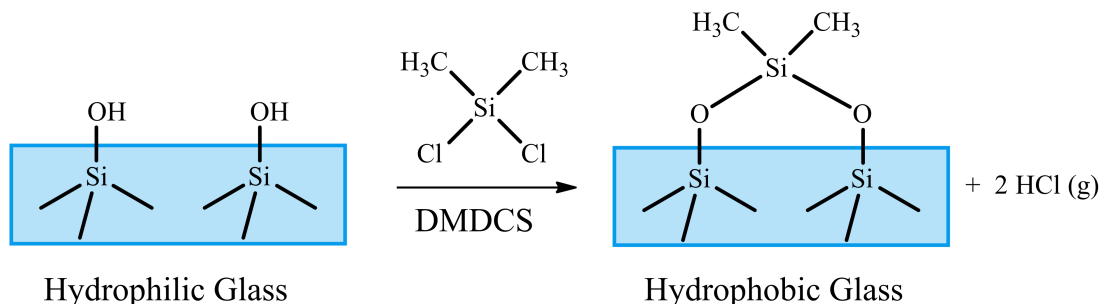
Figure 3.14: Deactivation of glass with DMDCS. The OH-groups on the surface of untreated glass makes it hydrophilic; after treatment with DMDCS the surface becomes hydrophobic.

The deactivation procedure was as follows: the microscope slides and cover slips were soaked in a 5% v/v DMDCS-toluene solution for 15 min and then rinsed twice with toluene. The glassware was then soaked in methanol for 15 min, rinsed with methanol and dried with inert argon gas. This reaction was done in the fume hood since hydrogen chloride gas is a byproduct and DMDCS is a flammable and toxic substance. Dehydrated toluene was used for the reaction since the presence of water reduces the effectiveness of the DMDCS solution. Both the DMDCS and dehydrated toluene were purchased from Sigma Aldrich, USA. Figure 3.15 shows how to test whether the deactivation was successful. When a droplet of water is placed on untreated glass the droplet will spread out but on deactivated glass it forms a bead. This confirms the hydrophobicity of the treated glass, since water is a polar molecule. A permanent marker can also be used to test deactivation since it will write on untreated glass but not on deactivated glass.
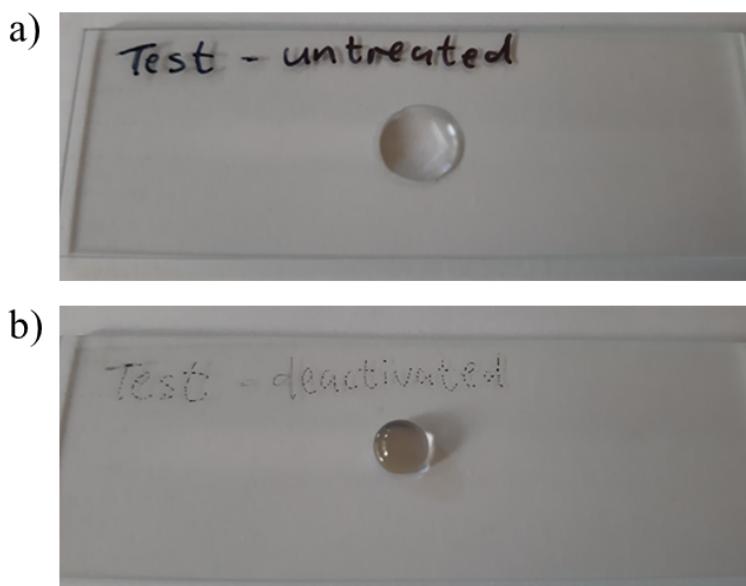
Figure 3.15: Water droplet and permanent marker test to determine whether glass is a) untreated or b) deactivated. A water droplet spreads out on untreated glass but forms a bead on deactivated glass. A permanent marker writes clearly on untreated glass but not on deactivated glass.

3.2.4 Proof of trapping

Successful trapping of a 2 μm particle is shown in Figure 3.16. The series of five images shows a trapped particle (circled in green) keeping its position while moving the sample with the stage controls. The reference particle, which moves with the sample, was moved around the trapped particle in a rectangular pattern. This particle starts at position 1 moves to positions 2 to 4 and back to position 1 to complete the rectangular pattern (Figures 3.16a-e). The particle was trapped with a laser power of 0.30 mW.

The motion of a free particle and a trapped particle were monitored for 5 min. The trajectory and the distribution of these particles' position in the Y-direction are shown in Figure 3.17. The particle position was tracked using the CCD camera and image analysis was done in Matlab®. From this figure, it is clear that the
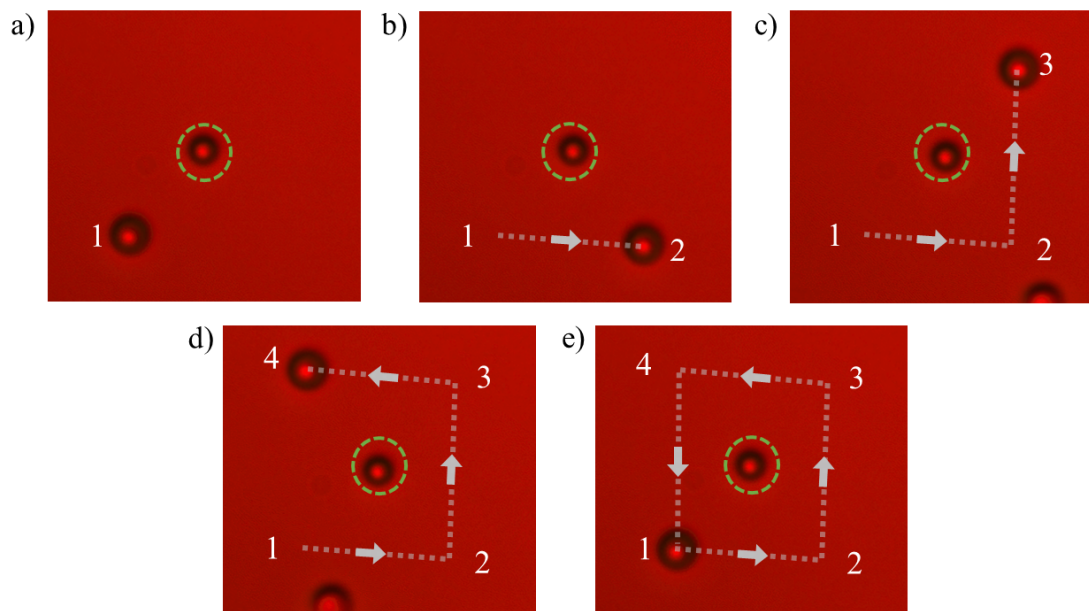
Figure 3.16: Trapping a 2 μm polymer bead. The trapped particle (circled in green) keeps its position while the sample is being moved in a rectangular pattern around the trapped bead. The reference particle that moves with the sample a) starts at position 1 b)-d) moves to positions 2, 3 and 4 and e) back to position 1 to complete the rectangular pattern.

free particle underwent random Brownian motion and moved over 138 pixels in the Y-direction (Figure 3.17a). The trapped particle was, however, confined to move only 5 pixels during the analysis time (Figure 3.17b).

The slight movement of the particle inside the trap is due to thermal noise pushing it out of the trap and the optical force drawing it back in. The trap strength can be calculated experimentally by monitoring this motion of the trapped particle, as discussed in Section 3.2.5.
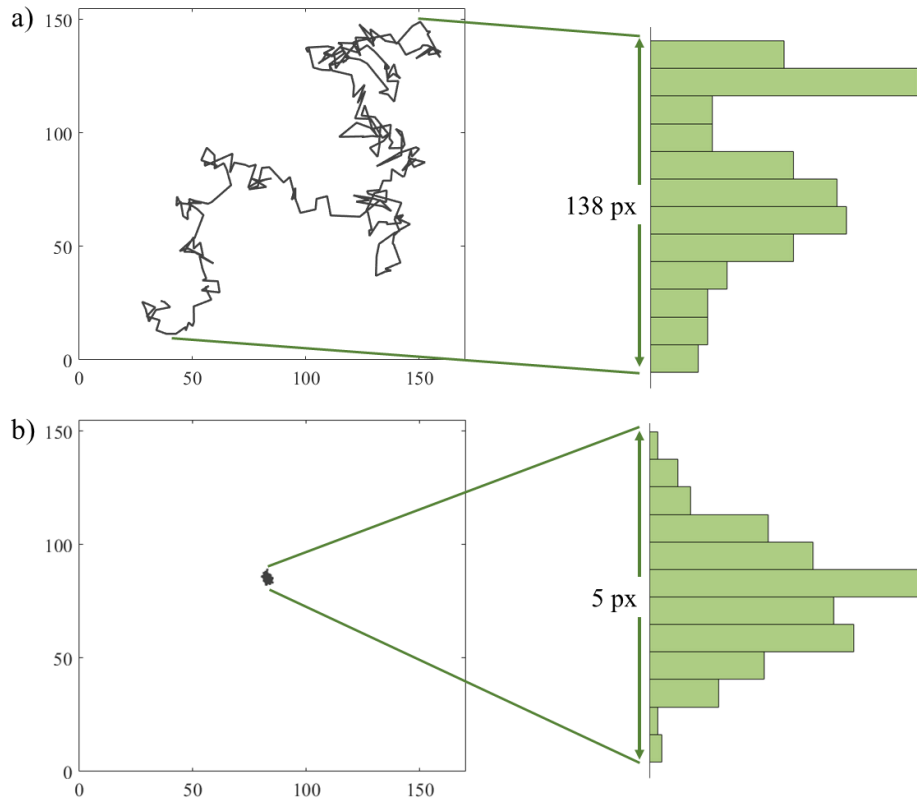
Figure 3.17: Trajectory and probability density in the y-direction of a) a free particle and b) a trapped particle over 5 min. The free particle exhibits Brownian motion and moves over 138 pixels whereas the trapped particle's movement is restricted to only 5 pixels.

3.2.5 Trap calibration

The theoretical calculation of forces exerted by optical traps, as described in Section 3.1.2, is in poor agreement with experimental data unless parameters like spherical aberration and astigmatism are taken into account, which was done by Rohrbach and Dutra *et al.* [129, 130]. Other parameters like the cover slip thickness, the position of the trap inside the sample, the exact refractive indices and specifications of the objective lens and the other optical components also influence the force of the trap [113]. It is therefore critical to have accurate calibration methods to determine these forces experimentally. Several methods can be used for calibration:

the drag force method, potential analysis, equipartition method, mean squared displacement analysis and the power spectral density method [113, 131]. In this study the equipartition method was used for determining the trap stiffness and potential analysis to visualize the potential wells created by the optical trap.

The equipartition method

An optical trap can be described as a microscopic spring. The particle is kept in the equilibrium position by a harmonic force defined by Hooke's law [113]

$$F_{OT} = -\kappa_x(x - x_{eq}), \tag{3.8}$$

where F_{OT} is the applied force by the optical trap, κ_x is called the trap stiffness in the x-direction and $(x - x_{eq})$ the displacement of the particle from the equilibrium position (x_{eq}). The force in the y-direction can be obtained by considering the displacement in this direction.

The resulting trapping potential is given by

$$U(x) = \frac{1}{2}\kappa_x \left(x - x_{eq} \right)^2 . \tag{3.9}$$

The equipartition theorem can then be used to measure the trap stiffness. This theorem states that the energy of a system at equilibrium is $\frac{1}{2}k_B T$ for each degree of freedom, with k_B Boltzmann's constant and T the temperature at equilibrium. Therefore,

$$\langle U\left(x\right)\rangle = \frac{1}{2}\kappa_x\langle(x - x_{eq})^2\rangle = \frac{1}{2}k_B T . \tag{3.10}$$

Let $\sigma_x^2 = \langle(x - x_{eq})^2\rangle$, the variance of the position of the trapped particle, then

$$\kappa_x = \frac{k_B T}{\sigma_x^2} . \tag{3.11}$$

Thus by measuring the position variance, the trap stiffness can be determined. The calculation of σ_x^2 is straightforward, but requires calibrated position detection which can be done using a CCD camera. The position of the particle is needed in units of meters, but since the camera gives the displacement in pixels a conversion is needed. The pixel size of the camera can be determined by using an object of known dimensions. The polystyrene sphere with a known diameter of 2 μm was used and the size of a pixel was determined to be 53.3 nm. A temperature of 22 °C and $k_B = 1.3806 \times 10^{-23}$ m^{2}kg/s^{2}K were used for the trap stiffness calculations.

The motion of a trapped polystyrene bead with a diameter of 2 μm was monitored for 5 min, taking a position measurement every second (sampling frequency = 0.0167 Hz). Five beads were trapped at each power measurement from which the trap stiffness was determined. The average trap stiffness at each power is plotted in Figure 3.18a with the error bars being the standard error. The linear relationship between the laser power and the trap stiffness is evident in this graph. Figure 3.18b shows the trajectory of the trapped particle at increasing powers of 30 μW, 120 μW and 300 μW. As the power increased, the displacement of the trapped particle from the equilibrium position decreased ($\kappa_x \propto \frac{1}{\sigma_x^2}$). The equipartition method can be reliably used to determine the trap stiffness at laser powers up to 350 mW [132].

The power was measured with a photodiode power sensor (Thorlabs, Germany) at the image plane after lens L4 (see Figure 3.9). However, the power after the objective was measured to be 40% less, mostly due to reflection from lenses, the dichroic mirror and the objective itself. Hence, the power values reported in this study were 60% of the measured power, to give a better estimation of the actual power in the trap. Also, the laser power was stable within 4 μW during the 5 min analysis time. Consider Figure 3.18 again; the trapping powers used were quite low (μW) compared to powers of a few milliwatts which optical tweezers usually operate at. The choice of such low powers was because our optical trapping

system was combined with fluorescence spectroscopy, which requires a much lower intensity beam for excitation; since trapping and excitation were done with the same laser in this study, the lowest possible powers were used for trapping (see Section 3.3 for more detail).
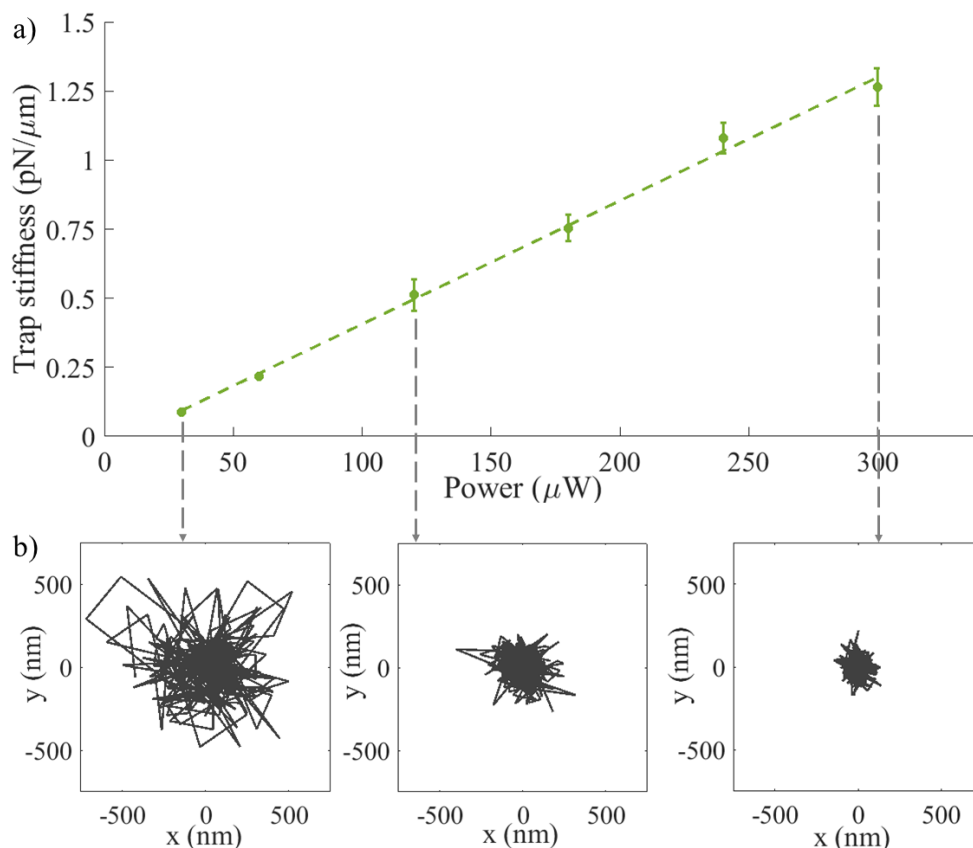
Figure 3.18: a) The trap stiffness (in the x-direction) at different laser powers when trapping a polystyrene bead with a diameter of 2 μm. b) The trajectory of a trapped particle at increasing powers of 30 μW, 120 μW and 300 μW, respectively.

Potential analysis

The equipartition method is a specific case of potential analysis where we assume harmonic potential. If harmonic potential is not assumed, the potential energy, $U(x)$, can be determined through the position probability distribution of the

trapped particle given by the Maxwell-Boltzmann equation [131]:

$$\rho(x) = N \exp\left(-\frac{U(x)}{k_B T}\right) \tag{3.12}$$

where N is the normalization constant so that $\int \rho(x)\,dx = 1$. By solving Equation 3.12 we obtain an expression for the potential energy:

$$U(x) = -k_B T \ln \frac{\rho(x)}{N} \tag{3.13}$$

Therefore, the potential well created by an optical trap can be determined by obtaining the probability distribution of the position of the particle from equilibrium. Figure 3.19a shows the x-displacement of the particle in a trap over 5 min. The equilibrium position is at $x = 0$. Figure 3.19b shows the corresponding position distribution with a fitted Gaussian curve and 3.19c the trap potential in units of $k_B T$ with a fitted parabolic function. In Figure 3.19d the the potential wells of optical traps at powers of 30 μW, 120 μW and 300 μW are shown - the wells became narrower as the power or trap stiffness increased.
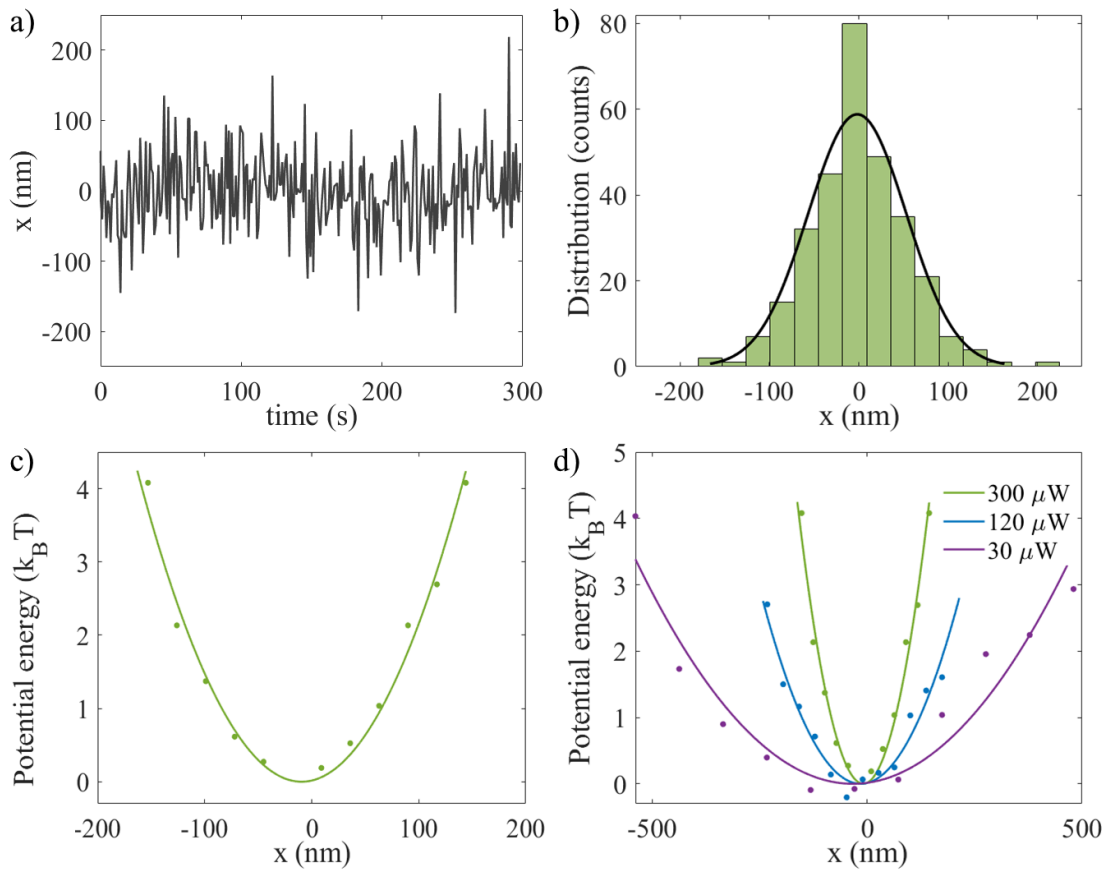
Figure 3.19: Potential analysis of a trapped particle. a) The displacement of the particle from the equilibrium position over time and b) the corresponding position distribution and c) potential energy of the trap. d) Comparison of optical trap potential wells at increasing powers of 30 μW, 120 μW and 300 μW.

3.3 Optical tweezers combined with fluorescence spectroscopy

In order to detect the fluorescence of QD probes (synthesis reported in Chapter 2), a fluorescence microscope was integrated into the optical tweezer setup. This section starts with a description of the challenges that arise when combining optical tweezers with fluorescence spectroscopy and how they have been overcome

(Section 3.3.1). The changes in the experimental setup and the detection of fluorescence are reported in Section 3.3.2

3.3.1 Background

Optical traps are the ideal tool for measuring mechanical properties of molecules since piconewton (pN) forces can be applied to the molecules in a controlled manner. However, this technique is blind to conformational and chemical changes in molecules - this is where single-molecule fluorescence techniques come into play.

The combination of optical tweezers and fluorescence detection has made a significant contribution to the joint field of single-molecule manipulation and visualization. The biological applications and technical details of this hybrid technique have been excellently documented in recent reviews [115, 120, 124].

Design considerations

The main difference between optical tweezers and fluorescence microscopy is the intensities of the light used in these techniques. The laser light needed for optical trapping is up to six orders of magnitude higher than that of fluorescence studies [133]. The intensity of light used for fluorescence excitation is low in order to minimize photobleaching of the fluorophores. Photobleaching is an irreversible process where fluorophores become non-fluorescent [134]. Photobleaching usually occurs because electrons already in the excited state continue to absorb photons, the dissociation then leads to permanent loss of fluorescence signal [115].

The photobleaching lifetime, which is the time fluorophores exhibit fluorescence when under continuous exposure to the excitation light before bleaching, can vary from microseconds to minutes depending on the intensity and wavelength of the excitation source and also the concentration and type of fluorophore [135]. Note

that the photobleaching lifetime of a fluorophore must not to be confused with its fluorescence lifetime which is the time a fluorophore remains in the excited state before emitting a photon and returning to the ground state. The fluorescence lifetime of fluorophores ranges from pico- to nanoseconds and is an intrinsic property of the molecule, meaning it is largely independent of the excitation source and concentration of the fluorophore [136].

In most setups two different light sources are therefore used – one for trapping (high intensity) and the other for fluorescence excitation (low intensity). To prevent photobleaching due to the trapping laser three general solutions have been demonstrated: (1) trapping with a non-resonant laser and the separation of the fluorescence and trapping in (2) space or in (3) time [115]. The trapping laser will not cause much bleaching if the fluorophore does not absorb at the specific wavelength of the laser – this is what is meant by a non-resonant laser [133]. For example, a lot of biological samples do not absorb well in the near-infrared range, which is why higher wavelength lasers are usually used for trapping in these applications. A second resonant light source is then used for fluorescence excitation.

Spatial separation of the trapped particle and the fluorophore is achieved by tethering the fluorophore to a bead through a long molecule (like DNA). The spatial separation can be between 1 – 14 μm [115]. The bead is then trapped by the high intensity (usually non-resonant) laser and the fluorophore illuminated a distance away by the low intensity excitation laser. To restrict the movement of the tethered fluorophore another bead can be attached on the other side, both beads can then be trapped in a dual trap with the fluorophore in the center [137]. Another method to restrict the movement is to attach the other side not to a second bead but to the surface of the sample holder [138]. This spatial separation method does not only serve as means to reduce bleaching, but also helps to measure the

applied force on the molecule. In order to measure the tension on a biomolecule an extra anchor is needed which can be achieved by a second trap or by attaching one end of the biomolecule to the surface of the sample holder as just stated. However, the sample preparation of these systems can get rather complicated. The combination of optical tweezers and fluorescence microscopy has been primarily used to investigate the conformational changes in biomolecules due to an applied force by the tweezer. The spatial separation method is the most widely used method, since it solves two of the challenges of this biological application.

The time separation method alternates the trapping and excitation laser, such that both never simultaneously illuminate the fluorophore. This method has proven to reduce the photobleaching, but has a fairly complicated setup [139].

Excitation methods

As mentioned in the previous discussion, the fluorescence excitation source is usually different from the trapping laser. The excitation is most commonly achieved by three methods: epi-fluorescence, confocal fluorescence and total internal reflection fluorescence (TIRF). We refer to epi-fluorescence when the excitation light and emitted light (from the fluorophore) travel through the same objective lens. Epi-fluorescence is a wide-field fluorescence technique meaning it illuminates the whole sample. This technique has a simple setup but suffers from background noise. In confocal fluorescence a small region of the sample is illuminated which reduces the background noise but shows increased bleaching of the fluorophores and has a more complicated setup. In TIRF, also a wide-field technique, the fluorophores are excited by an evanescent field caused by the reflection of the excitation beam on the sample surface. This evanescent field decays exponentially inside the sample, thus the depth of illumination is limited to only $\sim$200 nm. The TIRF fluorescence method is usually used in cases where the molecule is attached to the surface

because of the limited illumination depth.

In all the cases described above, separate sources were used for trapping and excitation, but both can be achieved by a single laser if two-photon excitation (TPE) fluorescence is used. In TPE, two photons are simultaneously absorbed by the fluorophore that then emits light of a shorter wavelength than the excitation wavelength. TPE only occurs at a measurable rate with high intensity lasers such as lasers used for optical trapping [140]. The laser must have a wavelength at least twice that of the absorbance of the fluorophore to show TPE [141]. TPE is harder to detect and not all fluorophores can exhibit this phenomenon. Trapping and two-photon excitation have been successfully done by several groups with a near-infrared laser where the fluorophores are QDs [140, 142–144].

Quantum dots in optical tweezers

This research project focuses on using optical tweezers in combination with QD fluorescent probes. See Chapter 2 for a discussion on the properties and synthesis of QDs. CdTe QDs were first successfully trapped by optical tweezers in 2007 by Pan *et al.*, the fluorescence from the QDs was observed through two-photon induced luminescence [143]. Individual QDs, agglomerations of QDs, silica coated QDs and QDs coupled to polystyrene beads have since been trapped and have found exciting applications [140,142,144–148]. The biosensing research group of Hong-Wu Tang has used a bead-based fluorescence assay in optical tweezers to detect a prostate-specific antigen as well as the H5N1 and H7N9 avian influenza virus genes with high sensitivity and detection limits as low as 1.0-2.0 pM [141, 149, 150].

3.3.2 Fluorescence detection

This section reports on how a fluorescence microscope was experimentally integrated into the optical tweezer setup to detect the fluorescence signal from a trapped

QD-tagged bead. Here, not only the final results, but also the process that lead up to them are presented.

Firstly, fluorescence detection tests were not only done with the QD-tagged probes since they were being synthesised and optimized in parallel to building this optical setup. Therefore, initial tests were carried out using commercial fluorescent beads (purchased from Thermo Fisher Scientific, South Africa). These beads were 2 μm in diameter, made from polystyrene and filled with a fluorescent dye called Nile red. In the discussions to follow, these commercial fluorophores are referred to as 'fluo-beads'.

The optical tweezer combined with fluorescence spectroscopy setup described in this study is different to any of the setups discussed in Section 3.3.1. Here, the same laser is used to trap and excite a fluorescent particle; and since the wavelength of the laser is $\lambda = 532$ nm it makes use of single photon excitation (not TPE). The absorbance spectra of the QD-tagged beads and the fluo-beads confirmed that both these fluorophores can be excited with a wavelength of 532 nm. Since the high intensity trapping laser was used for excitation, photobleaching of fluorophores in the optical trap was expected; however, Chapter 4 explores the use of structured light in the optical tweezer to reduce bleaching. Here, the focus is on only detecting the fluorescence signal.

Fluorescence detection with a CCD camera

The first fluorescence detection test was performed by keeping the setup just as described in Section 3.2.1 and using the CCD camera to detect the fluorescence from the fluo-beads and QD sample. The fluorescence emitted from the sample followed the same path as the illumination light, i.e. it travelled back through the objective lens, was transmitted by the dichroic mirror and imaged to the CCD camera (Figure 3.9). In this experiment, the particles were not trapped, the laser

was only moved over the particle to see if some signal could be observed. Note that the QD-tagged bead sample tested here was from attempt 2 (refer to Section 2.3.3). In this attempt of the QD-tagged bead synthesis, the QDs reacted with themselves to form large agglomerates; the TEM image of this sample is shown in Figure 2.26a. Therefore, to distinguish this sample from the other (uniformly coated) QD-tagged bead samples, it is called QD-agglomerates (not QD-tagged beads). The results are captured in Figure 3.20. The appearance of the samples under only the illumination light is shown on the left and the samples when the laser was incident on the sample are shown on the right. The fluorescence (bright yellow/orange light) emitted from a fluo-bead (top) and some QD-agglomerates (bottom) were therefore clearly seen with the CCD camera.
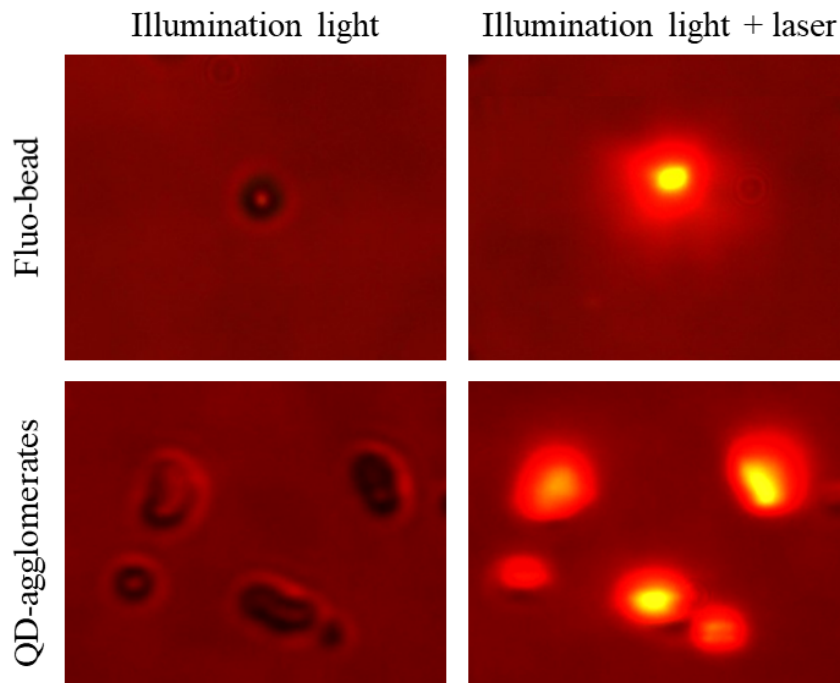
Figure 3.20: Fluorescence detection of a fluo-bead (top) and QD-agglomerates (bottom) with a CCD camera. Images of the fluo-beads and QD-agglomerates are shown without and with the laser switched on.

Next, a fluo-bead was trapped while monitoring its fluorescence emission with the CCD camera. The fluorescence emission was monitored for 40 s, taking a measurement every 0.2 s; all image processing was done with Matlab®. For these measurements it was important to ensure the fluorescence did not overexpose the camera and that the illumination light was switched off. Figure 3.21 shows the normalized fluorescence intensity of the optically trapped fluo-bead. The insets show the appearance of the fluo-bead at various times in the optical trap. It is clear from these results that the fluorescence of the particle quickly decreased (photobleached) upon entering the optical trap, however, after some time an almost stable (although low) signal was obtained (see the inset at point d).
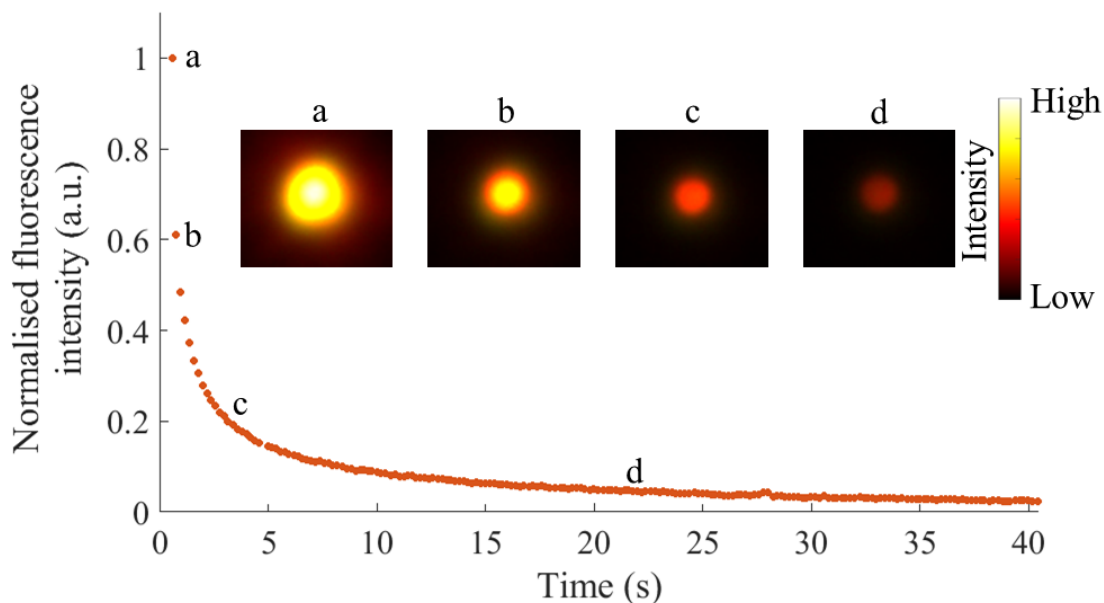
Figure 3.21: Fluorescence emission of an optically trapped fluo-bead detected with the CCD camera. The fluorescence intensity decreased initially, but stabilized later.

As the QD-tagged bead synthesis improved, the uniformly coated beads were trapped with the optical tweezer setup, but no fluorescence signal was observed with the CCD camera. Several attempts were made to increase the amount of QDs on the surface of the beads by changing the synthesis method (as discussed

in Section 2.3.3), however, each time the fluorescence signals were too weak to be detected with the CCD camera. The difference between the fluo-bead and the QD-tagged bead, is that the fluo-bead was fully loaded with a fluorophore (organic dye), whereas the QD-tagged bead only had a thin layer of fluorophores (QDs) on its surface; this resulted in a strong enough signal from the fluo-bead to be detected by the CCD, but not from the QD-tagged bead. Other studies, based on similar systems, all used more sensitive detectors like an EMCCD (electron multiplying CCD) or avalanche photodiode (APD) [150, 151]. Therefore, to be able to measure the fluorescence from a single QD-tagged bead, a detector more sensitive than the CCD was needed.

Changing the setup to provide more sensitive fluorescence detection

In optical tweezers, there is always some sort of position detector in the setup, which is needed to confirm trapping and visualize the sample. The available detectors, possibly more sensitive than the CCD camera, were a photodiode power sensor (Thorlabs, Germany) and a spectrometer (AvaSpec, Avantes, South Africa). Another, definitely more sensitive detector, was an APD which is a single photon detector. However, all three of these detectors are not spatially resolved, hence the CCD camera was still needed to visualize the sample and trapped particles. Figure 3.22 illustrates two ways the setup was changed to include the more sensitive detector. In the first method, a flip-mirror was added to either let the illumination light go to the CCD or the fluorescence signal to the new detector. In the second method a 50/50 beam splitter was added that splits the signal to go to both detectors; however, this meant the fluorescence signal was halved, which was not ideal since the signal was already weak.

The sensitivity of the power meter and spectrometer was tested by using the setup illustrated in Figure 3.22a. These two detectors, however, did not prove to be
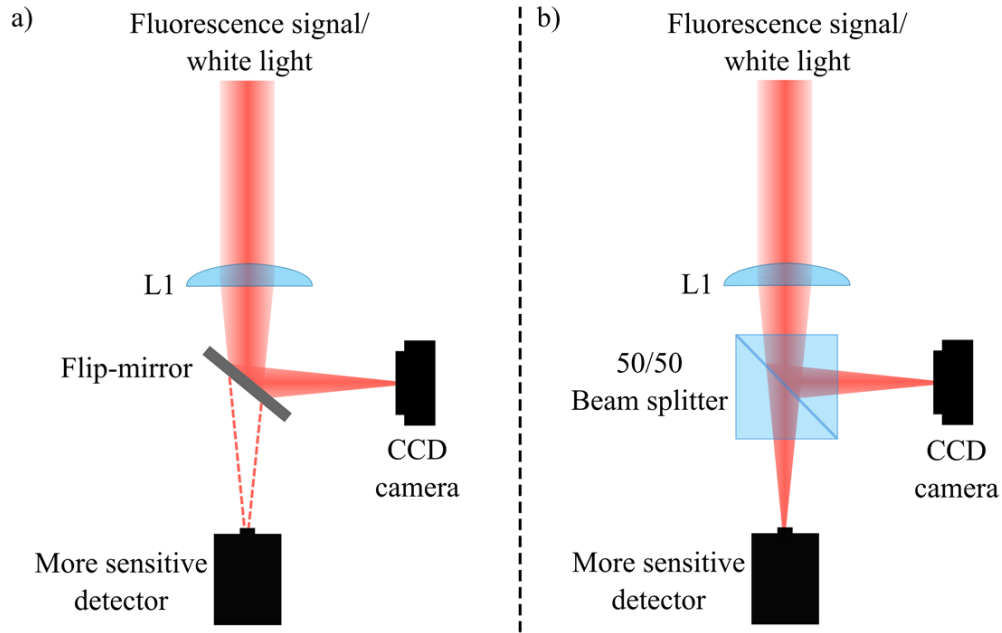
Figure 3.22: Two ways to a second (more sensitive) detector was added into the optical tweezer setup for fluorescence detection, while using the CCD camera for position detection. a) A flip-mirror was added to either let the illumination light go to the CCD or the fluorescence signal to the new detector or b) a 50/50 beam splitter was added that splits the signal to go to both detectors.

more sensitive than the CCD camera. Again, only the fluorescence emission of a fluo-bead and QD-agglomerates was detected, but not that of a singly trapped QD-tagged bead. Figure 3.23 shows the fluorescence emission spectrum from QD-agglomerations in the optical tweezer setup as measured with the spectrometer. This spectrum had the characteristic narrow, symmetrical shape expected from the QD sample. At 550 nm the spectrum seems to be 'cut off', this is due to a longpass filter added before the detector to remove any laser light. The spectra of the laser beam and the illumination light are also shown in this figure.

Finally, with an APD (COUNT®-250Blue single photon counting module from Laser Components, Germany) inserted into the setup, the fluorescence emission of

an optically trapped QD-tagged bead was detected. Before presenting the results from the APD, some comments regarding the imaging/detection system are first given.

Initially, the method shown in Figure 3.22b was used to add the APD into the setup, because the flip-mirror was quite unstable and the APD was sensitive enough for the signal to be halved. However, as can be seen from Figure 3.23, the spectra of the QDs and the illumination light overlap; meaning the illumination light cannot be removed with filters and has to be switched off when taking fluorescence measurements. This situation was not ideal, since either the sample could be imaged or the fluorescence could be detected, but not both simultaneously. It was therefore difficult to confirm whether the fluorescence signal observed on the APD came from a trapped particle or from some background noise, or whether the decrease in fluorescence signal was due to the particle escaping the trap or due to photobleaching. In summary, to be confident about where in the sample the
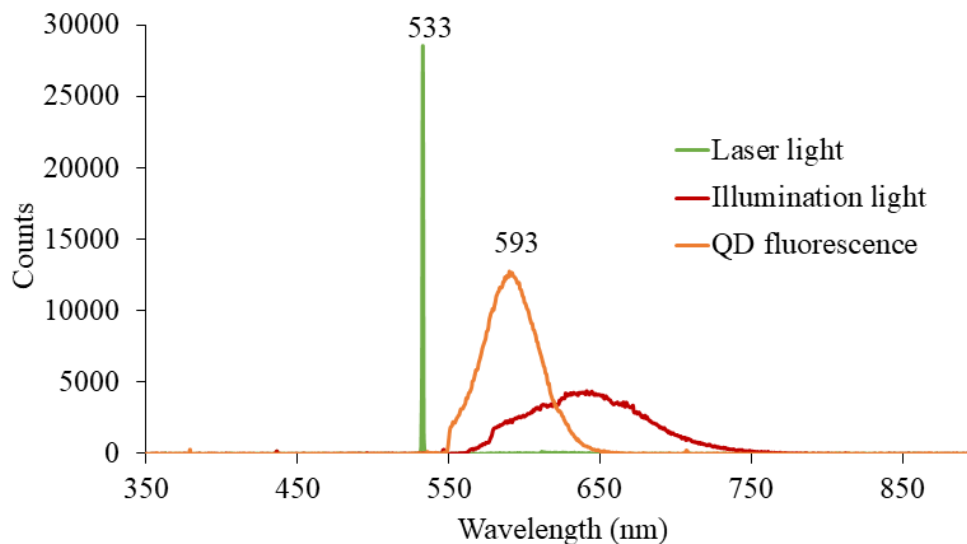
Figure 3.23: The fluorescence emission spectrum of QD-agglomerates were measured in the optical tweezer setup. The spectra of the $\lambda = 532$ nm laser and illumination light are also shown.

fluorescence signal (detected with the APD) was coming from, the sample had to be imaged concurrently. This lead to the design of a new imaging/detection setup illustrated in Figure 3.24. Here, a color filter (shortpass 550 nm) was added after the white LED illumination light in order to image the sample with blue light that does not overlap with the fluorescence emission spectrum of the QD sample. To get the blue illumination light to the CCD camera while detecting the fluorescence (around 600 nm) with the APD, two dichroic mirrors (DMs) were needed. The first notch DM (532 nm StopLine notch laser dichroic beam splitter) reflected only the green $\lambda = 532$ nm laser light into the objective lens, while transmitting the illumination and fluorescence signal. The second longpass DM reflected the illumination light (blue) but transmitted the fluorescence (red) signal. With this system, simultaneous position and fluorescence detection was achieved.
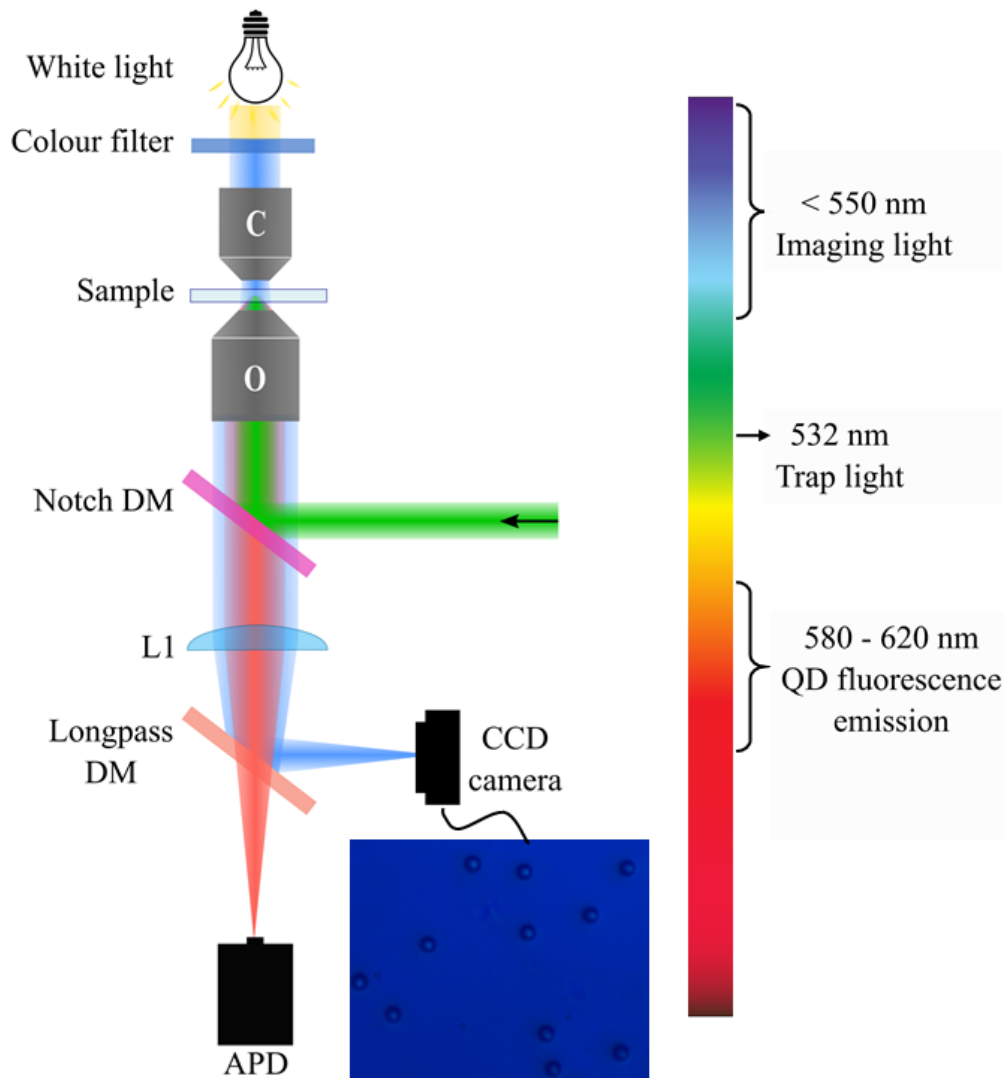
Figure 3.24: The setup used for simultaneous imaging and fluorescence detection. Blue illumination light with a wavelength < 550 nm was transmitted by the notch DM while being reflected from the longpass DM and imaged to a CCD camera. The fluorescence emitted by the fluorophores (580 - 620 nm) was transmitted through both DMs and detected with an APD. The green trapping and excitation laser with a wavelength of 532 nm was reflected by the notch DM into the objective.

Fluorescence detection with an APD

The fluorescence signal of the fluo-bead sample, detected with the APD, is shown in Figure 3.25. Firstly, the background noise from the laboratory (dark), the optical setup and from the sample itself are shown (all measurements were taken with an integration time of 300 ms). The dark counts (~ 40) were measured when the laser and illumination light were switched off; these counts therefore originated from ambient light like the PC screen or other light sources in the laboratory. The APD, being a single photon detector, is very sensitive and can detect fluorescence signals from other elements in the optical setup (due to the laser), like the immersion oil, the objective lens and the spacer used in the sample, amongst other things. This background noise from the optics (~ 1000 counts) was measured with the laser incident on a non-fluorescent polystyrene bead sample in the setup. Lastly, the background from the fluo-bead sample itself ($\sim 70\,000$
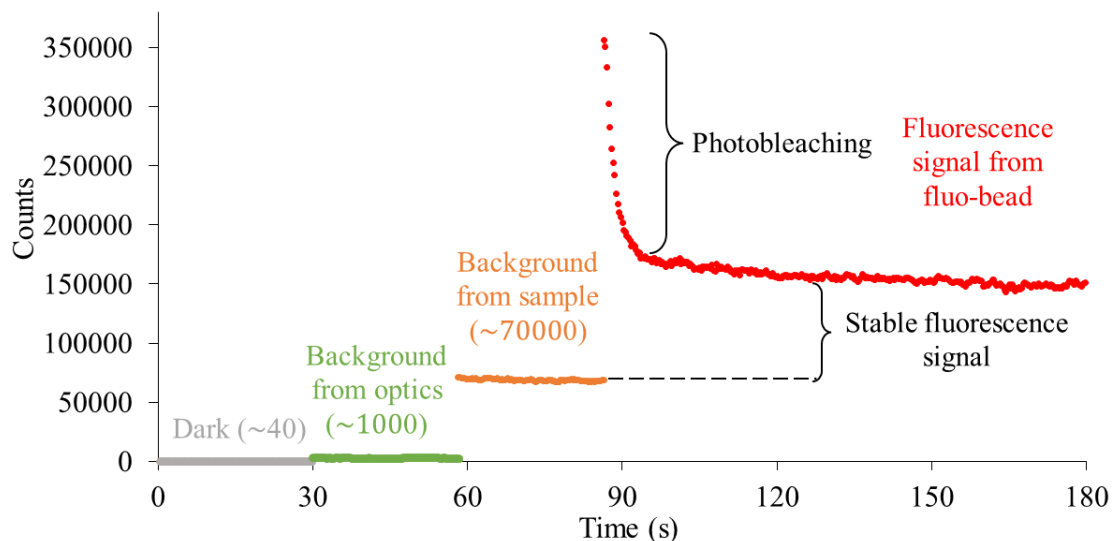
Figure 3.25: The signal from a fluo-bead sample detected with an APD. The dark and background counts from the optics and the sample are shown at times 0 - 90 s and the fluorescence emission from a trapped fluo-bead is shown from 90 - 180 s.

counts) was measured by having the laser beam incident on the sample, but not directly on a fluorophore. All this background noise was not picked up by the CCD camera, but can be detected with the APD. The high background noise of this sample was due to some of the fluorescent dye leaking out of the polystyrene spheres. Finally, the fluorescence emission from an optically trapped fluo-bead is shown from 90 to 180 s in Figure 3.25. The same result observed with the CCD camera is seen with the APD; initially there was a large decrease in fluorescence emission (photobleaching), but later a stable, almost constant fluorescence signal was detected. The constant signal can be obtained by subtracting the background noise.

The fluorescence signal from the QD-tagged bead sample, detected with the APD, is shown in Figure 3.26. The dark counts and background noise from the optics are the same as for the fluo-beads, since it is independent of the fluorophore sample. Note that the maximum counts from the fluo-bead sample were 350 000 whereas the maximum for QD-tagged bead sample was only 10 000. The background noise from the QD-sample is due to the presence of unreacted QDs that did not couple to the bead. The fluorescence emission of an optically trapped QD-tagged bead is shown from 30 - 180 s. The QD-tagged bead also experienced photobleaching inside the trap, but after ~ 90 s the QDs were completely bleached and no stable signal was observed (compare with the fluo-bead sample). The reason no stable signal was observed for the QD-tagged bead but was seen for the fluo-bead can again be explained in terms of where the fluorophore is on the bead – the fluo-bead is loaded with fluorescent dye throughout its volume, whereas the QDs are only on the surface of the bead and thus experienced complete bleaching in the optical trap.

Only the initial bleaching signal of the fluo-beads was considered for the photo-bleaching tests, since this part of the fluo-bead signal represents the behaviour
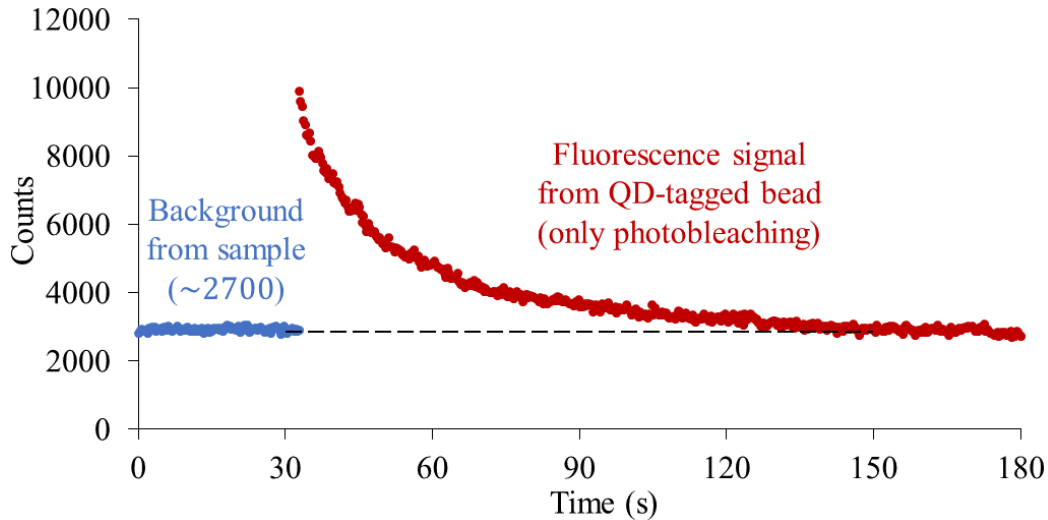
Figure 3.26: The fluorescence emission of an optically trapped QD-tagged bead detected with an APD (times 32 - 180 s) with the background counts shown at times 0 - 32 s.

of a QD-tagged bead in the optical trap the best (not the stable signal). More photobleaching tests are presented in Section 4.5. The normalized and background subtracted signal from an optically trapped QD-tagged bead and fluo-bead detected with the APD are shown in Figure 3.27.

Therefore, by making use of a sensitive photodetector and the detection system illustrated in Figure 3.24, the fluorescence emission from a single QD-tagged bead trapped in the optical tweezer setup was successfully measured.
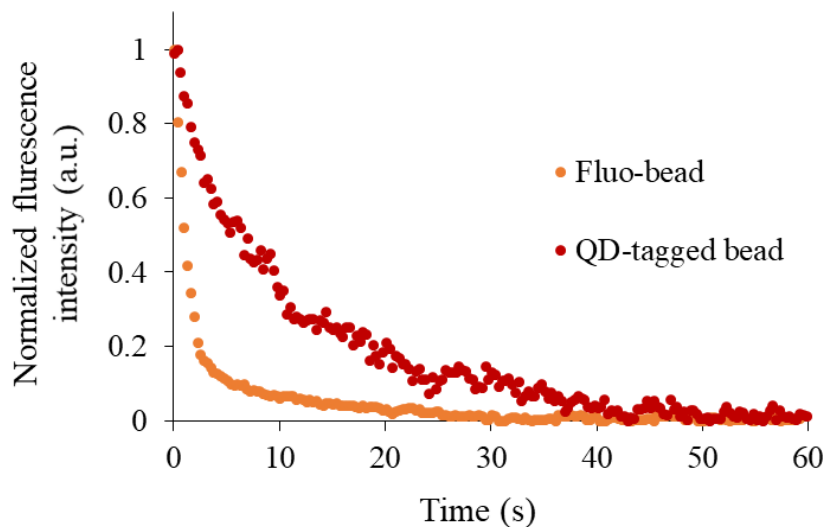
Figure 3.27: Fluorescence emission of an optically trapped QD-tagged bead and fluo-bead.

3.4 Chapter summary

Chapter 3 demonstrated the successful setup of an optical tweezer with an integrated fluorescence microscope. It started with a discussion on the basic concepts of optical tweezers including the most common trapping beam - the Gaussian beam, the forces in optical tweezers as well as the most important components needed to build this instrument. The second part of the chapter discussed the experimental setup and calibration of an optical tweezer. The chapter ended with a discussion on the process followed to detect the fluorescence emission of an optically trapped QD-tagged bead.

Chapter 4

Holographic optical tweezers

The term holographic optical tweezers (HOT) is used to describe optical tweezing systems that use structured light (generated with holograms) for trapping. This chapter starts with a discussion on structured light and how to create it with spatial light modulators (SLMs) – the device used in this study (Section 4.1). The implementation of a vectorial holographic optical trap with specific focus on vector flat-top beams is discussed in Sections 4.2 and 4.3. A further benefit of using vectorially structured light in optical systems is shown in Section 4.4. Finally, the chapter concludes by demonstrating the advantages of using the flat-top beam for fluorescence excitation and trapping compared to the traditional Gaussian beam (Section 4.5).

4.1   Structured light

Here, a brief discussion on structured light, how to create it and what has been done with it in optical tweezers is presented. Since this section serves only as an introduction to structured light, most of the technicalities, mathematical expressions and derivations are omitted from the discussion, but can be obtained in the given references.

4.1.1 What is structured light?

Structured light, beam shaping, laser beam modulation or complex light fields all refer to tailoring light mainly in amplitude, phase and/or polarization but also in time and frequency [12,13]. The conventional Gaussian output beam of most lasers might not suit a particular application — therefore there is a need to customize laser light fit for purpose. Examples of experimentally created structured light fields are shown in Figure 4.1.

Structured light can be created to have unique and completely different properties which is why it has become ubiquitous in research and industrial applications [152]. These tailored light fields have triggered advances in laser cutting [153], imaging [154], optical communication [155], microscopy [156,157], metrology [158] and in optical tweezers [18], just to name a few.
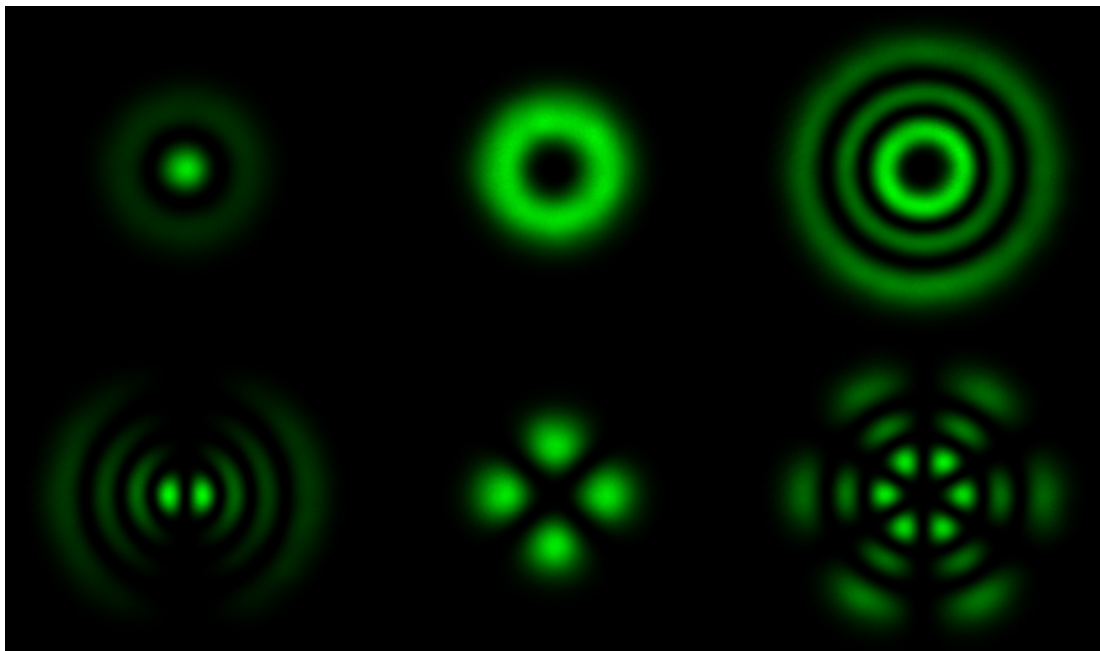
Figure 4.1: Examples of experimentally created structured light beams.

The tailoring of light most often happens outside the laser, meaning the laser output beam (usually Gaussian) is transformed by some means to the desired complex field, however, light can also be structured within the laser cavity [159]. Shaping the amplitude and phase of light was historically done by static diffractive or refractive optical elements [160]. The major drawback was that each optic can only create a specific structure, for a different structured beam a new (sometimes very expensive) optical element had to be obtained. This 'static' problem was overcome by the invention of digitally rewritable devices called spatial light modulators (SLMs) [161]. SLMs caused an explosion in structured light research and can be found in most optics laboratories today; more on SLMs in Section 4.1.3. Recently, digital micromirror devices (DMDs) are gaining more attention in the beam shaping community due to their extremely fast modulation rates [162, 163]. Both SLMs and DMDs use digital holograms to transform an incident beam to the desired structured beam.

4.1.2 How to shape light: complex amplitude modulation

Before delving into the workings of the SLM, the basic idea of transforming the amplitude and/or phase of an incident field to create a desired structured field (by means of a hologram) is considered. The arguments presented here follow those of references [164] and [165], although in less detail. The incident field, u_{in}, with amplitude A and phase ϕ can be defined as $u_{in} = A_{in} \exp(i\phi_{in})$. To transform u_{in} into the desired output field with a different amplitude and phase, $u_{out} = A_{out} \exp(i\phi_{out})$, a function is needed, this function is sometimes called a transfer or transmission function, here the function is called H referring to a hologram, so that

$$u_{in} \times H = u_{out} \tag{4.1}$$

$$\Rightarrow H = \left(\frac{A_{out}}{A_{in}}\right) \exp\left[i(\phi_{out} - \phi_{in})\right]. \tag{4.2}$$

From Equation 4.2 it is clear that the hologram function must be able to modulate in amplitude and phase. Encoding both the phase and amplitude in the hologram is rather difficult, but possible; this is the method used to fabricate the static optical elements mentioned earlier [166]. More commonly, devices are either amplitude-only modulators (DMDs) or phase-only modulators (SLMs). Fortunately, it is possible to use phase-only modulators to structure both the phase and the amplitude of a beam, this process is called complex amplitude modulation (CAM) [167–170].

The main idea of CAM is illustrated in Figure 4.2. Firstly, light cannot be created, therefore the desired field can only be generated by removing some of the light from the incident field until the desired amplitude is obtained – in other words the desired field is 'cut out' of the incident field. In Figure 4.2a an incident field is shown in blue (usually an expanded Gaussian beam) and an arbitrary desired field in green. To obtain the desired field all the incident light at point 1 must be kept, at point 2 all the incident light must be removed and at point 3 some fraction ($\sim 50\%$) of the light must be kept while the rest is removed. If a device can remove light in a spatially resolved manner like this, it can 'cut out' the desired field. A device used to structure light can be thought of as a grating with the desired beam generated in the first diffraction order, the unwanted incident light can therefore be removed to either the 0th (undiffracted) order or to higher orders. Removing the light to the 0th is done by changing the depth of the phase/grating (ranging from 0 to 2π) which changes its diffraction efficiency. Consider Figure 4.2b, if there is no grating (depth $= 0$) all the incident light is left undiffracted and at a grating depth of 2π all the light is diffracted to the desired first 1st order. At a depth between the two extremes some light is left undiffracted and some not. Note

that the relationship between the diffraction efficiency and the hologram depth is not entirely linear (it actually follows a sinc function) [164]. Therefore, to generate the desired field, the grating depth is changed in a spatially resolved manner. For example, to create the desired field in Figure 4.2a a grating depth of 2π is needed at point 1, at point 2 no grating and at point 3 a grating depth of $\sim \pi$ is needed. For the incident light to be removed to higher orders, the period of the grating is spatially adjusted instead of the depth.
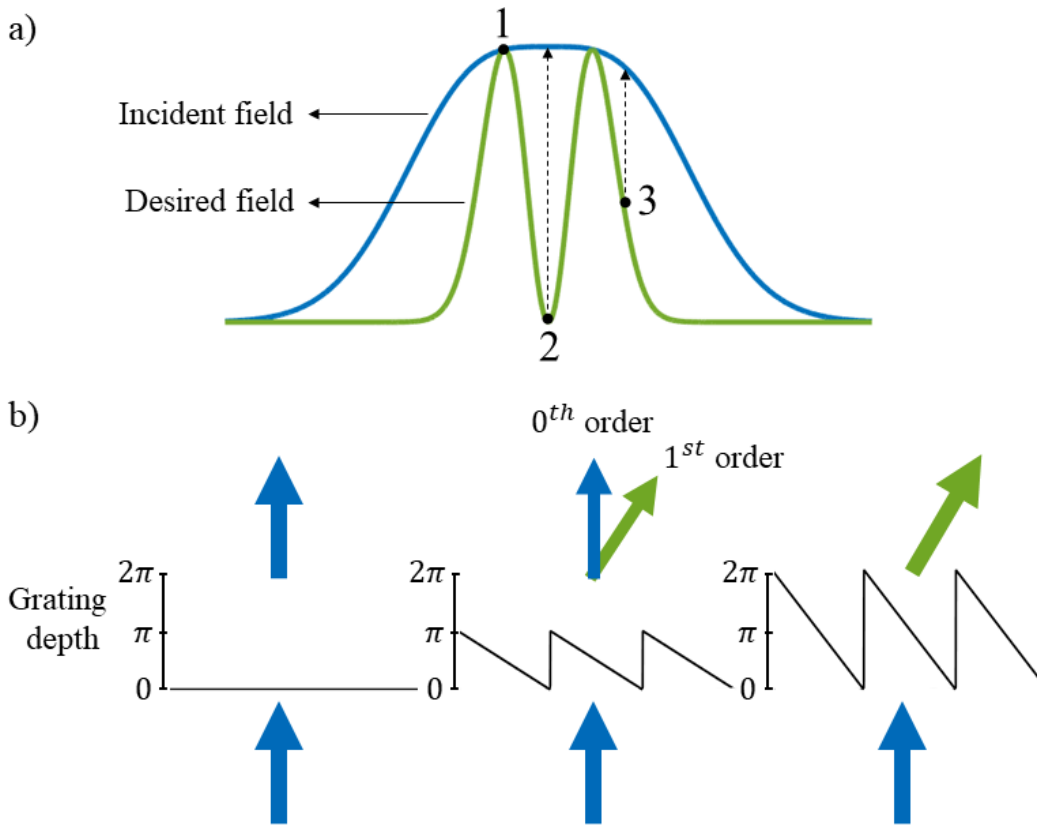
Figure 4.2: a) In complex amplitude modulation the desired field is obtained by removing incident light in a spatially resolved manner to either the 0th order or to higher orders. For instance to create the desired field at point 1 no light is removed, at point 2 all the incident light is removed and at point 3 only a fraction is removed. b) To move the incident light to the 0th order the phase depth is changed from 0 (no diffraction) to 2π (complete diffraction to the desired 1st order). At a phase depth between 0 and 2π some light is left undiffracted and some not.

This section only gave the conceptual idea on how to create holograms using CAM, for the mathematical detail and how to generate these holograms in practice see references [171] and [172]. All holograms created in this study used CAM, specifically the Arrizón type 3 method [171].

4.1.3 Spatial light modulators

The phase change of light incident on a material is dependent on the refractive index thereof. Thus, in order to spatially alter the phase of a beam, a material with a spatially varying refractive index is needed – this is achieved with liquid crystal spatial light modulators [164]. An SLM is made up of thousands of small birefringent liquid crystal (LC) cells or pixels as illustrated in Figure 4.3. The term 'birefringent' means the refractive index of the LC cell is dependent on the polarization and direction of the light passing through it. In SLMs the orientation of the LCs in each pixel can be individually controlled by applying a voltage over the electrodes. This means the refractive index of each pixel can be varied which then imparts a spatially varying phase change to the light incident on the SLM
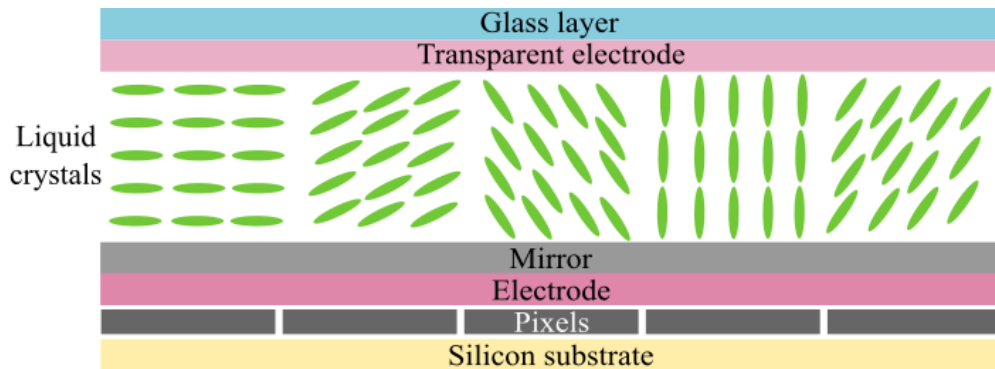
Figure 4.3: Schematic diagram of the cross section of a LCoS SLM. The orientation of the liquid crystals in each cell or 'pixel' can be controlled individually by applying a voltage across the electrodes. When the liquid crystals rotate their refractive index changes which then modulates the phase of the incident beam.

screen. Mainly two types of SLMs exists: 1) transmissive SLMs in which the incident light is modulated as it passes through the SLM and 2) reflective or liquid crystal on silicon (LCoS) SLMs. The latter is illustrated in Figure 4.3; in this SLM the light enters at the glass side of the SLM and gets modulated upon reflection (double pass through the LCs).

In order to control the voltage applied across each pixel, and hence the phase change, a 8-bit grey-scale image (allowing 256 colour levels) is displayed on the SLM, which is connected as a second screen to a PC. The image has the same resolution as the SLM screen (usually 1920 × 1080 pixels) with each pixel on the image corresponding to a grey-scale color which is associated with a specific phase shift from 0 (black) to 2π (white), where the in-between grey values and associated phase shift have a linear relationship. In summary, each pixel has a grey-scale value (256 different options). Controlling the voltage applied across that pixel rotates the LCs, changing their refractive index, and consequently changing the phase shift of the light incident on that pixel; the grey-scale image therefore controls the phase shift imparted to the beam. Calibration of the SLM is required to ensure a linear phase shift from 0 to 2π associated with the grey-scale colours from 0 to 255 for a specific wavelength. Refer to Appendix B for a practical guide on SLM calibration.

SLMs are not 100% efficient to start with due to the discrete pixels on the SLM screen. These pixels act as a diffraction grating themselves (independent of the hologram grating) causing the incoming light to diffract into many orders. Figure 4.4 shows the diffraction orders due to pixelation of the screen when a beam is incident on a SLM (no hologram displayed on the SLM). The diffraction orders can be seen on the walls and optical table in the laboratory, losing up to 40% of the incoming light [165]. There is an order, the $0th$ order, much brighter than the rest which is modulated when displaying a hologram on the SLM.
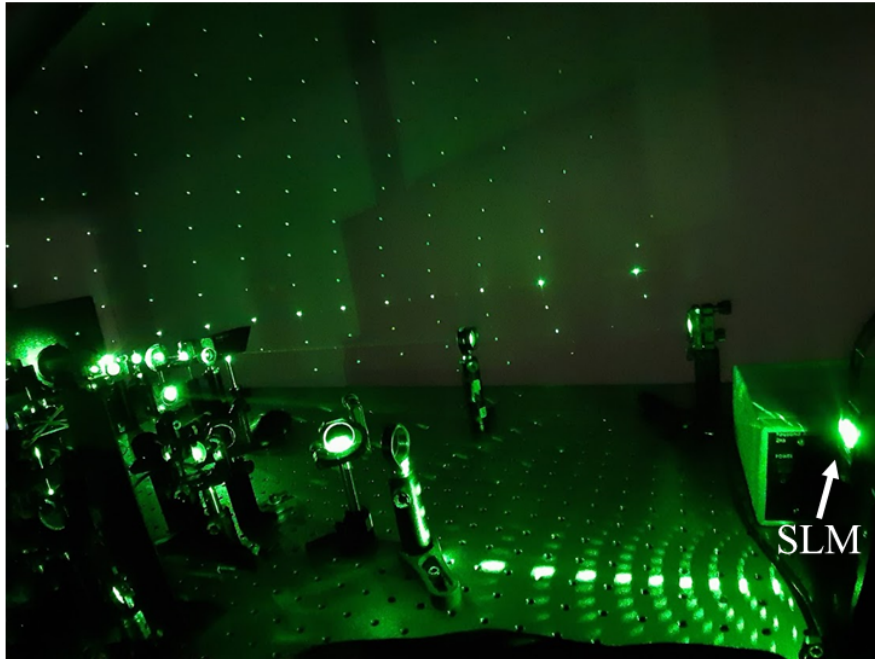
Figure 4.4: Diffraction orders of an incident beam due to the pixelation of a SLM. This photo shows the diffraction orders from the SLM which are visible on the walls and optical table in the laboratory.

SLMs are polarization sensitive; they only modulate light with polarization perpendicular to the optical axis of the LCs (horizontal polarization in most cases). Even if the polarization of the incident light is correct, the modulation is also not completely efficient and there is always some unmodulated light in the 0th order. This can be due to ineffective calibration or reflection from the glass or electrode layers. Therefore, the efficiency of SLMs is firstly reduced by the pixelation of the screen and secondly by incomplete phase modulation. In order to separate the desired structured light from the unmodulated 0th order, a blazed grating is added on the hologram. The effect of the grating is shown in Figure 4.5, the structured beam is generated in the first diffraction order due to the grating introduced on the hologram (shown as insets). The desired 1st diffraction order moves further away from the unmodulated light as the spatial frequency of the grating is increased.
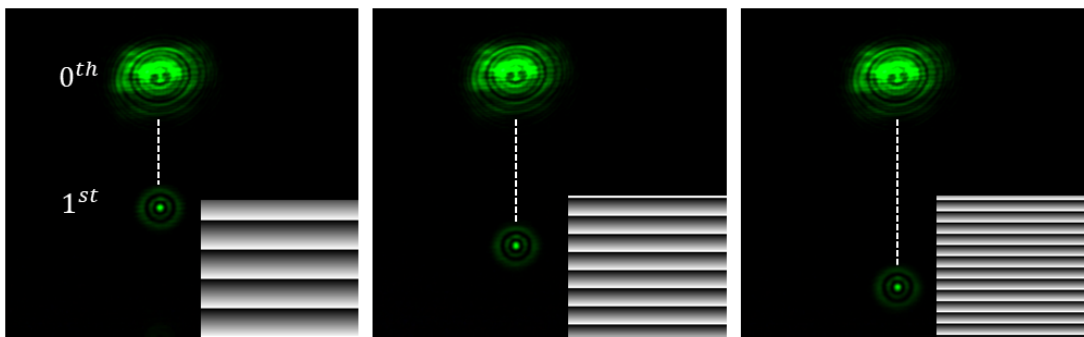
Figure 4.5: A grating is needed to separate the modulated beam (in the 1st diffraction order) from the unmodulated (0th order) beam. An increase in the frequency of the blazed grating (shown as insets) causes the modulated beam to move further from the 0th order.

Figure 4.6 shows the generation of two example structured light fields using a SLM. On the left the simulated desired field is shown, the holograms (generated using CAM) that were displayed on the SLM to create these fields are shown in the middle panels with and without a blazed grating. Lastly, on the right the experimentally generated beam is shown (imaged with a CCD camera).

Desired beam profile	Hologram (no grating)	Hologram with grating	Experimental beam
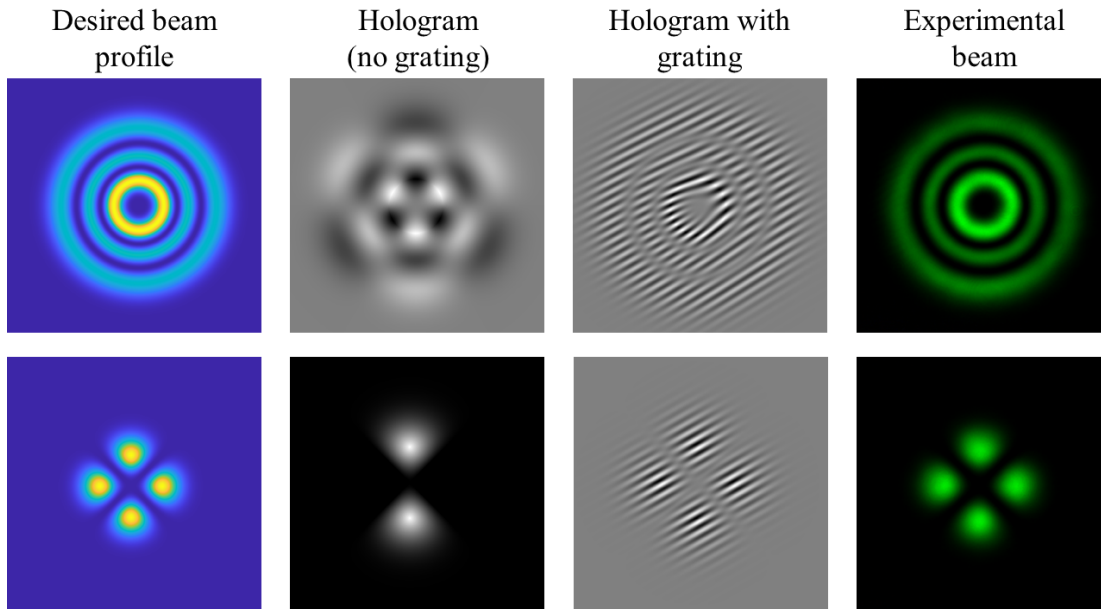
Figure 4.6: Two examples of holograms used to generate structured light beams. For each beam the theoretical profile of the desired beam is shown on the left. The hologram used to create the beam is shown in the middle panels with and without a grating. Lastly, the intensity profile of an experimentally generated beam is shown on the right.

Several structured fields (in fact over 200 modes [172]) can be created with a single hologram through a process called multiplexing, see Figure 4.7. Multiplexing is achieved by adding the holograms of different structured fields each with a unique grating (carrier frequency). The holograms of three different fields are shown in the top row, each having a different grating (shown as insets). The multiplexed hologram displayed on the SLM screen (the sum of the three individual holograms) is at the bottom left and the far-field image of the three beams created experimentally is shown on the bottom right.
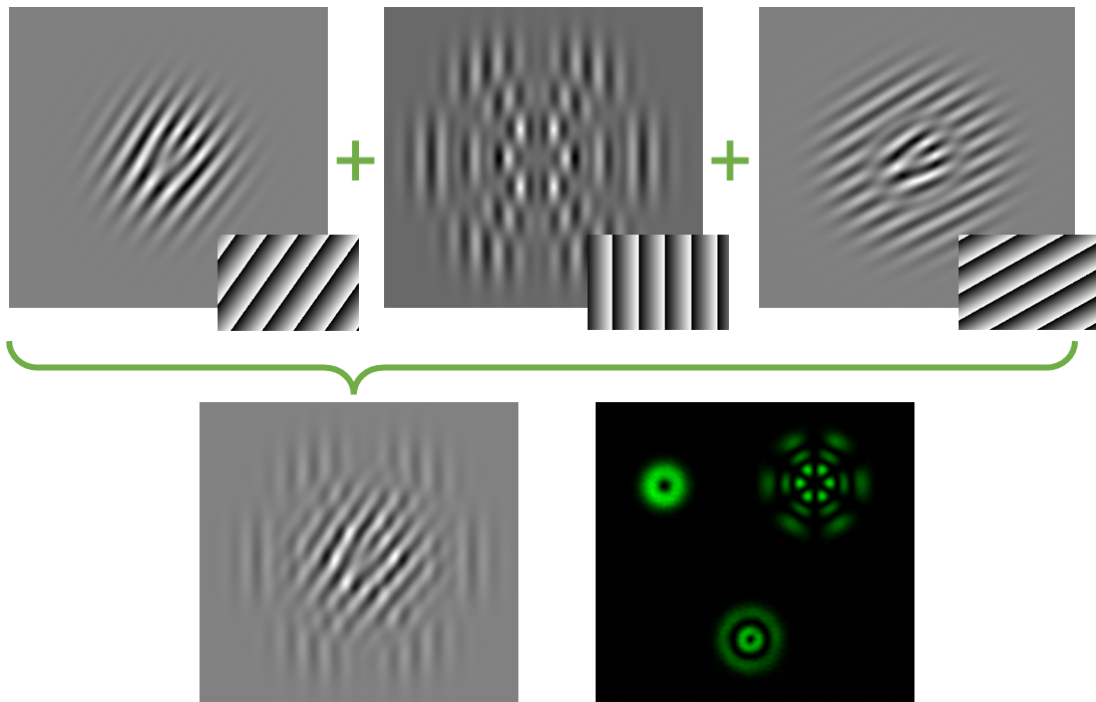
Figure 4.7: Multiplexing allows simultaneous generation of several beams that are spatially separated. The top row shows the holograms of three beams each having an unique spatial carrier grating (the gratings are shown as insets). By simply adding these three holograms a multiplex hologram is created (bottom left image) that results in the creation of the three beams at different positions in the far-field (bottom right image).

Aberrations are introduced to beams due imperfect optics; SLM screens for instance are not always perfectly flat or some deviation across the screen is present which causes the structured field to be aberrated. Fortunately, SLMs can be used to account for these aberrations by adding a phase correction to the hologram. Figure 4.8 shows a structured beam before and after aberration correction. In this study, aberration corrections were done using the Zernike polynomials by manually adjusting the Zernike coefficients to correct the wavefront [173].
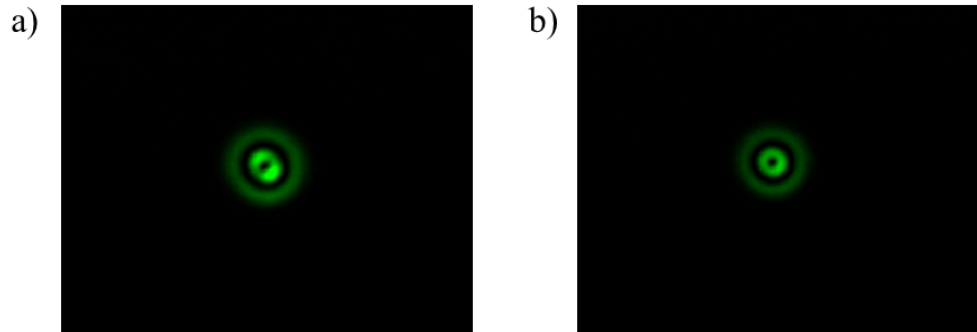
Figure 4.8: The SLM or other optics can cause aberrations in the beam, however the SLM can be used to correct for these aberrations. An experimentally generated beam (in the far-field) is shown a) before and b) after aberration corrections were done with the SLM.

4.1.4 Laguerre-Gaussian beams

So far in the discussion, no mention has been made of the 'types' of structured light beams that are physically possible to generate. In addition, in order to generate the holograms, the field of the desired beam must be known (mathematically). Most discussions on structured light starts with Maxwell's equations since these equations completely describe the behaviour of electromagnetic waves. The solution sets of Maxwell's equations yield physically realisable structured beans [174]. Many solutions exists including the Laguerre-Gaussian (LG), Hermite-Gaussian [175], Ince-Gaussian [176], Bessel-Gaussian [177] and Airy beams [178].

Here only the LG beams will be considered; these beams are specifically obtained by solving the paraxial Helmholtz wave equation in cylindrical coordinates and form an infinite set of solutions or structured beams. The LG_p^l field takes the

well-known form [164]

$$LG_p^l(r, \varphi, z) = \sqrt{\frac{2p!}{\pi(|l| + p)!}} \frac{1}{w(z)} \left(\frac{\sqrt{2}r}{w(z)}\right)^{|l|} L_p^{|l|}\left(\frac{2r^2}{w^2(z)}\right)$$
$$\times \exp[i(|l| + 2p + 1)\psi(z)] \exp[il\varphi] \qquad (4.3)$$
$$\times \exp\left[-\frac{ikr^2}{2R(z)}\right] \exp\left[-\frac{r^2}{w^2(z)}\right],$$

where p is the radial index (a positive integer) and l is the azimuthal index (an integer). $L_p^{|l|}$ is the associated Laguerre polynomial, w_0 is the Gaussian beam waist, $w(z) = w_0\sqrt{1 + \left(\frac{z}{z_R}\right)^2}$ is the beam radius, $z_R = \frac{\pi w_0^2}{\lambda}$ is the Rayleigh range, $R(z) = z\left(1 + \left(\frac{z_R}{z}\right)^2\right)$ is the radius of curvature and $\psi(z) = \arctan\left(\frac{z}{z_R}\right)$ is the Gouy phase. The (simulated) intensities of some LG_p^l modes are shown in Figure 4.9a. LG beams have a helical phase where l determines the number of twists (and direction) of the helix, p determines the number of rings (maxima) of the beam. When $l = p = 0$ the LG beam reduces to a Gaussian beam. All the structured beams created in this discussion (and in this study) were either LG beams or the superposition of two LG beams $(LG_p^l + LG_p^{-l})$ sometimes called petal beams. Two examples of petal beams are given in Figure 4.9b.
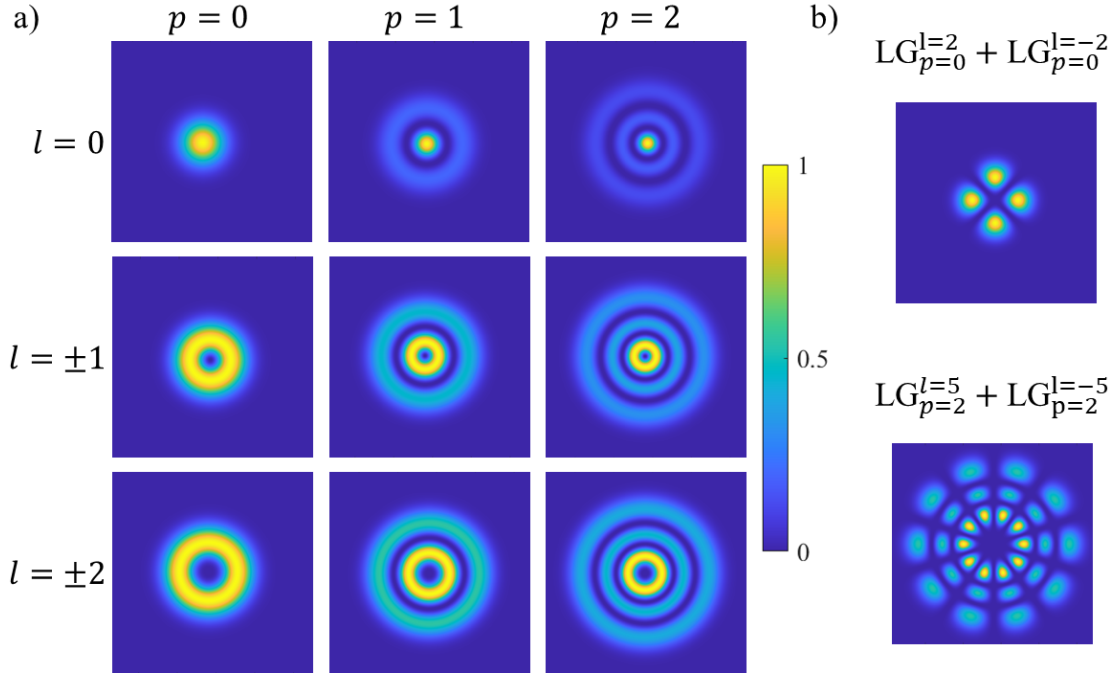
Figure 4.9: a) Intensity profiles of Laguerre-Gaussian beams with different p and l values. When $p = l = 0$ the LG beam reduces to the well-known Gaussian beam. b) Petal beams are created by the superposition of two LG beams that have the same p and $|l|$, but with l opposite in sign.

4.1.5 Structured light in optical tweezers

Optical trapping uses the intensity gradient of light (in other words its amplitude profile) to trap particles, it was therefore a natural process to combine optical tweezing with structured light (which modulates the amplitude). The first optical trapping experiment was demonstrated with a Gaussian beam [100] and this beam still dominates trapping experiments today. However, the introduction of structured beams in optical tweezers has enabled a myriad of applications and inventions [17, 18]. These structured light traps are a well-established technique today and since most structured beams are created by means of a hologram, they have been dubbed holographic optical tweezers (HOTs) [14].

With HOTs, an array of traps can be created to trap multiple particles simulta-

neously while being able to dynamically change this array pattern [156, 179, 180]. Structured beams that reconstruct themselves after being distorted by a trapped particle (Bessel beams) have allowed for trapping in multiple planes previously not possible [181]; another beam that allows 3D assembling of particles is the Mathieu beam [182]. Airy beams, for example, can guide a particle along a certain trajectory enabling selective removal of particles in a sample [183]. The fact that light carries linear momentum is well-known and the reason why light can trap particles as discussed in Section 3.1.2. Light can, however, also carry orbital angular momentum (OAM), LG beams have OAM due to the helical phase front mentioned previously. With these OAM carrying beams, optical tweezers also gain rotational control of particles [184–186].

So far the focus has mainly been on structured beams modulated in amplitude and phase – these are called scalar beams. The third spatial degree of freedom of light is polarization, when a beam is structured in all three degrees they are called vector beams. In other words, a vector beam does not only have a spatially varying amplitude and phase but also a varying polarization pattern. These beams can be created by the superposition of two orthogonal scalar fields with uniform polarization patterns [187]. Trapping with vector beams is the most recent avenue of structured light explored in optical tweezers and has already proven beneficial to the trapping community [17, 187]. For instance, the radially polarized vector beam is famous for achieving the smallest spot size when tightly focused [188, 189]; this property has been used to demonstrate stronger trapping in the axial direction [190, 191]. Another interesting use of polarization in traps is the so-called tractor beam that can exert a pushing or a pulling force on a particle depending on the polarization of the incident beams [192]. A further advancement in vector beam traps was demonstrated by Bhebhe *et al.* when they created an array of vector beams enabling simultaneous trapping of multiple particles with

beams of different polarization patterns [16].

The advances and applications of structured light combined with optical tweezers discussed here only scratch the surface of what has been done with this powerful technique. However, very little research has investigated the possibility of using structured light to assist with combining optical trapping and fluorescence spectroscopy and to mitigate the photobleaching of fluorescent particles in optical tweezers. Refer to Section 3.3 for a discussion on combining optical tweezers with fluorescence spectroscopy and the general solutions that have been implemented regarding photobleaching. Only very recently have Zhang and Milstein shown that trapping with a LG beam significantly improves the bleaching lifetime of the organic dye Alexa-647 positioned 1 μm below the trapped particle (separate trapping and excitation sources were used) [193].

This study further explored the benefits of using vector beams in optical tweezers with specific focus on vector flat-top beams and how they can be used to mitigate photobleaching, discussed in Sections 4.2 to 4.5.

4.2 Flat-top beam theory

To select a structured light beam that works for a specific application can be quite daunting because of the enormous 'menu' of structured beams to choose from. In this study, the structured beam must meet some requirements to be successfully employed. Firstly, in order for a beam to be a functional optical trap, it must have an intensity gradient and the steeper the better (see Section 3.1.2 for a full discussion on the forces in an optical trap). For the trapping beam to be able to reduce the photobleaching in the optical tweezer, it needs to have a low intensity incident on the fluorescent particle. Lastly, it is well known that Gaussian beams make excellent optical traps, so if a structured beam is to be used

it needs to be 'better' than the Gaussian beam in some way. After taking all this into consideration, a useful beam that potentially meets all these requirements is the flat-top beam. To explain why the flat-top beam is helpful for this application, consider Figure 4.10. The flat-top beam can be thought of as a Gaussian beam with the top half of the beam 'cut off' clearly living up to its name since the intensity profile is flat across the top. The flat-top beam still has a steep intensity gradient to provide a successful optical trap, but a lower peak intensity than the Gaussian beam to reduce photobleaching.
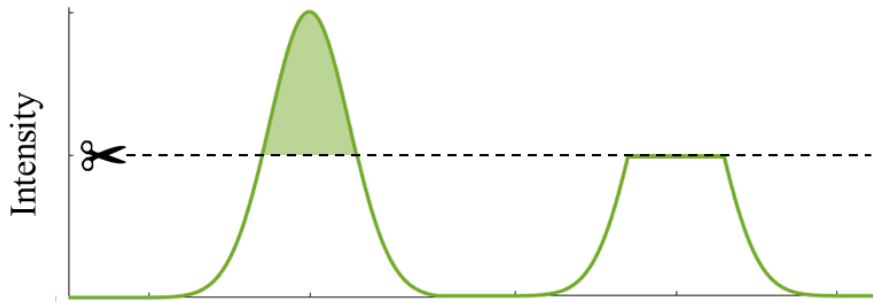
Figure 4.10: A flat-top beam can be thought of as a Gaussian beam with the top half 'cut off'. The resultant flat-top beam still has a steep intensity gradient to optically trap particles, but a lower peak intensity that will minimize photobleaching.

Section 4.2.1 focuses on approximations to the flat-top beam that can be created experimentally and in Section 4.2.2 the flat-top beam is (theoretically) compared to a Gaussian beam to determine in what aspects flat-top beams are superior to Gaussian beams (and vice versa).

4.2.1 Flat-top beam approximations

The ideal flat-top beam, or top-hat beam, has a uniform intensity that sharply drops down to zero at the edges (the green profile in Figure 4.11). This beam with its near uniform energy distribution is desirable for many applications including

optical communication, gravitational wave detectors, corneal treatment and (predominantly for) material processing, just to name a few [152, 194–197]. The ideal flat-top beam, having a fairly simple profile, is surprisingly difficult to generate in the laboratory (due to the fact that it needs an infinite spatial frequency spectrum). In fact, only approximations to flat-top beams can be physically created. Flat-top beams have been generated inside the laser cavity [198] or outside the laser by converting a Gaussian beam with diffractive and refractive elements or with holograms displayed on SLMs and DMD [199–202].
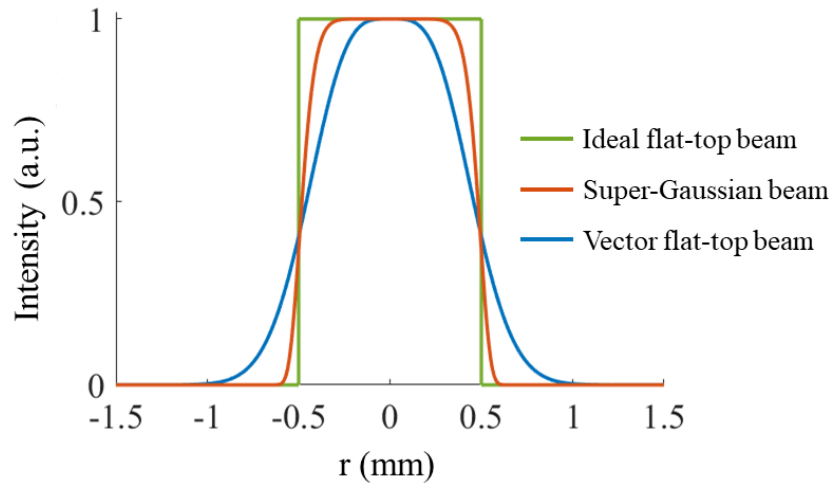
Figure 4.11: Intensity profiles of an ideal flat-top beam and two flat-top approximations namely the super-Gaussian (scalar) beam and the vector flat-top beam.

Several approximations to the flat-top beam exist and have been thoroughly investigated: super-Gaussian beams, flattened Gaussian beam, Fermi-Dirac and super-Lorentzian beams [203–206]. All these approximations will collectively be referred to as the scalar approximation, since they have a common property – they are propagation variant. A more recent approximation is the vector flat-top beam and in contrast to the others, it is propagation invariant [207]. The super-Gaussian and vector flat-top beam are shown in Figure 4.11 along with the ideal flat-top. These approximations are now considered in a bit more detail.

The scalar approximation

The two more familiar approximations, flattened and super-Gaussian beams, will be used to illustrate the properties of the scalar approximation. However, the approximations can easily be made indistinguishable by only tweaking some parameters as shown by Shealy and Hoffnagle [204].

The super-Gaussian beam has the form

$$SG_n(r) = \frac{4^{1/n}nP}{2\pi\Gamma(2/n)\omega^2} \exp\left[-2\left(\frac{r}{\omega}\right)^n\right],\tag{4.4}$$

with n the order of the beam, P the power, ω the beam width and $\Gamma(2/n)$ the gamma function evaluated at $2/n$. The order of the beam determines the flatness as illustrated in Figure 4.12 (the profiles are intensity normalized). Note that when $n = 2$ the beam reduces to the normal Gaussian beam and at a large n ($n = 40$) the super-Gaussian closely represents the ideal flat-top beam.
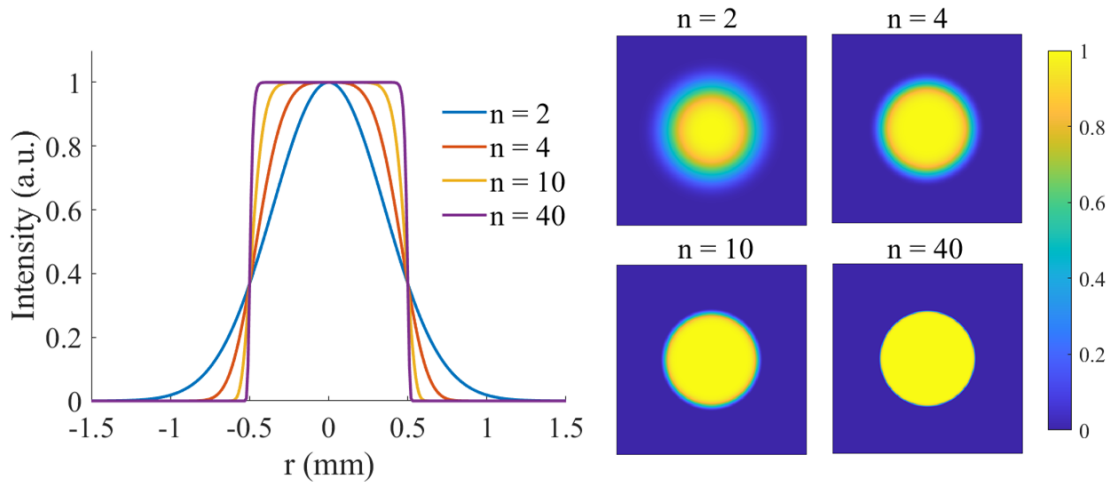
Figure 4.12: Intensity profiles of super-Gaussian beams with different values of n. The flatness of the beam increases with increasing order.

The simple expression of the super-Gaussian beam given by Equation 4.4 does not accurately describe the propagation of the beam. The beam propagation

can be modeled analytically using flattened Gaussian beams [203]; the difference between these beams and super-Gaussian beams are described by Santarsiero and Borghi [206]. As discussed earlier, the scalar beam approximations are not eigenmodes of free-space, meaning their intensity profile changes as it propagates. The propagation of the scalar flat-top beam (order $n = 25$) is given in Figure 4.13, clearly showing the drastic change in intensity even over a short distance. The flat-top profile of higher order beams unfortunately exists over even a shorter distance (they deform faster along the z-axis). The quick change in profile makes optical delivery of the flat-top profile at the trapping plane (through the high NA objective) extremely difficult. A beam that can simply be focused through the objective into the sample and keep its profile is much more ideal – which is achieved in vector flat-top beams.
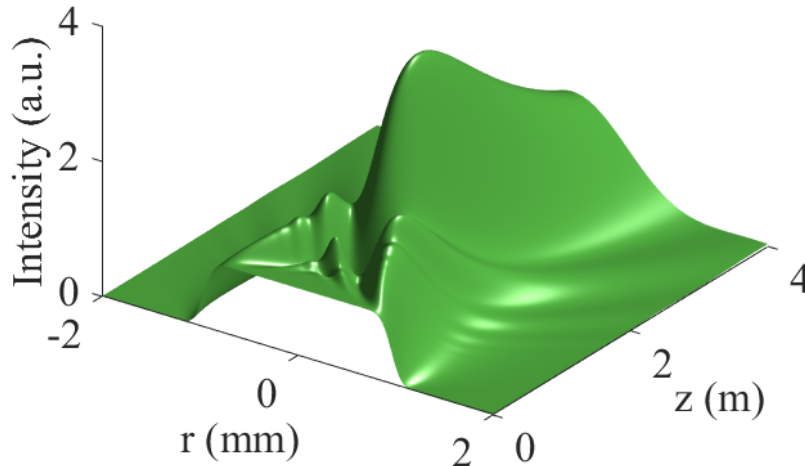
Figure 4.13: Propagation of a scalar flat-top beam simulated using the flattened Gaussian beam approach. The scalar flat-top quickly loses its shape when propagating, with the desired beam profile only present at a single plane ($z = 0$).

The vector approximation

A vector flat-top beam is obtained through the (vector) addition of a Gaussian and a vortex beam [208]. The vortex beam is simply an LG_0^1 beam, also sometimes called a doughnut beam. The field of the vector flat-top is therefore given by

$$U_{FT} = \sqrt{\alpha}LG_0^0\hat{\mathbf{e}}_{\mathbf{H}} + \sqrt{1-\alpha}LG_0^1\hat{\mathbf{e}}_{\mathbf{V}}, \quad (4.5)$$

where LG_0^0 is the Gaussian beam and LG_0^1 the vortex beam. A vector beam is formed by the addition of scalar fields with different but uniform polarization, here the Gaussian beam has horizontal polarization $\hat{\mathbf{e}}_{\mathbf{H}}$ and the vortex beam vertical polarization $\hat{\mathbf{e}}_{\mathbf{V}}$. Lastly, a factor α was introduced to weigh the two scalar beams, meaning any field from a vortex when $\alpha = 0$ to a Gaussian beam when $\alpha = 1$ can be generated; with the vector flat-top at equal weighting of $\alpha = 0.5$. The evolution of the vector beam as α changes is shown on the left in Figure 4.14 with the beam profiles at the critical α values on the right.
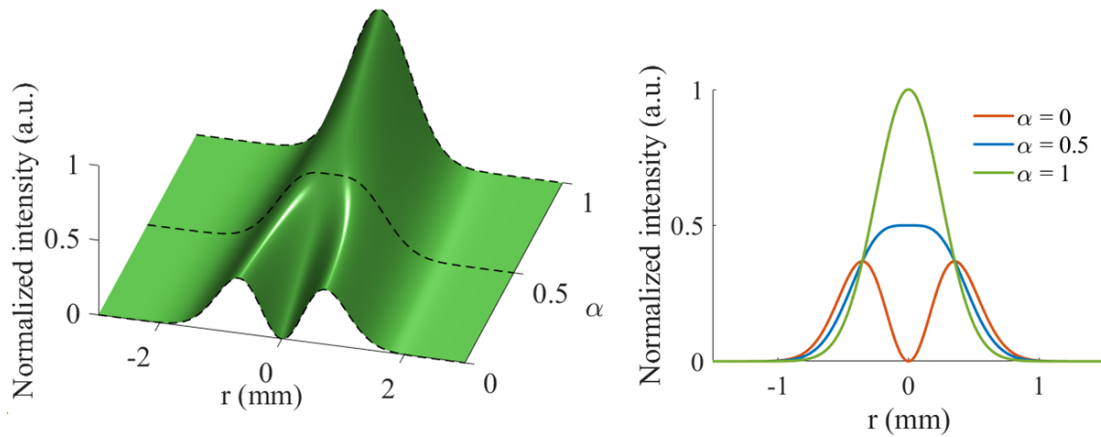
Figure 4.14: Intensity profile as α changes showing the evolution from a vortex to a flat-top to a Gaussian beam. The profiles of the vector beam at critical α values are shown on the right with the vortex beam at $\alpha = 0$, the vector flat-top beam at $\alpha = 0.5$ and the Gaussian beam at $\alpha = 1$.

All LG beams are eigenmodes of free-space, meaning their profile is unchanging during propagation (only subject to divergence). Since the vector flat-top is the sum of two LG mode, the vector flat-top is itself propagation invariant as shown in Figure 4.15.
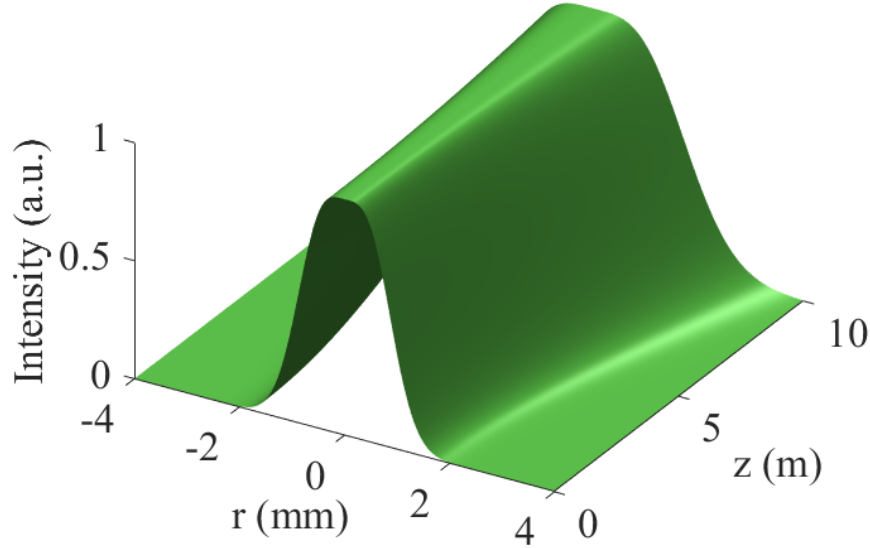
Figure 4.15: Propagation of a vector flat-top beam showing the unchanging flat-top profile. The peak intensities were normalized to better visualize the propagation invariance of this beam.

Even though the propagation invariant property of a vector flat-top beam is showcased here as the main benefit of this beam, there are other advantages for choosing a vector beam for optical trapping. For one, the versatility of the optical tweezer is enhanced, since it allows trapping with scalar Gaussian and vortex beams, as well as vectorial combinations of the two by only adjusting the α parameter. The vector beam creation is also not limited to Gaussian and vortex addition but any arbitrary vector beam can be created by simply superimposing different scalar beams.

4.2.2   Vector flat-top beam vs. the Gaussian beam

Here the vector flat-top beam is (theoretically) compared to the Gaussian beam in terms of power, peak intensity and trap strength. The intensity of the vector beam can generally be written as the sum of the intensities of the Gaussian and vortex beam (with some polarization requirements)

$$I_{vector} = \alpha |\text{LG}_0^0|^2 + (1 - \alpha)|\text{LG}_0^1|^2, \tag{4.6}$$

where the vector flat-top intensity is obtained by setting $\alpha = 0.5$ and the Gaussian intensity by $\alpha = 1$. The intensity profiles of the vector flat-top and Gaussian beam of the same power are plotted in Figure 4.16a. When generating a vector flat-top beam with the same power as a Gaussian beam, its peak intensity is half of the Gaussian peak intensity.

The gradient force (or trap strength) of a beam is proportional to the intensity gradient of the beam, $F_{grad} = c\nabla I$, with the proportionality constant given in Equation 3.5 in Section 3.1.2. Since only the relative forces of the vector flat-top and Gaussian beam are important, $c = 1$ is assumed such that

$$F_{grad} = \nabla I. \tag{4.7}$$

Therefore, if the intensity profile of a beam is known, its gradient force can easily be calculated. The gradient force over the vector flat-top and Gaussian beams, of the same power, are presented in Figure 4.16b. It is clear from this graph that at the same power, the Gaussian beam out performs the vector flat-top beam (in terms of trap strength). This is expected, since even though the intensity gradient of the vector flat-top is steeper, the high intensity peak of the Gaussian beam negates this effect.
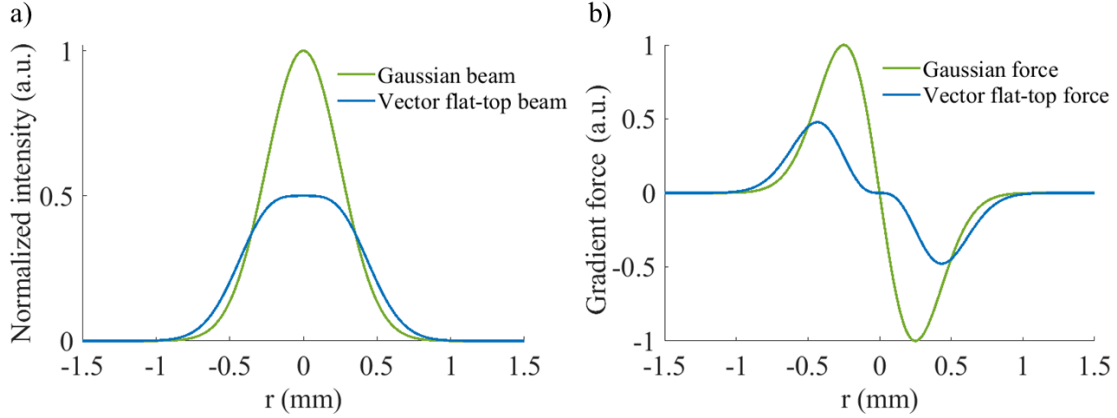
Figure 4.16: Comparison of the a) intensity profiles and b) gradient forces of a Gaussian and vector flat-top beams generated with the same power.

For the vector flat-top beam to be useful, two questions needed answering: 1) at which power is the trap strength of the vector flat-top beam equal to or greater than that of the Gaussian beam? and 2) is there still a lower peak intensity at this power in order to possibly reduce the photobleaching in the optical trap?

To answer these questions, the average gradient force ($\bar{F}_{grad}$) over the whole area of the beam, A, was considered

$$\bar{F}_{grad} = \frac{\int F_{grad}\,\mathrm{d}A}{\int \mathrm{d}A}\ . \tag{4.8}$$

More relevant is the ratio of the average gradient force of the flat-top (FT) to the Gaussian (G) beam, namely

$$\gamma = \frac{\bar{F}_{FT}}{\bar{F}_{G}}\ , \tag{4.9}$$

so that at $\gamma = 1$ the average gradient force of the flat-top and Gaussian beams are equal and at $\gamma > 1$ the vector flat-top has a stronger trap strength. For the case represented in Figure 4.16, where the Gaussian and the flat-top beam have the same power, $\gamma = 0.75$ meaning on average the gradient force of the Gaussian beam is stronger.

The ratio, γ, was calculated at different relative powers of the Gaussian and vector flat-top beams and plotted in Figure 4.17a. This figure, therefore, shows how the relative gradient forces of the two beams change when adjusting the power. Three special cases are indicated on the graph. Firstly, in the instance when the power of the two beams are equal (as just discussed), $\gamma = 0.75$, so the Gaussian beam is a stronger trap (blue line). Secondly, for the two beams to have the same average gradient force ($\gamma = 1$), the Gaussian beam must have 75% of the power of the vector flat-top beam (green line). Lastly, when the two beams have the same intensity, that is when the power of the Gaussian is half than that of the flat-top beam, then the flat-top beam trap is 1.5 times stronger than the Gaussian beam trap (orange line).

The corresponding intensity profiles of the three special cases are shown in Figure 4.17b. The vector flat-top beam along with Gaussian beams that have 1) the same power, 2) the same gradient force and 3) the same peak intensity as the flat-top are plotted. Most relevant is the 'same gradient force case'; here it is clear that when the vector flat-top beam and the Gaussian beam have the same trap strength (or gradient force), the peak intensity of the vector flat-top is lower than the Gaussian beam. This means that the vector flat-top beam can be used to trap a particle with the same strength but with a lower peak intensity (compared to the Gaussian beam) in order to possibly reduce photobleaching in the trap. The remainder of this chapter focuses on proving these theoretical claims experimentally.
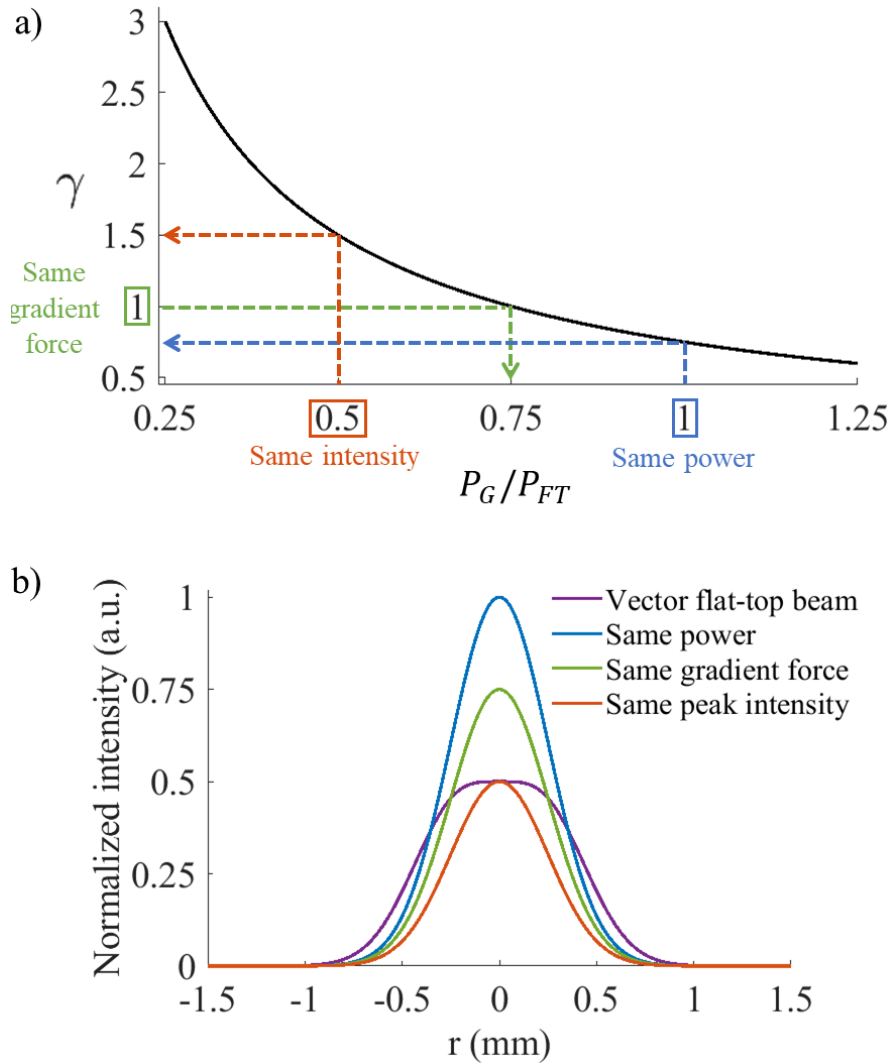
Figure 4.17: a) A plot showing the relationship between the relative gradient force and power of the Gaussian and vector flat-top beam. b) The intensity profiles corresponding to a Gaussian beam having the same power, gradient force and intensity as a vector flat-top beam.

4.3 Trapping with vector flat-top beams

In this section the experimental setup of a vectorial HOT, with specific focus on the generation of vector flat-top beams, is discussed. The versatility of this setup is shown experimentally by easily switching from a scalar to vector beam trap. Trap stiffness of the vector flat-top beam compared to a Gaussian beam trap is reported as well as the effect of the beam size on the trap.

4.3.1 Experimental setup

The optical tweezer setup described in Section 3.2.1 and shown in Figure 3.9 was used as the 'backbone' of the HOT setup. However, here the SLM was used to generate structured light beams and an interferometer was included 'inside' telescope 2 to create vector beams.

The experimental setup of a vector holographic optical trap is illustrated in Figure 4.18. A horizontally polarized Gaussian beam from a $\lambda = 532$ nm laser was expanded and collimated before illuminating the screen of a reflective SLM (Holoeye Pluto, Germany), aligned to only modulate horizontally polarized light. To create a vector flat-top beam, a Gaussian (LG_0^0) and a vortex beam (LG_0^1) with different propagation angles were created with the SLM (the insets shows the 2D intensity profiles of experimentally obtained beams). The multiplexed grey-scale hologram that was encoded on the SLM using CAM is shown in Figure 4.18b, with the different gratings of the two beams as insets. The Gaussian and vortex beams were separated using a D-shaped mirror (D-M) in order to direct the beams to a polarizing beam splitter (PBS) where they were interferometrically combined. The unwanted zeroth and higher orders were removed by spatial filtering before the PBS. A half wave plate (HWP) was added in the path of one beam to change its polarization from horizontal to vertical, to allow the superposition of orthogonal

polarized beams. The vector flat-top beam was therefore obtained after the PBS, see the inset showing the intensity profile of an experimentally obtained flat-top beam. The reflection of light from a dichroic mirror (DM) is slightly different for horizontally and vertically polarized light. In order to ensure that the DM did not change the profile of the vector beam (given that its performance varies slightly for the orthogonal polarizations), a quarter wave plate (QWP) at 45° was added in the path of the vector beam to change the polarization of each beam to circular (meaning the two beams making the vector light have the same 'amount' of vertical and horizontal polarization and the DM will have the same effect on both). The 4f-system (lenses L1 and L2) was included to ensure the generated beam reached the back aperture of the objective lens.

The rest of the optical tweezer setup was the same as reported previously. In short, the high NA objective lens O focused the beam to create the optical trap in the plane of the sample. The sample consisted of either 2 μm polystyrene beads (sample used for obtaining trap stiffness) or QD-tagged polystyrene beads (fluorescent sample) supported between a cover slip and microscope slide. An inverted microscope setup was implemented with a DM reflecting the laser light into the objective while letting the fluorescence and illumination light pass through. In order to simultaneously observe trapping and fluorescence emission from the sample, the imaging/detection system was set up as described in Figure 3.24 (Section 3.3.2). Blue light was used to illuminate the sample which was transmitted by the notch DM, reflected by the longpass DM and imaged to a CCD camera. The fluorescence emission from the sample was transmitted by both DMs to be detected by an avalanche photodiode (APD, a single photon detector). Since the DMs are not 100% effective, extra color filters were inserted to ensure no light from the trapping laser reached the camera or APD.
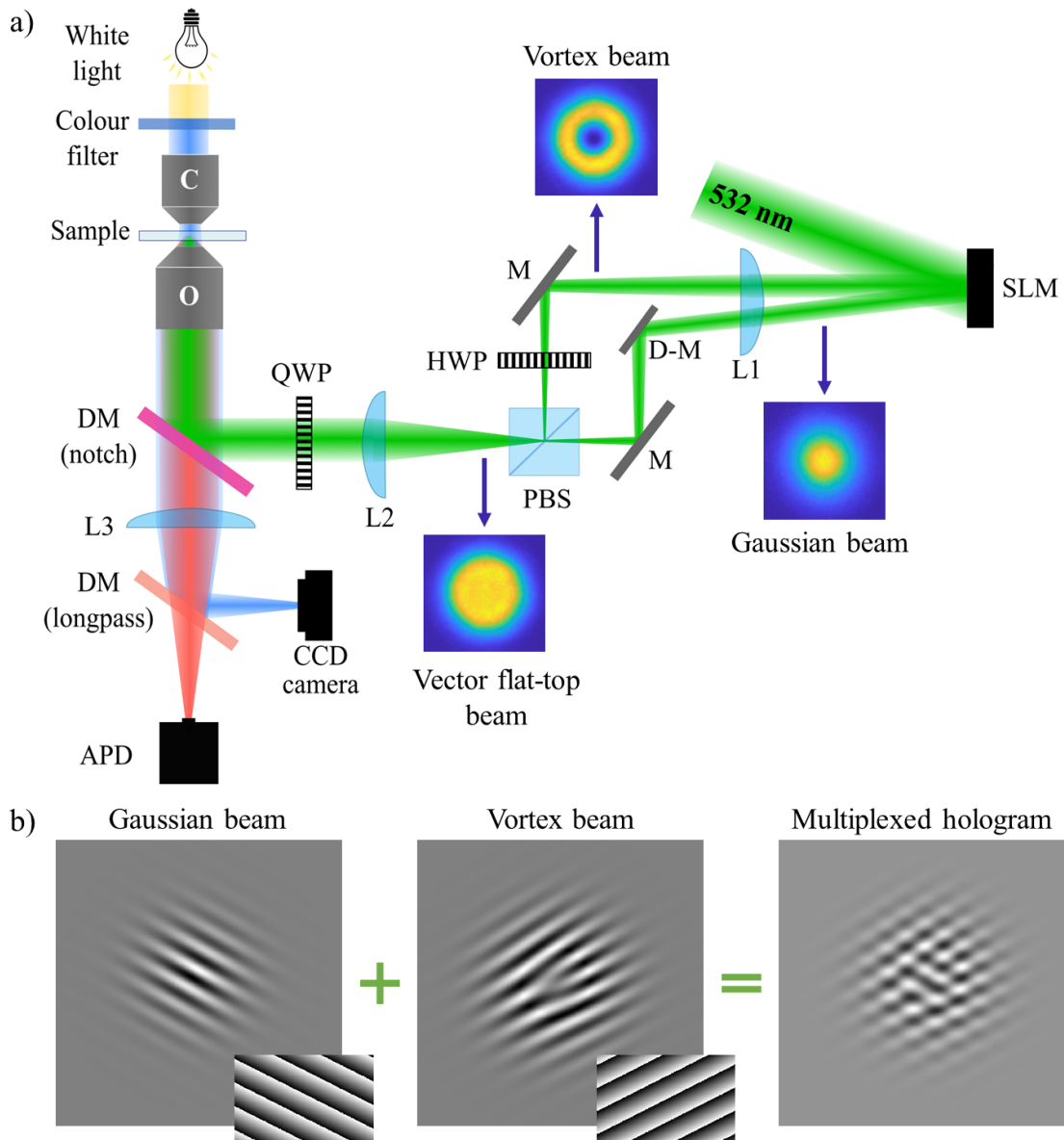
Figure 4.18: a)An illustration of the experimental setup of a vector flat-top holographic optical tweezer that can simultaneously image the sample to observe trapping (blue beam) and detect fluorescence with an APD (red beam). The insets show the experimentally generated vortex and Gaussian beams that were combined to form the vector flat-top beam. b) The multiplexed hologram that was encoded on the SLM to generate a Gaussian and vortex beam with different propagation angles.

Even though this study focused on creating vector flat-top beams, this setup can be used to generate any arbitrary vector beam by simply superimposing different scalar beams. For example, adding two vortex modes with $l = +1$ and $l = -1$, respectively, will create radially and azimuthally polarized vortex beams.

Figure 4.19 shows the intensity profile and cross-section of an experimentally generated vector flat-top beam in the near and far field. Theoretical profiles of the vector beam cross-sections (green) are shown with the experimentally measured data points (black). This confirms that the vector flat-top beam is shape invariant in both the near field (image plane) and the far field (Fourier plane), an important quality since the optical trap is generated in the far field. The near field was imaged at the image plane after L2 while the far field was imaged at the focus of a 500 mm focal length lens placed after L2 and using a flip-mirror to direct the beam to this lens.
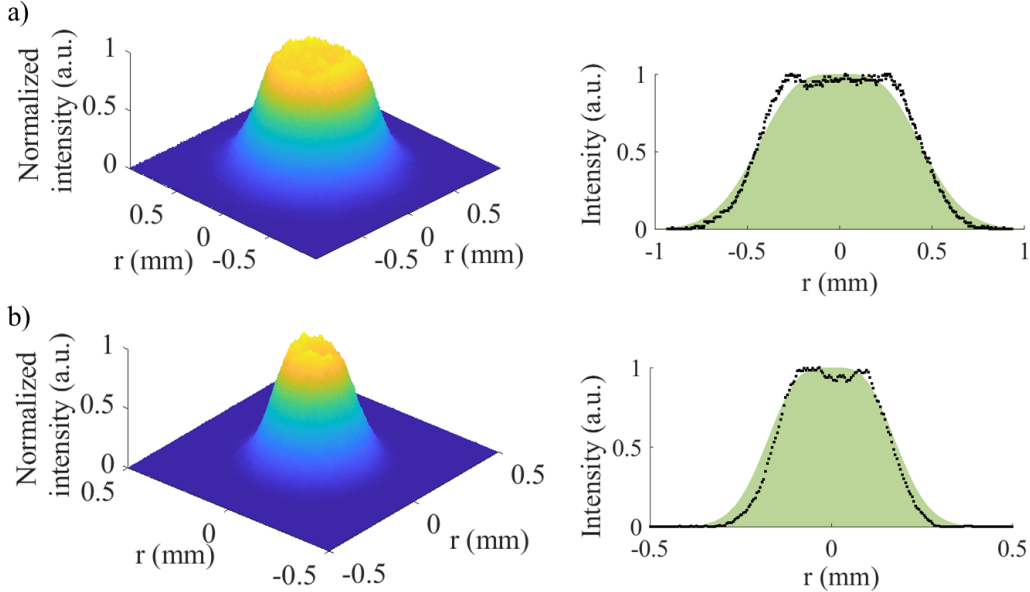
Figure 4.19: The intensity map (left) and cross-section (right) of an experimentally generated flat-top beam in the a) near field and b) far field. Theoretical cross-sections are presented in green with the experimental data points in black.

4.3.2 From scalar to vector beam trapping

As mentioned earlier, this holographic trap allows trapping with scalar Gaussian and vortex beams, as well as vectorial combinations of the two. When equally weighted, the resultant is the vector flat-top beam. The weighting factor was called α (refer to Equation 4.5). Figure 4.20 shows the intensity profiles of experimentally generated beams at different α values. The beams at the three critical α values are shown in the top row with the scalar vortex beam at $\alpha = 0$, the vector flat-top beam at at $\alpha = 0.5$ and the scalar Gaussian beam at at $\alpha = 1$. The beams at intermediate α values are shown in the bottom row. The theoretical profiles (plotted in green) were in good agreement with the experimental data (presented in black).
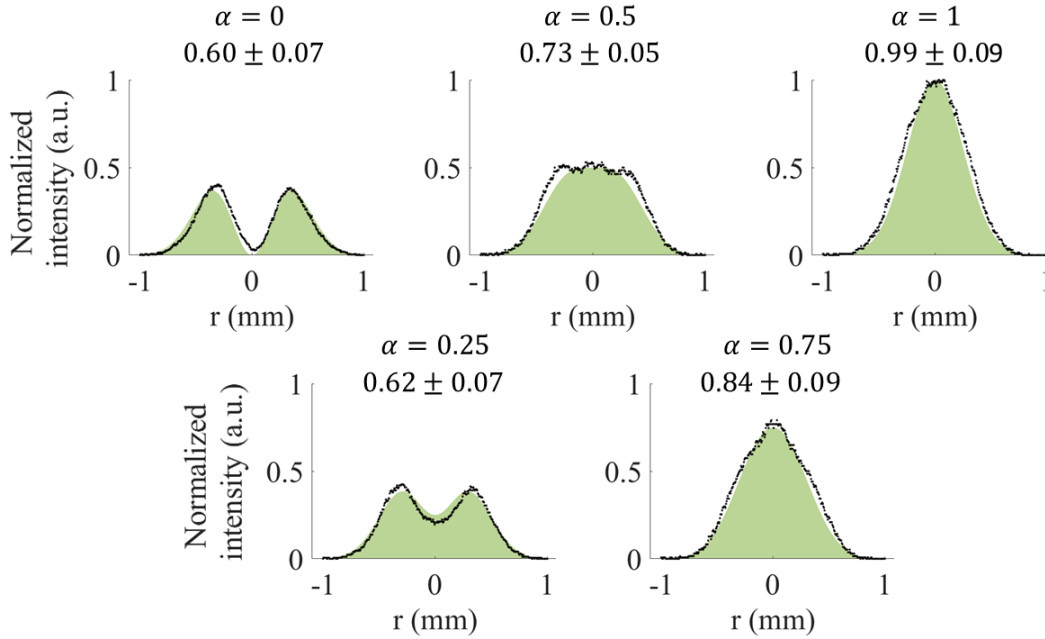
Figure 4.20: Intensity profiles of the beam generated at five different α values, with the trapping stiffness of each beam printed above the graph (unit: pN/μm). The experimental data points are plotted in black, whereas the theoretical profiles are given in green.

The trap stiffness of each beam is reported above the profile in Figure 4.20 (unit: pN/μm). Each beam was used to trap a 2 μm polystyrene particle for 3 min at a power of 180 μW; the trap stiffness was calculated using the equipartition method. The gradient force of the optical trap can therefore be adjusted by simply changing the trapping beam's profile. Since the power was kept constant, the trap stiffness was increased as the trapping beam became more Gaussian-like.

4.3.3   Comparing flat-top and Gaussian beam traps

From Figure 4.17 we concluded that at the same power, the Gaussian beam will theoretically create a stronger optical trap compared to the flat-top beam due to its high peak intensity. This was confirmed experimentally by determining the trap stiffness of these two beams at different powers – see Figure 4.21. Five 2 μm diameter beads were trapped at each power measurement for 3 min for both the Gaussian and the flat-top beam. The average trap stiffness of the five beads was plotted in Figure 4.21 with the standard error shown by the error bars. From this plot it is clear that the Gaussian beam outperformed the flat-top beam at each power measurement.

Another conclusion drawn from the theoretical calculations in Section 4.2.2 is that when the Gaussian and the flat-top are created with the same peak intensity, then the flat-top will be the stronger trap due to its steeper intensity gradient. Figure 4.22a shows the trap stiffness against the peak intensity of the two beams; again, the experimental results confirmed the theory. In this graph, the same data from Figure 4.21 was plotted but in terms of relative peak intensities. It is known theoretically, but also shown experimentally in Figure 4.22b, that the flat-top beam has half the peak intensity of the Gaussian beam at the same power. Therefore, if it is assumed that the Gaussian with the highest power has a peak intensity of 1, the rest can be scaled appropriately.
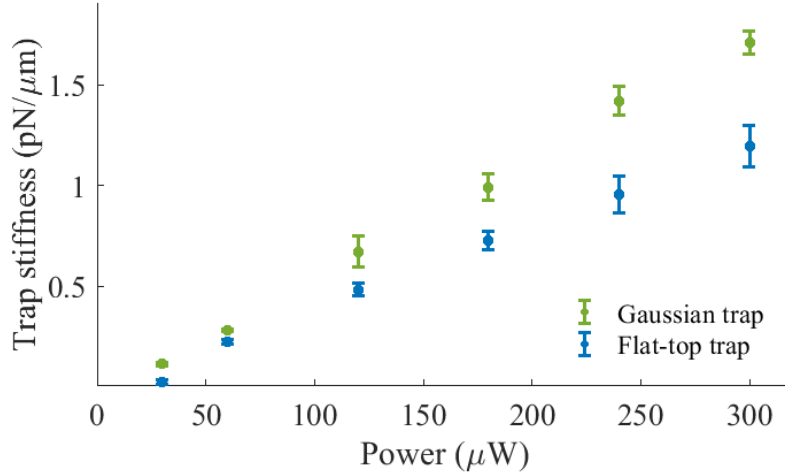
Figure 4.21: The trap stiffness of a Gaussian and flat-top beam at different powers.

To estimate the true peak intensity at the trap, the beam waist of the Gaussian beam at the trap must be known, since the peak intensity of a Gaussian beam is

$$I_{peak} = \frac{2P}{\pi \omega_0^2} \, . \tag{4.10}$$

To determine ω_0, the back reflection of the Gaussian beam from the sample slide was used. As mentioned previously, the dichroic mirrors are not 100% efficient, therefore some of the trapping beam was transmitted and imaged to a CCD camera. The camera was calibrated using the known diameter of the 2 μm beads in the sample. The Gaussian beam waist at the trapping plane was measured to be 0.9 μm. Therefore, at a trapping power of 300 μW the peak intensity of the Gaussian beam at the trap was calculated to be 24 kW/cm^2 (this absolute peak intensity corresponds to 1 in Figure 4.22). Since the exact power and beam size at the trapping plane, inside the sample, are never fully known, this value must be interpreted as only an estimation of the intensity.
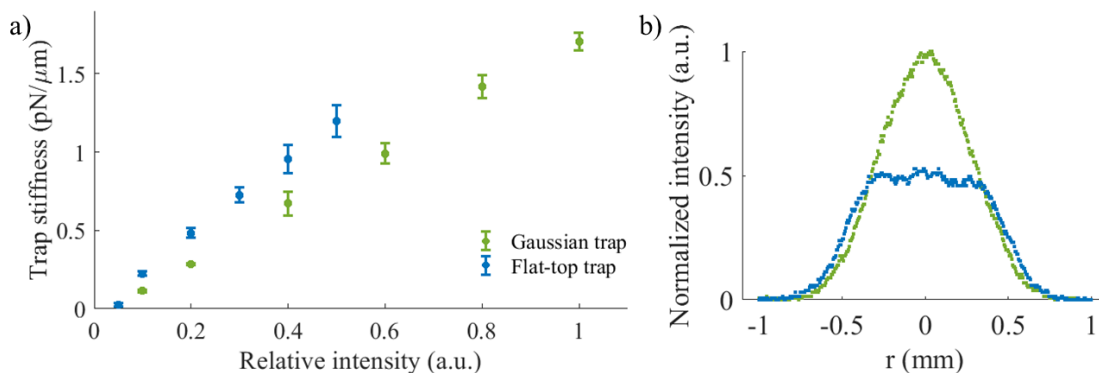
Figure 4.22: a) Trap stiffness of a Gaussian and flat-top beam trap at different peak intensities. b) Experimental proof that at the same power, the vector flat-top beam has half the peak intensity compared to a Gaussian beam.

4.3.4 Trapping with different beam sizes

The size of the beam at the trap plays an important roll in the trap stiffness. The optical trapping force a particle will experience (due to a focused beam) depends on the beam size relative to the particle. In all the calculations done in Section 4.2.2, the gradient force of the beam was determined by integrating over the total area of the beam. The particle will, however, only experience this total force if it 'sees' the whole beam; which is true when the beam at the trap is smaller than the particle. This has been the case up until now. All the traps created thus far have been smaller than the 2 μm beads, as just reported the Gaussian trap had a waist (radius) of 0.9 μm. To see the effect of a trapping beam that is larger than the particle, a telescope was added in the setup to reduce the beam size before entering the objective. Since the objective back aperture is not filled, the focus is less tight – creating a larger optical trap.

The top row in Figure 4.23 shows the movement of a 2 μm polystyrene bead in an optical trap where the beam is smaller (diameter of 1.8 μm) than the bead. A Gaussian, vortex and flat-top beam was used to trap the particle. The bottom row

shows the optical trap where the beam is larger (3.1 μm) than the bead. For the small traps, the movement of the bead was concentrated at the centre of all the beams with a little more movement in the vortex beam and more in the flat-top beam. The movement of the bead in the large Gaussian trap was also centred but less stiff than for the small Gaussian trap. The particle trapped in the large vortex beam, moved along the ring of the beam where the intensity gradient and consequently the trapping force exists. Lastly, the movement of the bead in the large flat-top trap was more uniform (not concentrated at a point). From these plots it is clear that the size and type of beam have a great influence on the strength of an optical trap. To determine the trap stiffness of the large vortex and flat-top beam, the equipartition method will not work, since a harmonic potential
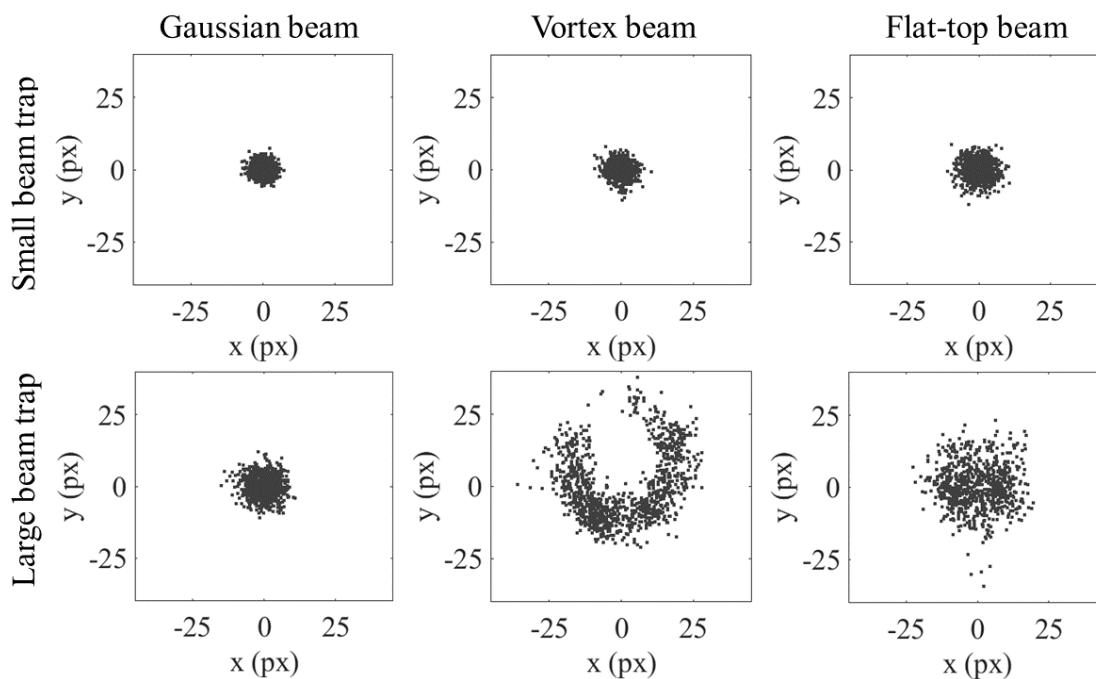
Figure 4.23: The movement of a bead in Gaussian, vortex and flat-top beam traps with a beam size smaller than the particle (top row) and larger than the particle (bottom row). The particle was a 2 μm polystyrene bead, the small trap had a beam diameter of 1.8 μm and the large trap a diameter of 3.1 μm.

does not exists; to determine the trap strength for these beams the drag force method, for example, is more suitable [113].

4.4 The robustness of vector beams in aberrated systems

This section is included to experimentally demonstrate another benefit of using vectorial structured light in optical systems. As mentioned several times throughout this chapter, vector beams are defined by their inhomogeneous polarization patterns. When a vector beam travels through perturbing media that cause aberrations, the beam appears distorted in its phase, amplitude and polarization structure, however, the inhomogeneity of vectorial light is immune to any such perturbations, given that the perturbing medium is unitary in nature (an inverse process exists that can undo the changes of the medium). This robustness of vector beams was shown in a recently accepted paper by our research group given in Appendix C.3. The aberrations can be caused when light propagates through water or turbulent air in the case of optical communication systems or (more relevant to optical trapping) when the beam goes through imperfect or misaligned optical elements. Due to the unchanging polarization inhomogeneity and the unitary nature of the perturbing medium, the effect of the aberrated system can be undone (either before or after the medium) to restore the spatial structure of the beam. For detail of the theory, experiments and significance of this robustness of vectorial light refer to the paper in Appendix C.3. Here, a part of the optical tweezing results is presented to highlight another advantage of trapping with vectorial light.

In order to exhibit the impact of unitary transformations to vector beams in a practical setting, a 2 μm polystyrene particle was trapped with an aberrated radially polarized vector vortex beam. The movement of the particle in the

aberrated trap along with the trap stiffness are shown in Figure 4.24a. The low trap stiffness is due to the distortion of the spatial structure of the beam. Far field intensity measurements of orthogonal polarization components of the aberrated beam were used to extract the perturbation, which was corrected using the SLM encoded with the conjugate of the aforementioned measurement. The corrected beam was then used to trap the particle; the trap stiffness and movement of the particle inside this corrected trap are given in Figure 4.24b. By undoing the effect of the perturbing medium (aberration) the trap stiffness was greatly improved from 0.023 ($\pm$ 0.008) to 0.10 ($\pm$ 0.03) pN/μm, since the spatial structure of the radially polarized vector vortex beam was restored.
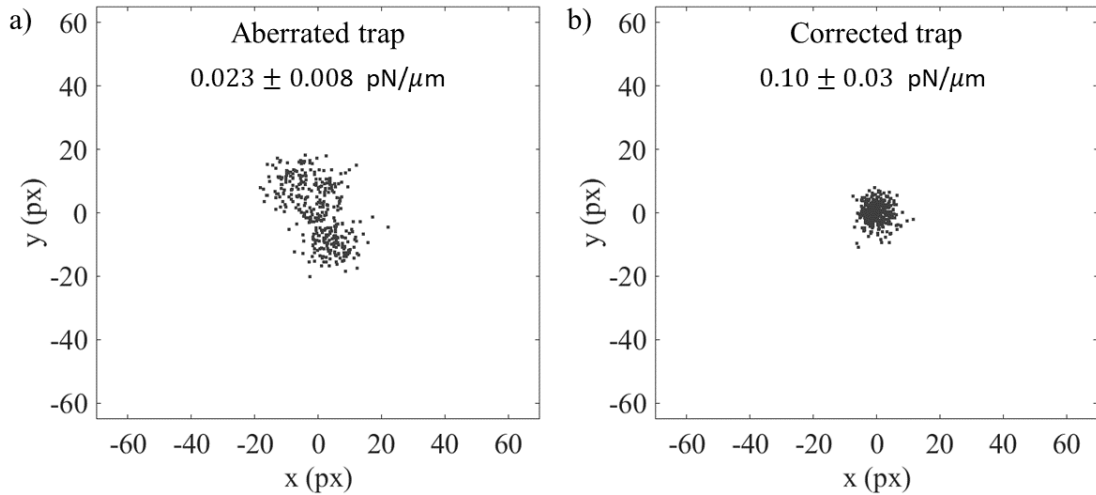
Figure 4.24: Particle movement in a vectorial beam optical tweezing system with a trap stiffness of a) 0.023 $\pm$ 0.008 pN/μm when the beam is aberrated and b) an increased trap stiffness of 0.10 $\pm$ 0.03 pN/μm when the aberration was corrected.

4.5   Fluorescent particle trapping

The vector flat-top beam can be generated to have the same gradient force as the Gaussian beam, but with a 25% reduced peak intensity (refer back to Figure 4.17).

This property of flat-top beams can be exploited to reduce photobleaching in optical traps. Moreover, if flat-top beams are generated with the same power as Gaussian beams, they have a 50% reduced peak intensity, with only a minimal loss of gradient force (trap strength) especially at low trapping powers (see Figure 4.21). For the end application of this project, which is to use optical tweezers and fluorescence detection for sensing purposes, the loss of trap strength when using a flat-top beam is insignificant. Therefore, for the rest of this study, the photobleaching effect of vector flat-top beams and Gaussian beams generated with the same power was compared to experimentally test whether flat-top beam trapping can reduce photobleaching in optical tweezers. Just to reiterate, photobleaching is the process where fluorophores permanently lose their fluorescence, and although not fully understood, bleaching most probably happens when electrons already in the excited state absorb a photon and escape, leaving the fluorophore positively charged and non-fluorescent.

The fluo-beads and the QD-tagged beads were used to investigate photobleaching in the optical tweezer; the initial photobleaching signal of the fluo-beads was used to model the behaviour of the QD-tagged beads as explained in Section 3.3.2. All the fluorescence intensity measurements presented in this section were normalized and background subtracted.

The first test looked at the effect of the trapping power on photobleaching. Figure 4.25 shows the photobleaching of trapped fluo-beads at different laser powers (measured with the APD). The higher the power, the quicker the fluo-beads bleached, which is as one would expect since a higher power means a higher intensity and more photons (per area) reaching the fluorophore that can induce bleaching. Note that the lowest power tested was 6 μW, however, at this power a bead cannot be trapped, so the light was shone on a stationary particle to test the effect of this low power. 60 μW is the minimum power at which stable

trapping (the particle does not escape the trap for 3 min) was observed for both the vector flat-top and Gaussian beam. This power was therefore mainly used for the photobleaching experiments.
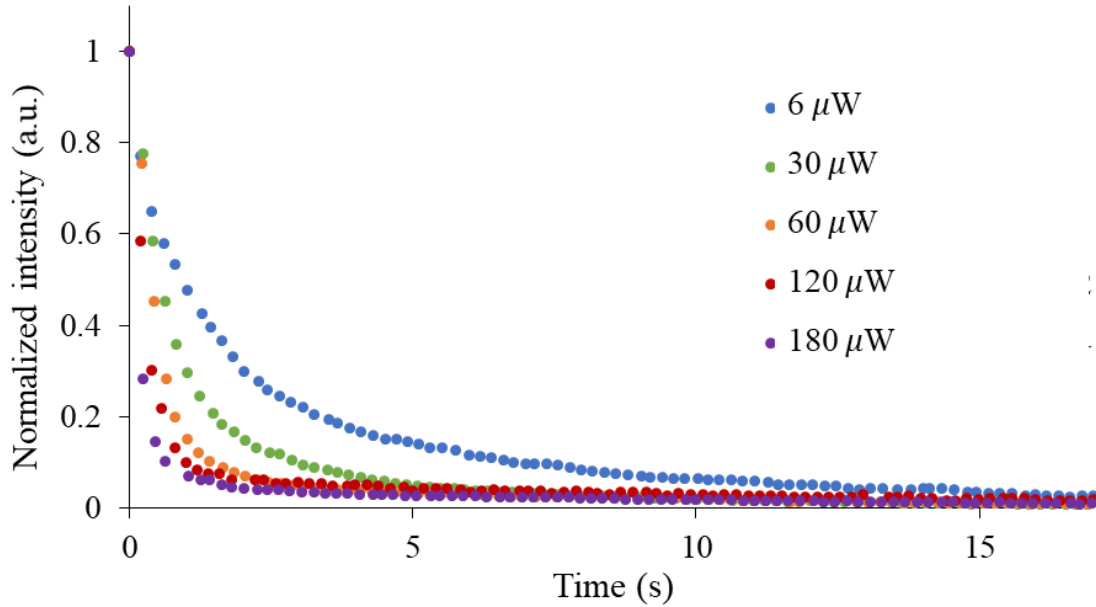
Figure 4.25: Photobleaching of fluo-beads at different trapping powers.

After creating the vector flat-top beam, a quick initial test was done to look at the effect of this beam on photobleaching. This test was done by exciting (not trapping) a fluo-bead with a Gaussian and flat-top beam respectively and looking at the fluorescence emission on the CCD camera – the results are shown in Figure 4.26. This preliminary test showed that the flat-top beam excitation increased the photobleaching lifetime of the fluo-bead significantly. Since this excitation result showed promise, further investigation was done to see if the beam has the same effect when used as the trapping beam (not only the excitation beam).
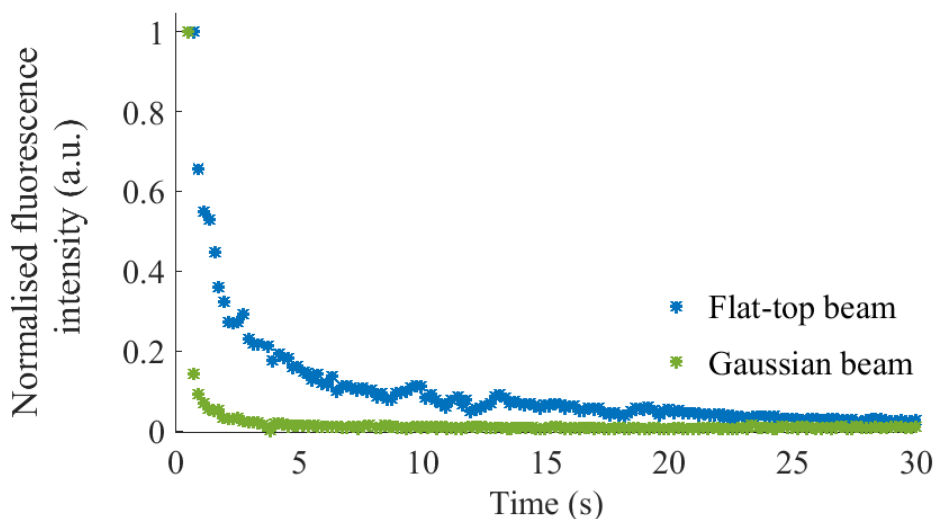
Figure 4.26: Photobleaching of fluo-beads under Gaussian and flat-top beam excitation.

The HOT setup as described in Section 4.3.1 was used to trap and excite QD-tagged beads and fluo-beads with a Gaussian and vector flat-top beam respectively. The results are presented in Figure 4.27. In contrast to the initial excitation test, no difference was observed in the bleaching lifetimes when trapping with the two different beams. The same bleaching lifetimes for the flat-top and Gaussian trap were seen for a QD-tagged bead at 60 μW (Figure 4.27b) as well as for fluo-beads at different trapping powers (Figure 4.27c). An explanation for these results might lie in beam size of the optical trap; these fluorophores were trapped with a beam smaller than the particle as illustrated in Figure 4.27a. This means that the particle 'sees' the whole beam. The vector flat-top and Gaussian beams were generated with the same power meaning they have the same number of photons (just spread differently). Therefore, the same number of photons reaches the fluorophore for both beams, causing the same extent of photobleaching. In an optical tweezer where the trap is smaller than the particle, the photobleaching is dependent on the number of photons (power) and independent of the spread of the photons (the intensity).
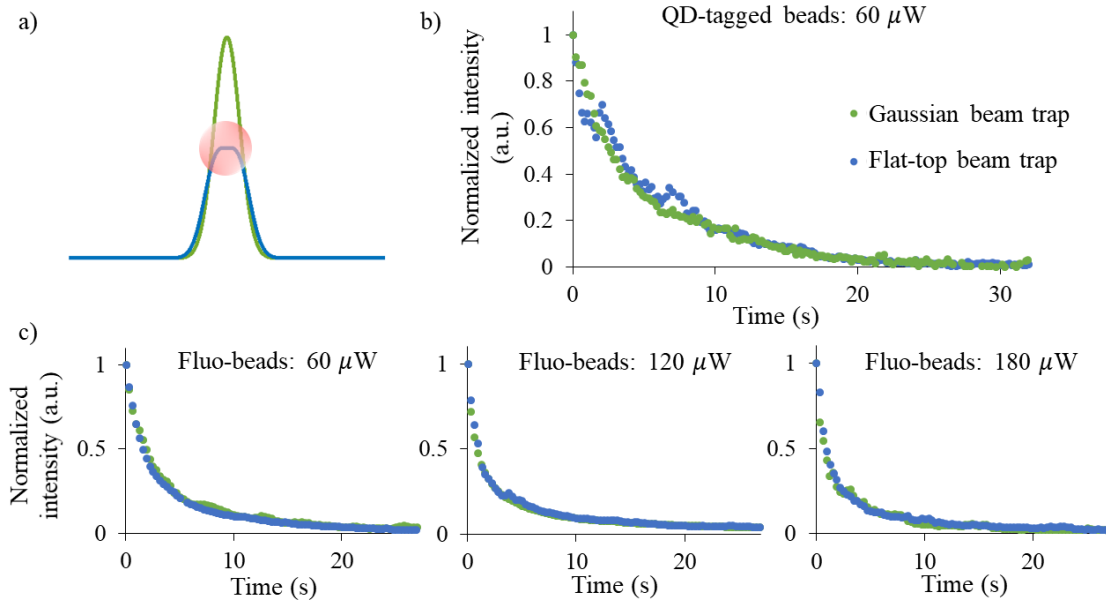
Figure 4.27: Photobleaching in small Gaussian and flat-top beam traps. a) An illustration of the beam size relative to the particle; the trapping beam was smaller than the particle. Photobleaching of a trapped b) QD-tagged bead and c) fluo-bead in Gaussian and flat-top beam traps at different powers. No improvement in the photobleaching lifetime was observed.

To test the above mentioned explanation, a trap larger than the particle was created. In this trap the fluorophore does not 'see' the whole beam and the part of the beam the fluorophore does 'see' depends on the intensity profile of the beam. The photobleaching in such a trap must therefore be dependent on the intensity or spread of the photons in the trapping beam. The photobleaching of a fluo-bead and a QD-tagged bead in such a trap are shown in Figure 4.28. Firstly, refer to the inset in Figure 4.28 showing the trap size relative to the particle size; more photons are incident on the fluorophore in the Gaussian beam trap than the flat-top beam trap since the fluorophore now only 'sees' the centre part of the beam where the Gaussian is much more intense. In this larger trap, the flat-top trapping beam increased the photobleaching lifetime of the fluo-beads (Figure 4.28a) and QD-tagged beads (Figure 4.28b) similar to the results seen in

the initial excitation test. The photobleaching of several QD-tagged beads were measured and the bleaching half-life of a bead in a Gaussian trap was determined to be 7.6 ± 0.6 s and the half-life in a vector flat-top trap 11 ± 1 s which is a 45% increase in the photobleaching half-life.

With all these results taken into consideration, vector flat-top beams (of the right size) can reduce photobleaching of a fluorophore in an optical tweezer system. In this study, the trapping and fluorescence excitation was (very unconventionally) done with the same laser, extensive photobleaching was therefore expected. However, implementing this structured light trapping in a dual laser system where trapping is done with a near-infrared laser (a wavelength which is less absorbent to the fluorophores) holds much promise to fluorescence studies in optical tweezers.
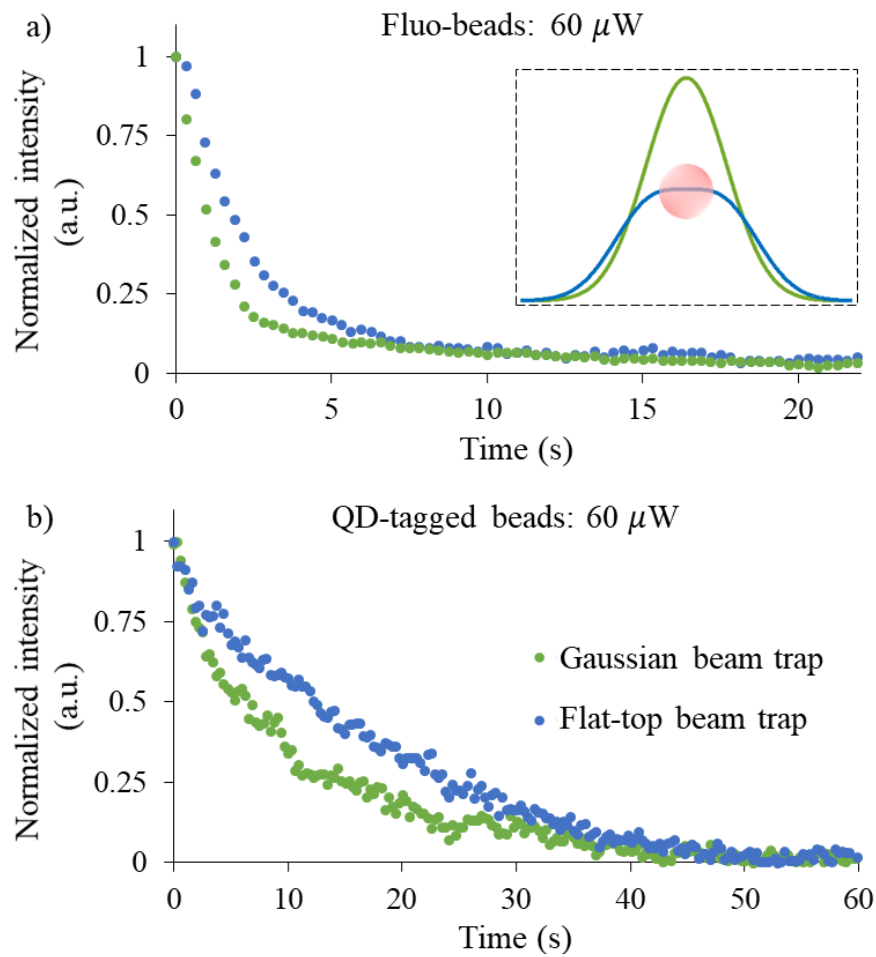
Figure 4.28: Photobleaching of a trapped a) fluo-bead and b) QD-tagged bead in large Gaussian and flat-top beam traps. The trap size was larger than the particle; the inset shows the beam size relative to the particle. Longer photobleaching lifetimes were observed for the fluorophores in the flat-top beam trap as compared to the Gaussian beam trap.

4.6 Chapter summary

In this chapter, the successful setup of a vectorial holographic optical tweezer, that can be used to reduce photobleaching in optical traps, was demonstrated. The chapter started with an introduction to structured light and shaping light with SLMs. The advantages of trapping particles with flat-top beams over Gaussian beams were discussed theoretically and shown experimentally. Trapping with scalar Gaussian and vortex beams, as well as vectorial combinations of the two, were demonstrated. QD-tagged beads and fluo-beads were used to test the effect of vector flat-top beams on photobleaching lifetimes in optical tweezers. Also, the large role the trap size plays on the trap stiffness and photobleaching inside optical tweezers was shown experimentally.

Chapter 5

Conclusion and outlook

This research project focused on tailoring optical tweezers for the fluorescence detection of quantum dots. The synthesis and characterization of micro-sized polymer beads functionalized with L-cysteine capped CdSe/ZnS core/shell QDs were presented. The optimization process of this synthesis was discussed in detail, highlighting the importance of size, adhesion and agglomeration control. To showcase the sensing ability of these QD fluorescent probes, they were used to detect atrazine, a harmful herbicide, at environmentally relevant surface water concentrations.

An optical tweezer setup was built with which trapping and *in-situ* fluorescence measurement of the QD probes were demonstrated. The experimental and technical difficulties of setting up an optical tweezer with integrated fluorescence detection were discussed. By employing structured light in the setup, a vectorial HOT was created, allowing for tailored gradient forces and light intensities within the trap. This advanced setup was used to deliver propagation invariant flat-top beams for uniform illumination and optical trapping. The added benefits of trapping with this vector flat-top beam over the conventional Gaussian beam were discussed theoretically and confirmed experimentally. It was shown that by simply tailoring the intensity landscape of the trapping beam, photobleaching in a single wavelength optical trap can be reduced; a result that will advance the field of optical manipulation of fluorescent particles.

The research presented in this dissertation laid the groundwork for a novel analytical instrument. In this study, QD probes fit for optical trapping and pollutant detection were synthesised, a holographic optical tweezer was set up with a built-in fluorescence microscope and the added benefits and applications of incorporating vectorially structured light into the system were investigated. In order to use the optical tweezer system for analytical sensing, a stable fluorescence signal (of at least for a few seconds) of the QD probe is necessary. Even though photobleaching was reduced by trapping with the flat-top beam, the current setup that used a single laser for trapping and excitation did not provide the required stable fluorescence signal. However, this challenge can be overcome by implementing the advantages of structured light for optical manipulation of fluorescent particles, as demonstrated in this dissertation, into a dual laser optical tweezer setup (separate trapping and excitation sources). Further work to optimise this analytical instrument includes the integration of a microfluidic channel into the setup, investigating possible methods to enhance the selectivity of the QD probes (such as coating the QDs with molecularly imprinted polymers) and optimising the physiochemical conditions for pollutant detection in the optical tweezer system. Even though the long term aim of this project is to create a novel analytical technique, the research and findings of the process to reach this goal as presented in this dissertation, is of great value to the optical manipulation and chemistry communities alike.

References

[1] Femina C Christopher, Ponnusamy S Kumar, Fetcia J Christopher, Ganesan J Joshiba, and Pavithra Madhesh. Recent advancements in rapid analysis of pesticides using nano biosensors: a present and future perspective. *Journal of Cleaner Production*, 269:122356, 2020.

[2] Kshitij RB Singh and Ravindra P Singh. Utility of nanobiosensors in environmental analysis and monitoring. In *Nanosensors for Environment, Food and Agriculture Vol. 1*, pages 229–246. Springer, 2021.

[3] Harpreet Singh, Archita Sharma, Sanjeev K Bhardwaj, Shailendra K Arya, Neha Bhardwaj, and Madhu Khatri. Recent advances in the applications of nano-agrochemicals for sustainable agricultural development. *Environmental Science: Processes & Impacts*, 23(2):213–239, 2021.

[4] Jiao Yang, Shu-Wei Chen, Bingwen Zhang, Qin Tu, Jinyi Wang, and Mao-Sen Yuan. Non-biological fluorescent chemosensors for pesticides detection. *Talanta*, 240:123200, 2022.

[5] Manuela F Frasco and Nikos Chaniotakis. Semiconductor quantum dots in chemical sensors and biosensors. *Sensors*, 9(9):7266–7286, 2009.

[6] Sifiso A Nsibande and Patricia BC Forbes. Fluorescence detection of pesticides using quantum dot materials–a review. *Analytica Chimica Acta*, 945:9–22, 2016.

[7] Rahul Roy, Sungchul Hohng, and Taekjip Ha. A practical guide to single-molecule FRET. *Nature Methods*, 5(6):507–516, 2008.

[8] Felix Ritort. Single-molecule experiments in biological physics: methods and applications. *Journal of Physics: Condensed Matter*, 18(32):R531, 2006.

[9] Taekjip Ha. Single-molecule methods leap ahead. *Nature Methods*, 11(10):1015–1018, 2014.

[10] Namik Akkilic, Stefan Geschwindner, and Fredrik Höök. Single-molecule biosensors: Recent advances and applications. *Biosensors and Bioelectronics*, 151:111944, 2020.

[11] Furqan M Fazal and Steven M Block. Optical tweezers study life under tension. *Nature Photonics*, 5(6):318–321, 2011.

[12] Halina Rubinsztein-Dunlop, Andrew Forbes, Michael V Berry, Mark R Dennis, David L Andrews, Masud Mansuripur, Cornelia Denz, Christina Alpmann, Peter Banzer, Thomas Bauer, et al. Roadmap on structured light. *Journal of Optics*, 19(1):013001, 2016.

[13] Andrew Forbes, Michael de Oliveira, and Mark R Dennis. Structured light. *Nature Photonics*, 15(4):253–262, 2021.

[14] K Dholakia and T Čižmár. Shaping the future of manipulation. *Nature Photonics*, 5(6):335–342, 2011.

[15] David G Grier. A revolution in optical manipulation. *Nature*, 424(6950):810–816, 2003.

[16] Nkosiphile Bhebhe, Peter AC Williams, Carmelo Rosales-Guzmán, Valeria Rodriguez-Fajardo, and Andrew Forbes. A vector holographic optical trap. *Scientific Reports*, 8(1):1–9, 2018.

[17] Eileen Otte and Cornelia Denz. Optical trapping gets structure: Structured light for advanced optical manipulation. *Applied Physics Reviews*,

7(4):041308, 2020.

[18] Yuanjie Yang, Yuxuan Ren, Mingzhou Chen, Yoshihiko Arita, and Carmelo Rosales-Guzmán. Optical trapping with structured light: a review. *Advanced Photonics*, 3(3):034001, 2021.

[19] Alexey I Ekimov and Alexei A Onushchenko. Quantum size effect in three-dimensional microscopic semiconductor crystals. *JETP Letters*, 34(6):345–348, 1981.

[20] Alexander L Efros and Al L Efros. Interband absorption of light in a semiconductor sphere. *Soviet Physics Semiconductors*, 16(7):772–775, 1982.

[21] Louis E Brus. A simple model for the ionization potential, electron affinity, and aqueous redox potentials of small semiconductor crystallites. *The Journal of Chemical Physics*, 79(11):5566–5571, 1983.

[22] Mark A Reed, RT Bate, K Bradshaw, WM Duncan, WR Frensley, JW Lee, and HD Shih. Spatial quantization in GaAs–AlGaAs multiple quantum dots. *Journal of Vacuum Science & Technology B: Microelectronics Processing and Phenomena*, 4(1):358–360, 1986.

[23] Andrew M Smith and Shuming Nie. Semiconductor nanocrystals: structure, properties, and band gap engineering. *Accounts of Chemical Research*, 43(2):190–200, 2010.

[24] Catherine J Murphy and Jeffery L Coffer. Quantum dots: a primer. *Applied Spectroscopy*, 56(1):16A–27A, 2002.

[25] Sumanth D Kumar, Jai B Kumar, and HM Mahesh. Quantum nanostructures (QDs): An overview. In *Synthesis of Inorganic Nanomaterials*, Micro and Nano Technologies, pages 59–88. Woodhead Publishing, 2018.

[26] Margaret Chern, Joshua C Kays, Shashi Bhuckory, and Allison M Dennis. Sensing with photoluminescent semiconductor quantum dots. *Methods and Applications in Fluorescence*, 7(1):012005, 2019.

[27] Louis E Brus. Electron–electron and electron-hole interactions in small semi-conductor crystallites: The size dependence of the lowest excited electronic state. *The Journal of Chemical Physics*, 80(9):4403–4409, 1984.

[28] Louis Brus. Electronic wave functions in semiconductor clusters: experiment and theory. *The Journal of Physical Chemistry*, 90(12):2555–2560, 1986.

[29] Igor L Medintz, H Tetsuo Uyeda, Ellen R Goldman, and Hedi Mattoussi. Quantum dot bioconjugates for imaging, labelling and sensing. *Nature Materials*, 4(6):435–446, 2005.

[30] Ute Resch-Genger, Markus Grabolle, Sara Cavaliere-Jaricot, Roland Nitschke, and Thomas Nann. Quantum dots versus organic dyes as fluorescent labels. *Nature Methods*, 5(9):763–775, 2008.

[31] Xavier Michalet, Fabien F Pinaud, Laurent A Bentolila, James M Tsay, SJJL Doose, Jack J Li, G Sundaresan, AM Wu, SS Gambhir, and S Weiss. Quantum dots for live cells, in vivo imaging, and diagnostics. *Science*, 307(5709):538–544, 2005.

[32] Ron Hardman. A toxicologic review of quantum dots: toxicity depends on physicochemical and environmental factors. *Environmental Health Perspectives*, 114(2):165–172, 2006.

[33] Dhermendra K Tiwari, Takashi Jin, and Jitendra Behari. Bio-distribution and toxicity assessment of intravenously injected anti-HER2 antibody conjugated CdSe/ZnS quantum dots in Wistar rats. *International Journal of Nanomedicine*, 6:463, 2011.

[34] Shi Y Lim, Wei Shen, and Zhiqiang Gao. Carbon quantum dots and their applications. *Chemical Society Reviews*, 44(1):362–381, 2015.

[35] Jamie H Warner, Akiyoshi Hoshino, Kenji Yamamoto, and Richard D Tilley. Water-soluble photoluminescent silicon quantum dots. *Angewandte Chemie International Edition*, 44(29):4550–4554, 2005.

[36] Jana Drbohlavova, Vojtech Adam, Rene Kizek, and Jaromir Hubalek. Quantum dots—characterization, preparation and usage in biological systems. *International Journal of Molecular Sciences*, 10(2):656–673, 2009.

[37] Debasis Bera, Lei Qian, Teng-Kuan Tseng, and Paul H Holloway. Quantum dots and their multimodal applications: a review. *Materials*, 3(4):2260–2345, 2010.

[38] Christina M Tyrakowski and Preston T Snee. A primer on the synthesis, water-solubilization, and functionalization of quantum dots, their use as biological sensing agents, and present status. *Physical Chemistry Chemical Physics*, 16(3):837–855, 2014.

[39] Rajib Ghosh Chaudhuri and Santanu Paria. Core/shell nanoparticles: classes, properties, synthesis mechanisms, characterization, and applications. *Chemical Reviews*, 112(4):2373–2433, 2012.

[40] Yanjie Zhang and Aaron Clapp. Overview of stabilizing ligands for biocompatible quantum dot nanocrystals. *Sensors*, 11(12):11036–11055, 2011.

[41] Jihad René Albani. *Principles and applications of fluorescence spectroscopy*. John Wiley & Sons, 2008.

[42] Joseph R Lakowicz. *Principles of Fluorescence Spectroscopy, 1999*. Springer, second edition, 1999.

[43] Douglas A Skoog, F James Holler, and Stanley R Crouch. *Principles of instrumental analysis*. Cengage Learning, 2017.

[44] Alun TR Williams, Stephen A Winfield, and James N Miller. Relative fluorescence quantum yields using a computer-controlled luminescence spectrometer. *Analyst*, 108(1290):1067–1071, 1983.

[45] Laurent Porres, Adam Holland, Lars-Olof Pålsson, Andrew P Monkman, Chris Kemp, and Andrew Beeby. Absolute measurements of photoluminescence quantum yields of solutions using an integrating sphere. *Journal of Fluorescence*, 16(2):267–273, 2006.

[46] Senthil P Kumar, Grace K Pavithra, and Mu Naushad. Characterization techniques for nanomaterials. In *Nanomaterials for Solar Cell Applications*, pages 97–124. Elsevier, 2019.

[47] Stefanos Mourdikoudis, Roger M Pallares, and Nguyen TK Thanh. Characterization techniques for nanoparticles: comparison and complementarity upon studying nanoparticle properties. *Nanoscale*, 10(27):12871–12934, 2018.

[48] Andrey L Rogach. *Semiconductor Nanocrystal Quantum Dots*. Springer, Vienna, 2008.

[49] Brian C Smith. *Fundamentals of Fourier transform infrared spectroscopy*. CRC press, 2011.

[50] Gwénaël Gouadec and Philippe Colomban. Raman spectroscopy of nanomaterials: How spectra relate to disorder, particle size and mechanical properties. *Progress in Crystal Growth and Characterization of Materials*, 53(1):1–56, 2007.

[51] Yasuhiro Shirasaki, Geoffrey J Supran, Moungi G Bawendi, and Vladimir Bulović. Emergence of colloidal quantum-dot light-emitting technologies.

Nature Photonics, 7(1):13–23, 2013.

[52] Timothy Jamieson, Raheleh Bakhshi, Daniela Petrova, Rachael Pocock, Mo Imani, and Alexander M Seifalian. Biological applications of quantum dots. *Biomaterials*, 28(31):4717–4732, 2007.

[53] Yasaman-Sadat Borghei and Saman Hosseinkhani. Semiconductor quantum dots in biomedical opportunities. *Journal of Luminescence*, page 118626, 2021.

[54] Elham Abbasi, Tayebeh Kafshdooz, Mohsen Bakhtiary, Nasrin Nikzamir, Nasim Nikzamir, Mohammad Nikzamir, Mozhdeh Mohammadian, and Abolfazl Akbarzadeh. Biomedical and biological applications of quantum dots. *Artificial Cells, Nanomedicine, and Biotechnology*, 44(3):885–891, 2016.

[55] Shangxin Lin and Xiaogang Peng. Current status and challenges of solar cells based on semiconductor nanocrystals. *Energy & Fuels*, 35(23):18928–18941, 2021.

[56] Prashant V Kamat. Quantum dot solar cells. semiconductor nanocrystals as light harvesters. *The Journal of Physical Chemistry C*, 112(48):18737–18753, 2008.

[57] Weiguang Chi and Sanjay K Banerjee. Development of perovskite solar cells by incorporating quantum dots. *Chemical Engineering Journal*, 426:131588, 2021.

[58] Rodney Maluleke and Oluwatobi S Oluwafemi. Synthetic approaches, modification strategies and the application of quantum dots in the sensing of priority pollutants. *Applied Sciences*, 11(24):11580, 2021.

[59] Lei Cui, Xiao-Peng He, and Guo-Rong Chen. Recent progress in quantum dot based sensors. *RSC Advances*, 5(34):26644–26653, 2015.

[60] Mohammad M Sabzehmeidani and Mahmood Kazemzad. Quantum dots based sensitive nanosensors for detection of antibiotics in natural products: A review. *Science of The Total Environment*, 810:151997, 2021.

[61] Wenshuo Zhang, Hongda Zhong, Pingping Zhao, Aiguo Shen, Houbin Li, and Xinghai Liu. Carbon quantum dot fluorescent probes for food safety detection: Progress, opportunities and challenges. *Food Control*, 133:108591, 2022.

[62] Chunyu Cheng, Qinghua Liang, Ming Yan, Zhifeng Liu, Qingyun He, Ting Wu, Songhao Luo, Yuan Pan, Chenhui Zhao, and Yang Liu. Advances in preparation, mechanism and applications of graphene quantum dots/semiconductor composite photocatalysts: A review. *Journal of Hazardous Materials*, 424:127721, 2022.

[63] Haiping Huang and Jun-Jie Zhu. The electrochemical applications of quantum dots. *Analyst*, 138(20):5855–5865, 2013.

[64] Bryan Kelleher, Michael Dillane, and Evgeny A Viktorov. Optical information processing using dual state quantum dot lasers: complexity through simplicity. *Light: Science & Applications*, 10(1):1–15, 2021.

[65] Peihao Huang. Dephasing of exchange-coupled spins in quantum dots for quantum computing. *Advanced Quantum Technologies*, 4(11):2100018, 2021.

[66] Garth A Jones and David S Bradshaw. Resonance energy transfer: from fundamental theory to recent applications. *Frontiers in Physics*, 7:100, 2019.

[67] Niko Hildebrandt, Christopher M Spillmann, W Russ Algar, Thomas Pons, Michael H Stewart, Eunkeu Oh, Kimihiro Susumu, Sebastian A Diaz, James B Delehanty, and Igor L Medintz. Energy transfer with semiconductor quantum

dot bioconjugates: a versatile platform for biosensing, energy harvesting, and other developing applications. *Chemical Reviews*, 117(2):536–711, 2017.

[68] Kenny F Chou and Allison M Dennis. Förster resonance energy transfer between quantum dot donors and quantum dot acceptors. *Sensors*, 15(6):13288–13325, 2015.

[69] John F Callan, Ray C Mulrooney, Sukanta Kamila, and Bridgeen McCaughan. Anion sensing with luminescent quantum dots–a modular approach based on the photoinduced electron transfer (pet) mechanism. *Journal of Fluorescence*, 18(2):527–532, 2008.

[70] Hanieh Montaseri, Oluwasesan Adegoke, and Patricia BC Forbes. Development of a thiol-capped core/shell quantum dot sensor for acetaminophen. *South African Journal of Chemistry*, 72:108–117, 2019.

[71] Hanieh Montaseri and Patricia BC Forbes. A triclosan turn-on fluorescence sensor based on thiol-capped core/shell quantum dots. *Spectrochimica Acta Part A: Molecular and Biomolecular Spectroscopy*, 204:370–379, 2018.

[72] Sifiso A Nsibande and Patricia BC Forbes. Development of a quantum dot molecularly imprinted polymer sensor for fluorescence detection of atrazine. *Luminescence*, 34(5):480–488, 2019.

[73] Suzanne Fery-Forgues and Dominique Lavabre. Are fluorescence quantum yields so tricky to measure? a demonstration using familiar stationery products. *Journal of Chemical Education*, 76(9):1260, 1999.

[74] Douglas Magde, Roger Wong, and Paul G Seybold. Fluorescence quantum yields and their relation to lifetimes of rhodamine 6g and fluorescein in nine solvents: Improved absolute standards for quantum yields. *Photochemistry and Photobiology*, 75(4):327–334, 2002.

[75] Hanieh Montaseri and Patricia BC Forbes. Molecularly imprinted polymer coated quantum dots for fluorescence sensing of acetaminophen. *Materials Today Communications*, 17:480–492, 2018.

[76] Xiaobo Nie, Ying Zhang, Xiaojuan Wang, Chunguang Ren, Shu-Qin Gao, and Ying-Wu Lin. Direct visualization of ligands exchange on the surfaces of quantum dots by a two-phase approach. *ChemistrySelect*, 3(8):2267–2271, 2018.

[77] Shaukatali N Inamdar, Pravin P Ingole, and Santosh K Haram. Determination of band structure parameters and the quasi-particle gap of cdse quantum dots by cyclic voltammetry. *ChemPhysChem*, 9(17):2574–2579, 2008.

[78] Vicky VT Doan-Nguyen, Patrick J Carroll, and Christopher B Murray. Structure determination and modeling of monoclinic trioctylphosphine oxide. *Acta Crystallographica Section C: Structural Chemistry*, 71(3):239–241, 2015.

[79] Minho Noh, Taehoon Kim, Hosub Lee, Chang-Koo Kim, Sang-Woo Joo, and Kangtaek Lee. Fluorescence quenching caused by aggregation of water-soluble cdse quantum dots. *Colloids and Surfaces A: Physicochemical and Engineering Aspects*, 359(1-3):39–44, 2010.

[80] Thermo Scientific. *Thermo Scientific crosslinking technical handbook*. Thermo Scientific, USA, 2012.

[81] Greg T Hermanson. Microparticles and nanoparticles. In *Bioconjugate techniques*, pages 549–587. Academic press, 2013.

[82] Yan Ji, Xiaoliang Yang, Zhi Ji, Linhui Zhu, Nana Ma, Dejun Chen, Xianbin Jia, Junming Tang, and Yilin Cao. Dft-calculated ir spectrum amide i, ii, and iii band contributions of n-methylacetamide fine components. *ACS Omega*, 5(15):8572–8578, 2020.

[83] Oluwasesan Adegoke and Patricia BC Forbes. L-cysteine-capped core/shell/shell quantum dot–graphene oxide nanocomposite fluorescence probe for polycyclic aromatic hydrocarbon detection. *Talanta*, 146:780–788, 2016.

[84] John Coates. Interpretation of infrared spectra, a practical approach. In R. A. Meyers, editor, *Encyclopedia of Analytical Chemistry*, pages 10815–10837. John Wiley & Sons, 200.

[85] Keith R Solomon, David B Baker, R Peter Richards, Kenneth R Dixon, Stephen J Klaine, Thomas W La Point, Ronald J Kendall, Carol P Weisskopf, Jeffrey M Giddings, John P Giesy, et al. Ecological risk assessment of atrazine in north american surface waters. *Environmental Toxicology and Chemistry: An International Journal*, 15(1):31–76, 1996.

[86] Simranjeet Singh, Vijay Kumar, Arun Chauhan, Shivika Datta, Abdul Basit Wani, Nasib Singh, and Joginder Singh. Toxicity, degradation and analysis of the herbicide atrazine. *Environmental Chemistry Letters*, 16(1):211–237, 2018.

[87] Louis H Du Preez, PJ Jansen Van Rensburg, AM Jooste, JA Carr, John P Giesy, Timothy S Gross, RJ Kendall, EE Smith, G Van Der Kraak, and Keith R Solomon. Seasonal exposures to triazine and other pesticides in surface waters in the western highveld corn-production region in south africa. *Environmental Pollution*, 135(1):131–141, 2005.

[88] Felicia P de Albuquerque, Jhones L de Oliveira, Viviane Moschini-Carlos, and Leonardo F Fraceto. An overview of the potential impacts of atrazine in aquatic environments: Perspectives for tailored solutions based on nanotechnology. *Science of The Total Environment*, 700:134868, 2020.

[89] Michelle Graymore, Frank Stagnitti, and Graeme Allinson. Impacts of atrazine in aquatic ecosystems. *Environment International*, 26(7-8):483–495, 2001.

[90] James M Dabrowski, Justinus M Shadung, and Victor Wepener. Prioritizing agricultural pesticides used in south africa based on their environmental mobility and potential human health effects. *Environment International*, 62:31–40, 2014.

[91] Renata M de Souza, Daiana Seibert, Heloise B Quesada, Fátima de Jesus Bassetti, Márcia R Fagundes-Klen, and Rosângela Bergamasco. Occurrence, impacts and general aspects of pesticides in surface water: a review. *Process Safety and Environmental Protection*, 135:22–37, 2020.

[92] Tyrone B Hayes, Lloyd L Anderson, Val R Beasley, Shane R De Solla, Taisen Iguchi, Holly Ingraham, Patrick Kestemont, Jasna Kniewald, Zlatko Kniewald, Valerie S Langlois, et al. Demasculinization and feminization of male gonads by atrazine: consistent effects across vertebrate classes. *The Journal of Steroid Biochemistry and Molecular Biology*, 127(1-2):64–73, 2011.

[93] Jacob A Cleary, Donald E Tillitt, Frederick S Vom Saal, Diane K Nicks, Rachel A Claunch, and Ramji K Bhandari. Atrazine induced transgenerational reproductive effects in medaka (oryzias latipes). *Environmental Pollution*, 251:639–650, 2019.

[94] Margaux McBirney, Stephanie E King, Michelle Pappalardo, Elizabeth Houser, Margaret Unkefer, Eric Nilsson, Ingrid Sadler-Riggleman, Daniel Beck, Paul Winchester, and Michael K Skinner. Atrazine induced epigenetic transgenerational inheritance of disease, lean phenotype and sperm epimutation pathology biomarkers. *PLOS One*, 12(9):e0184306, 2017.

[95] Devin A Bowes and Rolf U Halden. Breast cancer and dietary intake of endocrine disruptors: a review of recent literature. *Current Pathobiology Reports*, 7(3):41–46, 2019.

[96] Paolo Boffetta, Hans-Olov Adami, Colin Berry, and Jack S Mandel. Atrazine and cancer: a review of the epidemiologic evidence. *European Journal of Cancer Prevention*, 22(2):169–180, 2013.

[97] Adriana C Bejarano and G Thomas Chandler. Reproductive and developmental effects of atrazine on the estuarine meiobenthic copepod amphiascus tenuiremis. *Environmental Toxicology and Chemistry: An International Journal*, 22(12):3009–3016, 2003.

[98] Frank Ackerman. The economics of atrazine. *International Journal of Occupational and Environmental Health*, 13(4):437–445, 2007.

[99] M Machete and JM Shadung. Detection of selected agricultural pesticides in river and tap water in letsitele, lomati and vals–renoster catchments, south africa. *Water SA*, 45(4):716–720, 2019.

[100] Arthur Ashkin. Acceleration and trapping of particles by radiation pressure. *Physical Review Letters*, 24(4):156, 1970.

[101] Matthew C Asplund, Jeremy A Johnson, and James E Patterson. The 2018 Nobel Prize in physics: optical tweezers and chirped pulse amplification. *Analytical and Bioanalytical Chemistry*, 411(20):5001–5005, 2019.

[102] Keir C Neuman and Steven M Block. Optical trapping. *Review of Scientific Instruments*, 75(9):2787–2809, 2004.

[103] Nunzia Malagnino, Giuseppe Pesce, Antonio Sasso, and Ennio Arimondo. Measurements of trapping efficiency and stiffness in optical tweezers. *Optics Communications*, 214(1-6):15–24, 2002.

166

[104] Arthur Ashkin. Forces of a single-beam gradient laser trap on a dielectric sphere in the ray optics regime. *Biophysical Journal*, 61(2):569–582, 1992.

[105] Paul Bartlett and Stuart Henderson. Three-dimensional force calibration of a single-beam optical gradient trap. *Journal of Physics: Condensed Matter*, 14(33):7757, 2002.

[106] Yasuhiro Harada and Toshimitsu Asakura. Radiation forces on a dielectric sphere in the rayleigh scattering regime. *Optics Communications*, 124(5-6):529–541, 1996.

[107] Kuan F Ren, Gérard Gréhan, and Gérard Gouesbet. Prediction of reverse radiation pressure by generalized lorenz–mie theory. *Applied Optics*, 35(15):2702–2710, 1996.

[108] Gérard Gouesbet, Bruno Maheu, and Gérard Gréhan. Light scattering from a sphere arbitrarily located in a gaussian beam, using a bromwich formulation. *JOSA A*, 5(9):1427–1443, 1988.

[109] Paolo Polimeno, Alessandro Magazzu, Maria A Iati, Francesco Patti, Rosalba Saija, Cristian D E Boschi, Maria G Donato, Pietro G Gucciardi, Philip H Jones, Giovanni Volpe, et al. Optical tweezers and their applications. *Journal of Quantitative Spectroscopy and Radiative Transfer*, 218:131–150, 2018.

[110] Ferdinando Borghese, Paolo Denti, Rosalba Saija, and Maria A Iati. Optical trapping of nonspherical particles in the T-matrix formalism. *Optics Express*, 15(19):11984–11998, 2007.

[111] Gerard Gouesbet. T-matrix formulation and generalized Lorenz–Mie theories in spherical coordinates. *Optics Communications*, 283(4):517–521, 2010.

[112] Timo A Nieminen, Vincent LY Loke, Alexander B Stilgoe, Gregor Knöner, Agata M Brańczyk, Norman R Heckenberg, and Halina Rubinsztein-Dunlop.

Optical tweezers computational toolbox. *Journal of Optics A: Pure and Applied Optics*, 9(8):S196, 2007.

[113] Jan Gieseler, Juan R Gomez-Solano, Alessandro Magazzù, Isaac Pérez Castillo, Laura Pérez García, Marta Gironella-Torrent, Xavier Viader-Godoy, Felix Ritort, Giuseppe Pesce, Alejandro V Arzola, Karen Volke-Sepúlveda, and Giovanni Volpe. Optical tweezers — from calibration to applications: a tutorial. *Advances in Optics and Photonics*, 13(1):74–241, 2021.

[114] Nan Li, Xun-min Zhu, Wen-qiang Li, Zhen-hai Fu, Meng-zhu Hu, and Hui-zhu Hu. Review of optical tweezers in vacuum. *Frontiers of Information Technology & Electronic Engineering*, 20(5):655–673, 2019.

[115] Guoteng Ma, Chunguang Hu, Shuai Li, Xiaoqin Gao, Hongbin Li, and Xiaotang Hu. Simultaneous, hybrid single-molecule method by optical tweezers and fluorescence. *Nanotechnology and Precision Engineering*, 2(4):145–156, 2019.

[116] Onofrio M Maragò, Philip H Jones, Pietro G Gucciardi, Giovanni Volpe, and Andrea C Ferrari. Optical trapping and manipulation of nanostructures. *Nature Nanotechnology*, 8(11):807–819, 2013.

[117] Michelle D Wang, Hong Yin, Robert Landick, Jeff Gelles, and Steven M Block. Stretching DNA with optical tweezers. *Biophysical Journal*, 72(3):1335–1346, 1997.

[118] Michael T Woodside, Peter C Anthony, William M Behnke-Parks, Kevan Larizadeh, Daniel Herschlag, and Steven M Block. Direct measurement of the full, sequence-dependent folding landscape of a nucleic acid. *Science*, 314(5801):1001–1004, 2006.

[119] Jeffrey T Finer, Robert M Simmons, and James A Spudich. Single myosin molecule mechanics: piconewton forces and nanometre steps. *Nature*, 368(6467):113–119, 1994.

[120] Dhawal Choudhary, Alessandro Mossa, Milind Jadhav, and Ciro Cecconi. Bio-molecular applications of recent developments in optical tweezers. *Biomolecules*, 9(1):23, 2019.

[121] Ashok A Deniz, Samrat Mukhopadhyay, and Edward A Lemke. Single-molecule biophysics: at the interface of biology, physics and chemistry. *Journal of the Royal Society Interface*, 5(18):15–45, 2008.

[122] David G Grier and Yael Roichman. Holographic optical trapping. *Applied Optics*, 45(5):880–887, 2006.

[123] Abhay Kotnala, Yi Zheng, Jianping Fu, and Wei Cheng. Microfluidic-based high-throughput optical trapping of nanoparticles. *Lab on a Chip*, 17(12):2125–2134, 2017.

[124] Maryam Hashemi Shabestari, Anna EC Meijering, Wouter H Roos, Gijs JL Wuite, and Erwin JG Peterman. Recent advances in biological single-molecule applications of optical tweezers and fluorescence microscopy. *Methods in Enzymology*, 582:85–119, 2017.

[125] Spas Nedev, Alexander S Urban, Andrey A Lutich, and Jochen Feldmann. Optical force stamping lithography. *Nano Letters*, 11(11):5066–5070, 2011.

[126] Mohd FM Yusof, Shahrul K Ayop, Faridah L Supian, and Yusnita Juahir. Optical trapping of organic solvents in the form of microdroplets in water. *Chemical Physics Letters*, 749:137407, 2020.

[127] Ivan D Rukhlenko, Nikita V Tepliakov, Anvar S Baimuratov, Semen A Andronaki, Yurii K Gun'ko, Alexander V Baranov, and Anatoly V Fedorov.

Completely chiral optical force for enantioseparation. *Scientific Reports*, 6(1):1–8, 2016.

[128] Georgiy Tkachenko and Etienne Brasselet. Helicity-dependent three-dimensional optical trapping of chiral microparticles. *Nature Communications*, 5(1):1–8, 2014.

[129] Alexander Rohrbach. Stiffness of optical traps: quantitative agreement between experiment and electromagnetic theory. *Physical Review Letters*, 95(16):168102, 2005.

[130] Rafael S Dutra, NB Viana, Paulo A Maia Neto, and Herch M Nussenzveig. Absolute calibration of forces in optical tweezers. *Physical Review A*, 90(1):013825, 2014.

[131] Giuseppe Pesce, Philip H Jones, Onofrio M Maragò, and Giovanni Volpe. Optical tweezers: theory and practice. *The European Physical Journal Plus*, 135(12):1–38, 2020.

[132] Mohammad Sarshar, Winson Wong, and Bahman Anvari. Comparative study of methods to calibrate the stiffness of a single-beam gradient-force optical tweezers over various laser trapping powers. *Journal of Biomedical Optics*, 19(11):115001, 2014.

[133] Meindert A van Dijk, Lukas C Kapitein, Joost van Mameren, Christoph F Schmidt, and Erwin JG Peterman. Combining optical trapping and single-molecule fluorescence spectroscopy: enhanced photobleaching of fluorophores. *The Journal of Physical Chemistry B*, 108(20):6479–6484, 2004.

[134] Alberto Diaspro, Giuseppe Chirico, Cesare Usai, Paola Ramoino, and Jurek Dobrucki. Photobleaching. In *Handbook of Biological Confocal Microscopy*, pages 690–702. Springer, 2006.

[135] Loling Song, EJ Hennink, I Ted Young, and Hans J Tanke. Photobleaching kinetics of fluorescein in quantitative fluorescence microscopy. *Biophysical journal*, 68(6):2588–2600, 1995.

[136] Mikhail Y Berezin and Samuel Achilefu. Fluorescence lifetime measurements and biological imaging. *Chemical reviews*, 110(5):2641–2684, 2010.

[137] Akihiko Ishijima, Hiroaki Kojima, Takashi Funatsu, Makio Tokunaga, Hideo Higuchi, Hiroto Tanaka, and Toshio Yanagida. Simultaneous observation of individual ATPase and mechanical events by a single myosin molecule during interaction with actin. *Cell*, 92(2):161–171, 1998.

[138] Matthew J Lang, Polly M Fordyce, and Steven M Block. Combined optical trapping and single-molecule fluorescence. *Journal of Biology*, 2(1):1–4, 2003.

[139] Ricardo R Brau, Peter B Tarsa, Jorge M Ferrer, Peter Lee, and Matthew J Lang. Interlaced optical force-fluorescence measurements for single molecule biophysics. *Biophysical Journal*, 91(3):1069–1077, 2006.

[140] Liselotte Jauffred and Lene B Oddershede. Two-photon quantum dot excitation during optical trapping. *Nano Letters*, 10(5):1927–1930, 2010.

[141] Cheng-Yu Li, Di Cao, Ya-Feng Kang, Yi Lin, Ran Cui, Dai-Wen Pang, and Hong-Wu Tang. Fluorescence detection of H5N1 virus gene sequences based on optical tweezers with two-photon excitation using a single near infrared nanosecond pulse laser. *Analytical Chemistry*, 88(8):4432–4439, 2016.

[142] Héctor Rodríguez-Rodríguez, María Acebrón, Francisco J Iborra, Ricardo J Arias-Gonzalez, and Beatriz H Juárez. Photoluminescence activation of organic dyes via optically trapped quantum dots. *ACS Nano*, 13(6):7223–7230, 2019.

[143] Lingyun Pan, Atsushi Ishikawa, and Naoto Tamai. Detection of optical trapping of CdTe quantum dots by two-photon-induced luminescence. *Physical Review B*, 75(16):161305, 2007.

[144] Wei-Yi Chiang, Tomoki Okuhata, Anwar Usman, Naoto Tamai, and Hiroshi Masuhara. Efficient optical trapping of CdTe quantum dots by femtosecond laser pulses. *The Journal of Physical Chemistry B*, 118(49):14010–14016, 2014.

[145] Héctor Rodríguez-Rodríguez, María Acebrón, Beatriz H Juárez, and Ricardo J Arias-Gonzalez. Luminescence dynamics of silica-encapsulated quantum dots during optical trapping. *The Journal of Physical Chemistry C*, 121(18):10124–10130, 2017.

[146] Liselotte Jauffred, Andrew C Richardson, and Lene B Oddershede. Three-dimensional optical control of individual quantum dots. *Nano Letters*, 8(10):3376–3380, 2008.

[147] Cheng-Yu Li, Di Cao, Chu-Bo Qi, Hong-Lei Chen, Ya-Tao Wan, Yi Lin, Zhi-Ling Zhang, Dai-Wen Pang, and Hong-Wu Tang. One-step separation-free detection of carcinoembryonic antigen in whole serum: Combination of two-photon excitation fluorescence and optical trapping. *Biosensors and Bioelectronics*, 90:146–152, 2017.

[148] Héctor Rodríguez-Rodríguez, Sara de Lorenzo, Leonor de la Cueva, Gorka Salas, and Ricardo J Arias-Gonzalez. Optical trapping of single nanostructures in a weakly focused beam. application to magnetic nanoparticles. *The Journal of Physical Chemistry C*, 122(31):18094–18101, 2018.

[149] Di Cao, Cheng-Yu Li, Ya-Feng Kang, Yi Lin, Ran Cui, Dai-Wen Pang, and Hong-Wu Tang. Dual-component gene detection for H7N9 virus – the com-

bination of optical trapping and bead-based fluorescence assay. *Biosensors and Bioelectronics*, 86:1031–1037, 2016.

[150] Di Cao, Cheng-Yu Li, Chu-Bo Qi, Hong-Lei Chen, Dai-Wen Pang, and Hong-Wu Tang. Multiple optical trapping assisted bead-array based fluorescence assay of free and total prostate-specific antigen in serum. *Sensors and Actuators B: Chemical*, 269:143–150, 2018.

[151] Matthew J Lang, Polly M Fordyce, Anita M Engh, Keir C Neuman, and Steven M Block. Simultaneous, coincident optical trapping and single-molecule fluorescence. *Nature Methods*, 1(2):133–139, 2004.

[152] Fred M Dickey and Todd E Lizotte. *Laser beam shaping applications*, volume 1. CRC Press, 2017.

[153] Shugo Matsusaka, Yuichi Kozawa, and Shunichi Sato. Micro-hole drilling by tightly focused vector beams. *Optics Letters*, 43(7):1542–1545, 2018.

[154] Jason Geng. Structured-light 3d surface imaging: a tutorial. *Advances in Optics and Photonics*, 3(2):128–160, 2011.

[155] Alan E Willner, Hao Huang, Yan Yan, Yongxiong Ren, Nisar Ahmed, Goudong Xie, Changjing Bao, L Li, Y Cao, Z Zhao, et al. Optical communications using orbital angular momentum beams. *Advances in Optics and Photonics*, 7(1):66–106, 2015.

[156] Susumu Segawa, Yuichi Kozawa, and Shunichi Sato. Resolution enhancement of confocal microscopy by subtraction method with vector beams. *Optics Letters*, 39(11):3118–3121, 2014.

[157] Peter Török and Peter RT Munro. The use of gauss-laguerre vector beams in sted microscopy. *Optics Express*, 12(15):3605–3617, 2004.

[158] Carmelo Rosales-Guzmán, Nathaniel Hermosa, Aniceto Belmonte, and Juan P Torres. Experimental detection of transverse particle movement with structured light. *Scientific Reports*, 3(1):1–5, 2013.

[159] Andrew Forbes. Structured light from lasers. *Laser & Photonics Reviews*, 13(11):1900140, 2019.

[160] Adoph W Lohmann and DP Paris. Binary fraunhofer holograms, generated by computer. *Applied Optics*, 6(10):1739–1748, 1967.

[161] Grigory Lazarev, Po-Ju Chen, Johannes Strauss, Nicolas Fontaine, and Andrew Forbes. Beyond the display: phase-only liquid crystal on silicon devices and their applications in photonics. *Optics Express*, 27(11):16206–16249, 2019.

[162] Yu-Xuan Ren, Rong-De Lu, and Lei Gong. Tailoring light with a digital micromirror device. *Annalen der Physik*, 527(7-8):447–470, 2015.

[163] Sergey Turtaev, Ivo T Leite, Kevin J Mitchell, Miles J Padgett, David B Phillips, and Tomáš Čižmár. Comparison of nematic liquid-crystal and dmd based spatial light modulation in complex photonics. *Optics Express*, 25(24):29874–29884, 2017.

[164] Carmelo Rosales-Guzmán and Andrew Forbes. *How to shape light with spatial light modulators*. SPIE Press, 2017.

[165] Andrew Forbes, Angela Dudley, and Melanie McLaren. Creation and detection of optical modes with spatial light modulators. *Advances in Optics and Photonics*, 8(2):200–227, 2016.

[166] Joseph P Kirk and Alan L Jones. Phase-only complex-valued spatial filter. *JOSA*, 61(8):1023–1028, 1971.

[167] Victor Arrizón. Complex modulation with a twisted-nematic liquid-crystal spatial light modulator: double-pixel approach. *Optics Letters*, 28(15):1359–1361, 2003.

[168] Victor Arrizón. Optimum on-axis computer-generated hologram encoded into low-resolution phase-modul ation devices. *Optics Letters*, 28(24):2521–2523, 2003.

[169] Victor Arrizón, Guadalupe Méndez, and David Sánchez-de La-Llave. Accurate encoding of arbitrary complex fields with amplitude-only liquid crystal spatial light modulators. *Optics Express*, 13(20):7913–7927, 2005.

[170] Eliot Bolduc, Nicolas Bent, Enrico Santamato, Ebrahim Karimi, and Robert W Boyd. Exact solution to simultaneous intensity and phase encryption with a single phase-only hologram. *Optics Letters*, 38(18):3546–3549, 2013.

[171] Victor Arrizón, Ulises Ruiz, Rosibel Carrada, and Luis A González. Pixelated phase computer holograms for the accurate encoding of scalar complex fields. *JOSA A*, 24(11):3500–3507, 2007.

[172] Carmelo Rosales-Guzmán, Nkosiphile Bhebhe, Nyiku Mahonisi, and Andrew Forbes. Multiplexing 200 spatial modes with a single hologram. *Journal of Optics*, 19(11):113501, 2017.

[173] Gordon D Love. Wave-front correction and production of zernike modes with a liquid-crystal spatial light modulator. *Applied Optics*, 36(7):1517–1524, 1997.

[174] Larry C Andrews and Ronald L Phillips. *Laser beam propagation through random media*. SPIE Press, 2 edition, 2005.

[175] Andrew Forbes. *Laser beam propagation: generation and propagation of customized light*. CRC Press, 2014.

[176] Miguel A Bandres and Julio C Gutiérrez-Vega. Ince–gaussian beams. *Optics Letters*, 29(2):144–146, 2004.

[177] Franco Gori, Giorgio Guattari, and C Padovani. Bessel-gauss beams. *Optics Communications*, 64(6):491–495, 1987.

[178] Michael V Berry and Nandor L Balazs. Nonspreading wave packets. *American Journal of Physics*, 47(3):264–267, 1979.

[179] Eric R Dufresne, Gabriel C Spalding, Matthew T Dearing, Steven A Sheets, and David G Grier. Computer-generated holographic optical tweezer arrays. *Review of Scientific Instruments*, 72(3):1810–1816, 2001.

[180] Stephen C Chapin, Vincent Germain, and Eric R Dufresne. Automated trapping, assembly, and sorting with holographic optical tweezers. *Optics Express*, 14(26):13095–13100, 2006.

[181] V Garcés-Chávez, David McGloin, H Melville, Wilson Sibbett, and Kishan Dholakia. Simultaneous micromanipulation in multiple planes using a self-reconstructing light beam. *Nature*, 419(6903):145–147, 2002.

[182] C Alpmann, Richard Bowman, M Woerdemann, Miles Padgett, and Cornelia Denz. Mathieu beams as versatile light moulds for 3d micro particle assemblies. *Optics Express*, 18(25):26084–26091, 2010.

[183] Jörg Baumgartl, Michael Mazilu, and Kishan Dholakia. Optically mediated particle clearing using airy wavepackets. *Nature Photonics*, 2(11):675–678, 2008.

[184] Marlies EJ Friese, Timo A Nieminen, Norman R Heckenberg, and Halina Rubinsztein-Dunlop. Optical alignment and spinning of laser-trapped microscopic particles. *Nature*, 394(6691):348–350, 1998.

[185] V Garcés-Chávez, David McGloin, Miles J Padgett, W Dultz, H Schmitzer, and Kishan Dholakia. Observation of the transfer of the local angular momentum density of a multiringed light beam to an optically trapped particle. *Physical Review Letters*, 91(9):093602, 2003.

[186] Miles Padgett and Richard Bowman. Tweezers with a twist. *Nature Photonics*, 5(6):343–348, 2011.

[187] Carmelo Rosales-Guzmán, Bienvenu Ndagano, and Andrew Forbes. A review of complex vector light fields and their applications. *Journal of Optics*, 20(12):123001, 2018.

[188] Susanne Quabis, Ralf Dorn, M Eberler, O Glöckl, and Gerd Leuchs. Focusing light to a tighter spot. *Optics Communications*, 179(1-6):1–7, 2000.

[189] Eileen Otte, Kemal Tekce, and Cornelia Denz. Tailored intensity landscapes by tight focusing of singular vector beams. *Optics Express*, 25(17):20194–20201, 2017.

[190] Hassan Moradi, Vahid Shahabadi, Ebrahim Madadi, Ebrahim Karimi, and Faegheh Hajizadeh. Efficient optical trapping with cylindrical vector beams. *Optics Express*, 27(5):7266–7276, 2019.

[191] Masaki Michihata, Terutake Hayashi, and Yasuhiro Takaya. Measurement of axial and transverse trapping stiffness of optical tweezers in air using a radially polarized beam. *Applied Optics*, 48(32):6143–6151, 2009.

[192] Vladlen Shvedov, Arthur R Davoyan, Cyril Hnatovsky, Nader Engheta, and Wieslaw Krolikowski. A long-range polarization-controlled optical tractor

beam. *Nature Photonics*, 8(11):846–850, 2014.

[193] Z Zhang and JN Milstein. Extending the photobleaching lifetime in the presence of an optical tweezers by wavefront engineering. *Journal of Optics*, 22(9):095301, 2020.

[194] Halil T Eyyuboğlu, Çağlar Arpali, and Yahya Baykal. Flat topped beams and their characteristics in turbulent media. *Optics Express*, 14(10):4196–4207, 2006.

[195] Marco G Tarallo, John Miller, J Agresti, E D'Ambrosio, R DeSalvo, D Forest, B Lagrange, JM Mackowsky, Ch Michel, JL Montorio, et al. Generation of a flat-top laser beam for gravitational wave detectors by means of a nonspherical fabry-perot resonator. *Applied Optics*, 46(26):6648–6654, 2007.

[196] Yajun Li. Light beams with flat-topped profiles. *Optics Letters*, 27(12):1007–1009, 2002.

[197] Lucio Buratto and Elisabetta Böhm. The use of the femtosecond laser in penetrating keratoplasty. *American Journal of Ophthalmology*, 143(5):737–742, 2007.

[198] Igor A Litvin and Andrew Forbes. Intra–cavity flat–top beam generation. *Optics Express*, 17(18):15891–15903, 2009.

[199] Haotong Ma, Zejin Liu, Pu Zhou, Xiaolin Wang, Yanxing Ma, and Xiaojun Xu. Generation of flat-top beam with phase-only liquid crystal spatial light modulators. *Journal of Optics*, 12(4):045704, 2010.

[200] Zhangrong Mei, Daomu Zhao, and Juguan Gu. Comparison of two approximate methods for hard-edged diffracted flat-topped light beams. *Optics Communications*, 267(1):58–64, 2006.

[201] XiangYu Ding, YuXuan Ren, and RongDe Lu. Shaping super-gaussian beam through digital micro-mirror device. *Science China Physics, Mechanics & Astronomy*, 58(3):1–6, 2015.

[202] Darryl Naidoo, A Harfouche, Michael Fromager, Kamel Ait-Ameur, and Andrew Forbes. Emission of a propagation invariant flat-top beam from a microchip laser. *Journal of Luminescence*, 170:750–754, 2016.

[203] Franco Gori. Flattened gaussian beams. *Optics Communications*, 107(5-6):335–341, 1994.

[204] David L Shealy and John A Hoffnagle. Laser beam shaping profiles and propagation. *Applied Optics*, 45(21):5118–5131, 2006.

[205] Sandro De Silvestri, Paolo Laporta, Vittorio Magni, and Orazio Svelto. Solid-state laser unstable resonators with tapered reflectivity mirrors: the super-gaussian approach. *IEEE Journal of Quantum Electronics*, 24(6):1172–1177, 1988.

[206] Massimo Santarsiero and Riccardo Borghi. Correspondence between super-gaussian and flattened gaussian beams. *JOSA A*, 16(1):188–190, 1999.

[207] Wei Han, Wen Cheng, and Qiwen Zhan. Flattop focusing with full poincaré beams under low numerical aperture illumination. *Optics Letters*, 36(9):1605–1607, 2011.

[208] Nkosi Bhebhe, Carmelo Rosales-Guzman, and Andrew Forbes. Classical and quantum analysis of propagation invariant vector flat-top beams. *Applied Optics*, 57(19):5451–5458, 2018.

Appendix A

Synthesis optimization

The details of the QD and QD-tagged bead syntheses, as described in Chapter 2, are reported in this appendix. The synthesis of L-cysteine capped CdSe/ZnS QDs was optimized after four batches. The details of the reaction conditions, fluorescence emission, problems and improvements of each batch are summarized in Table A.1.

The QD-tagged bead synthesis method was optimized after five attempts. Table A.2 compares the reaction conditions and results of these attempts. As discussed in Section 2.3, Figures A.1 to A.3 show TEM images of the QD-tagged beads at various stages in the optimizing process.

Table A.1: Reaction conditions and properties of batches 1 to 4 of synthesized L-cysteine capped CdSe/ZnS QDs.

	Batch 1	Batch 2	Batch 3	Batch 4
	Reaction conditions			
Precursor mixing	Overnight at room temperature (warm day)	Overnight at room temperature (cold day)	5 h at 40 °C	5 h at 40 °C
Volume of Se-precursor added (ml)	20	20	25	25
Core growth (min)	15	30	15	15
Volume of core extracted for analysis (ml)	30	20	30	30
Extra aliquots of shell precursor added	2	None	None	None

Table A.1 – continue

	Batch 1	Batch 2	Batch 3	Batch 4
Shell growth time (min)	75 (before addition of extra shell aliquots)	60	40	40
Purify hydrophobic core/shell QDs	No	No	Yes	Yes
Mass of L-cysteine used (g)	2	2	2	3
Functionalized some CdSe core QDs with L-cysteine	No	Yes	Yes	Yes

	Batch 1	Batch 2	Batch 3	Batch 4
Purification solvents	acetone (×2) chloroform (×2) chloroform: acetone:water (1:2:1) (×2) acetone (×1)	acetone chloroform chloroform: acetone:water (1:2:1) methanol and ethanol (multiple repetitions)	ethanol (×4) acetone (×2)	ethanol (×4) acetone (×2)
Fluorescence emission peak maxima (nm)				
CdSe core	570	565	595	574
CdSe/ZnS core/shell	588	571	609	584
L-cysteine capped CdSe core	-	567	592	-
L-cysteine capped CdSe/ZnS core/shell	621	595	620	602
Physical properties of the final L-cysteine capped CdSe/ZnS QDs				

Table A.1 – continue

	Batch 1	Batch 2	Batch 3	Batch 4
Large agglomerations present	Yes	No	No	No
Monodispersed	Yes (with agglomerations)	Relative (even after repeated rigorous purification still impurities present)	Yes	Yes
Fluorescence emission properties of the final L-cysteine capped CdSe/ZnS QDs				
Narrow symmetrical peak	Yes	No (unsymmetrical)	Yes	Yes
Peak $\geq$ 595 nm	Yes	Yes	Yes	Yes
FWHM (nm)	35	46	46	44
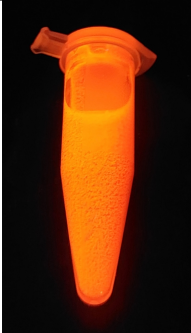
	Batch 1	Batch 2	Batch 3	Batch 4
Appearance under UV-light				
Intensity	Good	Good	After purification the intensity diminished but recovered when dispersed in water.	After purification the intensity diminished but recovered when dispersed in water.
Conclusion				
Successfully synthesized water-soluble QDs	Yes	Yes	Yes	Yes

185

	Batch 1	Batch 2	Batch 3	Batch 4
Problem with batch	Large agglomerates present	Unsymmetrical fluorescence emission peak	Fluorescence intensity quenching	Method reproducibility highly dependent on the nucleation temperature
Possible reason for the problem	Extra aliquots of shell precursor added	Impurities in the sample	QD agglomerates formed after purification	Nucleation temperature must be more controlled for future syntheses
Improvement to method	-	Did not add extra aliquots of shell	Purified hydrophobic core/shell QDs	Repeated exactly as batch 3 to test reproducibility

Table A.2: Reaction conditions and properties of attempts 1 to 5 of synthesized QD-tagged beads.

	Attempt 1	Attempt 2	Attempt 3	Attempt 4	Attempt 5
Reaction conditions					
Reaction temperature	Room temperature	Ice bath	Ice bath	Ice bath	Ice bath/ room temperature when in sonicator
Stirring time for carboxyl activation (min)	30	30	35	30	30
Remove excess EDC before adding QDs	No	No	Yes (NHS was added after removal of excess EDC)	Yes (NHS was added before removal of excess EDC)	Yes (NHS was added before removal of excess EDC)
Mixing method	Stirring	Stirring	Stirring	Stirring	Ultra-sonication
Batch of QDs used	1	1	3	3	4

Table A.2 – continue

	Attempt 1	Attempt 2	Attempt 3	Attempt 4	Attempt 5
Mixing time for conjugation reaction (h)	24	24	16	16	3
Number of replicates for each attempt	1	1	1	5 (increasing amount of QD added)	1
Solvent used for purification	Acetone	Water	Water	Water	Water
Storage condition of QD-tagged bead product	Dried powder at room temperature	In solution (water) in the fridge	In solution (water) in the fridge	In solution (water) in the fridge	In solution (water) in the fridge
Quantities					
Beads (μl)	200	200	100	100	50
Volume 0.1 M EDC (ml)	5	5	5	5	2.5

	Attempt 1	**Attempt 2**	**Attempt 3**	**Attempt 4**	**Attempt 5**
Volume 0.1 M NHS (ml)	5	5	5	5	2.5
QDs (mg)	20	20	6	5-20	3
Conclusions					
Successful coupling	No	Yes	Yes	Yes	Yes
Problem with attempt	No intact bead was observed	Large QD agglomerations formed	The beads were coated with too little QDs, coating was not uniform.	Increasing the amount of QDs added did not increase the amount coupled to the surface of the beads.	Excess unreacted QDs

Table A.2 – continue

	Attempt 1	Attempt 2	Attempt 3	Attempt 4	Attempt 5
Possible reason for the problem	Acetone dissolved the polymer beads.	Excess EDC activated carboxylic groups on QDs which then reacted with themselves.	The unstable O-acylisourea intermediate was purified with water which could have made the reaction less efficient.	Water-soluble QDs that tend to clump together prevented uniform coating.	Sonication causes more QDs to react thus less QDs are necessary.
Improvement to method	-	Only used water for purification; store product in water and use an ice bath for the reaction.	Removed excess EDC before adding QDs.	Added NHS before removing access EDC and add more QDs.	Used ultra-sonication.
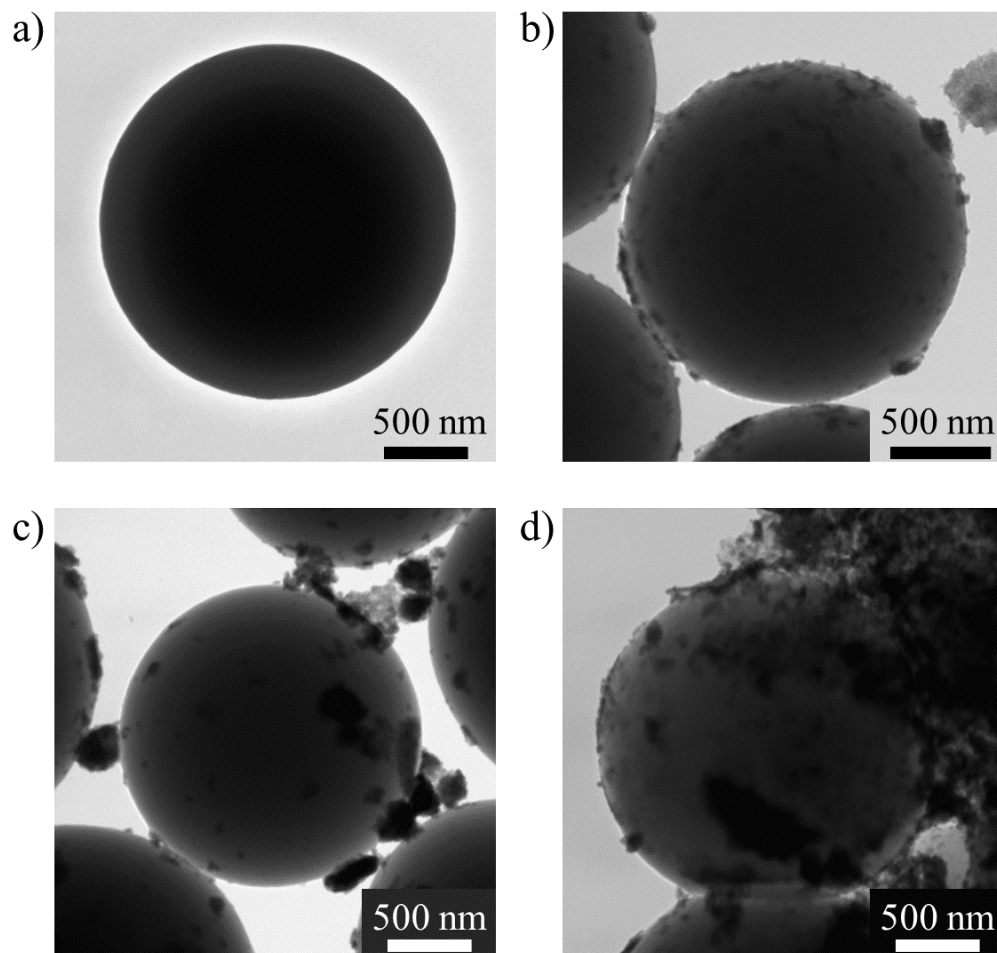
Figure A.1: TEM images showing the inconsistency of the QD coating within a sample of the QD-tagged beads (attempt 4). In a single batch, beads were imaged that were coated with a) no QDs, b) some QDs, c) small QD agglomerates and d) with large amount of QDs.
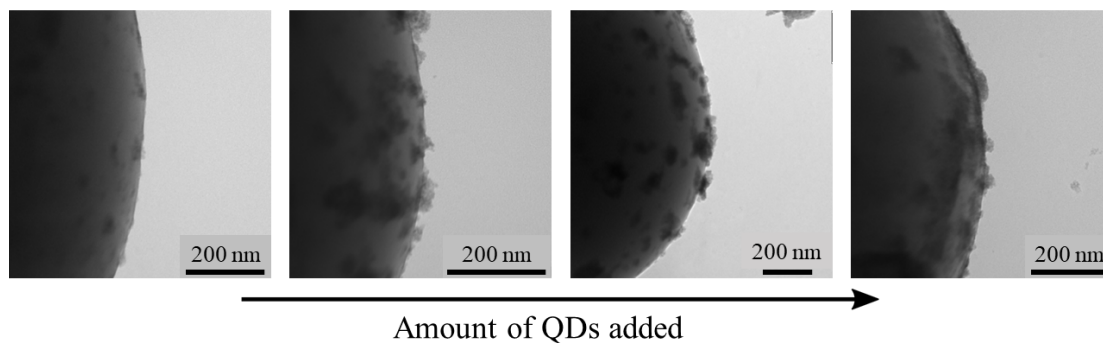
Amount of QDs added

Figure A.2: TEM images of the surface of QD-tagged beads (of attempt 4) where increasing amounts of 5 mg, 10 mg, 15 mg and 20 mg of QDs were added for each replicate synthesis. The increase in QDs did not significantly increase the amount of QDs on the bead surface. The consistency of the QD coating also did not improve.
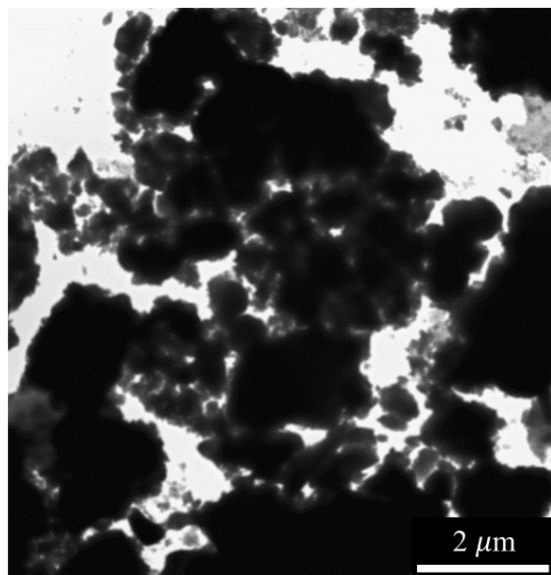
Figure A.3: Appearance of the QD-tagged beads from attempt 1. No intact bead was observed since the acetone used to purify the product dissolved and deformed the polystyrene beads.

Appendix B

SLM calibration

This appendix discusses the SLM calibration process used in the experimental setup. Calibration of the SLM is necessary since the phase modulation imparted to a beam by the SLM is dependent on the wavelength of the laser light. It is therefore necessary to ensure that a linear phase ramp from 0 to 2π (higher also possible) is obtained when changing the grey levels of the hologram from 0 (black) to 255 (white).

The first step in calibrating the SLM was to determine the phase change of the beam over the 256 grey levels. This was done by interfering two beams that were reflected from the SLM, where the one beam stayed unmodulated while the other beam was modulated over all the grey levels which caused a shift in the interference pattern. The setup used for SLM calibration is given in Figure B.1.

An expanded beam was sent through a double pinhole mask to create two beams of equal size. These beams were directed to the SLM screen where they were incident on separate halves of the screen. Thus, the phase modulation imparted to each beam was controlled by changing the grey scale value displayed on each half of the SLM. The two beams interfered at the focus of lens L3, while the objective was used to enlarge the interference pattern. Example holograms displayed on the SLM with the corresponding shift in the interference pattern (after calibration) are shown as insets. The line drawn on the interference patterns helps to visualise the shift in the pattern as the grey levels were changed. First both halves of the SLM
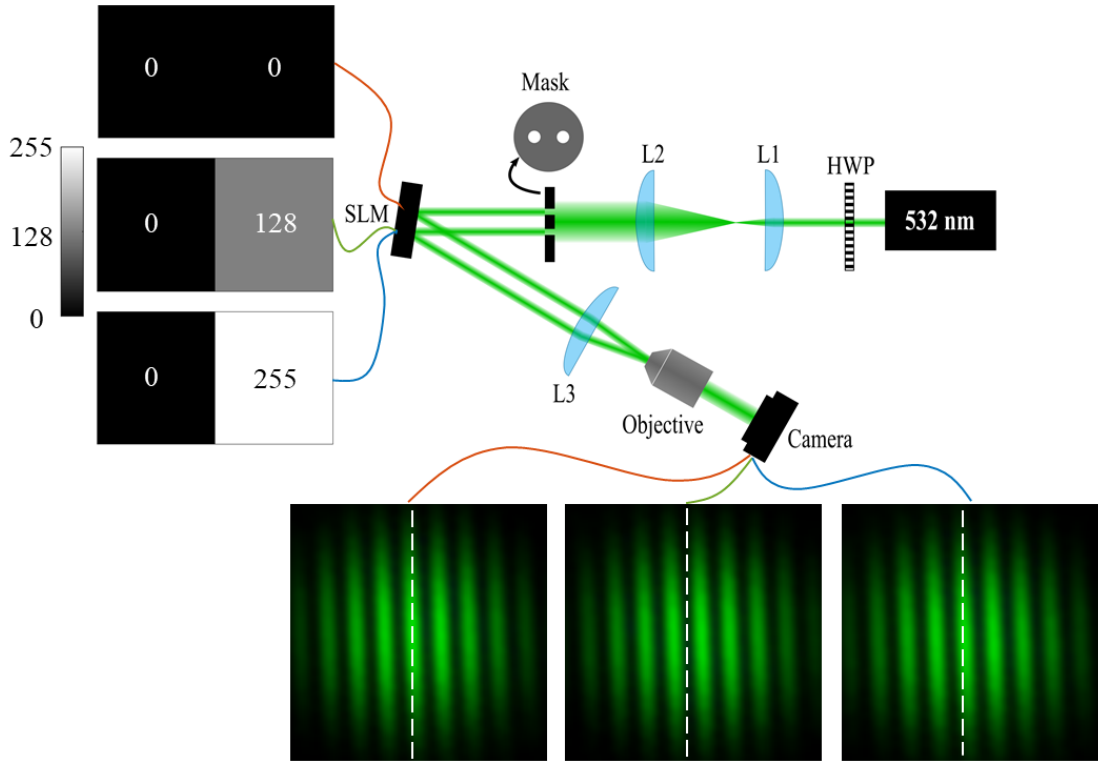
Figure B.1: Schematic of the the experimental SLM calibration setup.

screen were black (grey level = 0) which imparted no relative phase shift to the beams. When the one half was changed to grey level 128, which corresponds to a phase shift of π, the maximum marked by the white line changed to a minimum. In the last hologram one half of the SLM was changed to white (255) corresponding to a 2π phase shift moving the maximum back again.

The Holoeye Phasecam software was used to track the shift in the interference pattern while running through all 256 grey levels on one half of the screen (not only three as shown in Figure B.1). The software identifies a minimum in the interference pattern and then tracks this point as the interference pattern shifts. The shift in interference pattern obtained by Phasecam before and after calibration is shown in Figure B.2. These plots consist of 256 rows, each containing the intensity profile of the interference pattern for that particular grey level.

194

a)

b)
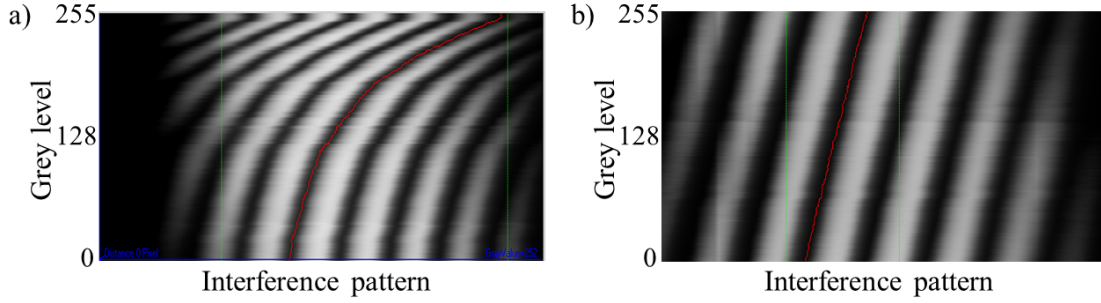
Figure B.2: Interference pattern shifts a) before and b) after calibration obtained with Phasecam.

The phase shift relates to the interference pattern shift by

$$\text{Phase shift}(\pi) = \frac{\text{Interference shift}}{0.5 \times T}, \tag{B.1}$$

where T is the period of the interference pattern. The calculated phase shift at different grey levels before and after calibration are shown in Figure B.3. Before calibration, the phase shift was non-linear and had a maximum shift of 2.8π.

To calibrate the SLM, the applied voltage across the electrodes (or digital potentiometer) is adjusted until a linear response is obtained. The manufacturer provides a calibration file, also known as the 'gamma-file', that maps the grey levels to specific voltages. In principle, when this file is uploaded with the specified potentiometer values, it should calibrate the SLM for a specific wavelength. However, these suggested voltage values are not always effective and usually need some manual tweaking to achieve calibration.
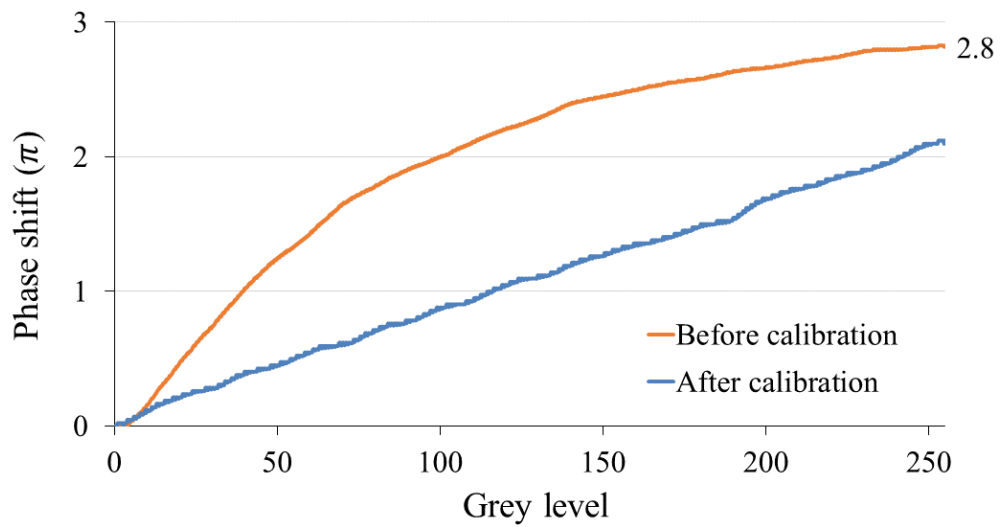
Figure B.3: Modulated phase shift at different grey levels before and after calibration.

Appendix C

Research outputs

C.1   Conference proceeding

SPIE Photonics Europe conference proceeding presented on 5 April 2022 in Strasbourg, France.

A vectorial structured light holographic optical trap for control of fluorescent particles

Ané Kritzinger[a,b], Valeria Rodríguez-Fajardo[b], Sifiso A. Nsibande[a], Patricia B. C. Forbes[a], and Andrew Forbes[b]

[a]Department of Chemistry, University of Pretoria, Pretoria, South Africa
[b]School of Physics, University of the Witwatersrand, Johannesburg, South Africa

ABSTRACT

Here we create a holographic trap that allows trapping with scalar Gaussian and vortex beams, as well as vectorial combinations of the two. When equally weighted, the resultant is a propagation invariant flat-top beam trap. The set-up includes a spatial light modulator in an interferometer to combine the beams, an inverted microscope for imaging, and a photon counting fluorescence detection stage. We outline the functionality of this system, measure the trap stiffness for some example beams, and show in-situ fluorescence measurement from quantum dots attached to micro-scale beads.

Keywords: holographic optical tweezers, vector beam, spatial light modulator, fluorescence spectroscopy, quantum dots

1. INTRODUCTION

Optical trapping or tweezing refers to the manipulation of micro and nano particles with tightly focused laser light. This technique has found countless applications in the fields of physics and biology ever since its advent in 1970 by Arthur Ashkin.[1] The invaluable contribution of optical tweezers to the science community, won its creator the 2018 Nobel Prize in Physics.[2] Optical trapping was first demonstrated with a Gaussian beam[1] and this beam still dominates trapping experiments today. However, the introduction of structured light[3,4] (varying light's intensity, phase and polarization) in optical tweezers, has sprouted a myriad of applications and inventions. Structured light has made it possible to not only trap but to direct, move and orient particles; the advances made in structured light combined with optical tweezers were extensively discussed in two recent review articles.[5,6] Structured light can be generated in numerous ways, but it was the development of spatial light modulators[7,8] that enabled the advancement of tailored light in optical traps which is a well-established technique today, called holographic optical tweezers (HOTs).

Structured light beams can broadly be classified as scalar or vector beams. Scalar beams are structured in amplitude and phase whereas vector beams are tailored in polarization as well. Trapping with vector beams is the most recent avenue of structured light explored in optical tweezers and has already proven beneficial to the trapping community.[6,9] The radially polarized vector beam is famous for achieving the smallest spot size when tightly focused,[10,11] this property has been used to demonstrate stronger axial trapping.[12,13] Another interesting use of polarization in traps is the so-called tractor beam that can exert a pushing or a pulling force on a particle depending on the polarization of the incident beams.[14] A further advancement in vector beam traps was demonstrated by Bhebhe *et al.* when they created an array of vector beams enabling simultaneous trapping of multiple particles with beams of different polarization patterns.[15]

Even though the inclusion of structured light in optical tweezers has made it a powerful tool, this technique is still blind to conformational and chemical changes of molecules - this is where fluorescence spectroscopy comes into play. The combination of optical tweezers with single molecule fluorescence has made the visualization of chemical and structural changes possible within the optical tweezer setup and is today an invaluable and pioneering tool for biological studies.[16–18] The main difficulty when combining optical tweezers and fluorescence microscopy is that the intensity of the trapping light is up to six orders of magnitude higher than the intensity of excitation

light used for fluorescence studies.[19] The high intensity light used in optical tweezers causes photobleaching of the fluorophores which is an irreversible process where the fluorophore loses its fluorescence.[20] Although not fully understood, photobleaching usually occurs because electrons already in the excited state continue to absorb photons and the resulting dissociation then leads to permanent loss of fluorescence signal.[21] Because of the difference in intensity of the two techniques, in most setups two different light sources are used – one for trapping (high intensity) and the other for fluorescence excitation (low intensity). To prevent photobleaching due to the trapping laser three general solutions have been demonstrated: (1) trapping with a non-resonant laser,[19] and the separation of the fluorescence and trapping in (2) space[21–23] or in (3) time.[24] In all the cases described above separate sources were used for trapping and excitation, but both can be achieved by a single laser if two-photon excitation (TPE) fluorescence is used. In TPE two photons are simultaneously absorbed by the fluorophore that then emits light with a shorter wavelength than the excitation wavelength. TPE only occurs at a measurable rate with high intensity lasers such as lasers used for optical trapping.[25] Very little research has investigated the possibility to use structured light to mitigate the photobleaching effect of the trapping laser. Only very recently have Zhang and Milstein shown that trapping with a Laguerre-Gaussian beam (or 'doughnut' beam) significantly improves the bleaching lifetime of the organic dye Alexa-647 positioned 1 μm below the trapped particle (separate trapping and excitation sources were used).[26]

In this work we explored the advantages of a vector trapping beam, specifically a vector flat-top beam, compared to the conventional Gaussian trapping beam. We used the dynamic control of the SLM to easily switch between scalar to vectorial light, tailoring the gradient forces and light intensities within the trap. We also explain why the vector flat-top beam is a superior trapping beam for fluorescent particles. The fluorescent particles we focused on in this study are semiconducting nanocrystals known as quantum dots (QDs) that exhibit interesting optical properties.[27] One of the properties of QDs is their ability to be used as sensors due to their fluorescence emission being extremely sensitive to the surface environment. The presence of a target analyte can result in either QD fluorescence quenching or enhancement due to a physical or chemical interaction;[28, 29] they have therefore been used to detect numerous analytes.[30] Combining single-molecule (or particle) manipulation of optical tweezers with the sensing ability of QDs has the possibility of being an ultra-sensitive analytical technique as shown by the biosensing research group of Hong-Wu which obtained detection limits as low as 1.0-2.0 pM for different virus genes.[31–33]

This paper, therefore, shows the potential bright future for the threefold combination of optical tweezers, structured (vector) light and fluorescence spectroscopy.

2. VECTOR FLAT-TOP BEAMS

A vector beam can typically be generated by the superposition of two orthogonally polarized scalar fields.[9] More specifically, a vector flat-top beam (U_{FT}) is created by the superposition of a Gaussian and a vortex mode[34]

$$U_{FT} = \sqrt{1-\alpha}\,\mathrm{LG}_1^0\hat{\mathbf{e}}_{\mathbf{H}} + \sqrt{\alpha}\,\mathrm{LG}_0^0\hat{\mathbf{e}}_{\mathbf{V}}, \tag{1}$$

where LG_l^p refers to the Laguerre-Gaussian modes with the radial order p and the azimuthal order l, so that $l = p = 0$ gives the Gaussian beam (vertically polarized) and $p = 0$, $l = 1$ gives the vortex beam (horizontally polarized). α weighs the two scalar beams in order to easily generate any field from a vortex when $\alpha = 0$ to a Gaussian when $\alpha = 1$ with the vector flat-top at $\alpha = 0.5$. The intensity profile as α changes is given in Fig. 1 along with the profiles at the critical α values.

The authors would like to stress the fact that even though vector flat-top beams were generated, it is just as easy to superimpose different scalar beams to create any arbitrary polarization pattern. For example, adding two vortex modes with $l = +1$ and $l = -1$ to create radially or azimuthally polarized light.[15]
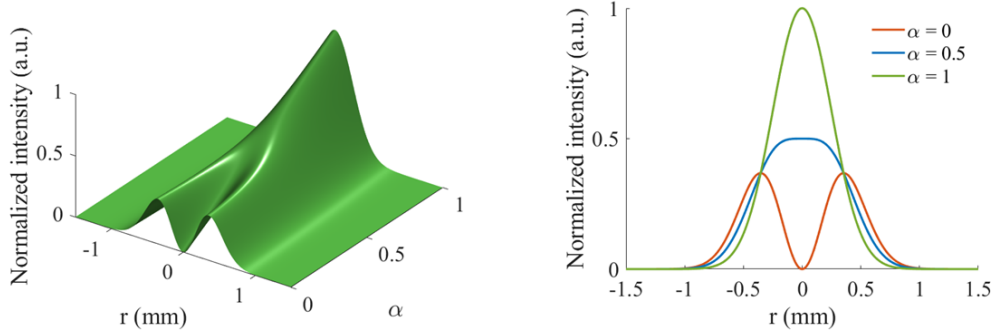
Figure 1. Intensity profile as α changes showing the evolution from a vortex to a Gaussian beam. The profiles of the vortex beam at $\alpha = 0$, the vector flat-top beam at $\alpha = 0.5$ and the Gaussian beam at $\alpha = 1$ are shown on the right.

An ideal flat-top beam has a uniform intensity profile where the intensity drops to zero at the edges. In reality, there only exists approximations for flat-top beams, like the vector flat-top approximation discussed in this paper. Other scalar approximations include super-Gaussian beams, Fermi-Dirac and flattened Gaussian beams to name a few.[35, 36] The major drawback of the scalar approximations is that their intensity profile varies as they propagate as shown in Fig. 2, the flat-top intensity profile is only obtained at a certain plane after which the profile changes quite drastically. On the contrary, vector flat-top beams are propagation invariant (see Fig. 2). This is true since they are the superposition of two eigenmodes of free-space (LG modes) making them an eigenmode of free-space. To have a propagation invariant beam makes the experimental optical delivery of the flat-top beam at the trapping plane much easier which is a highly favourable property of vector flat-top beams.
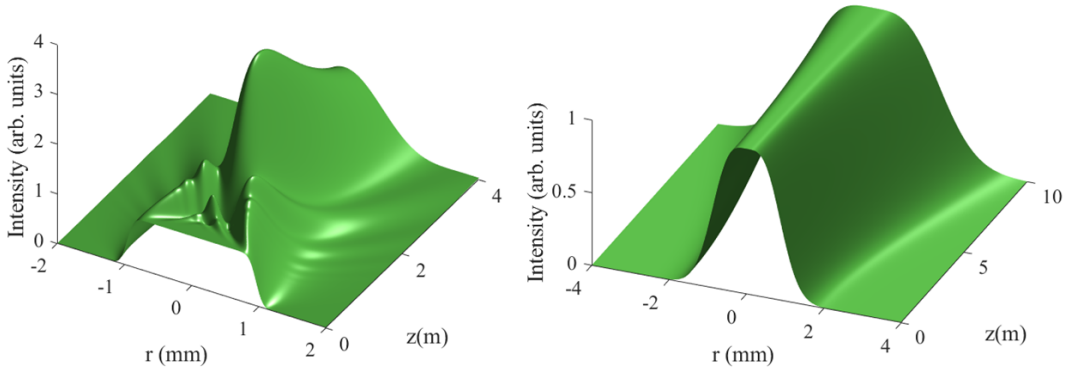
Figure 2. Propagation of a scalar flat-top beam (left) simulated using the flattened Gaussian beam approach[36] and of a vector flat-top beam (right). The scalar flat-top quickly loses its shape while the vector flat-top is propagation invariant. The peak intensity was normalized to better visualize the unchanging intensity profile of the vector flat-top.

3. RESULTS

The dynamics of a trapped particle can traditionally be described by two forces, the scattering force and the gradient force.[37] The former force is also known as the radiation pressure and is due to the reflection of light incident on a particle. This scattering force acts on the particle in the direction of light propagation therefore pushing the particle away from the beam. The gradient force is due to refraction of incident rays on a particle (momentum transfer); this force acts in the direction of the most intense region of the beam (the spatial intensity gradient) and is also known as the trapping force. The gradient or trapping force of a beam can therefore be

estimated using the intensity gradient of the beam ($F_{gradient} \propto \nabla I$). Thus, for a structured field to be a successful trapping beam, it must have a steep intensity gradient, which is the case for a flat-top beam.

Fig. 3 shows the experimental intensity profiles (shown in black) at different α values with the theoretical profiles in green. Each beam was used to trap a 2 μm bead with the trap stiffness reported (trap stiffness pN/μm $\pm$ std. error).
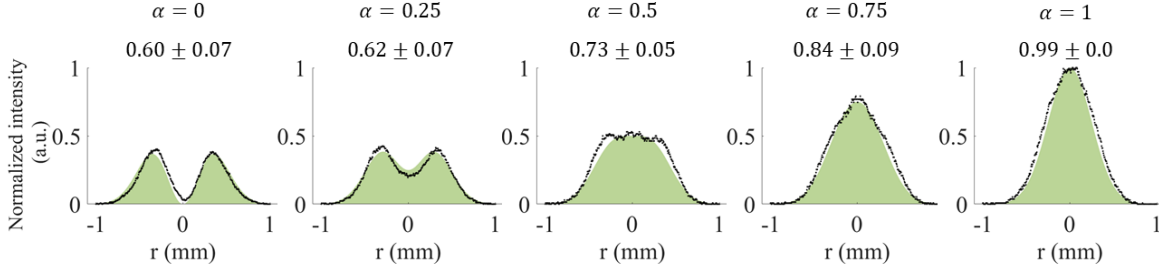
Figure 3.   Experimentally obtained intensity profiles (shown in black) with the theoretical profiles (in green) at five different α values with the trapping stiffness shown above (unit: pN/μm)

In Fig. 4 the profile of a vector flat-top is shown with the intensity profile of a Gaussian beam having (1) the same power and (2) the same effective gradient force as the vector flat-top. Therefore, when trapping fluorescent particles with a vector flat beam the trapping (and/or excitation) light has half the peak intensity compared to the conventional Gaussian beam, with only a minimal loss of trapping efficiency as shown experimentally on the right of Fig. 4. Similarly, if one considers the intensity profile of a Gaussian beam that has the same (theoretical) gradient force as the flat-top beam, the peak intensity of the Gaussian is still around 1.5 times higher than the flat-top. This shows that vector flat-top beams can be used to reduce the peak intensity (reduce photobleaching) while maintaining the trap efficiency.

We used the same laser (wavelength $\lambda = 532$ nm) to trap and excite the QD-tagged beads which induced excessive photobleaching even at a low power of 100 μW. However, preliminary results showed that the half-life of the fluorophore was increased by 73% when using a vector flat-top trap compared to a Gaussian beam trap (the half-life improved from 0.98 s to 1.7 s). This is compelling evidence for using a flat-top beam as the trapping beam (in a dual-laser setup) to help solve the bleaching phenomenon.
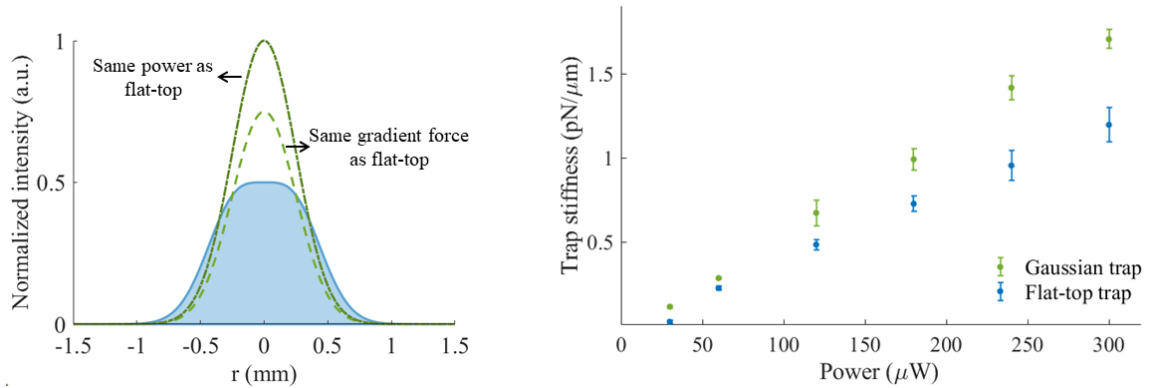
Figure 4.   Comparison of the intensity profiles of a vector flat-top beam and a Gaussian beam with the same power and with the same gradient force (left). The experimental trap stiffness of a Gaussian and vector flat-top trap at different powers (right). Even though the flat-top has a steeper intensity gradient, at the same power the Gaussian beam trap is stiffer due to a higher peak intensity. The equipartition method was used to determine the trap stiffness.[38]

4. EXPERIMENTAL SETUP AND SAMPLE PREPARATION

A schematic of the experimental setup used to create a vector holographic optical trap is illustrated in Fig. 5. A horizontally polarized Gaussian beam from a $\lambda = 532$ nm laser was expanded and collimated before illuminating the screen of the liquid crystal SLM. The multiplexed grey-scale hologram that was encoded on the SLM through complex amplitude modulation is shown in Fig. 5a. To create a vector flat-top beam, a Gaussian and a vortex beam with different propagation angles were created with the SLM which was aligned to only modulate horizontally polarized light. A half wave plate (HWP) was added in the path of one beam to change its polarization from horizontal to vertical to allow the superposition of orthogonal polarized beams to create the vector beam. A D-shaped mirror (D-M) was used to direct the path of the vortex beam in order to combine the two scalar beams interferometrically in the polarizing beam splitter (PBS). The 4f-system (lenses L1 and L2) was included to ensure the generated beam reached and filled the back aperture of the objective lens ($100\times$, Nikon oil immersed, NA 1.3). The high NA objective lens focused the beam to create the optical trap in the sample holder. The sample consisted of either uncoated 2 μm polystyrene beads (sample used for obtaining trap stiffness) or QD-tagged polystyrene beads (fluorescent sample) supported between a cover slip and microscope slide. An inverted microscope setup was implemented with a dichroic mirror (DM) reflecting the laser light into the objective while letting the fluorescence and illumination light pass through. A white LED illuminated the sample from above and imaged the sample through the objective and eyepiece lens L3 to a CCD camera (detector) when taking position measurements of the trapped bead. However, for fluorescence detection, the illumination light was switched off, and the fluorescence (travelling the same path as the illumination light) was detected with an avalanche photodiode (detector).
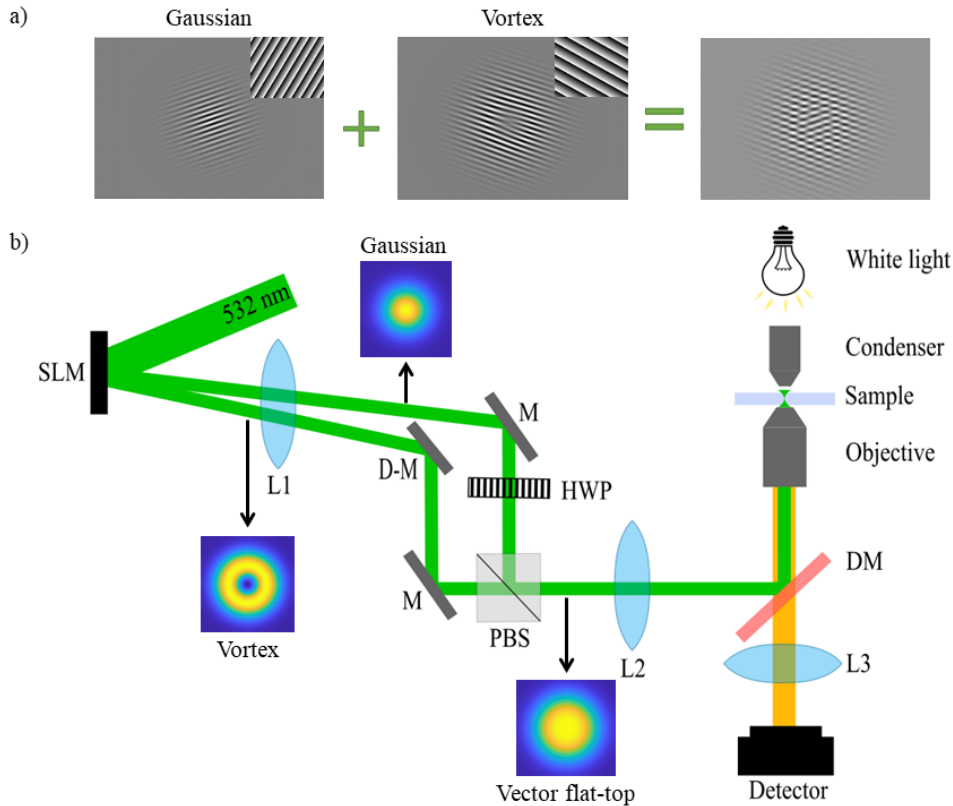
Figure 5.   a) The multiplexed hologram that was encoded on the SLM to generate a Gaussian and vortex beam with different propagation angles. b) Schematic illustration of the experimental setup used to generate a vector flat-top holographic optical tweezer.

202

The fluorophores used in this study were L-cysteine capped CdSe/ZnS QDs coupled to 2 μm polystyrene beads. The QDs were synthesized and coupled to commercial beads through EDC/NHS chemistry. The success of the coupling reaction was confirmed by the TEM images of the surface of an uncoated bead and a QD-tagged bead shown in Fig. 6. The right-hand image in Fig. 6 shows the fluorescence emission of a QD-tagged bead under a confocal micrope.
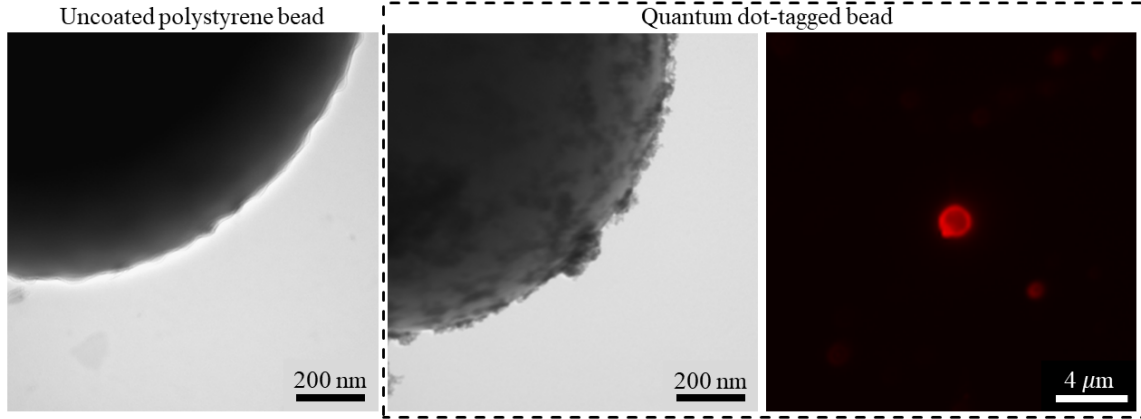
Figure 6. Transmission electron microscope (TEM) images of the surface of a 2 μm diameter uncoated polystyrene bead (left) and a QD-tagged bead (middle), showing the successful coating of the beads with QDs. On the right the appearance of the QD-tagged bead under the fluorescence microscope, clearly showing the fluorescence emission from the QDs around the bead.

5. CONCLUSION

A vectorial holographic optical tweezing system was used to tailor the gradient forces and light intensities within the optical trap. The versatility of the system was demonstrated by generating propagation invariant vector flat-top beams and easily switching from scalar to vectorial light. We also showed the possibility of using these structured beams to prolong the fluorescence half-life of QDs in the optical trap.

ACKNOWLEDGMENTS

REFERENCES

[1] Ashkin, A., "Acceleration and trapping of particles by radiation pressure," *Physical Review Letters* **24**(4), 156 (1970).

[2] Asplund, M. C., Johnson, J. A., and Patterson, J. E., "The 2018 Nobel Prize in physics: optical tweezers and chirped pulse amplification," *Analytical and Bioanalytical Chemistry* **411**(20), 5001–5005 (2019).

[3] Rubinsztein-Dunlop, H., Forbes, A., Berry, M. V., Dennis, M. R., Andrews, D. L., Mansuripur, M., Denz, C., Alpmann, C., Banzer, P., Bauer, T., et al., "Roadmap on structured light," *Journal of Optics* **19**(1), 013001 (2016).

[4] Forbes, A., de Oliveira, M., and Dennis, M. R., "Structured light," *Nature Photonics* **15**(4), 253–262 (2021).

[5] Yang, Y., Ren, Y., Chen, M., Arita, Y., and Rosales-Guzmán, C., "Optical trapping with structured light: a review," *Advanced Photonics* **3**(3), 034001 (2021).

[6] Otte, E. and Denz, C., "Optical trapping gets structure: Structured light for advanced optical manipulation," *Applied Physics Reviews* **7**(4), 041308 (2020).

[7] Forbes, A., Dudley, A., and McLaren, M., "Creation and detection of optical modes with spatial light modulators," *Advances in Optics and Photonics* **8**(2), 200–227 (2016).

[8] Lazarev, G., Chen, P.-J., Strauss, J., Fontaine, N., and Forbes, A., "Beyond the display: phase-only liquid crystal on silicon devices and their applications in photonics," *Optics express* **27**(11), 16206–16249 (2019).

[9] Rosales-Guzmán, C., Ndagano, B., and Forbes, A., "A review of complex vector light fields and their applications," *Journal of Optics* **20**(12), 123001 (2018).

[10] Quabis, S., Dorn, R., Eberler, M., Glöckl, O., and Leuchs, G., "Focusing light to a tighter spot," *Optics Communications* **179**(1-6), 1–7 (2000).

[11] Otte, E., Tekce, K., and Denz, C., "Tailored intensity landscapes by tight focusing of singular vector beams," *Optics Express* **25**(17), 20194–20201 (2017).

[12] Moradi, H., Shahabadi, V., Madadi, E., Karimi, E., and Hajizadeh, F., "Efficient optical trapping with cylindrical vector beams," *Optics Express* **27**(5), 7266–7276 (2019).

[13] Michihata, M., Hayashi, T., and Takaya, Y., "Measurement of axial and transverse trapping stiffness of optical tweezers in air using a radially polarized beam," *Applied Optics* **48**(32), 6143–6151 (2009).

[14] Shvedov, V., Davoyan, A. R., Hnatovsky, C., Engheta, N., and Krolikowski, W., "A long-range polarization-controlled optical tractor beam," *Nature Photonics* **8**(11), 846–850 (2014).

[15] Bhebhe, N., Williams, P. A., Rosales-Guzmán, C., Rodriguez-Fajardo, V., and Forbes, A., "A vector holographic optical trap," *Scientific Reports* **8**(1), 1–9 (2018).

[16] Cordova, J. C., Das, D. K., Manning, H. W., and Lang, M. J., "Combining single-molecule manipulation and single-molecule detection," *Current Opinion in Structural Biology* **28**, 142–148 (2014).

[17] Choudhary, D., Mossa, A., Jadhav, M., and Cecconi, C., "Bio-molecular applications of recent developments in optical tweezers," *Biomolecules* **9**(1), 23 (2019).

[18] Shabestari, M. H., Meijering, A., Roos, W., Wuite, G., and Peterman, E., "Recent advances in biological single-molecule applications of optical tweezers and fluorescence microscopy," *Methods in Enzymology* **582**, 85–119 (2017).

[19] van Dijk, M. A., Kapitein, L. C., van Mameren, J., Schmidt, C. F., and Peterman, E. J., "Combining optical trapping and single-molecule fluorescence spectroscopy: enhanced photobleaching of fluorophores," *The Journal of Physical Chemistry B* **108**(20), 6479–6484 (2004).

[20] Diaspro, A., Chirico, G., Usai, C., Ramoino, P., and Dobrucki, J., "Photobleaching," in [*Handbook of Biological Confocal Microscopy*], Pawley, J. B., ed., 690–702, Springer (2006).

[21] Ma, G., Hu, C., Li, S., Gao, X., Li, H., and Hu, X., "Simultaneous, hybrid single-molecule method by optical tweezers and fluorescence," *Nanotechnology and Precision Engineering* **2**(4), 145–156 (2019).

[22] Ishijima, A., Kojima, H., Funatsu, T., Tokunaga, M., Higuchi, H., Tanaka, H., and Yanagida, T., "Simultaneous observation of individual ATPase and mechanical events by a single myosin molecule during interaction with actin," *Cell* **92**(2), 161–171 (1998).

[23] Lang, M. J., Fordyce, P. M., and Block, S. M., "Combined optical trapping and single-molecule fluorescence," *Journal of biology* **2**(1), 1–4 (2003).

[24] Brau, R. R., Tarsa, P. B., Ferrer, J. M., Lee, P., and Lang, M. J., "Interlaced optical force-fluorescence measurements for single molecule biophysics," *Biophysical journal* **91**(3), 1069–1077 (2006).

[25] Jauffred, L. and Oddershede, L. B., "Two-photon quantum dot excitation during optical trapping," *Nano letters* **10**(5), 1927–1930 (2010).

[26] Zhang, Z. and Milstein, J., "Extending the photobleaching lifetime in the presence of an optical tweezers by wavefront engineering," *Journal of Optics* **22**(9), 095301 (2020).

[27] Smith, A. M. and Nie, S., "Semiconductor nanocrystals: structure, properties, and band gap engineering," *Accounts of Chemical Research* **43**(2), 190–200 (2010).

[28] Frasco, M. F. and Chaniotakis, N., "Semiconductor quantum dots in chemical sensors and biosensors," *Sensors* **9**(9), 7266–7286 (2009).

[29] Nsibande, S. and Forbes, P., "Fluorescence detection of pesticides using quantum dot materials–a review," *Analytica Chimica Acta* **945**, 9–22 (2016).

[30] Cui, L., He, X.-P., and Chen, G.-R., "Recent progress in quantum dot based sensors," *RSC Advances* **5**(34), 26644–26653 (2015).

[31] Li, C.-Y., Cao, D., Kang, Y.-F., Lin, Y., Cui, R., Pang, D.-W., and Tang, H.-W., "Fluorescence detection of H5N1 virus gene sequences based on optical tweezers with two-photon excitation using a single near infrared nanosecond pulse laser," *Analytical chemistry* **88**(8), 4432–4439 (2016).

[32] Cao, D., Li, C.-Y., Kang, Y.-F., Lin, Y., Cui, R., Pang, D.-W., and Tang, H.-W., "Dual-component gene detection for H7N9 virus – the combination of optical trapping and bead-based fluorescence assay," *Biosensors and Bioelectronics* **86**, 1031–1037 (2016).

[33] Cao, D., Li, C.-Y., Qi, C.-B., Chen, H.-L., Pang, D.-W., and Tang, H.-W., "Multiple optical trapping assisted bead-array based fluorescence assay of free and total prostate-specific antigen in serum," *Sensors and Actuators B: Chemical* **269**, 143–150 (2018).

[34] Bhebhe, N., Rosales-Guzman, C., and Forbes, A., "Classical and quantum analysis of propagation invariant vector flat-top beams," *Applied optics* **57**(19), 5451–5458 (2018).

[35] De Silvestri, S., Laporta, P., Magni, V., and Svelto, O., "Solid-state laser unstable resonators with tapered reflectivity mirrors: the super-gaussian approach," *IEEE journal of quantum electronics* **24**(6), 1172–1177 (1988).

[36] Gori, F., "Flattened gaussian beams," *Optics Communications* **107**(5-6), 335–341 (1994).

[37] Neuman, K. C. and Block, S. M., "Optical trapping," *Review of scientific instruments* **75**(9), 2787–2809 (2004).

[38] Gieseler, J., Gomez-Solano, J. R., Magazzù, A., Castillo, I. P., García, L. P., Gironella-Torrent, M., Viader-Godoy, X., Ritort, F., Pesce, G., Arzola, A. V., Volke-Sepúlveda, K., and Volpe, G., "Optical tweezers — from calibration to applications: a tutorial," *Advances in Optics and Photonics* **13**(1), 74–241 (2021).

C.2   Journal paper

Research paper based on the work presented in this dissertation, submitted to *Nanoscale.*

Journal Name

Optical trapping and fluorescence control with vectorial structured light

Ané Kritzinger,[a] Andrew Forbes[b] and Patricia B.C. Forbes[a*]

Here we functionalized micro-scaled polymer beads with nano-scaled quantum dots and demonstrate optical trapping and tweezing, with *in-situ* fluorescence measurement, in an all-digital all-optical configuration. We outline the chemistry required to facilitate this, from deactivating the optical trapping environment to size, adhesion and agglomeration control. We introduce a novel holographic optical trapping set-up that leverages on vectorially structured light, allowing for the delivery of tuneable forms of light from purely scalar to purely vector, including propagation invariant flat-top beams for uniform illumination and tailored intensity gradient landscapes. Finally, we show how this has the potential to quench bleaching in a single wavelength trap by linear (spatial mode) rather than non-linear effects, advancing the nascent field of optics for chemistry.

1 Introduction

Optical trapping or tweezing describes the manipulation of nano- to micro-sized particles through momentum transfer from tightly focused light. Optical tweezing was first demonstrated by Arthur Ashkin in 1970 with a Gaussian beam[1] and half a decade later this beam still dominates optical trapping experiments. However, the employment of structured light (varying the intensity, phase and polarization of light) in optical tweezers has made it possible to not only trap but to move, rotate and direct particles. These structured light traps are a well-established technique today and since most structured beams are created by means of a hologram, they have been dubbed holographic optical tweezers (HOTs).[2,3]

With HOTs, an array of traps can be created to trap multiple particles simultaneously while being able to dynamically change this array pattern.[4–6] Structured beams that reconstruct themselves after being distorted by a trapped particle (Bessel beams) have allowed for trapping in multiple planes previously not possible.[7] Airy beams, for example, can guide a particle along a certain trajectory enabling selective removal of particles in a sample.[8] The fact that light carries linear momentum is well-known and is the reason why light can trap particles, however, light can also carry orbital angular momentum (OAM), like Laguerre-Gaussian (LG) beams. By employing these OAM carrying beams, optical tweezers also gain rotational control of particles.[9–11]

So far research has focused mainly on structured beams modulated in amplitude and phase – these are called scalar beams. On the other hand, vector beams are structured in polarization as well, meaning they have a spatially varying polarization pattern. Trapping with vector beams is the most recent avenue of structured light explored in optical tweezers and has already proven beneficial to the trapping community.[12,13] The radially polarized vector beam, for example, is famous for achieving the smallest spot size when tightly focused,[14,15] this property has been used to create stronger axial optical traps.[16,17] A further advancement in vector beam traps was demonstrated by Bhebhe *et al.* when they created a vector HOT which enabled optical trapping with a dynamic array of different vector (and/or scalar) beams.[18]

Using structured light in optical tweezers has made it a powerful technique, furthermore, combining this tool with fluorescence spectroscopy made it possible to not only exert forces on a particle but also to observe chemical and structural changes of molecules within the trap. For this reason, optical tweezers combined with single molecule fluorescence is an invaluable and pioneering tool in biology research today.[19–21] The integration of fluorescence microscopy into optical tweezers is however not trivial, since the trapping light has an intensity up to six orders of magnitude higher than that of excitation light used in fluorescence experiments.[22] The high intensity trapping light causes photobleaching of the trapped fluorophores, which is an irreversible process whereby fluorophores become non-fluorescent.[23] Although not fully understood, photobleaching usually occurs because electrons already in the excited state continue to absorb photons and the resulting dissociation then leads to permanent loss of fluorescence signal.[24] Several solutions exist to overcome this problem, most of them using different sources for trapping and excitation.[24–27] Very little research, however, has investigated the possibility of using structured light to assist with integrating fluorescence spectroscopy in optical tweezers. Only very recently have Zhang and Milstein shown that trapping with a vortex or

[a] *Department of Chemistry, University of Pretoria, Pretoria, South Africa*
[b] *School of Physics, University of the Witwatersrand, Johannesburg, South Africa*
* Corresponding author email: patricia.forbes@up.ac.za

207

'doughnut' beam improves the bleaching lifetime of an organic dye positioned 1 μm below the trapped particle, while still using separate trapping and excitation sources.[28]

Here the advantages of trapping with vectorial light are explored further, especially for the control of fluorescent particles. We demonstrate a vectorial HOT setup with which purely scalar to purely vector beams can be used for trapping, allowing us to tailor the gradient forces and intensity profiles within the trap. We specifically focused on the propagation invariant vector flat-top beam and show its potential to reduce photobleaching in a single wavelength optical tweezer setup. The fluorescent particles used in this study were semiconducting nanocrystals known as quantum dots (QDs). The process to create QD probes fit for optical trapping is discussed in detail, including the QD synthesis and the coupling thereof to micro-sized polymer beads.

2 Results and discussion

2.1 Functionalizing micro-sized beads with quantum dots

CdSe/ZnS core/shell QDs were prepared using the hot-injection colloidal synthesis method followed by a ligand exchange reaction to functionalize the surface with L-cysteine. A schematic of the synthesis process followed is shown in Fig. 1a. The TEM image of the hydrophobic QDs and their size distribution in Fig 1b show that the QDs had an average diameter of 5.2 ± 0.6 nm. To create fluorescence probes that can be trapped with the optical tweezer setup, these QDs were coupled to micro-sized polymer beads as shown in Fig. 1c. Well-known and widely used EDC/NHS chemistry was used to bond the QDs to the surface of the beads. The carboxyl groups present on the surface of the commercial polystyrene beads reacted with the primary amine group of the L-cysteine ligands on the QDs to form a covalent bond between the bead and the QD. TEM images of the surface of an uncoated commercial polymer bead and a QD-tagged bead are compared in Fig. 1d. The uncoated polymer bead had a smooth surface whereas the surface of the QD-tagged bead had a rough or 'fuzzy' appearance from the QD coating, confirming the success of the coupling reaction. The normalized fluorescence intensity of QDs at different times during the synthesis is shown in Fig. 1e. Longer growth time for the CdSe core and CdSe/ZnS core/shell QDs lead to larger particles (smaller bandgap) and therefore a red-shift in
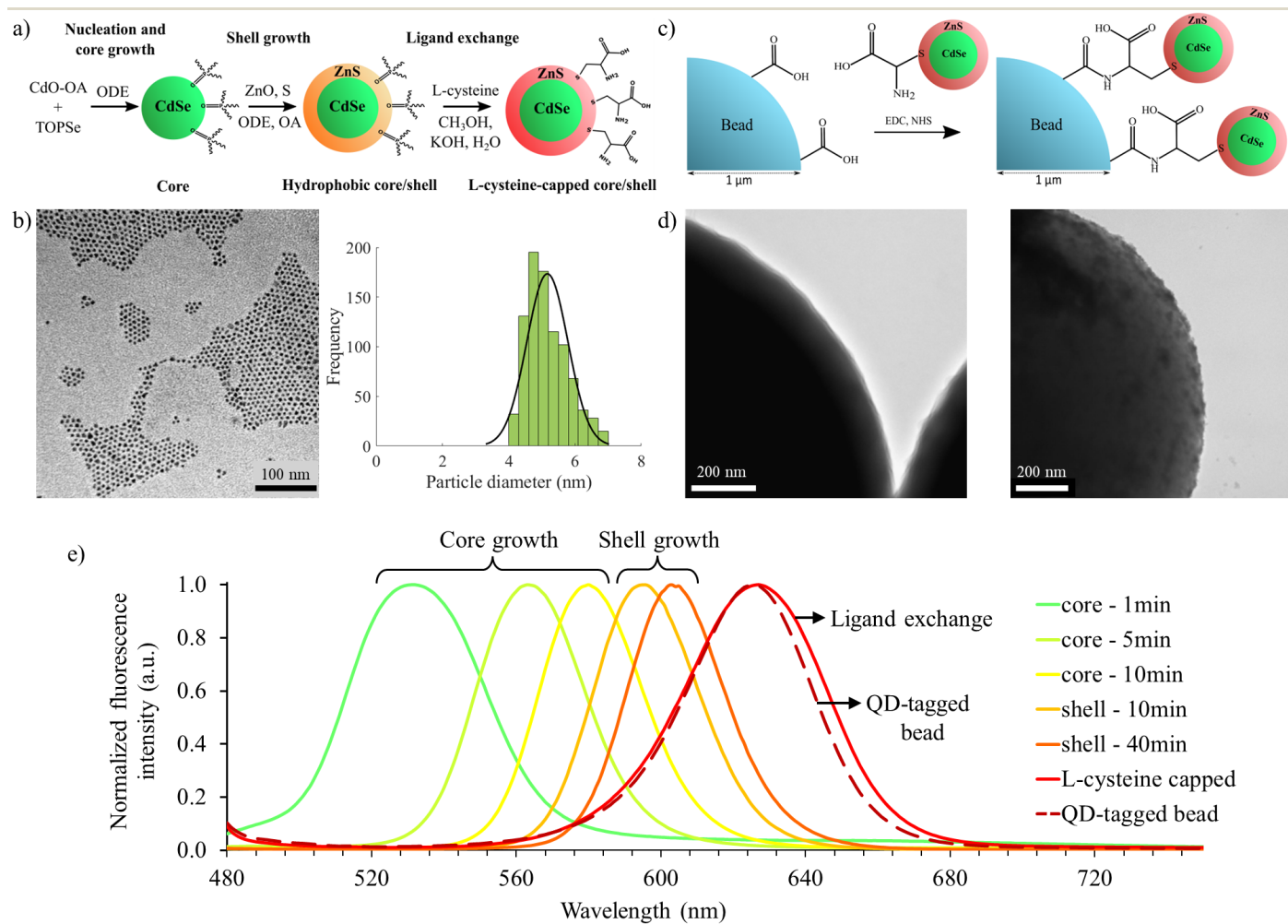
Fig. 1 a) L-cysteine capped CdSe/ZnS QD synthesis steps. b) TEM image of CdSe/ZnS QDs with their corresponding size distribution; the average diameter was 5.2 ± 0.6 nm. c) The coupling reaction of L-cysteine capped QDs to the surface of micro-sized beads through EDC/NHS chemistry. d) TEM images of the surface of an uncoated polymer (left) and a QD-tagged bead (right), confirming the success of the coupling reaction. e) Fluorescence emission of the QDs at different times throughout the synthesis.

the fluorescence emission wavelength was observed. The ligand exchange reaction also caused a red-shift in the emission wavelength. After the coupling reaction, however, a slight blue shift was observed. In order to detect the fluorescence emission of the QD-tagged beads in the optical tweezer setup, the fluorescence light had to pass through a dichroic mirror that transmits light with wavelengths 582-825 nm (see Section 2.2.2). To ensure most of the emission peak is longer than 582 nm, the QDs were grown to have a fluorescence peak maximum of 595 nm or longer.

The importance of optimising some of the synthesis steps when preparing the QD-tagged beads are highlighted in Fig. 2. Firstly, the purification of the L-cysteine capped QDs can be time consuming, but is a crucial step in order to have a monodispersed and impurity free QD sample and consequently a uniform QD coating on the polymer beads. In Fig. 2a, the appearance of purified L-cysteine capped QDs is shown on the left, here individual QDs are visible, whereas a TEM image of crude L-cysteine capped CdSe/ZnS QDs before purification is shown on the right. The crude sample is clumped together with many impurities between the QDs so that no individual QD can be seen. The large surface area of QDs provides organic impurities with much space for attachment, therefore the need for rigorous purification.

After purification and drying of the L-cysteine-capped CdSe/ZnS QDs, their fluorescence intensity was quenched. However, after some time the fluorescence intensity recovered when they were redispersed in water as shown in Fig. 2b. This figure shows the recovery of the fluorescence over a period of 5

days; the first measurement was taken directly after the purified QDs were redisperesd in water. This quenching phenomenon can be explained by the research published by Noh *et al.*[29]. In this work they showed that the fluorescence of water-soluble CdSe QDs quenched when the QDs formed aggregates. Similarly, we know that the L-cysteine capped QDs exhibit hydrogen bonding and tend to clump together. Thus the L-cysteine QDs possibly formed aggregates when concentrated which resulted in the fluorescence quenching. When they were redispersed in water the aggregates dispersed and the fluorescence emission recovered. To ensure the fluorescence signal from the QDs was recovered and stable, the QDs were stored in deionized water for several days before performing the coupling reaction.

On the left of Fig. 2b a TEM image of a QD-tagged bead with a uniform QD coating is shown, whereas insets 1-3 show QD-tagged beads when some synthesis steps were not carried out optimally. Inset 1 shows a QD-tagged bead when the excess EDC was not thoroughly removed before adding the QDs. The unreacted EDC activated not only the carboxyl groups on the beads but also the carboxyl groups of L-cysteine on the QDs. These activated QDs then reacted with each other to form large aggregates. Inset 2 shows the uneven QD coating when the coupling reaction was carried out with magnetic stirring. The amount of QDs on the surface of this bead ranged from almost nothing on the one side to large clumps on the other, however performing the reaction in an ultra-sonic bath greatly improved the uniformity of the QD coating (as shown on the left). Lastly, we would like to point out
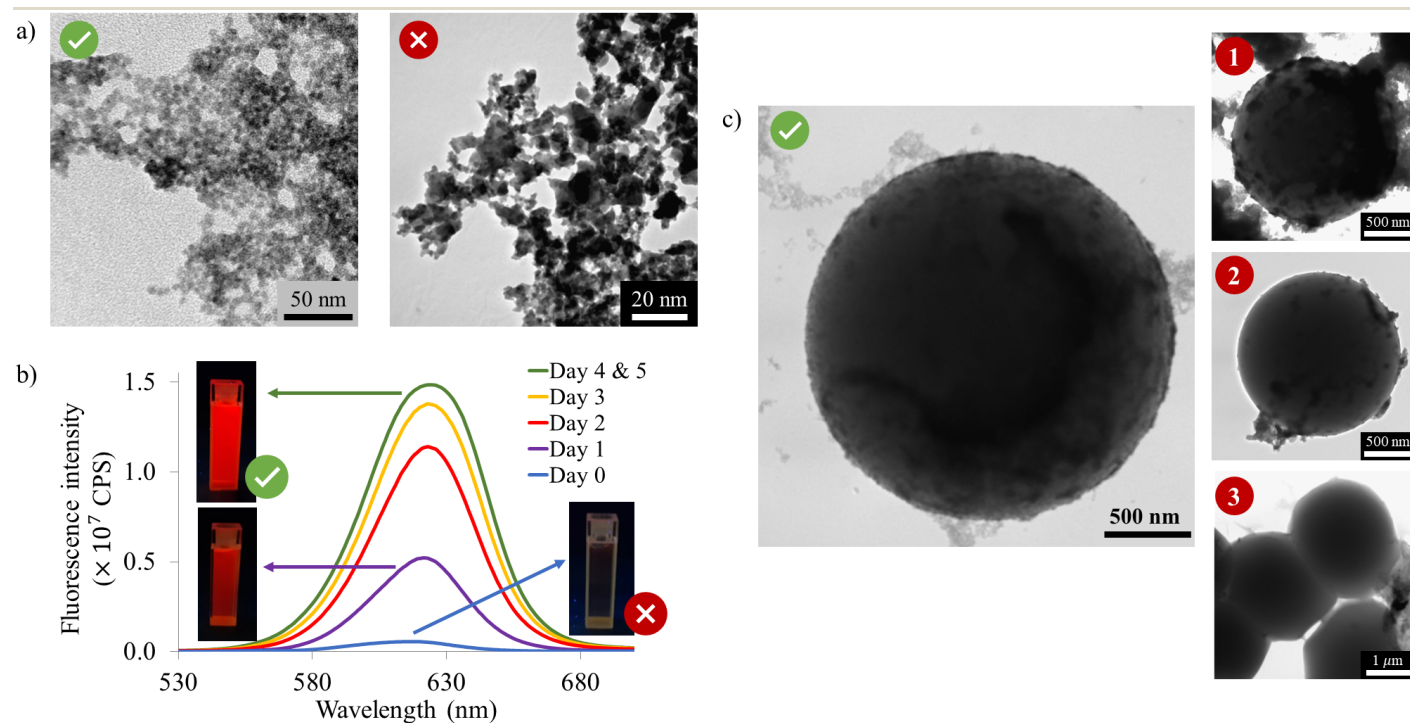
Fig. 2 a) TEM images of purified (left) and crude (right) L-cysteine capped CdSe/ZnS QDs. b) Fluorescence intensity recovery of L-cysteine capped CdSe/ZnS QDs over five days. The photo insets show the appearance of the sample under UV-light on certain days. c) The TEM image on the left shows a QD-tagged bead uniformly coated with QDs, whereas insets 1-3 shows QD-tagged beads when some synthesis steps were not carried out optimally. In inset 1 the excess EDC was not removed before adding the QDs, inset 2 shows the reaction done with magnetic stirring as opposed to ultra-sonication and inset 3 shows the deformation of the polymer beads due to the presence of acetone.

209

the importance of carefully studying the system under investigation before attempting a synthesis. Even though acetone proved to be an excellent solvent for purification of the QDs, in the QD-bead system this solvent caused the polymer beads to deform as shown in inset 3; only distilled water was thus used for purifying the QD-tagged beads.

2.2 Vectorial holographic optical tweezer

Here we demonstrate a vectorial HOT by focusing on vector flat-top beams. This beam is beneficial for optical trapping of fluorescent particles since it provides uniform excitation illumination, it is a propagation invariant beam and has a steep intensity gradient (meaning it can produce a strong optical trap), while having a lower peak intensity to reduce photobleaching.

2.2.1 Vector flat-top beams

An ideal flat-top beam has a uniform intensity profile and falls to zero at the edges. However, in the laboratory only approximations to a flat-top beam can be created; some approximations include the super-Gaussian, flattened Gaussian and Fermi-Dirac beams.[30,31] The major drawback of all these approximations is that their intensity profile varies as they propagate, the flat-top intensity profile is only obtained at a certain plane after which the profile changes quite drastically as shown in Fig. 3a. The

quick change in profile makes optical delivery of the flat-top profile at the tightly focused trapping plane extremely difficult. A beam that can simply be focused through the objective onto the sample and keep its profile is much more ideal – this is achieved by vector flat-top beams. Vector flat-top beams are propagation invariant since they are created by the superposition of two eigenmodes of free-space; the propagation of a vector flat-top beam is shown in Fig. 3b.

A vector flat-top beam is obtained through the (vector) addition of a Gaussian and a vortex beam.[32] The field is therefore given by

$$U_{FT} = \sqrt{\alpha}\,\mathrm{LG}_0^0 \hat{\mathbf{e}}_\mathbf{H} + \sqrt{1-\alpha}\,\mathrm{LG}_0^1 \hat{\mathbf{e}}_\mathbf{V}, \tag{1}$$

where LG_p^l refers to the Laguerre-Gaussian (LG) modes with p the radial index and l the azimuthal index. LG_0^0 is thus the Gaussian beam and LG_0^1 the vortex beam. A vector beam is formed by the addition of orthogonal scalar fields with uniform polarization, here the Gaussian beam has horizontal polarization $\hat{\mathbf{e}}_\mathbf{H}$ and the vortex beam vertical polarization $\hat{\mathbf{e}}_\mathbf{V}$. In Eq. 1, a factor α was introduced to weigh the two scalar beams, meaning any field from a vortex when $\alpha = 0$ to a Gaussian beam when $\alpha = 1$ can be generated; with the vector flat-top at equal weighting of $\alpha = 0.5$. The evolution of the vector beam as α changes is shown in Fig. 3 along with the beam profiles at the critical α values ($\alpha = 0, 0.5$
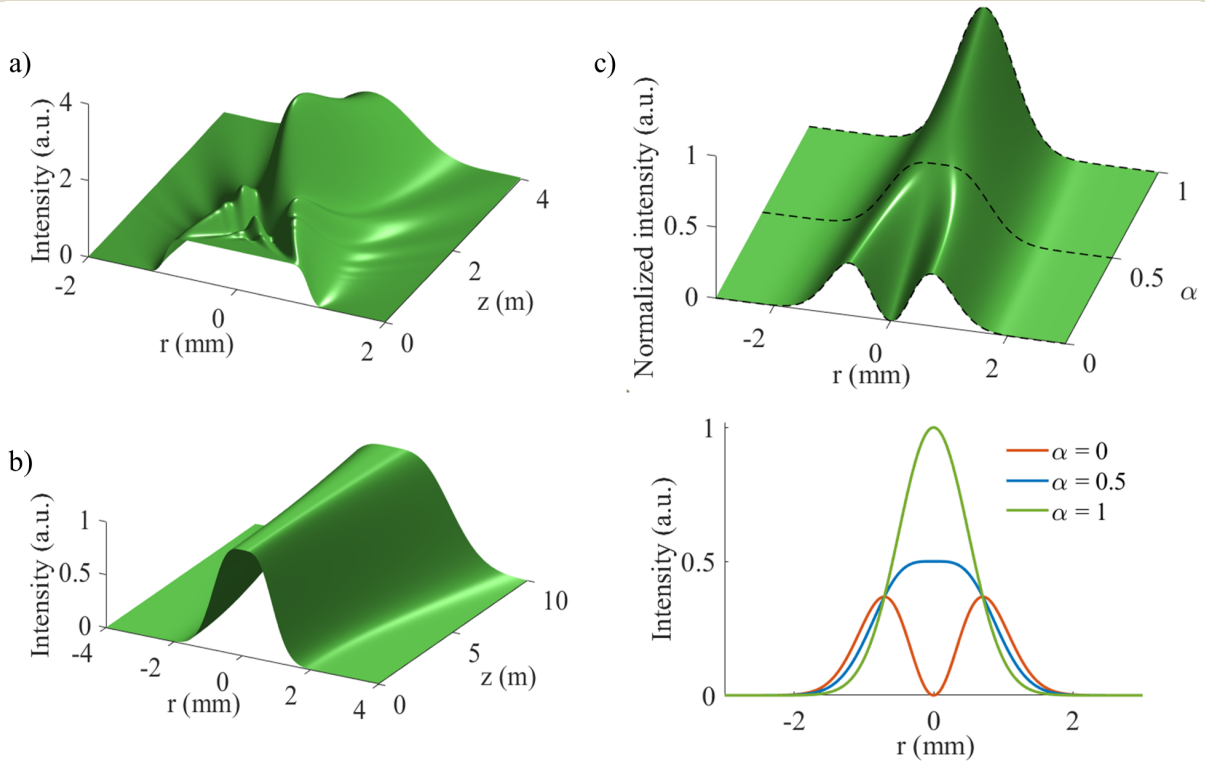
Fig. 3 a) Propagation of a scalar flat-top beam simulated using the flattened Gaussian beam approach. b) Propagation of a vector flat-top beam showing the unchanging flat-top profile. The peak intensities were normalized to better visualize the propagation invariance of this beam. c) Intensity profile as α changes showing the evolution from a vortex to a flat-top to a Gaussian beam. The profiles of the vector beam at critical α values are shown in the bottom panel with the vortex beam at $\alpha = 0$, the vector flat-top beam at $\alpha = 0.5$ and the Gaussian beam at $\alpha = 1$.

210

and 1). The LG_p^l field takes the well-known form[33]

$$LG_p^l(r,\varphi,z) = \sqrt{\frac{2p!}{\pi(|l|+p)!}}\frac{1}{w(z)}\left(\frac{\sqrt{2}r}{w(z)}\right)^{|l|}L_p^{|l|}\left(\frac{2r^2}{w^2(z)}\right)$$

$$\times \exp[i(|l|+2p+1)\psi(z)]\exp[il\varphi] \qquad (2)$$

$$\times \exp\left[-\frac{ikr^2}{2R(z)}\right]\exp\left[-\frac{r^2}{w^2(z)}\right],$$

where $L_p^{|l|}$ is the associated Laguerre polynomial, $w(z) = w_0\sqrt{1+\left(\frac{z}{z_R}\right)^2}$, w_0 is the Gaussian beam radius, $z_R = \frac{\pi w_0^2}{\lambda}$ is the Rayleigh range, $R(z) = z\left(1+\left(\frac{z_R}{z}\right)^2\right)$ is the radius of curvature and $\psi(z) = \arctan\left(\frac{z}{z_R}\right)$ is the Gouy phase.

Here we (theoretically) compare the vector flat-top beam to a Gaussian beam to determine in what aspects flat-top beams are superior to Gaussian beams (and vice versa). The intensity of the vector beam can generally be written as the sum of the intensities of the Gaussian and vortex beam (with some polarization requirements)

$$I_{vector} = \alpha|LG_0^0|^2 + (1-\alpha)|LG_0^1|^2, \qquad (3)$$

where the vector flat-top intensity is obtained by setting $\alpha = 0.5$ and the Gaussian intensity by $\alpha = 1$.

The gradient force (or trap strength) of a beam is proportional to the intensity gradient of the beam, $F_{grad} = c\nabla I$.[34-36] Since only the relative forces of the vector flat-top and Gaussian beam are important, $c = 1$ can be assumed such that

$$F_{grad} = \nabla I. \qquad (4)$$

Therefore, if the intensity profile of a beam is known, its gradient force can easily be calculated.

For the vector flat-top beam to be useful for trapping fluorescent particles, it must have a similar trap strength as a Gaussian beam but a lower peak intensity to possibly reduce photobleaching. To test when this is true, the average gradient force ($\bar{F}_{grad}$) over the whole area of the beam, A, was considered

$$\bar{F}_{grad} = \frac{\int F_{grad}\,dA}{\int dA}. \qquad (5)$$

More relevant is the ratio of the average gradient force of the flat-top (FT) to the Gaussian (G) beam

$$\gamma = \frac{\bar{F}_{FT}}{\bar{F}_G}, \qquad (6)$$

so that at $\gamma = 1$ the average gradient force of the flat-top and Gaussian beams are equal and at $\gamma > 1$ the vector flat-top has a stronger trap strength.

The ratio, γ, was calculated at different relative powers of the Gaussian and vector flat-top beams and plotted in Fig. 4a. This figure, therefore, shows how the relative gradient forces of the two beams change when adjusting the power. Three special cases are indicated on the graph with the corresponding intensity profiles shown in Fig. 4b: the vector flat-top beam along with Gaus-

sian beams that have 1) the same power, 2) the same gradient force and 3) the same peak intensity as the flat-top are plotted. Firstly, in the instance when the power of the two beams are equal, $\gamma = 0.75$, meaning the Gaussian beam is a stronger trap (blue line). This is expected, since even though the intensity gradient of the vector flat-top is steeper, the high intensity peak of the Gaussian beam negates this effect. Secondly, for the two beams to have the same average gradient force ($\gamma = 1$), the Gaussian beam must have 75% of the power of the vector flat-top beam (green line). Lastly, when the two beams have the same peak intensity, that is when the power of the Gaussian is half that of the flat-top beam, then the flat-top beam trap is 1.5 times stronger than the Gaussian beam trap (orange line). Most relevant is the case when the two beams have the same gradient force; here it is clear that when the vector flat-top beam and the Gaussian beam have the same trap strength (or gradient force), the peak intensity of the vector flat-top is lower than the Gaussian beam. This means that the vector flat-top beam can be used to trap a particle with the same strength but with a lower peak intensity.
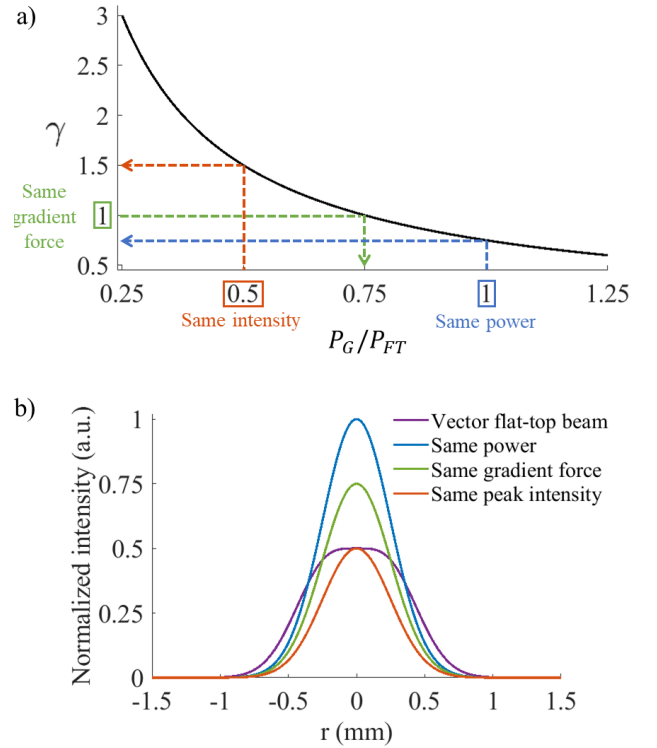
Fig. 4 a) The relationship between the relative gradient force and power of a Gaussian and vector flat-top beam. b) The intensity profiles corresponding to a Gaussian beam having the same power, gradient force and intensity as a vector flat-top beam.

2.2.2 Vector HOT setup

The experimental setup of the vector holographic optical trap is illustrated in Fig. 5. A horizontally polarized Gaussian beam from a $\lambda = 532$ nm laser was expanded and collimated before illuminating the screen of a reflective spatial light modulator (SLM, Holoeye Pluto, Germany). The SLM was aligned to only modulate horizontally polarized light. To create a vector flat-top beam,

211

a Gaussian (LG_0^0) and a vortex beam (LG_0^1) with different propagation angles were created with the SLM (the insets show the 2D intensity profiles of experimentally obtained beams). The multiplexed grey-scale hologram that was encoded on the SLM using complex amplitude modulation, is shown in the top panel, with the different gratings of the two beams as insets. The Gaussian and vortex beams were separated using a D-shaped mirror (D-M) in order to direct the beams to a polarizing beam splitter (PBS) where they were interferometrically combined. The unwanted zeroth and higher orders were removed by spatial filtering before the PBS. A half wave plate (HWP) was added in the path of one beam to change its polarization from horizontal to vertical, to allow for the superposition of orthogonal polarized beams. The vector flat-top beam was therefore obtained after the PBS; the bottom panel shows the cross-section of an experimentally obtained flat-top beam in the near and far field.

The reflection of light from a dichroic mirror (DM) is slightly different for horizontally and vertically polarized light. In order to ensure that the DM did not change the profile of the vector beam (given that its performance varies slightly for the orthogonal polarizations), a quarter wave plate (QWP) at 45° was added in the path of the vector beam to change the polarization of each beam to circular (meaning the two beams making the vector light have the same 'amount' of vertical and horizontal polarization and the DM will have the same effect on both). The 4f-system (lenses L1 and L2) was included to ensure the generated beam reached the back aperture of the objective lens. The high NA objective lens O focused the beam to create the optical trap in the plane of the sample.

The sample consisted of either 2 μm polystyrene beads (sample used for obtaining trap stiffness) or QD-tagged polystyrene beads (fluorescent sample) supported between a cover slip and microscope slide. Untreated glassware contains silanol groups (Si-OH), which make the surface of the glass hydrophilic, causing polar compounds to adsorb to the surface through hydrogen bonding. In this study, the polystyrene beads and the QD-tagged beads contained polar groups on their surfaces. Thus, due to these groups, the beads became immobilized on the surface of untreated glass which caused a problem when attempting to trap the particles. To solve this, the glassware (microscope slides and cover slips) was deactivated before assembling the samples. Deactivation of the glassware increased its hydrophobicity and prevented the
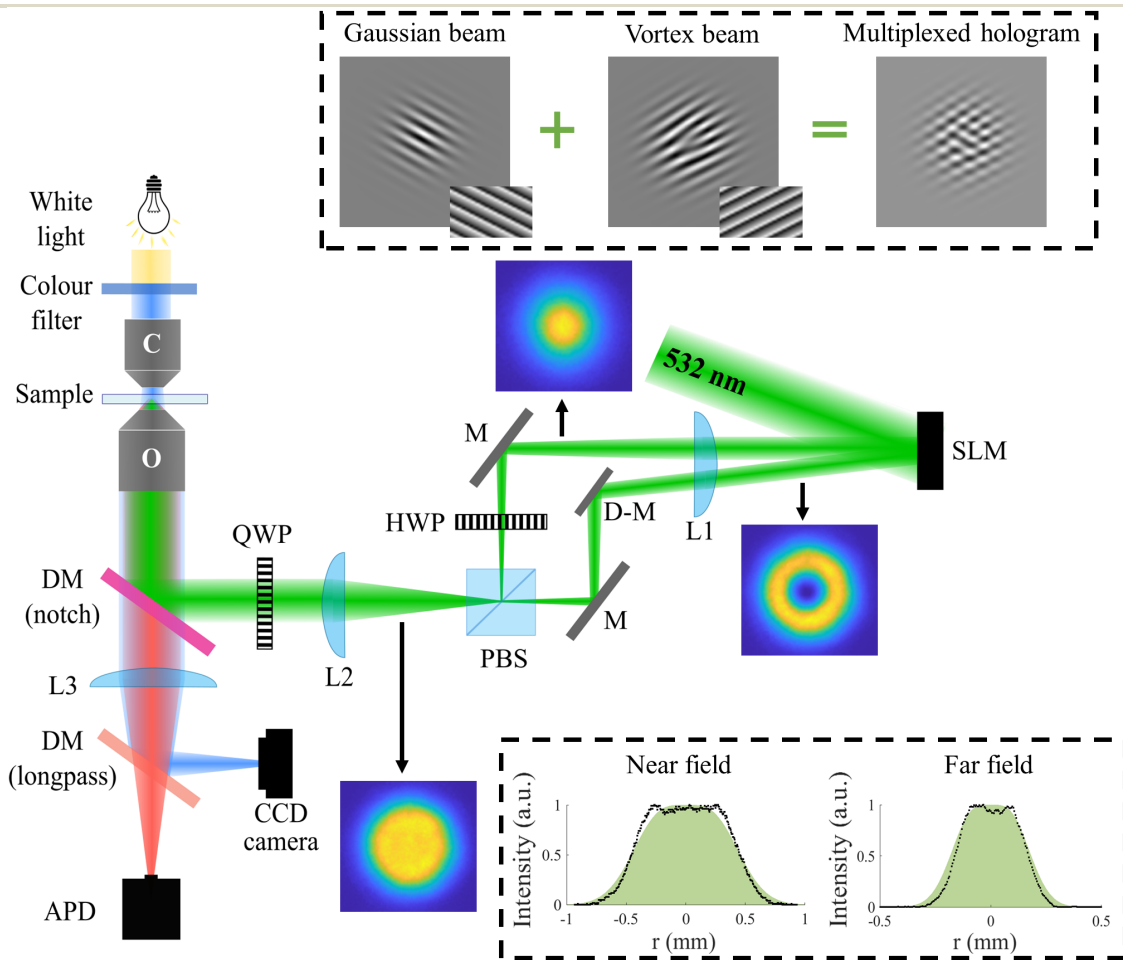
Fig. 5 An illustration of the experimental setup of a vector holographic optical tweezer. The insets show the experimentally generated vortex and Gaussian beams that were combined to form the vector flat-top beam. The multiplexed hologram that was encoded on the SLM to generate a Gaussian and vortex beam with different propagation angles is shown in the top panel. The bottom panel shows the cross-section of an experimentally generated flat-top beam in the near and far field. Theoretical cross-sections are presented in green with the experimental data points in black.

212

unwanted adsorption of polar compounds. Deactivation was achieved by reacting the glassware with dimethyldichlorosilane (DMDCS).

An inverted microscope setup was implemented with a DM reflecting the laser light into the objective while letting the fluorescence and illumination light pass through. The same laser was used for both trapping and excitation. In order to simultaneously observe trapping and fluorescence emission from the sample, the imaging/detection system was set up such that blue light was used to illuminate the sample which was transmitted by the notch DM, reflected by the longpass DM and imaged to a CCD camera. The fluorescence emission (red beam) from the sample was transmitted by both DMs to be detected by an avalanche photodiode (APD, a single photon detector). This sensitive photon detector was necessary to detect the fluorescence coming from a single QD-tagged bead. Since the DMs are not 100% effective, extra color filters were inserted to ensure no light from the trapping laser reached the camera or APD.

Even though this study focused on creating vector flat-top beams, this setup can be used to generate any arbitrary vector beam by simply superimposing different scalar beams. For example, adding two vortex modes, LG_0^1 and LG_0^{-1}, will create radially and azimuthally polarized vortex beams.

2.2.3 Trapping with vector flat-top beams

The motion of a free particle and a particle trapped with a vector flat-top beam were monitored for 5 min. The trajectory and the distribution of these particles' position in the Y-direction are shown in Fig. 6a. The particle position was tracked using the CCD camera and all image analysis was done in Matlab. From this figure, it is clear that the free particle underwent random Brownian motion and in 5 min moved over 7.33 μm (in the Y-direction). The trapped particle was, however, confined to move only 0.44 μm during the analysis time, which proves successful optical trapping with a vector flat-top beam.

The slight movement of the particle inside the trap is due to thermal noise pushing it out of the trap and the optical force drawing it back in. By monitoring this movement, the trap strength could be determined using the equipartition method which relates the trap strength to the position variance of the trapped particle.[37] The motion of a trapped bead was tracked for 5 min, taking a position measurement every second. Five beads were trapped for each power measurement at which the trap stiffness was determined. The average trap stiffness at each power is plotted in Fig. 6b with the error bars being the standard error. The linear relationship between the laser power and the trap stiffness is evident from this graph. The insets show the trajectory of the trapped particle at increasing powers of 30 μW, 120 μW and 300 μW.

2.2.4 Tailoring the trap

In Fig. 7 the tuneability of the vector HOT is demonstrated by changing the trapping beam from purely scalar Gaussian and vortex beams to their vectorial combination; here we also demonstrate the effect of trapping with different beam sizes. In the top row the theoretical profiles (plotted in color) of the trapping beams are shown and are in good agreement with the experimental data (presented in black).

The optical trapping force a particle will experience (due to a focused beam) depends on the beam size relative to the particle. In the theory presented earlier, the average gradient force
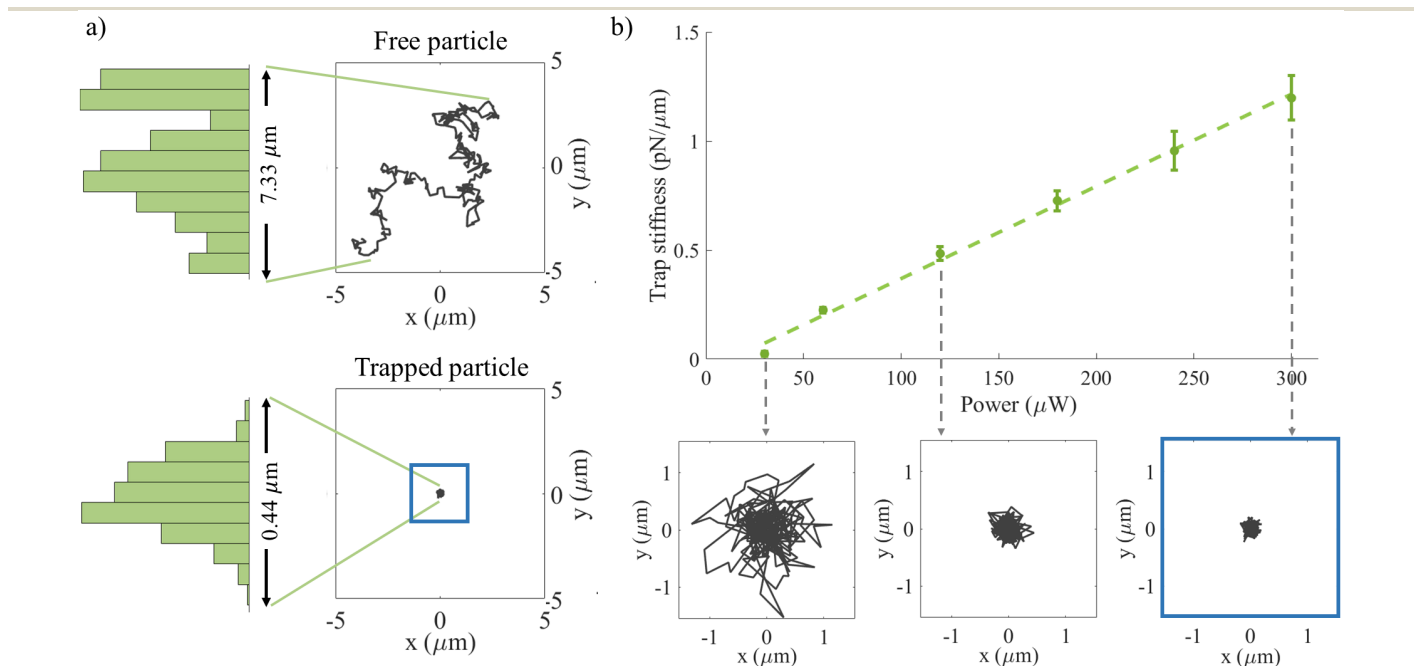
Fig. 6 a) Trajectory and probability density (in the y-direction) of a free particle and a particle trapped with a vector flat-top beam, monitored for 5 min. The free particle exhibits Brownian motion and moves over 7.33 μm whereas the trapped particle's movement is restricted to only 0.44 μm. b) Vector flat-top trap stiffness (in the x-direction) at different laser powers. The insets show the trajectory of a trapped particle at increasing powers of 30 μW, 120 μW and 300 μW, respectively.

213

of the beam was determined by integrating over the total area of the beam. The particle will, however, only experience this total force if it intercepts the entire beam; which is true when the beam at the trap is smaller than the particle size. This was the case for the trapped beads in the middle row of Fig. 7, here 2 μm beads were trapped with a beam diameter of 1.8 μm. The bottom row shows the movement of a bead in an optical trap where the beam is larger (3.1 μm) than the bead. For the small traps, the movement of the bead was concentrated at the centre of all the beams with a little more movement in the vortex beam and more in the flat-top beam. Harmonic oscillation could be assumed and the trap stiffness (calculated with the equipartition method) is reported for these traps (unit: pN/μm). The movement of the bead in the large Gaussian trap was also centred but less stiff than for the small Gaussian trap. The particle trapped in the large vortex beam, moved along the ring of the beam where the intensity gradient and consequently the trapping force exists. Lastly, the movement of the bead in the large flat-top trap was more uniform, corresponding to the uniform beam profile (only a gradient force exists at the edges of the beam). From these plots it is clear that the size and type of beam have a great influence on the strength and properties of an optical trap.
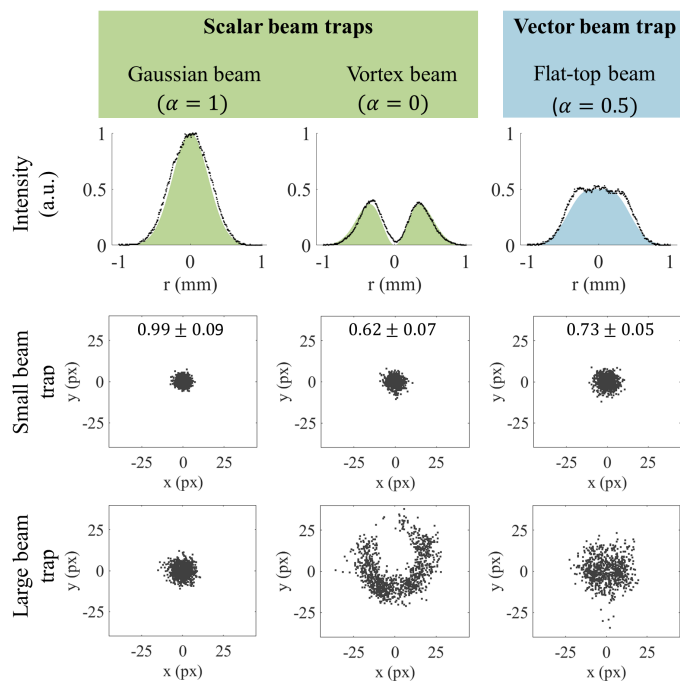
Fig. 7 Movement of beads trapped with a Gaussian, vortex and vector flat-top beam when the beam size is smaller than the particle (small beam trap) or larger than the particle (large beam trap). The bead had a 2 μm diameter, the small trap had a beam diameter of 1.8 μm and the large trap a diameter of 3.1 μm. The trap strengths for the small beam traps are reported (unit: pN/μm).

2.3 Photobleaching effect

The vector flat-top beam can be generated to have the same gradient force as the Gaussian beam, but with a 25% reduced peak intensity (refer to Fig. 4). This property of flat-top beams can be exploited to reduce photobleaching in optical traps. Moreover,

if flat-top beams are generated with the same power as Gaussian beams, they have a 50% reduced peak intensity, with only a minimal loss of gradient force (trap strength) especially at low trapping powers (as shown in Fig. S1). Fig. 8 shows the fluorescence emission of a QD-tagged bead trapped with a Gaussian or a flat-top beam in a single wavelength trap. For both traps the fluorescence of the particle reduced upon entering the trap. The fluorescence signals were normalized and background subtracted (detail in Fig. S2). However, the flat-top beam increased the photobleaching lifetime of the fluorescent particles. The photobleaching of several QD-tagged beads were measured and the bleaching half-life of a QD-tagged bead in a Gaussian trap was determined to be 7.6 $\pm$ 0.6 s and the half-life in a vector flat-top trap 11 $\pm$ 1 s, which is a 45% increase in the photobleaching half-life.
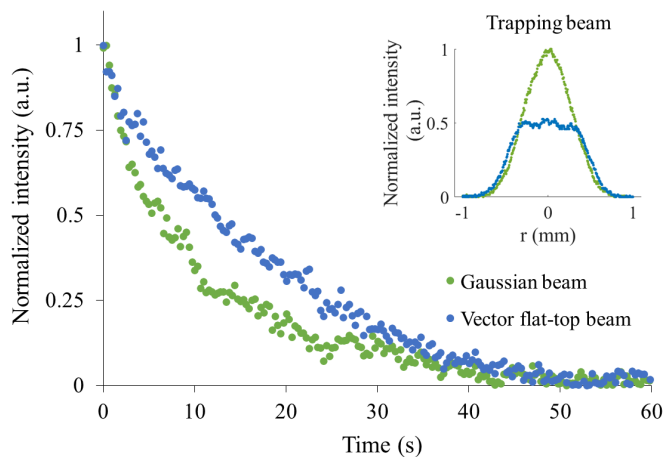
Fig. 8 Photobleaching of a trapped QD-tagged bead in a Gaussian and flat-top beam trap (at a trapping power of 60 μW). Longer photobleaching lifetimes were observed for the fluorophores in the flat-top beam trap as compared to the Gaussian beam trap. The inset shows the experimental profiles of the trapping beams.

3 Conclusion

Overall, this research demonstrated an optical tweezer setup leveraging on vectorial light to trap QD fluorescent probes. We outlined the chemistry involved to functionalize micro-sized polymer spheres with QDs, highlighting the importance of size, adhesion and agglomeration control. The versatility of the vector HOT was demonstrated by switching between scalar and vector beams and trapping particles with different beam sizes. By trapping with a propagation invariant vector flat-top beam, we showed that photobleaching in a single wavelength optical trap can be reduced by simply tailoring the intensity gradient landscape.

4 Materials and methods

4.1 Chemicals

Cadmium oxide (CdO), octadec-1-ene (ODE), oleic acid (OA), trioctylphosphine oxide (TOPO), selenium (Se), zinc oxide (ZnO), sulfur (S), L-cysteine, N-(3-dimethylaminopropyl)-N'-ethylcarbodiimide hydrochloride (EDC), N-hydroxysuccinimide (NHS), methanol and acetone were purchased from Sigma

214

Aldrich (USA). Chloroform, ethanol and potassium hydroxide (KOH) were purchased from Associated Chemical Enterprises (South Africa). Argon gas baseline 5.0 from Afrox (South Africa) was used. Deionized water used during the syntheses was from an in-house Drawell Eco-Q deionized water system (China). Invitrogen™ 2 μm carboxyl functionalized latex beads were purchased from Thermo Fisher Scientific (South Africa).

4.2 Quantum dot synthesis

Firstly, selenium (0.30 g Se, 1.94 g TOPO and 25 ml ODE), zinc (0.21 g ZnO, 10 ml OA and 15 ml ODE) and sulphur precursor solutions were prepared. These solutions were stirred at 40 °C for 5 hr to ensure thorough mixing. The QD synthesis setup included a three-necked round bottom flask fitted with a condenser, thermometer and an argon gas inlet positioned on a heating mantle. The whole reaction was done under argon conditions. 1.3 g CdO, 50 ml ODE and 30 ml OA were added to the flask and stirred vigorously at 260 °C until a colourless solution formed indicating the formation of the Cd-OA complex. The Se-precursor was added to the flask (25 ml) and nucleation and core growth were allowed to proceed for 15 min at a temperature of ∼240 °C. The epitaxial ZnS shell growth around the core was initiated by adding 10 ml of the Zn-precursor, and swiftly thereafter 10 ml of the S-precursor to the core solution. Shell growth was left to proceed for 40 min at a temperature of 240 °C. After 40 min the reaction was cooled to room temperature. The QDs were purified with methanol by centrifugation which then yielded the hydrophobic CdSe/ZnS QDs capped with OA and TOPO.

A ligand-exchange reaction was carried out next to functionalize the surface of the CdSe/ZnS QDs with L-cysteine in order to make them hydrophilic. A solution of 4.4 g KOH, 60 ml MeOH and 3 g L-cysteine was prepared and placed in an ultrasonic bath for 10 min to ensure all the L-cysteine dissolved. The hydrophobic CdSe/ZnS QD solution was suspended in chloroform and added to the L-cysteine solution. Deionized water was slowly added to the mixture while stirring at room temperature which changed the transparent orange solution to milky. After an hour of stirring, the solution was left to stand overnight to ensure complete separation of the organic and aqueous phases. The L-cysteine capped QDs, now in the aqueous phase, were purified by centrifugation with ethanol (×4) and acetone (×2). Rigorous purification was necessary to remove the excess organic compounds from the surface of the QDs to achieve a monodispersed QD solution with no agglomerates. The absorbance and FTIR spectra of the QD-products are shown in Fig. S3 and S4, respectively.

4.3 Coupling reaction

To couple the L-cysteine-capped QDs to micro-sized polymer beads, 2.5 ml of EDC (0.1 M) and 2.5 ml NHS (0.1 M) were added to 50 μl of the polymer beads (diluted in 1 ml water) and stirred for 30 min in an ice bath to activate the carboxylic acid groups on the beads. Excess EDC was removed by centrifugation with deionized water. After centrifuging, the activated beads were redispersed in 4 ml water and 3 mg of QDs was added. The coupling reaction was left to proceed in an ultrasonic bath for 2 h to ensure even coating of the QDs on the beads. The coupled product was purified by centrifugation with water (×3) and stored in deionized water in the fridge. The FTIR spectra of the QD-tagged beads are shown in Fig. S5.

Conflicts of interest

There are no conflicts to declare.

Acknowledgements

References

1 A. Ashkin, *Physical Review Letters*, 1970, **24**, 156.

2 D. G. Grier, *Nature*, 2003, **424**, 810–816.

3 K. Dholakia and T. Čižmár, *Nature Photonics*, 2011, **5**, 335–342.

4 E. R. Dufresne, G. C. Spalding, M. T. Dearing, S. A. Sheets and D. G. Grier, *Review of Scientific Instruments*, 2001, **72**, 1810–1816.

5 S. Segawa, Y. Kozawa and S. Sato, *Optics Letters*, 2014, **39**, 3118–3121.

6 S. C. Chapin, V. Germain and E. R. Dufresne, *Optics Express*, 2006, **14**, 13095–13100.

7 V. Garcés-Chávez, D. McGloin, H. Melville, W. Sibbett and K. Dholakia, *Nature*, 2002, **419**, 145–147.

8 J. Baumgartl, M. Mazilu and K. Dholakia, *Nature Photonics*, 2008, **2**, 675–678.

9 M. E. Friese, T. A. Nieminen, N. R. Heckenberg and H. Rubinsztein-Dunlop, *Nature*, 1998, **394**, 348–350.

10 V. Garcés-Chávez, D. McGloin, M. J. Padgett, W. Dultz, H. Schmitzer and K. Dholakia, *Physical Review Letters*, 2003, **91**, 093602.

11 M. Padgett and R. Bowman, *Nature Photonics*, 2011, **5**, 343–348.

12 E. Otte and C. Denz, *Applied Physics Reviews*, 2020, **7**, 041308.

13 C. Rosales-Guzmán, B. Ndagano and A. Forbes, *Journal of Optics*, 2018, **20**, 123001.

14 S. Quabis, R. Dorn, M. Eberler, O. Glöckl and G. Leuchs, *Optics Communications*, 2000, **179**, 1–7.

15 E. Otte, K. Tekce and C. Denz, *Optics Express*, 2017, **25**, 20194–20201.

16 H. Moradi, V. Shahabadi, E. Madadi, E. Karimi and F. Hajizadeh, *Optics Express*, 2019, **27**, 7266–7276.

17 M. Michihata, T. Hayashi and Y. Takaya, *Applied Optics*, 2009, **48**, 6143–6151.

18 N. Bhebhe, P. A. Williams, C. Rosales-Guzmán, V. Rodriguez-Fajardo and A. Forbes, *Scientific Reports*, 2018, **8**, 1–9.

19 J. C. Cordova, D. K. Das, H. W. Manning and M. J. Lang, *Current Opinion in Structural Biology*, 2014, **28**, 142–148.

215

20 D. Choudhary, A. Mossa, M. Jadhav and C. Cecconi, *Biomolecules*, 2019, **9**, 23.

21 M. Hashemi Shabestari, A. E. Meijering, W. H. Roos, G. J. Wuite and E. J. Peterman, *Methods in Enzymology*, 2017, **582**, 85–119.

22 M. A. van Dijk, L. C. Kapitein, J. van Mameren, C. F. Schmidt and E. J. Peterman, *The Journal of Physical Chemistry B*, 2004, **108**, 6479–6484.

23 A. Diaspro, G. Chirico, C. Usai, P. Ramoino and J. Dobrucki, *Handbook of Biological Confocal Microscopy*, Springer, 2006, pp. 690–702.

24 G. Ma, C. Hu, S. Li, X. Gao, H. Li and X. Hu, *Nanotechnology and Precision Engineering*, 2019, **2**, 145–156.

25 A. Ishijima, H. Kojima, T. Funatsu, M. Tokunaga, H. Higuchi, H. Tanaka and T. Yanagida, *Cell*, 1998, **92**, 161–171.

26 M. J. Lang, P. M. Fordyce and S. M. Block, *Journal of Biology*, 2003, **2**, 1–4.

27 R. R. Brau, P. B. Tarsa, J. M. Ferrer, P. Lee and M. J. Lang, *Biophysical Journal*, 2006, **91**, 1069–1077.

28 Z. Zhang and J. Milstein, *Journal of Optics*, 2020, **22**, 095301.

29 M. Noh, T. Kim, H. Lee, C.-K. Kim, S.-W. Joo and K. Lee, *Colloids and Surfaces A: Physicochemical and Engineering Aspects*, 2010, **359**, 39–44.

30 S. De Silvestri, P. Laporta, V. Magni and O. Svelto, *IEEE Journal of Quantum Electronics*, 1988, **24**, 1172–1177.

31 F. Gori, *Optics Communications*, 1994, **107**, 335–341.

32 N. Bhebhe, C. Rosales-Guzman and A. Forbes, *Applied Optics*, 2018, **57**, 5451–5458.

33 C. Rosales-Guzmán and A. Forbes, *How to shape light with spatial light modulators*, SPIE Press, 2017.

34 K. C. Neuman and S. M. Block, *Review of Scientific Instruments*, 2004, **75**, 2787–2809.

35 P. Bartlett and S. Henderson, *Journal of Physics: Condensed Matter*, 2002, **14**, 7757.

36 Y. Harada and T. Asakura, *Optics Communications*, 1996, **124**, 529–541.

37 J. Gieseler, J. R. Gomez-Solano, A. Magazzù, I. Pérez Castillo, L. Pérez García, M. Gironella-Torrent, X. Viader-Godoy, F. Ritort, G. Pesce, A. V. Arzola, K. Volke-Sepúlveda and G. Volpe, *Advances in Optics and Photonics*, 2021, **13**, 74–241.

216

C.3 Co-author journal paper

Co-author research paper accepted for publication in *Nature Photonics.*

Author contribution: performed the optical trapping experiments presented in FIG. 7b.

Revealing the invariance of vectorial structured light in perturbing media

Isaac Nape,[1, *] Keshaan Singh,[1, *] Asher Klug,[1] Wagner Buono,[1] Carmelo Rosales-Guzman,[2, 3] Amy McWilliam,[4]
Sonja Franke-Arnold,[4] Ané Kritzinger,[5, 1] Patricia Forbes,[5] Angela Dudley,[1] and Andrew Forbes[1, †]

[1]*School of Physics, University of the Witwatersrand, Private Bag 3, Wits 2050, South Africa*
[2]*Centro de Investigaciones en Óptica, A. C., Loma del Bosque 115,*
Col. Lomas del Campestre, 37150, León, Gto., México
[3]*Wang Da-Heng Collaborative Innovation Center for Quantum Manipulation and Control,*
Harbin University of Science and Technology, Harbin 150080, China
[4]*School of Physics and Astronomy, University of Glasgow, Glasgow G12 8QQ, Scotland*
[5]*Department of Chemistry, University of Pretoria, Pretoria, South Africa*
(Dated: February 28, 2022)

Optical aberrations have been studied for centuries, placing fundamental limits on the achievable resolution in focusing and imaging. In the context of structured light, the spatial pattern is distorted in amplitude and phase, often arising from optical imperfections, element misalignment, or even from dynamic processes in perturbing media such as turbulent air, underwater and optical fibre. Here we show that the polarisation inhomogeneity that defines vectorial structured light is immune to all such perturbations, provided they are unitary. By way of example, we study the robustness of vector vortex beams through highly aberrated systems, demonstrating that the inhomogeneous nature of the polarisation remains unaltered even as the structure itself changes. The unitary nature of the channel allows us to undo this change through a simple lossless operation, tailoring light that appears robust in all its spatial structure regardless of the medium. Our insight highlights the overlooked role of measurement in describing classical vectorial light fields, in doing so resolving prior contradictory reports on the robustness of vector beams in complex media. This paves the way to the versatile application of vectorial structured light, even through non-ideal optical systems, crucial in applications such as imaging and optical communication across noisy channels.

Non-paraxial light is vectorial in 3D and has given rise to exotic states of structured light [1] such as optical skyrmions [2, 3], knotted strands of light [4, 5], flying donuts [6, 7] and Möbius strips [8]. Paraxial light too is vectorial, in 2D, characterised by an inhomogeneous polarisation structure across the transverse plane [9]. Vectorial structured light in 2D and 3D has been instrumental in a range of applications (see Refs. [10–13] and references therein), for example, to drive currents with a direction dictated by the vectorial nature of the optical field [14, 15], imprinting the spatial structure into matter [16], enhanced metrological measurements [17, 18], probing single molecules [19], and to encode more information for larger bandwidths [20–23]. They are easy to create in the laboratory using simple glass cones [24], stressed optics [25] and GRIN lenses [26], as well as from spatial light modulators and digital micro-mirror devices [27, 28], non-linear crystals [29, 30], geometric phase elements [31, 32], metasurfaces [33] and directly from lasers [34].

Given the importance of these structured light fields, much attention has been focused on their propagation through optical systems that are paraxial [35], guided [36] and tight focusing [37, 38], as well as in perturbing media such as turbid [39–42], turbulent [43–50] and underwater [51–53]. The conclusions are seemingly contradictory, with compelling evidence that the vectorial structure is stable, and equally compelling evidence that it is not, while the specific nature of each study prohibits making general conclusions on the robustness of vectorial light in arbitrary complex media.

Here we show that the inhomogeneity of a vectorial light field is impervious to complex channels so long as they are unitary (where an inverse process exists), a condition fulfilled for many aberrated optical systems. We illustrate this with two examples featuring strong aberrations: a tilted lens, and atmospheric turbulence simulated on a spatial light modulator. We then demonstrate the power of our framework by testing it for transmission through chiral liquids, optical fibre, turbulent air and complex optical aberrations. Our quantum-inspired framework explains the robustness of vectorial light fields by virtue of unitary operations on the vectorial state, manifesting as an intact inhomogeneity even if the vectorial pattern appears spatially distorted due to modal scattering in the component scalar spatial modes. We show that the channel action can be reversed by a reciprocal unitary process applied either pre-channel or post-channel, as well as cross-talk free detection of vectorial fields through complex media. Our study highlights the importance of measurement in the context of vectorial light fields, in doing so resolving a standing paradox on

_____

* author contributions: These authors contributed equally to the work
† email: andrew.forbes@wits.ac.za

the robustness of vectorial light to perturbations, and provides a general framework for understanding the impact of arbitrary optical aberrations on vectorial structured light fields.

RESULTS

Vectorial light and unitary channels. A vectorial structured light field can be written compactly in a quantum notation as the unnormalised state

$$|\Psi\rangle = |e_1\rangle_A |u_1\rangle_B + |e_2\rangle_A |u_2\rangle_B, \qquad (1)$$

highlighting the non-separable nature of the two degrees of freedom (DoFs), A and B, denoting the polarization and the spatial degree of freedom, respectively. In this way, the vectorial field is treated as a quantum-like state (but not quantum and without non-local correlations), by virtue of its non-separable DoFs, akin to a locally entangled state [54–58]. The polarisation DoF is expressed as any pair of orthonormal states, $\{|e_1\rangle$ and $|e_2\rangle\}$ while the spatial mode DoF is given by the orthonormal basis states $\{|u_1\rangle$ and $|u_2\rangle\}$. In a quantum sense, this vectorial structured field would be called a pure state. The vectorial nature can be quantified through a measure of its non-separability [59], a Vector Quality Factor (VQF) (equivalently concurrence) which for succinctness we will call its "vectorness", ranging from 0 (homogeneous polarisation structure of scalar light) to 1 (ideally inhomogeneous vectorial polarisation structure).
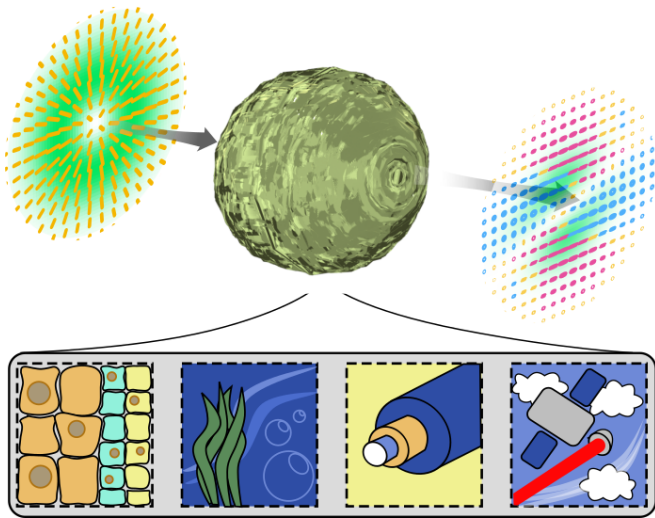

FIG. 1: **Complex light in complex channels.** A vectorial light field propagates through a perturbing medium. Examples of such perturbing media could be turbid, underwater, optical fibre or turbulent air. Here and elsewhere the beam profiles illustrate intensities (green gradients) overlaid with polarisation ellipses indicating right-handed (red), left-handed (blue) and linear (orange) polarisations.

Now imagine that our vectorial light field, $|\Psi_{\text{in}}\rangle$, passes through an arbitrary aberrated optical channel, as illustrated in Figure 1, e.g., static imperfect optics or dynamic turbulent air. If the channel acts on only one DoF then this can be considered a one-sided channel, terminology borrowed from quantum communication theory, describing a situation where only one of the two entangled photons is affected. For our classical light, an example would be when the spatial mode (DoF B) is affected (distorted), while the polarisation (DoF A) is not, or vice versa. In our analysis here we will use DoF A as unaffected, but this can be changed by a simple relabeling exercise. An open question is whether distortions acting only on the spatial DoF would keep the entire structure of the vectorial light field intact? It has been argued that the unaffected DoF acts as an anchor of sorts, keeping the entire field structure intact, and sometimes phrased as a 'topological protection' of the optical mode when discussing perturbations that affect the spatial but not the polarisation DoF.

To answer this question we employ a quantum framework, with full details provided in the Supplementary Information (SI). We show that a unitary one-sided channel, since it may be written as a positive trace-preserving map, transforms a vectorial (pure) input state $|\Psi_{\text{in}}\rangle$ into a vectorial (pure) output state $|\Psi_{\text{out}}\rangle$. Such a transformation may be expressed as

$$|\Psi_{\text{out}}\rangle = (\mathbb{1}_A \otimes T_B) |\Psi_{\text{in}}\rangle, \qquad (2)$$

where $|\Psi_{\text{in}}\rangle$ is of the form Eq. 1, the identity operator $\mathbb{1}_A$ acts on the polarisation DoF A, while the transmission matrix T_B acts on the spatial DoF B. Without loss of generality, the transmission matrix may be expressed as $T_B = \Sigma_{i,j} t_{ij} |u_i\rangle \langle u_j|$, and for a unitary channel $t_{ij} = t_{ji}^*$. This allows us to write the output state as

$$|\Psi_{\text{out}}\rangle = |e_1\rangle |v_1\rangle + |e_2\rangle |v_2\rangle, \qquad (3)$$

where $|v_1\rangle = t_{11} |u_1\rangle + t_{12} |u_2\rangle$ and $|v_2\rangle = t_{21} |u_1\rangle + t_{22} |u_2\rangle$. The fact that the channel is unitary moreover preserves the overlap between the spatial basis states, $\langle v_1|v_2\rangle = \langle u_1| T_B^\dagger T_B |u_2\rangle = \langle u_1|u_2\rangle$, and hence the vectorness of the beams. Orthogonal input modes are transformed into another set of orthogonal output modes, and the vectorness remains invariant. We may interpret the action of the channel as a simple change of basis in the spatial DoF, a rotation of the input basis $|u_i\rangle$ into an adjusted basis set $|v_i\rangle$.

The answer to our question is then as follows: the output remains a non-separable vector beam with the same vectorness as the initial beam (see SI for the full proof). Its spatial structure, however, including its amplitude, phase and polarisation profile, will be altered by the distorting medium, and our description of the vectorial structure has changed from Eq. 1 to Eq. 3, expressed in an adjusted basis set $|v_i\rangle$. This is a direct manifestation of the Choi–Jamiolkowski isomorphism in quantum mechanics [60], which establishes a correspondence between a channel operator and a quantum state, so that
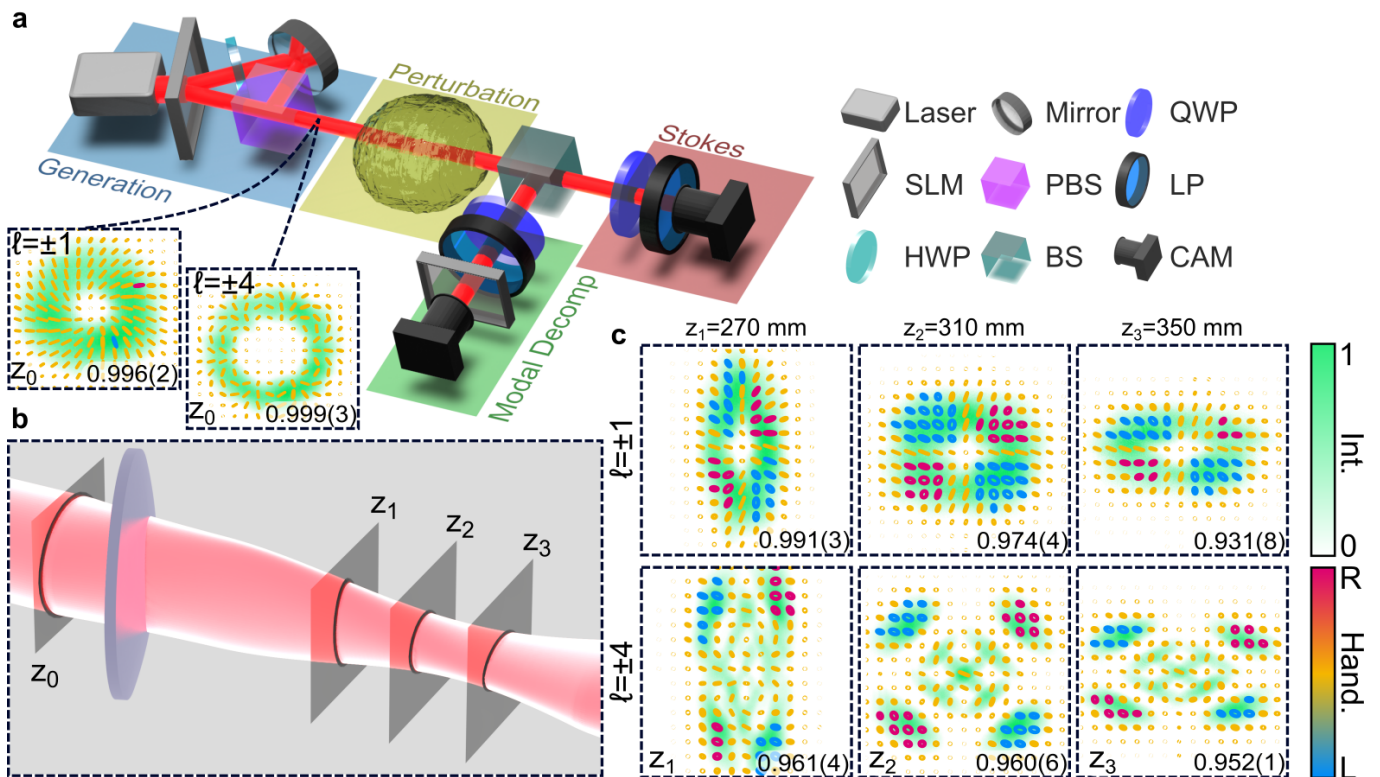
FIG. 2: **Vectorial light through a tilted lens.** (a) The experiment has four stages: a generation stage to create the vectorial fields, a perturbation stage to pass it through a perturbing medium, and two detection stages to perform Stokes projections and modal decomposition. The insets show the initial $\ell = \pm 1$ (left panel) and $\ell = \pm 4$ (right panel) beams at plane Z_0. (b) Illustration of the propagation through a tilted lens, with exemplary measurement planes indicated as Z_1 through to Z_3. (c) The output $\ell = \pm 1$ and $\ell = \pm 4$ beams at these distances, confirm that the spatial structure alters with distance but that the vectorness (the inset number to each beam frame) does not, remaining above 93%. The optical elements comprise a HWP: half-wave plate, PBS: polarising beam splitter, Pol: polariser, BS: beam splitter, QWP: quarter-wave plate, and CAM: camera, with the laser at wavelength $\lambda = 633$ nm. All beam profiles are shown as false colour intensity and polarisation maps. Full experimental details given in the Methods.

a measurement on one returns the other [61, 62]. Applied to classical vectorial light, justified because of its non-separability [63], we find that the channel is fully described by its action on the vectorial beam, and to measure the beam fully characterises the channel.

A property of a unitary channel is that the inverse process can be written as

$$|\Psi_{\text{in}}\rangle = (\mathbb{1}_A \otimes T_B)^{-1} |\Psi_{\text{out}}\rangle, \qquad (4)$$

because the Hermitian adjoint of the channel operator is simply its inverse, $(\mathbb{1}_A \otimes T_B)^{-1} = (\mathbb{1}_A \otimes T_B)^{\dagger}$, or in experimental terms: the aberration introduced by transmission through the unitary channel can be undone, when sending the beam back through the channel. Equations (2) and (4) suggest that: (i) the vectorial nature of the final field shares the same vectorness as the initial field, (ii) the mapping results in a new adjusted basis which can be used for efficient characterisation of the state, and (iii) since the mapping is unitary it can always be unravelled

before or after the channel in a lossless manner. Note that in this analysis we have not needed to specify details of the DoFs (what the modes or polarisation might look like), nor the channel itself (water, air, etc). We now showcase this generality through a series of exemplary test cases covering a wide range of input fields and channel conditions.

Experimental demonstration: the tilted lens. To validate this perspective, we built the set-up shown in Figure 2 (a), first creating our test vectorial fields before passing them through some perturbing medium. Without any loss of generality, we chose the left- and right-circular basis, $\{|e_1\rangle \equiv |R\rangle$ and $|e_2\rangle \equiv |L\rangle\}$, for the polarisation degree of freedom and spatial modes imbued with orbital angular momentum (OAM) following $\{|u_1\rangle \equiv |\ell\rangle$ and $|u_2\rangle \equiv |-\ell\rangle\}$, with ℓ the topological charge, forming the topical cylindrical vector vortex beams [64]. The resulting vectorial field was then analysed by both Stokes measurements and modal decomposition (see Methods).
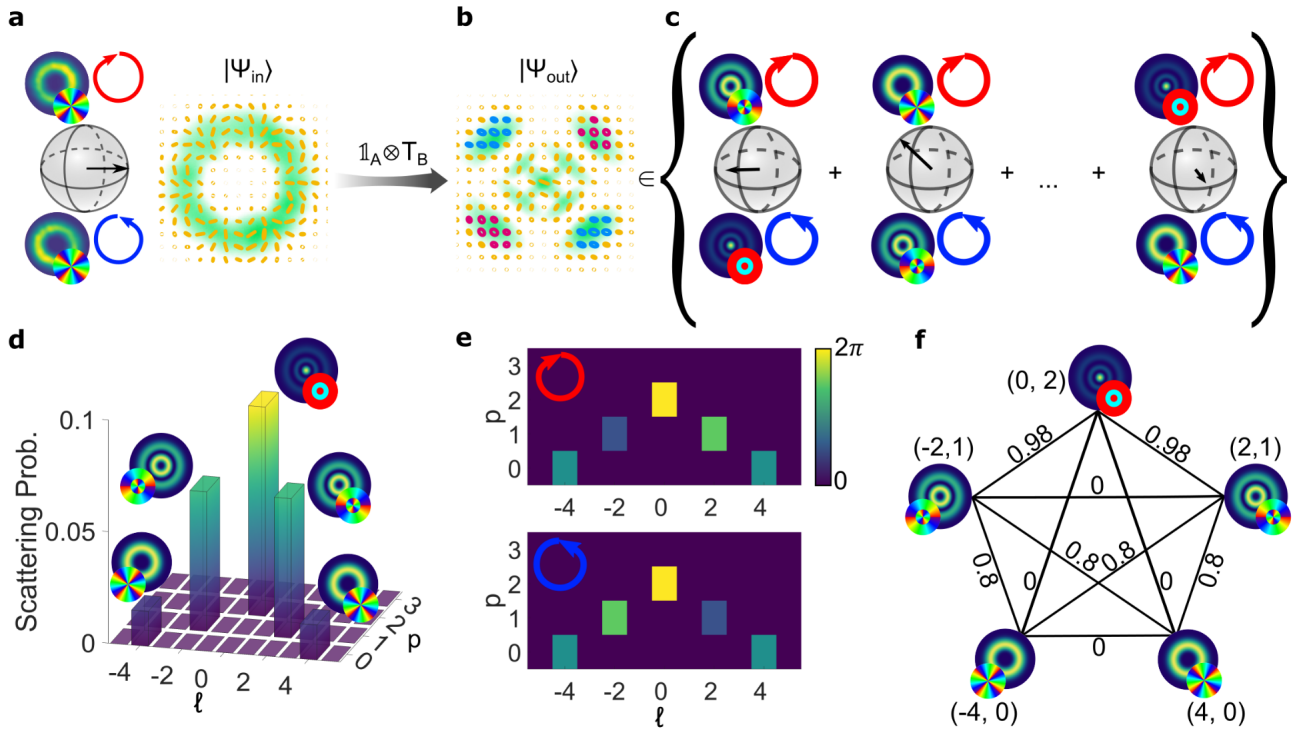
FIG. 3: **Impact of scattering across multiple subspaces**. (a) The initial vector beam is geometrically represented by an equatorial state vector of unit length on a single $\ell = \pm 4$ HOP Sphere, indicative of a maximally non-separable pure state. The experimental basis states are shown on the poles (as intensities with their respective polarisation state on the right) and the vectorial sum (amplitude and polarisation structure) is shown on the equator. The tilted lens deforms the initial mode into (b), and this new state can be mapped to multiple HOP Spheres, each spanned by a different OAM and radial mode (c). Each of these potentially describes a mixed state of some degree of non-separability (non-unit and/or non-equatorial state vectors). The (d) scattering probabilities and (e) phases over the OAM (ℓ) and radial (p) modes for the right (left) ($R(L)$) circular polarisation components after the $\ell = \pm 4$ vectorial field traverses the tilted lens channel. The right and left components have equivalent scattering probabilities. There are $N = 5$ states, (ℓ, p), with non-zero probabilities and $N(N-1)/2 = 10$ pairs of multiple subspaces that can be formed. (f) The pairs of states constituting the subspace and corresponding VQF for the vector field in that particular subspace can be represented with a graph having a set of vertices (as the contributing states) connected by weighted edges, respectively. The weights of the edges correspond to the VQF.

The superimposed intensity and polarisation profile of the initial beams (no perturbation) are shown in the inset of Figure 2 (a) for $\ell = \pm 1$ and $\ell = \pm 4$, both with a radial mode of $p = 0$, with corresponding mode numbers $N = 2p + |\ell| + 1$ of 2 and 5 respectively.

Next, we pass these beams through a highly aberrated system, a tilted lens, illustrated in Figure 2 (b). This is known to severely distort OAM modes [65] and is routinely used as an OAM detector by breaking the beam into countable fringes [66]. The results at illustrative distances (Z_1 to Z_3) after the lens are shown in Figure 2 (c), for typical tilt angles up to 15° (adjusted to significantly distort the beam). The superimposed intensity and polarisation profiles reveal that while the vectorial structure distorts as one moves towards the far-field, the inhomogeneity as measured by the vectorness does not, corroborated by the vectorness of each beam (reported in the insets), all remaining above 93%, i.e., remaining

fully vectorial as predicted by the unitary nature of the channel.

In contrast we see that the intensity profiles change morphology, and concomitantly polarisation structure. This change can be explained by the coupling of modes outside the original subspace by virtue of the channel operator: the channel scatters the original OAM modes into new mode sets that maintain the same mode number as the input modes. We can visualise this using the Higher Order Poincaré (HOP) Sphere, a geometric representation of vectorial structured light [67, 68]. The case for $\ell = \pm 4$ is shown in Figure 3 as an illustrative example. The initial cylindrical vector vortex beam is visualised as an equatorial vector of unit length (a pure state), shown in Figure 3 (a). The channel (our tilted lens) maps this initial state to a new field, shown in Figure 3 (b), expressed across multiple HOP Spheres, illustrated in Figure 3 (c).
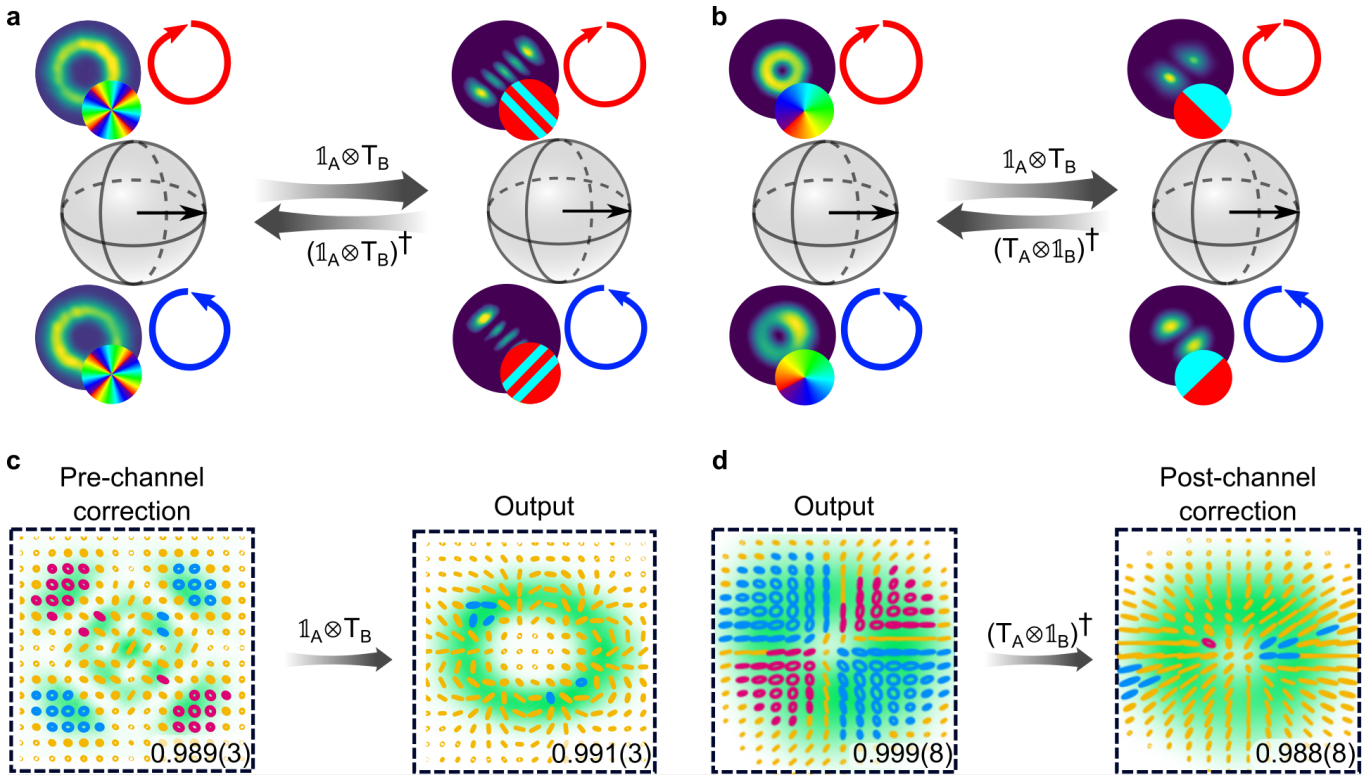
FIG. 4: **The unitary channel mapping and its inversion.** The unitary channel (tilted lens) $\mathbb{1}_A \otimes T_B$ maps the initial $\ell \pm 4$ vector field from the equator of its corresponding subspace onto a new HOP Sphere spanned by an adjusted basis (shown as experimental images on the poles) where the vectorial structure is also a maximally non-separable pure state. (a) shows the $\ell = \pm 4$ example and (b) the $\ell = \pm 1$ example. Because the unitary channel is a change of basis, the inverse $(\mathbb{1}_A \otimes T_B)^\dagger$ can be applied to map the field back to the original sphere. In (c) the state $(\mathbb{1}_A \otimes T_B)^\dagger |\Psi_{\text{in}}\rangle$ is inserted as a pre-channel correction, resulting in the initial field $|\Psi_{\text{in}}\rangle$ as the output, shown here for $\ell = \pm 4$. In (d) post-channel correction is achieved on the output, shown for $\ell = \pm 1$, where the operation is simply a quarter waveplate, since $\mathbb{1}_A \otimes T_B = T_A \otimes \mathbb{1}_B$ for this subspace.

The new HOP Spheres are made up of all modal pairings that have non-zero modal powers (scattering probabilities). We quantify this by reporting the scattering probabilities and phases for every subspace, shown in Figures 3 (d) and (e), respectively. The initial modes ($\ell_{\text{in}} = \pm 4, p_{\text{in}} = 0$) now only contain $\approx 12\%$ of the total modal power, with new modal subspaces emerging to carry the rest. The HOP Spheres are made of *pairings* of these modes, one on each pole, but not all contribute to the vectorness. To determine the contributing pairs, we measure the vectorness for every possible pairing (there are $N(N-1)/2 = 10$ possibilities), with the results shown as a graph in Figure 3 (f). In the graph, each vertex corresponds to a non-zero state from (d) and the edges represent possible pairings to form a HOP Sphere. The weight of each edge corresponds to the vectorness of that pairing. The initial subspace $(\pm 4, 0)$ is no longer a non-separable state, with a vectorness of 0, while some of the new subspaces (new HOP Spheres) can be as high as 98%, i.e., pure vectorial states. The graph can be re-arranged with the zero weighted edges removed to reveal a $K_{3,2}$ bipartite graph structure with two independent vertex sets,

$\mathcal{U} = \{(\pm 4, 0), (2, 0)\}$ and $\mathcal{V} = \{(\pm 2, 1)\}$, connected by 6 edges (see SI). Thus of the 10 unique subspaces created from the five scattered modes, only six are non-separable states, occurring for mapping combinations of states between $\mathcal{U}$ and $\mathcal{V}$. One can appreciate that this becomes ever more complicated as the complexity of the medium (and modal scattering) increases.

From this conventional perspective the situation is complicated, but only because the original (OAM) basis modes ($\{|u_1\rangle \equiv |\ell\rangle$ and $|u_2\rangle \equiv |-\ell\rangle\}$) are used to form the HOP Spheres. We offer a simplification by recognising the unitary nature of the transformation: one can visualise the action of the channel as a mapping (after the channel operation $(\mathbb{1}_A \otimes T_B)$ to a *single* HOP Sphere spanned by the new vectors forming an *adjusted basis*, $|v_1\rangle$ and $|v_2\rangle$, shown in Figure 4 (a). This mapping is a result of channel state duality, where the new spatial basis states that the non-separable vectorial field maps onto are isomorphic to the basis states of the unitary channel operation [60]. In this new HOP Sphere the state vector is again maximally non-separable and pure. The new adjusted basis states are complex structured light fields

(one may say distorted modes due to the noisy channel), shown as experimental images on the poles. In some special cases the mode may be recognisable: for the $\ell = \pm 1$ state shown in Figure 4 (b) the mapping returns the Hermite-Gaussian modes as the adjusted basis. This is a special case resulting from the symmetry of the example. Pertinently, the initial state vector in the original HOP Sphere, and the new state vector in the adjusted HOP Sphere are both equatorial and of unit length, representing a maximally non-separable pure state. This means that the vectorness remains intact, even if the polarisation structure looks rather different. Our framework explains why the polarisation structure appears to change (a change in HOP Sphere) yet the inhomogeneity does not (the same state vector in each HOP Sphere). Since the mapping is unitary it is possible to invert the action of the channel either as a pre-channel action or post-channel correction, both lossless; conveniently, the experimental steps to determine the channel unitary are straightforward: modal and Stokes projections (see SI and Methods), and may be implemented in a variety of ways, including sophisticated state-of-the-art adaptive approaches [69–71]. Using a pre-channel corrective step, we insert the adjusted basis vectorial mode into the tilted lens and allow the aberrations to unravel it back to the original initial state, shown in Figure 4 (c). For the $\ell = \pm 1$ example the required inversion operator is just a quarter wave plate, which can be derived analytically from Eq. (4) (see SI). The counter-intuitive notion that a polarisation element can be used to correct a channel that acts only on the spatial mode DoF is explained by the fact that the channel correction, $(\mathbb{1}_A \otimes T_B)^\dagger (\mathbb{1}_A \otimes T_B)$ can be rewritten as $T_A^\dagger T_A \otimes T_B^\dagger T_B = (T_A^\dagger \otimes \mathbb{1}_B)(T_A \otimes \mathbb{1}_B)$, so that the post-channel unitary, $T_B^\dagger = T_A^\dagger$, can be applied to the polarisation degree of freedom for $\ell = \pm 1$ (not in general for all modes as this is a special case). The impact of this unitary is shown in Figure 4 (d) as a post-channel correction, restoring the full vectorial initial state.

The role of measurement. Given that the state vector after the channel lives on many HOP Spheres in the original basis, $\{|u_1\rangle \text{ and } |u_2\rangle\}$, but only one HOP Sphere in the adjusted basis, $\{|v_1\rangle \text{ and } |v_2\rangle\}$, it is pertinent to ask in which basis (or HOP Sphere) should one make the vectorial measurement? In the quoted vectorness values thus far, we have circumvented this problem by using a Stokes measurement approach to extract the degree of non-separability [72], with the benefit of sampling in a basis-independent fashion (see Methods). In contrast, many measurements of structured light are basis dependent, e.g., in classical and quantum communication, where the basis elements form the communication alphabet. In Figure 5 (a) we show the outcome of a basis-dependent vectorness measurement (see Methods) in the original basis and in the adjusted basis, using the tilted lens as the channel. We see that for some symmetries the choice of basis has no impact on the outcome, as in
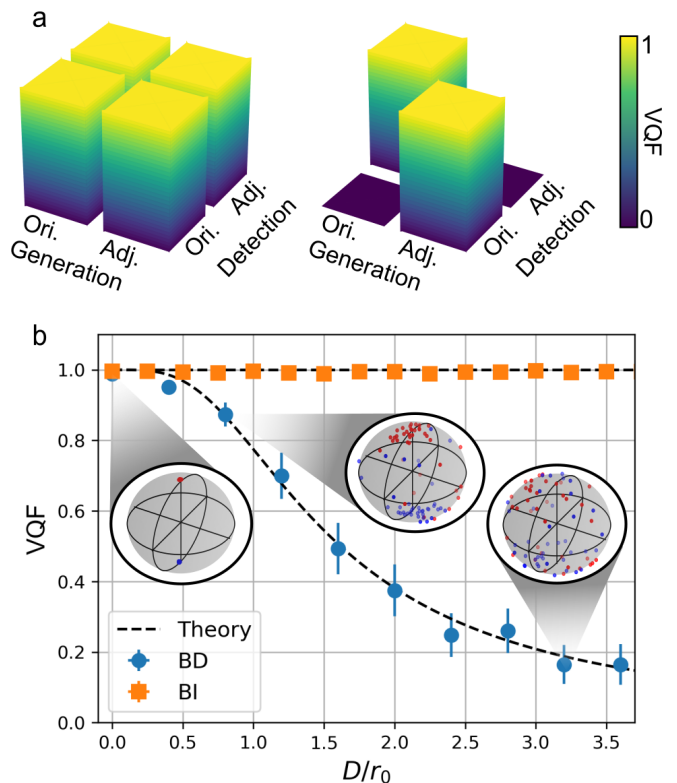
FIG. 5: **The choice of measurement basis.** (a) Measurement of the vectorness in the original (Ori.) and adjusted (Adj.) basis $\ell = \pm 1$ (left) and $\ell = \pm 4$ (right) in the far-field of the tilted lens. (b) Measurement of the vectorness of an initial $\ell = \pm 1$ mode through experimentally simulated atmospheric turbulence as a function of the turbulence strength (D/r_0). A basis-dependent (BD) measurement in the original basis ($\ell = \pm 1$) shows a decay in vectorness, while the basis-independent (BI) approach reveals an invariance. Experimental data (points) show excellent agreement with theory (dashed curves). The insets show the left (red) and right (blue) polarisation projections on the $\ell = \pm 1$ modal sphere for three example turbulence strengths (low, medium and strong). Each point on the spheres represents one instance from the experimental turbulence ensemble. Error bars are plotted as standard deviations from 50 instances of simulated turbulence.

the case of $\ell = \pm 1$, while for other vectorial fields the impact is significant ($\ell = \pm 4$). It should be noted that the $\ell = \pm 1$ beam through a tilted lens is a special case, because in modal space the state vector has simply been rotated. In general, it is the adjusted basis that always reveals the invariance of the vectorness. The failure of the measurement in the original basis is easily explained by the concatenation of the measurement subspace to just one of the many HOP Spheres in which the state resides, and the consequent reduction of the state vector to a mixed and separable state because information is lost

to other OAM subspaces.

Simulated atmospheric turbulence. To make clear that the tilted lens is not a special case, we alter the channel to atmospheric turbulence simulated on a spatial light modulator, and this time measure the vectorness as a function of the turbulence strength in the original basis and in a basis independent fashion, with the result shown in Figure 5 (b). We find that a measurement in the original basis shows a decay in the vectorial nature of the light as the turbulence strength increases, whereas the basis-independent approach reveals the unitary nature of turbulence: while the spatial structure is complex and altered, its vectorness remains intact and invariant to the turbulence strength. Here, all the measurements were performed in the far-field, so that the phase-only perturbations manifest as phase and amplitude effects. We clearly see the paradox: the vectorial structure can appear robust or not depending on how the measurement was done. This result highlights the important role of measurement in determining the salient properties of vectorial light fields.

The inset spheres in Figure 5 (b) show the left (red) and right (blue) state vector projections on the $\ell = \pm 1$ modal sphere [73] for low, medium and strong turbulence. Each instance of a turbulence strength is a red (blue) point, the scatter of which and deviation from the poles is indicative of modal cross-talk. This is a visual representation of why the vectorness decays when one considers only one sphere in the original basis: the original states are orthogonal (points on opposite poles with little scatter) but as turbulence increases they disperse across the sphere, resulting in superpositions of OAM, which become maximally mixed. For example, looking only at the $\ell = \pm 1$ subspace, the state may evolve following (ignoring normalisation): $|R\rangle |1\rangle \rightarrow |R\rangle |1\rangle + i |R\rangle |-1\rangle$ and likewise $|L\rangle |-1\rangle \rightarrow |L\rangle |-1\rangle - i |L\rangle |1\rangle$. The original vectorial state becomes $|R\rangle |1\rangle + |L\rangle |-1\rangle \rightarrow |L\rangle |-1\rangle + i |L\rangle |1\rangle + |R\rangle |1\rangle + |R\rangle |-1\rangle = (|R\rangle + i |L\rangle)(|1\rangle + |-1\rangle))$, which is a scalar, diagonally polarised, Hermite-Gaussian beam with a vectorness of 0. One can deduce from this simple example that if only some modal spaces are considered in the beam analysis, then vectorial modes can reduce to scalar modes, but not vice versa.

In Figure 6 (a) and (b) we show typical cross-talk matrices with and without turbulence, respectively, where the input and output modes are both expressed in the original basis, $\{|R\rangle |u_1\rangle , |R\rangle |u_2\rangle , |L\rangle |u_1\rangle , |L\rangle |u_2\rangle\}$. The cross-talk in (b) is deleterious for both classical and quantum communication. However, the unitary nature of the channel means that there is an adjusted basis, $\{|R\rangle |v_1\rangle , |R\rangle |v_2\rangle , |L\rangle |v_1\rangle , |L\rangle |v_2\rangle\}$, where the state vector is pure. Consequently, a post- or pre-channel unitary can undo the action of the channel, removing the cross-talk, as shown in Figure 6 (c) and (d). The post-channel unitary is simply a measurement in the new adjusted basis, requiring nothing more than a change to the detection optics (holograms in our example) based on the channel under study. In Figure 6 (d), the preparation optics are programmed to prepare the state in the adjusted basis, but measure it in the original basis, once again returning a cross-talk free result. While the action of the channel is to distort the initial beam, as shown in Figure 6 (e), the channel action can be reversed as shown in Figure 6 (f), restoring the initial beam. This is a visualisation of the low cross-talk matrix in part (d): sending in the adjusted basis but measuring in the original basis. The scalar version of the basis modes are shown in Figures 6 (e) and (f) as insets below each polarisation profile, starting with the original modes, which become perturbed due to turbulence. The adjusted basis, with scalar versions shown in the insets of Figure 6 (f), maintains the orthogonality of the modes, and shows the key to the restoration of the initial field. When the adjusted basis is the input, the output is the corrected mode in the original basis. These results suggest that cross-talk free communication is possible with a judiciously selected basis set for the preparation or measurement, exploiting the fact that the vectorial state is intact in the adjusted basis. We use this fact in (g) to encode graphical information using our modal set, send it across the channel, and decode it on the other side. Turbulence causes cross-talk, distorting the image, but this can easily be overcome by simply decoding (measuring) in the adjusted basis, with results shown for medium and strong turbulence. A measurement in the adjusted basis reveals minimal modal decay, minimal cross-talk and high-fidelity information transfer across this noisy channel, with the small deviations due to experimental imperfections.

Demonstrating and exploiting the invariance. Finally, in Figure 7, we show results that highlight the power and versatility of this framework, and the importance of its implications, with full experimental details given in the Supplementary Information. The central message is the invariance of the polarisation inhomogeneity of vectorial light in a wide range of complex media. In Figure 7 (a) we report results on a 200 mm physical path through a heated channel where the induced temperature gradients in the air path results in optical distortions (measured in the far field). Although the medium is dynamically changing, in principle in some unknown manner, the vectorness remains intact, a fact tested across multiple input vectorial states (see SI) and shown in the middle panel for $\ell = \pm 10$. Data was collected at ≈ 38 Hz, with the inset showing a zoomed time window. Controlling the source temperature to alter the aberration strength does not alter the vectorness, shown for $\ell = \pm 1$ and $\ell = \pm 5$ examples in the right panel. We also show results measured in the original modal basis: in this case the invariance is lost, again confirming the important role of measurement in the context of vectorial light.

In Figure 7 (b) we deliver a radially polarised vectorial beam through a setup for optical trapping and tweezing, and introduce aberrations into the path. We show that without any correction the trap stiffness (a measure of
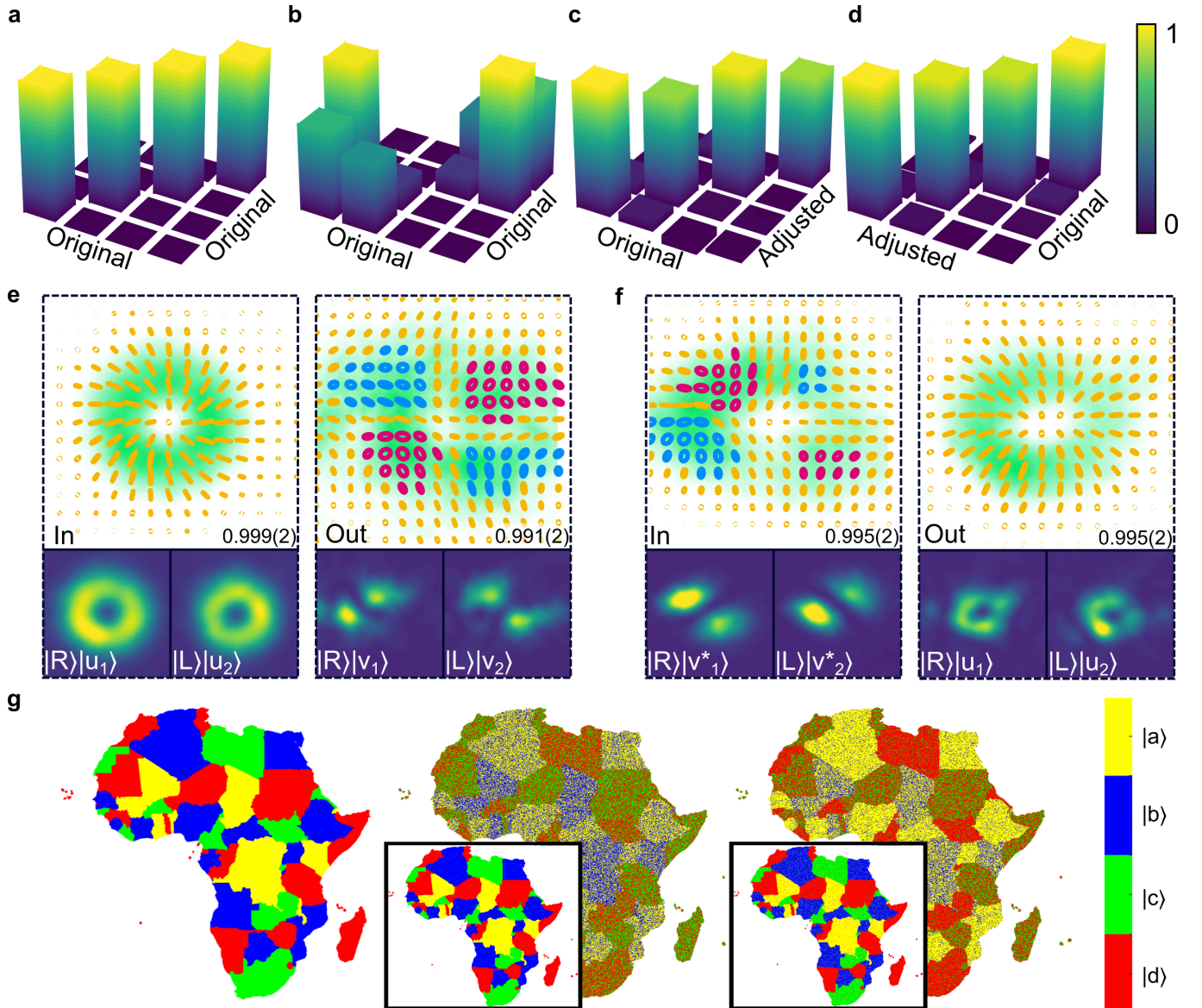
FIG. 6: **Unravelling turbulence.** Cross-talk matrices for preparation and measurement in the original basis for (a) no turbulence and (b) medium turbulence ($D/r_0 = 1.6$). (c) Measuring or (d) preparing in the adjusted basis removes the cross-talk. (e) The unitary action of the channel distorts the polarization structure of the initial beam but not its vectorial homogeneity, with the vectorness given in the insets. Below the polarisation structure are the spatial modes composing the original basis ($u_{1,2}$) and perturbed basis ($v_{1,2}$) along with their polarization states $|R\rangle$ and $|L\rangle$. (f) The unravelling of the turbulence by a lossless unitary applied pre-channel, restoring the initial beam after the turbulence. The adjusted basis modes ($v_{1,2}^*$) and the corrected basis modes ($u_{1,2}$) are shown below the polarisation structures with their respective polarisation states. In (g), an image (left) encoded in the original basis is distorted after transmission through moderately weak (middle) and medium (right) turbulence characterized by $D/r_0 = 1$ and $D/r_0 = 1.6$, respectively. The same image is transmitted through the channel but decoded in the adjusted basis, for distortion-free communication, shown in the insets.

how good the trap is) decreases by $10\times$; after applying a pre-channel unitary transformation we can recover most ($6\times$) of the original trap performance, as illustrated by the restricted motion of the particle in the trap. In our case the adaptive optical routines were rudimentary (explained in the Methods and SI) whereas the state-of-the-

art vectorial adaptive solutions [69–71] promise a much enhanced performance and potentially full recovery.

So far all the channels have acted on the spatial mode and left the polarisation as the unaffected DoF. In Figure 7 (c) we show results after passing $\ell = \pm 1$ vectorial beams through a 1 m length of few-mode optical fibre,
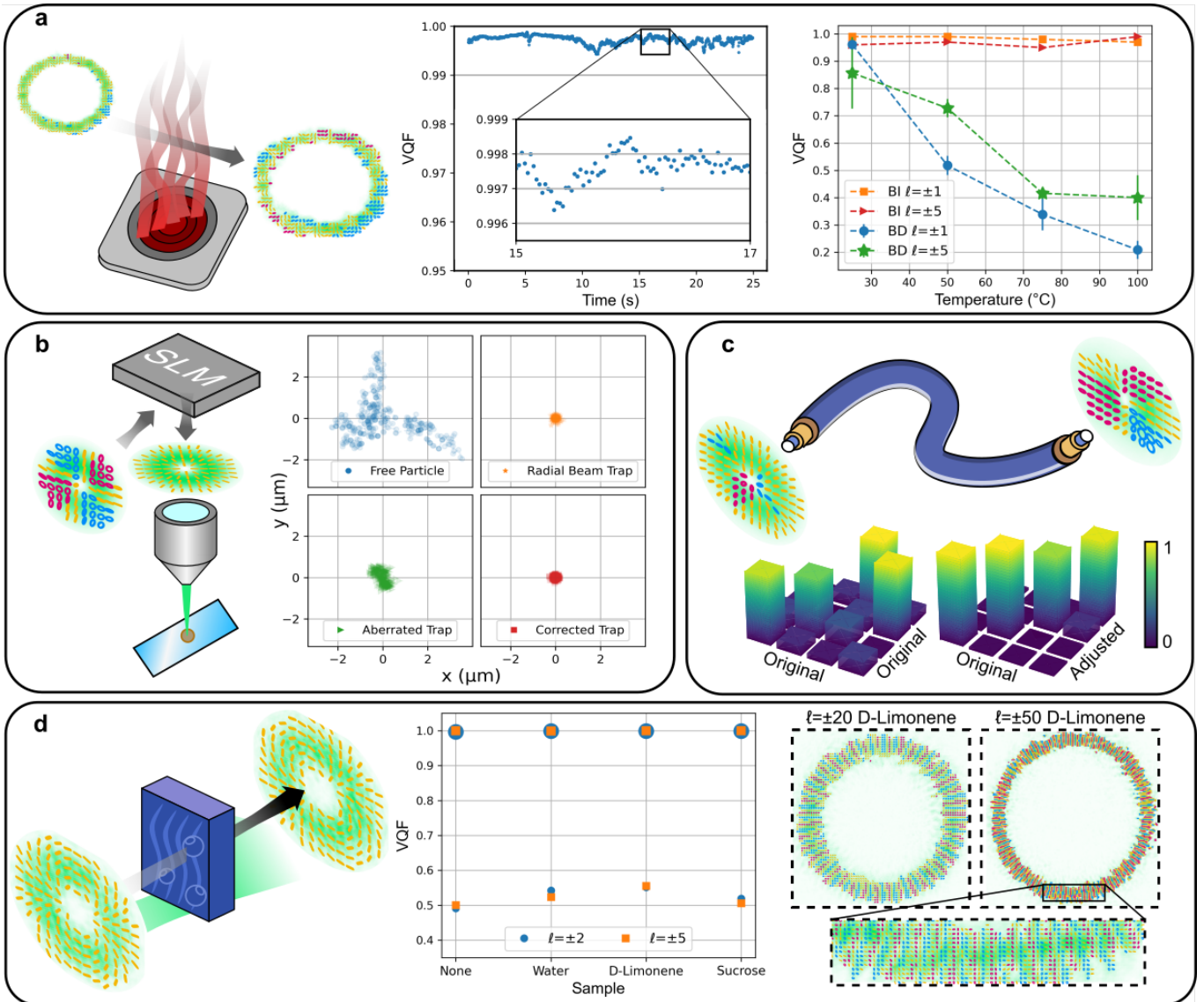
FIG. 7: **Real-world channels.** (a) Measured VQF as a function of time for an $\ell = \pm10$ beam over a temperature controlled hot plate (≈ 200 mm path), with the inset showing a zoomed time window. The right panel shows the averaged VQF for particular temperature settings for $\ell = \pm1$ and $\ell = \pm5$ beams, showing the invariance of the vectorness for a basis independent (BI) measurement, and a decay when measured in a basis dependent (BD) fashion. (b) Particle movement (measured in x and y co-ordinates) in an optical trapping and tweezing system shows a trap stiffness decrease by $10\times$ when aberrated, recovering by $6\times$ when a pre-channel unitary is applied. (c) Delivery of vectorial light through a 1 m length of few-mode optical fibre shows a low Fidelity of 39% due to cross-talk when measured in the original basis, but increasing to 90% when measured in the adjusted basis. (d) After a 50 mm passage through a liquid medium, the vectorness remains intact (for input VQF of 0.5 and 1) even for chiral media such as D-Limonene. The graph shows VQF measurements for $\ell = \pm2$ and $\ell = \pm4$ through various liquids. The insets in the right panel show $\ell = \pm20$ and $\ell = \pm50$ output beams after the D-Limonene sample, both with a VQF above 0.99.

stressed and bent to induce polarisation coupling. The output beams were measured in both the original basis and adjusted basis, with the cross-talk matrices shown for both in the bottom panels. The results show high cross-talk when measured in the original basis (Fidelity of 39%) and minimum cross-talk when measured in the adjusted basis (Fidelity of 90%), confirming that there is a new HOP Sphere where no correction is needed in order to recover the information carried by the state, important for optical communications.

Finally, in Figure 7 (d) we show results after passing vectorial beams through liquid media of 50 mm length,

from water to the chiral media of D-Limonene and Sucrose. In the chiral media, the polarisation is the affected DoF, with a local polarisation rotation of about $40°$, as can be seen in the example data included in the left panel. Regardless of the medium and input beam type, the vectorness remains invariant. The graph (middle panel) shows results for $\ell = \pm 2$ and $\ell = \pm 5$, with input VQFs of 0.5 and 1. The insets on the right show $\ell = \pm 20$ and $\ell = \pm 50$ output beam profiles from the D-Limonene medium, both with a VQF above 0.99.

DISCUSSION AND CONCLUSION

Our results show that vectorial structured light in complex media will evolve from the near-field to the far-field, generally appearing spatially distorted in amplitude, phase and polarisation structure, although unaltered in vectorial inhomogeneity. This is explained by the unitary nature of such channels, mapping the state from a HOP Sphere spanned by the original basis to a new HOP Sphere spanned by an adjusted basis, as if only our perspective has altered. Any measurement in the original basis will show an apparent decay of the vectorness in strongly perturbing media even though the degree of polarisation remains intact - a hidden invariance that can be observed through a judicious measurement. The role of measurement in quantum studies is well appreciated, and here too the vectorness of a classical beam can be found to be high *and* low, seemingly contradictory outcomes, yet both equally valid based on the choice of measurement. This is not only of fundamental importance but also of practical relevance: we have shown how to make a basis choice for preparation and/or measurement to negate modal cross-talk, with obvious benefits in classical and quantum communication across noisy channels, as well as in imaging through complex media.

The argument for robustness of vectorial light in channels where the polarisation is not directly affected is egregious: our quantum notation makes clear that the entire state is altered since its two DoFs are non-separable, in the same way that a true bi-photon quantum state is altered if just one of the two photons is perturbed - both examples of one-sided channels. Our statement is corroborated here by theoretical examples and experimental proof, particularly illustrated by the example of operating on the "unaffected" polarisation DoF to correct the entire vectorial state.

Our analysis has considered unitary complex channels where one of the two DoFs is unaffected, covering a myriad of practical cases. These include channels with absolute losses (the same for each mode), which can be accounted for by a renormalisation, while reduced amplitudes and adjusted phases due to modal or polarisation cross-talk are fully accounted for in the theory. We remark that not all channels are one-sided and unitary, for example in strongly scattering biological systems [74].

Although scattering can in many cases be reversible and thus handled by our theory, there are cases when this will not be true. Here it is the *relative* modal losses of the initial states, say $|L\rangle |\ell\rangle$ and $|R\rangle |-\ell\rangle$, that breaks the reversibility, often due to detection that is either time averaged or inefficient: not all the light is collected, and the deficiency is mode dependent. Such cases may be handled by extending the applied quantum toolbox to cover a two-sided channel, and to introduce tools for mixed quantum states, e.g., quantum state tomographies and purity measures, to cover the non-unitary channels. We also point out that the decay dynamics of the channel can be determined from a non-separable state irrespective of whether the channel is unitary [61]. Thus while the invariance of the vectorness requires that the channel is unitary, the pre- and post-channel correction does not, although it may no longer be lossless. Our work has already revealed the benefit of a quantum framework applied to classical vectorial light, and thus one can anticipate further benefits and insights as the scope is extended.

In conclusion, we have provided a general framework for understanding the impact of aberrations on vectorial light fields, in doing so revealing the unitary nature of many complex media. Our work resolves a standing debate on the robustness of vectorial light in complex media, and will be invaluable to the exploding community working with vectorial structured light and its applications.

MATERIALS AND CORRESPONDENCE

Correspondence and requests for materials should be addressed to AF.

ACKNOWLEDGMENTS

AF thanks the NRF-CSIR Rental Pool Programme.

AUTHORS' CONTRIBUTION

IN, WB, AK (Klug), AM, KS, CRG and AK (Kritzinger) performed the experiments. All authors contributed to data analysis and writing of the manuscript. AF supervised the project.

COMPETING FINANCIAL INTERESTS

The authors declare no financial interests.

METHODS

Vector beam generation. To generate vector beams, a horizontally polarized Gaussian beam from a HeNe laser (wavelength $\lambda = 633$ nm) was expanded and collimated using a $10\times$ objective and a 250 mm focal length lens. The expanded beam was then passed through a half-wave plate (HWP) before being separated into its horizontally (H) and vertically (V) polarized components using a Wollaston prism (WP). The plane at the WP was then imaged onto the screen of a digital micromirror device (DMD - DLP6500) using a 4f system. The separation angle of the polarization components from the WP of $\approx 1^\circ$ resulted in the diffracted 0th order components overlapping. To create a desired scalar component mode of the form $U(\mathbf{r}) = |U(\mathbf{r})| \exp(i\Phi)$, where Φ is the phase of the field and U has maximum unit amplitude, the DMD was programmed with a hologram given by

$$H = \frac{1}{2} - \frac{1}{2}\text{sign}\left(\cos\left(\pi\phi + 2\pi G\right) - \cos(\pi A)\right) \quad (5)$$

with $G(\mathbf{r}) = \mathbf{g} \cdot \mathbf{r}$ a phase ramp function with grating frequencies $\mathbf{g} = (g_x, g_y)$, and $A(\mathbf{r}) = \arcsin(|U(\mathbf{r})|)/\pi$ and $\phi(\mathbf{r}) = \Phi/\pi$ are the respective, appropriately enveloped, amplitude and phase of the desired complex fields at pixel positions $\mathbf{r} = (x, y)$. Holograms for each polarization component (denoted as H_A and H_B) were multiplexed on the DMD, where the grating frequencies (g_x, g_y) could be chosen to cause the H polarized 1st diffraction order from H_A and the V polarized 1st diffraction order from H_B to spatially overlap. This combined 1st order contained our vector field which was subsequently spatially filtered at the focal plane of a 4f imaging system and imaged onto a second DMD. The second DMD was addressed with a single hologram of the same form as $H_{A/B}$ onto which the turbulence phase screens, along with any correlation filters were encoded (a quater-wave plate, QWP, was used to convert H and V polarization to right (R) and left (L) circular respectively). Polarization projections were made using a linear polarizer (LP) and a QWP before the second DMD. The intensities at the Fourier plane were captured using a CCD (FLIR Grasshopper 3) placed at the focal plane of a 2f imaging system.

Non-separability measurements. We measured the non-separability of the vector beams in a basis dependent and independent approach using Stokes parameters and modal decomposition, respectively (see SI for further details). Firstly, to measure the Stokes parameters, we used the reduced set of four Stokes intensities, I_H, I_D, I_R and I_L corresponding to the linearly polarized horizontal (H), diagonal (D) and the circular right (R) and left (L) polarizations. From these measurements we

extracted the Stokes parameters,

$$S'_0 = I_R + I_L \qquad (6)$$
$$S'_1 = 2I_H - S_0 \qquad (7)$$
$$S'_2 = 2I_D - S_0 \qquad (8)$$
$$S'_3 = I_R - I_L. \qquad (9)$$

The four intensity projections were acquired through the use of a linear polarizer (for I_H and I_D) rotated by 0 and $\pi/4$ radians together with a quarter-wave plate (for I_R and I_L), oriented at $\pm\pi/4$ radians relative to the fast axis. Subsequently, the basis independent VQF (equivalently non-separability) was determined from $V = \sqrt{1 - (S_1^2 + S_2^2 + S_3^2)/S_0^2}$, with $S_i = \int S'_i(\mathbf{r})d\mathbf{r}$ being the global Stokes parameters integrated over the transverse plane.

For the basis dependent approach, the overlap between orthogonally polarized projections of the field in question was used as a measure of non-separability, with unity overlap signalling that the field is completely scalar, while a zero overlap indicated a maximally non-separable vector field. This overlap can be characterized by the magnitude of the Bloch vector, s, lying on the surface of a sphere spanned by superpositions of a chosen pair of basis states $|\psi_{1,2}\rangle$. The magnitude can then be seen as a sum-in-quadrature of the Pauli matrix expectation values $\langle\sigma_i\rangle$, as their operation on the basis states gives the unit vectors of the sphere. We can determine these expectation values using projections $\langle P|$ into superpositions of the spatial basis components described by

$$\langle P_j| = \alpha_j\langle\psi_1| + \beta_j\langle\psi_2|. \qquad (10)$$

With $(\alpha,\beta) = \{(1,0),(0,1),\frac{1}{\sqrt{2}}(1,1),\frac{1}{\sqrt{2}}(1,-1),$ $\frac{1}{\sqrt{2}}(1,i),\frac{1}{\sqrt{2}}(1,-i)\}$ for both $|R\rangle$ and $|L\rangle$. These 12 on axis intensity projections are used to calculate the length of the Bloch vector according to

$$\langle\sigma_1\rangle = (I_{13} + I_{23}) - (I_{14} + I_{24}) \qquad (11)$$
$$\langle\sigma_2\rangle = (I_{15} + I_{25}) - (I_{16} + I_{26}) \qquad (12)$$
$$\langle\sigma_3\rangle = (I_{11} + I_{21}) - (I_{11} + I_{22}) \qquad (13)$$

where the i index of I_{ij} corresponds to the $\langle R, L|$ polarization projections and the j index represents the spatial mode projections defined above. The nonseparability is then given by $V = \sqrt{1 - s^2}$. In this work the projections into the right- and left-circular polarization components was achieved using a linear polarizer and QWP. The subsequent spatial mode projections were performed using a correlation filter encoded into a digital micro-mirror device (DMD), and a Fourier lens to produce on-axis intensities I_{ij}.

Adjusted basis measurement. To determine the adjusted basis, the complex amplitude of an aberrated probe field $|\Psi\rangle_{\text{probe}}$ needs to be measured (see SI). This field was approximated using a maximum likelihood estimation procedure, where far field intensities of the right- and left-polarized components of the ideal vector beam through turbulence were captured:

$$I_{\text{probe}}^{R,L} = \langle R, L|\psi(\mathbf{k}=0)\rangle_{\text{probe}} \qquad (14)$$

Where $|\psi\rangle_{\text{probe}}$ denotes the Fourier transform of $|\Psi\rangle_{\text{probe}}$ and $\mathbf{k} = (k_x, k_y)$. Simulated Fourier intensities, $|\psi\rangle_{\text{Zern}}$, of ideal beams modulated by a phase (modelled by possible weighted combinations of Zernike polynomials Z_j),

$$|\Psi_{\pm1}\rangle_{\text{Zern}} = \text{LG}_0^{\pm1}\exp\left(i\sum_j c_j Z_j\right), \qquad (15)$$

were generated (spatial dependence has been omitted). The set of coefficients c_j which lead to the lowest square difference in intensity between the experimental and simulated cases,

$$\chi^2 = (I_{\text{probe}}^R - I_{\text{Zern}}^R)^2 + (I_{\text{probe}}^L - I_{\text{Zern}}^L)^2 \qquad (16)$$

was used to determine the required basis for recovery of the initial beam.

[1] A. Forbes, M. de Oliveira, and M. R. Dennis, Nature Photonics **15**, 253 (2021).

[2] Y. Shen, Y. Hou, N. Papasimakis, and N. I. Zheludev, arXiv preprint arXiv:2103.08431 (2021).

[3] S. Gao, F. C. Speirits, F. Castellucci, S. Franke-Arnold, S. M. Barnett, and J. B. Götte, Physical Review A **102**, 053513 (2020).

[4] H. Larocque, D. Sugic, D. Mortimer, A. J. Taylor, R. Fickler, R. W. Boyd, M. R. Dennis, and E. Karimi, Nature Physics **14**, 1079 (2018).

[5] E. J. Galvez, B. L. Rojec, V. Kumar, and N. K. Viswanathan, Physical Review A **89**, 031801 (2014).

[6] A. Zdagkas, Y. Shen, C. McDonnell, J. Deng, G. Li, T. Ellenbogen, N. Papasimakis, and N. Zheludev, arXiv preprint arXiv:2102.03636 (2021).

[7] S. Keren-Zur, M. Tal, S. Fleischer, D. M. Mittleman, and T. Ellenbogen, Nature communications **10**, 1 (2019).

[8] T. Bauer, P. Banzer, E. Karimi, S. Orlov, A. Rubano, L. Marrucci, E. Santamato, R. W. Boyd, and G. Leuchs, Science **347**, 964 (2015).

[9] T. G. Brown, Progress in Optics **56**, 81 (2011).

[10] J. Wang, F. Castellucci, and S. Franke-Arnold, AVS Quantum Science **2**, 031702 (2020).

[11] E. Otte, C. Alpmann, and C. Denz, Laser & Photonics Reviews **12**, 1700200 (2018).

[12] C. Rosales-Guzmán, B. Ndagano, and A. Forbes, Journal of Optics **20**, 123001 (2018).

[13] A. Forbes and I. Nape, AVS Quantum Science **1**, 011701 (2019).

[14] S. Sederberg, F. Kong, F. Hufnagel, C. Zhang, E. Karimi, and P. B. Corkum, Nature Photonics **14**, 680 (2020).

[15] Y. Fang, M. Han, P. Ge, Z. Guo, X. Yu, Y. Deng, C. Wu, Q. Gong, and Y. Liu, Nature Photonics **15**, 115 (2021).

[16] M. El Ketara, H. Kobayashi, and E. Brasselet, Nature Photonics **15**, 121 (2021).

[17] R. D. Hawley, J. Cork, N. Radwell, and S. Franke-Arnold, Scientific Reports **9** (2019), 10.1038/s41598-019-39118-0.

[18] L. Fang, Z. Wan, A. Forbes, and J. Wang, Nature Communications **12**, 1 (2021).

[19] V. Curcio, L. A. Alemán-Castañeda, T. G. Brown, S. Brasselet, and M. A. Alonso, Nature communications **11**, 1 (2020).

[20] G. Milione, M. P. Lavery, H. Huang, Y. Ren, G. Xie, T. A. Nguyen, E. Karimi, L. Marrucci, D. A. Nolan, R. R. Alfano, *et al.*, Optics Letters **40**, 1980 (2015).

[21] J. Zhang, X. Wu, J. Li, L. Lu, J. Tu, Z. Li, and C. Lu, Journal of Lightwave Technology (2021).

[22] Z. Zhu, M. Janasik, A. Fyffe, D. Hay, Y. Zhou, B. Kantor, T. Winder, R. W. Boyd, G. Leuchs, and Z. Shi, Nature communications **12**, 1 (2021).

[23] Y. Zhao and J. Wang, Optics Letters **40**, 4843 (2015).

[24] N. Radwell, R. Hawley, J. Götte, and S. Franke-Arnold, Nature communications **7**, 1 (2016).

[25] A. M. Beckley, T. G. Brown, and M. A. Alonso, Optics express **18**, 10777 (2010).

[26] C. He, J. Chang, Q. Hu, J. Wang, J. Antonello, H. He, S. Liu, J. Lin, B. Dai, D. S. Elson, *et al.*, Nature communications **10**, 1 (2019).

[27] C. Rosales-Guzmán, X.-B. Hu, A. Selyem, P. Moreno-Acosta, S. Franke-Arnold, R. Ramos-Garcia, and A. Forbes, Scientific Reports **10**, 1 (2020).

[28] J. Chen, Y. Wang, C. Wan, K. Lu, Y. Liu, and Q. Zhan, Optics Communications , 127112 (2021).

[29] H.-J. Wu, H.-R. Yang, C. Rosales-Guzmán, W. Gao, B.-S. Shi, Z.-H. Zhu, *et al.*, Physical Review A **100**, 053840 (2019).

[30] Y. Tang, K. Li, X. Zhang, J. Deng, G. Li, and E. Brasselet, Nature Photonics **14**, 658 (2020).

[31] L. Marrucci, C. Manzo, and D. Paparo, Physical Review Letters **96**, 163905 (2006).

[32] M. G. Nassiri and E. Brasselet, Physical Review Letters **121**, 213901 (2018).

[33] R. C. Devlin, A. Ambrosio, N. A. Rubin, J. B. Mueller, and F. Capasso, Science **358**, 896 (2017).

[34] A. Forbes, Laser & Photonics Reviews **13**, 1900140 (2019).

[35] A. M. Beckley, T. G. Brown, and M. A. Alonso, Optics express **20**, 9357 (2012).

[36] Z. Ma and S. Ramachandran, Nanophotonics **1** (2020).

[37] D. P. Biss and T. Brown, Optics express **12**, 384 (2004).

[38] K. S. Youngworth and T. G. Brown, Optics Express **7**, 77 (2000).

[39] S. Mamani, L. Shi, T. Ahmed, R. Karnik, A. Rodríguez-Contreras, D. Nolan, and R. Alfano, Journal of biophotonics , e201800096 (2018).

[40] I. Gianani, A. Suprano, T. Giordani, N. Spagnolo, F. Sciarrino, D. Gorpas, V. Ntziachristos, K. Pinker, N. Biton, J. Kupferman, *et al.*, Advanced Photonics **2**, 036003 (2020).

[41] N. Biton, J. Kupferman, and S. Arnon, Scientific Reports **11**, 1 (2021).

[42] A. Suprano, T. Giordani, I. Gianani, N. Spagnolo, K. Pinker, J. Kupferman, S. Arnon, U. Klemm, D. Gorpas, V. Ntziachristos, *et al.*, Optics Express **28**, 35427 (2020).

[43] M. A. Cox, N. Mphuthi, I. Nape, N. Mashaba, L. Cheng, and A. Forbes, IEEE Journal of Selected Topics in Quantum Electronics **27**, 1 (2020).

[44] Y. Gu, O. Korotkova, and G. Gbur, Optics letters **34**, 2261 (2009).

[45] W. Cheng, J. W. Haus, and Q. Zhan, Optics express **17**, 17829 (2009).

[46] Y. Cai, Q. Lin, H. T. Eyyuboğlu, and Y. Baykal, Optics express **16**, 7665 (2008).

[47] P. Ji-Xiong, W. Tao, L. Hui-Chuan, and L. Cheng-Liang, Chinese Physics B **19**, 089201 (2010).

[48] T. Wang and J. Pu, Optics communications **281**, 3617 (2008).

[49] M. A. Cox, C. Rosales-Guzmán, M. P. J. Lavery, D. J. Versfeld, and A. Forbes, Optics Express **24**, 18105 (2016).

[50] P. Lochab, P. Senthilkumaran, and K. Khare, Physical Review A **98**, 023831 (2018).

[51] F. Hufnagel, A. Sit, F. Bouchard, Y. Zhang, D. England, K. Heshami, B. J. Sussman, and E. Karimi, New Journal of Physics **22**, 093074 (2020).

[52] F. Bouchard, A. Sit, F. Hufnagel, A. Abbas, Y. Zhang, K. Heshami, R. Fickler, C. Marquardt, G. Leuchs, E. Karimi, *et al.*, Optics express **26**, 22563 (2018).

[53] Y. Ren, L. Li, Z. Wang, S. M. Kamali, E. Arbabi, A. Arbabi, Z. Zhao, G. Xie, Y. Cao, N. Ahmed, *et al.*,

Scientific reports **6**, 1 (2016).

[54] R. J. C. Spreeuw, Foundations of Physics **28**, 361 (1998).

[55] A. Forbes, A. Aiello, and B. Ndagano, Progress in Optics **64**, 99 (2019).

[56] K. H. Kagalwala, G. Di Giuseppe, A. F. Abouraddy, and B. E. Saleh, Nature Photonics **7**, 72 (2013).

[57] X.-F. Qian and J. Eberly, Optics Letters **36**, 4110 (2011).

[58] S. M. Reyes, D. A. Nolan, L. Shi, and R. R. Alfano, Optics Communications **464**, 125425 (2020).

[59] M. McLaren, T. Konrad, and A. Forbes, Physical Review A **92**, 023833 (2015).

[60] M. Jiang, S. Luo, and S. Fu, Physical Review A **87**, 022310 (2013).

[61] T. Konrad, F. De Melo, M. Tiersch, C. Kasztelan, A. Aragão, and A. Buchleitner, Nature physics **4**, 99 (2008).

[62] N. H. Valencia, S. Goel, W. McCutcheon, H. Defienne, and M. Malik, Nature Physics **16**, 1112 (2020).

[63] B. Ndagano, B. Perez-Garcia, F. S. Roux, M. McLaren, C. Rosales-Guzman, Y. Zhang, O. Mouane, R. I. Hernandez-Aranda, T. Konrad, and A. Forbes, Nature Physics **13**, 397 (2017).

[64] Q. Zhan, Advances in Optics and Photonics **1**, 1 (2009).

[65] S. Mamani, E. Bendau, J. Secor, S. Ashrafi, J. J. Tu, and R. R. Alfano, Applied Optics **56**, 2171 (2017).

[66] P. Vaity, J. Banerji, and R. Singh, Physics Letters A **377**, 1154 (2013).

[67] G. Milione, H. Sztul, D. Nolan, and R. Alfano, Physical review letters **107**, 053601 (2011).

[68] A. Holleczek, A. Aiello, C. Gabriel, C. Marquardt, and G. Leuchs, Optics express **19**, 9714 (2011).

[69] C. He, J. Antonello, and M. J. Booth, arXiv preprint arXiv:2110.02606 (2021).

[70] Q. Hu, C. He, and M. J. Booth, Journal of Optics **23**, 065602 (2021).

[71] A. de Oliveira, N. R. da Silva, R. M. de Araújo, P. S. Ribeiro, and S. Walborn, Physical Review Applied **14**, 024048 (2020).

[72] A. Selyem, C. Rosales-Guzmán, S. Croke, A. Forbes, and S. Franke-Arnold, Physical Review A **100**, 063842 (2019).

[73] M. J. Padgett and J. Courtial, Optics letters **24**, 430 (1999).

[74] C. He, H. He, J. Chang, B. Chen, H. Ma, and M. J. Booth, Light: Science & Applications **10**, 1 (2021).